Design and performance of kinetic inductance detectors for cosmic microwave background polarimetry

Heather McCarrick

Submitted in partial fulfillment of the
requirements for the degree of
Doctor of Philosophy
in the Graduate School of Arts and Sciences

COLUMBIA UNIVERSITY

2018

ABSTRACT

Design and performance of kinetic inductance detectors for cosmic microwave background polarimetry

Heather McCarrick

This thesis presents the development of kinetic inductance detectors (KIDs) for cosmic microwave background (CMB) polarimetry. Increasingly precise measurements of the CMB have led to much of our understanding of the observable universe; future measurements of the CMB will require the development of new detectors as progressively fainter signals are targeted. In particular, a measurement of the primordial B-mode polarization signal, which would offer strong evidence of inflation, will require at least a 50 times increase in detector count. KIDs are an attractive detector option for next-generation CMB experiments due to their low-noise and high-multiplexing factor. In this thesis, I present KIDs optimized for ground-based CMB observations, which are sensitive to a 150 GHz spectral band where the CMB spectrum peaks. This research demonstrates the first systematic studies of lumped-element KIDs (LEKIDs) optimized for CMB surveys and shows the readiness of the detectors for on-sky observations. First, I present the design and performance of horn-coupled LEKIDs, which are sensitive to a single polarization. I show that KIDs can meet the stringent noise and sensitivity requirements necessary for a competitive CMB detector. Second, I present a novel method for reducing crosstalk between LEKIDs, which is important for controlling instrument systematics. Third, I present the design and performance of dual-polarization LEKIDs, which are sensitive to orthogonal polarizations within a single spectral band and double the number of detectors per array, increasing the sensitivity. Finally, I present the initial analysis of millimeter-wave observations of a nearby galaxy cluster, Abell 2443, taken with the LEKID-based NIKA2 instrument on the IRAM 30 m telescope. This is part of ongoing research to make high-resolution measurements of the Sunyaev–Zel'dovich effect, seen as a distortion in the CMB spectrum.

Contents

List of Figures

List of Tables

Acknowledgments

I thank Brad Johnson for his advice and guidance during graduate school. I am also grateful to Max Abitbol, Peter Day, Jeremy Dodd, Daniel Flanigan, Glenn Jones, Michele Limon, Phil Mauskopf, Amber Miller, Tony Mroczkowski, Charles Romero, and Ross Williamson. I thank the Institut de Radioastronomie Millimétrique (IRAM) for hosting me in late 2017. From 2015–2018, I was supported by a NASA Earth and Space Science Fellowship (NESSF).

Thesis Structure

This thesis is organized as follows:

- In Chapter 1, I briefly present cosmology as related to the cosmic microwave background (CMB), and the scientific goals of both current and next-generation CMB experiments, which motivate this work.
- In Chapter 2, I explain the physics governing kinetic inductance detectors (KIDs) and the expected performance.
- In Chapter 3, I give an overview of the experimental system including the cryogenic testbed and readout.
- In Chapter 4, I present the development, testing and analysis of single-polarization, horn-coupled lumped-element kinetic inductance detectors (LEKIDs). This work was published in McCarrick et al. [2014].
- In Chapter 5, I present a novel method for controlling crosstalk in KIDs. This work was published in McCarrick et al. [2016b].
- In Chapter 6, I present the development of dual-polarization KIDs. This work was published in McCarrick et al. [2016a].
- In Chapter 7, I present the design and performance of the dual-polarization LEKIDs, which demonstrate their readiness for on-sky observations. This work was published in McCarrick et al. [2018].

- In Chapter 8, I discuss the initial analysis of observations of Abell 2443, a nearby galaxy cluster, to measure the Sunyaev-Zel'dovich (SZ) effect. The observations were made with the LEKID-based instrument NIKA2 on the IRAM 30 m telescope.

- In Chapter 9, I offer a few concluding remarks and potential pathways forward for KIDs within experimental cosmology.

Chapter 1

Cosmology with the cosmic microwave background

Measurements of the cosmic microwave background (CMB) have informed our understanding of the make-up and evolution of the observable universe. The CMB is nearly uniform radiation from the early universe [Dicke et al., 1965, Penzias and Wilson, 1965] and is close to a perfect blackbody. The CMB has angular temperature anisotropies, which originated from density fluctuations in the early universe [Smoot et al., 1992]. Temperature anisotropy measurements show that the universe can be well described by a Lambda-cold dark matter (ΛCDM) model [Spergel et al., 2003]. The CMB also contains polarization anisotropies, which are commonly decomposed into curl-free and curl components, respectively called E and B-modes. Measurements of E-modes are consistent with a ΛCDM universe [Bennett et al., 2013, Planck Collaboration et al., 2018b]. Primordial B-mode polarization is theorized to have originated from gravitational waves during the time of inflation [Guth, 1981], and, if measured, would provide strong evidence of an inflationary epoch [Kamionkowski et al., 1997]. Measuring this fundamental aspect of the universe will require advances in complementary fields, including device physics. With this motivation, I have focused my work on kinetic inductance detectors (KIDs), a novel superconducting device, which can act

as a photon-noise limited detector for millimeter-wave radiation.

In the remainder of this chapter, I review the physics behind the CMB, the main goals of current and future experiments, and the motivation behind my research. First, I discuss the cosmic microwave background (Sec. 1.1). I pay particular attention to the CMB temperature and polarization anisotropies as well as the Sunyaev-Zel'dovich effect (SZE). Second, I discuss the status of CMB experiments and the detector developments necessary to achieve current and future cosmological goals (Sec. 1.2), which motivate the device physics research in the rest of the thesis.

1.1 Cosmic microwave background

The CMB is radiation from shortly after ($\sim 380,000$ years) the Big Bang and carries information from the early universe [Dodelson, 2003]. The universe was initially comprised of an ionized plasma in which photons and baryons were tightly coupled in thermal equilibrium. During these early times, photons were continuously interacting with electrons. As the universe expanded and cooled, neutral atoms, primarily hydrogen, were formed during the time of recombination. The photons were then decoupled from the baryons, and the universe was no longer ionized nor opaque. Near the end of recombination, photons interacted with baryons a final time and this is referred to as the surface of last scattering. These photons have been free streaming towards us since z = 1100 and comprise the CMB. Imprinted in the statistics of the photons is information not only from the time of last scattering but also from the physical processes both before – such as recombination and, possibly, inflation - and after - such as reionization and secondary scatterings, like the Sunyaev-Zel'dovich effect.

The CMB is a nearly isotropic and homogeneous blackbody as measured by the Far Infrared Absolute Spectrophotometer (FIRAS) on Cosmic Background Explorer (COBE) (Fig. 1.1). The temperature is currently $T_{\rm CMB} = 2.725 \pm .002$ K [Mather et al., 1999] with a spectral peak near 160 GHz and a wavelength of $\lambda_{\rm CMB} = 2$ mm. Additionally, we

know the universe to be not only expanding, but accelerating, from type Ia supernovae observations [Riess et al., 1998, Perlmutter et al., 1999]. These observations support the ΛCDM model.

1.1.1 Anisotropies

The CMB is not perfectly isotropic but contains structure in its temperature as a function of angular position. Further, the polarization of the CMB can be decomposed into curl-free and divergence-free components respectively called E-mode polarization and B-mode polarization [Kamionkowski et al., 1997], both of which have anisotropies. The angular power spectra of temperature, E-mode and B-mode polarizations can constrain the Lambda-Cold Dark Matter (ΛCDM) cosmological parameters that describe the observable universe. Assuming a flat universe ($k = 0$), the ΛCDM parameters are spectral index $n_{\rm s}$, optical depth τ, acoustic angular scale $\theta_{\rm MC}$, adiabatic perturbations amplitude $A_{\rm s}$, and the densities of dark matter $\Omega_{\rm c}h^2$ and baryonic matter $\Omega_{\rm b}h^2$ [Planck Collaboration et al., 2018a].

1.1.1.1 Temperature

The temperature fluctuations, or anisotropies, in the CMB are dependent on angular scale. These fluctuations can be decomposed into spherical harmonics that are a function of the multipole value ℓ, which corresponds to the angular size of the anisotropy. The multipole value ℓ can be approximated $\sim 180^{\rm o}/\theta$, where θ is the angle subtended on the sky. The temperature anisotropy map as measured by Planck is shown in Fig. 1.2a. The temperature angular power spectrum C_ℓ^{TT}, which shows power as a function of angular scale, is plotted in Fig. 1.2b. We note that the size of the largest anisotropy is 10^{-4} times smaller than the average temperature of the CMB. Different physical processes in the primordial plasma correspond to fluctuations on different angular scales and explain the shape of the temperature power spectrum [Dodelson, 2003]. At large scales ($\ell < 180$), the oscillations are due to the Sachs-Wolfe effect. At the surface of last scattering, the density fluctuations and differences

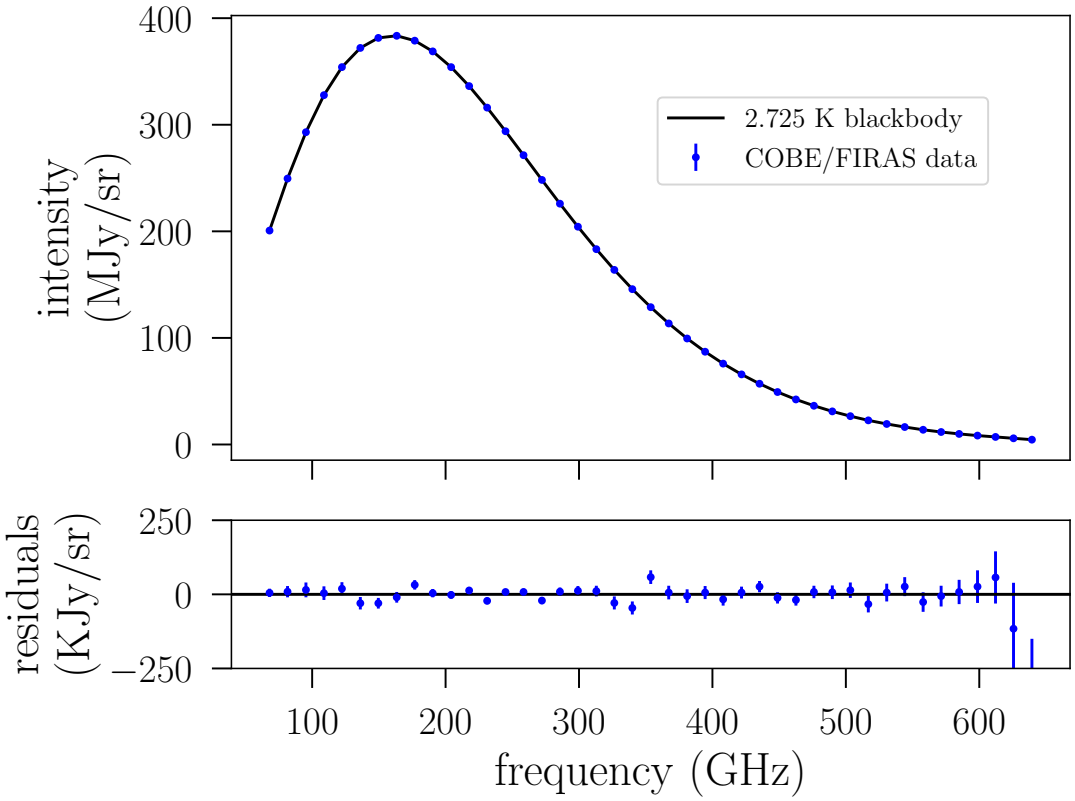

Figure 1.1: Intensity spectrum of the CMB as measured by the FIRAS instrument on the COBE satellite. The CMB is a blackbody with a temperature of 2.725 K and a spectral peak at 160 GHz. The error bars in the top panel are smaller than the points. The residuals, shown in the bottom panel, are 10^{-3} smaller than the measurement. Figure plotted with data from Fixsen et al. [1996].

in gravitational potential caused photons to be Doppler shifted. This created hot and cold spots depending on whether the photon was in a potential minima or maxima and moving towards or away from us. The oscillations at $\ell > 180$ in C_ℓ^{TT} are due to baryon acoustic oscillations (BAO) in the primordial photon-baryon fluid. These oscillations were caused by the alternating inward collapse due to gravity and outward motion due to radiation pressure, which produced standing waves. Finally, the overall damping at high-ℓ is due to photon diffusion during recombination, commonly called Silk damping [Silk, 1968].

The WMAP experiment first measured the temperature anisotropies in the CMB and helped establish the ΛCDM cosmological model. By fitting the cosmological model to the temperature power spectrum, the six primary cosmological parameters can be con-

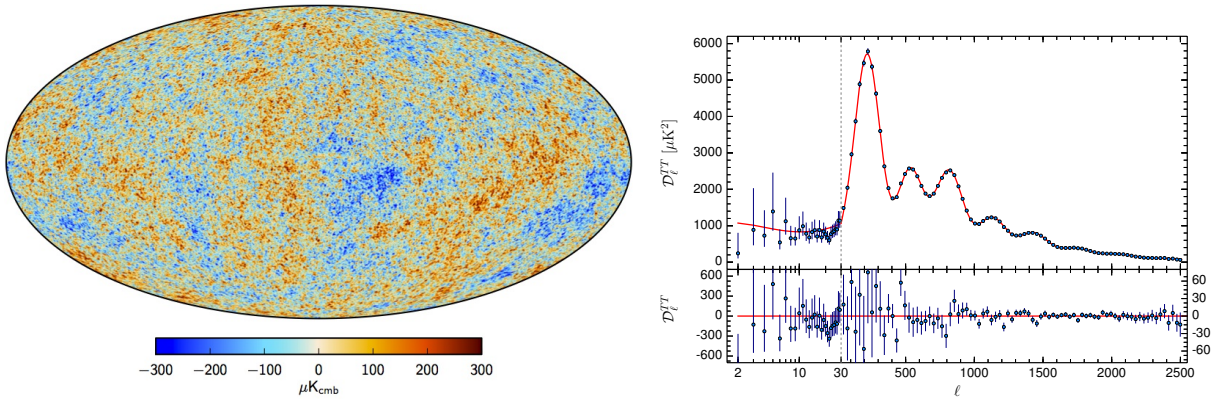

(a) (b)

Figure 1.2: **a.** Temperature map of the CMB as measured by Planck, in combination with data from WMAP and 408 MHz. The temperature anisotropies are plotted relative to the average temperature of the CMB $T_{\rm cmb} = 2.725$ K with the dipole subtracted. **b.** Temperature power spectrum of the CMB as measured by Planck. The red line in the upper panel is the best fit ΛCDM model. The residuals are plotted in the lower panel. Figures from Planck Collaboration et al. [2016a].

strained [Spergel et al., 2003]. Recent results from the Planck satellite are in good agreement with WMAP [Planck Collaboration et al., 2018b]. From the six base ΛCDM parameters, secondary parameters can be calculated, often in combination with BAO data. Planck found the age of the universe is $t = 13.7$ Gyr and the relative energy densities of the universe are matter $\Omega_b = 31.53\%$ and dark energy $\Omega_\Lambda = 68.47\%$. The universe is currently dominated by the cosmological constant Λ and is expanding, with a scale factor that goes as $a(t) \propto \exp(Ht)$, where H is the Hubble constant and $H = \sqrt{\Lambda/3}$.

1.1.1.2 Polarization

The CMB is polarized at a level approximately two orders of magnitude less than the temperature anisotropies. The polarization of radiation can be represented by the Stokes parameters I, Q, U, and V. The Stokes parameter I is the unpolarized light. Q and U represent linearly polarized light, measured at a difference of 45°. Finally, V represents circularly polarized light, which is expected to be zero in the CMB.

The linearly polarized components Q and U can be combined as $Q \pm iU$ and expanded

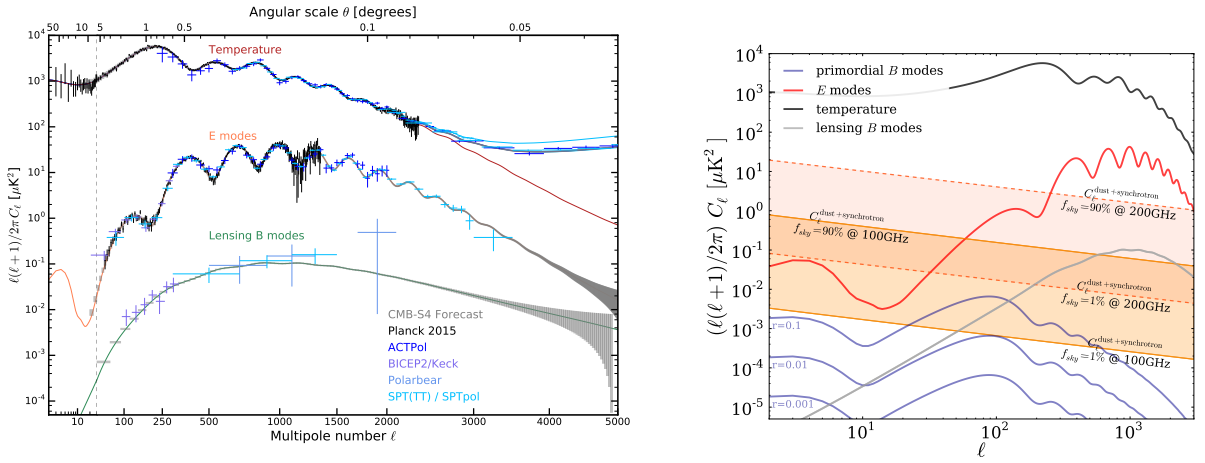

(a) (b)

Figure 1.3: **a.** Measured temperature (TT), E-mode (EE) and B-mode (BB) angular power spectra from current experiments. Temperature and E-mode measurements yield consistent ΛCDM parameters. B-mode polarization from weak lensing of CMB photons has recently been measured. The forecast for CMB-S4, a planned experiment, is shown in grey, assuming r = 0. **b.** Predicted B-mode power spectra for r = 0.1, 0.01, and 0.001. The expected amplitude of the primordial B-mode power spectrum depends on the inflationary model. A measurement of it would provide strong evidence for inflation and the energy scale at which it happened. Also plotted are the expected foreground levels for different sky fractions. The primordial B-mode power spectrum is expected to be below the lensing B-mode and foreground signals, and at least two orders of magnitude fainter than the E-mode signal. Thus measuring the primordial B-mode power spectrum will require cleaning the lensing B-mode and foreground signals. Figures from Abazajian et al. [2016].

much like the temperature anisotropies in terms of spherical harmonics. These can be decomposed into symmetric and antisymmetric components, and the linear combination of the symmetric terms correspond to E-mode polarization and of the antisymmetric terms to B-mode polarization.

The CMB is expected to be linearly polarized due to Thomson scattering in the presence of quadrupole anisotropies during recombination [Zaldarriaga, 2004]. Incident radiation with a quadrupole moment excites an electron, which then re-emits a photon. The re-emitted photons have an overall linear polarization. The quadrupole anisotropies are generated from physical processes from before the surface of last scattering, which we discuss in more detail below.

E-mode polarization

E-mode, or curl free polarization, is expected to arise primarily from velocity gradients, or scalar perturbations, in the photon-baryon fluid. These velocity gradients create quadrupole anisotropies, which, as described above, create a polarized photon through Thomson scattering. The quadrupole anisotropies due to velocity gradients create only E and not B-mode polarization. The E-mode power spectrum C_ℓ^{EE} has been measured by a number of experiment as shown in Fig. 1.3. The bump at $\ell < 20$ is due to polarization induced during reionization. This provides an important constraint on the optical depth τ and the scalar index n_s [Kogut et al., 2003]. The E-mode polarization power spectrum is generally consistent with the ΛCDM parameters yielded by the temperature power spectrum [Planck Collaboration et al., 2018a]. Additional E-mode polarization observations could allow for an independent measurement of the ΛCDM parameters.

B-mode polarization

B-mode polarization is expected to contain an imprint from the time of inflation. Measuring the B-mode polarization angular power spectrum is the focus of most CMB experiments at this time. The inflationary model predicts a period of exponential growth after the Big Bang. Inflation was theorized [Guth, 1981, Linde, 1982, Starobinskii, 1979] as a solution to three observed problems - the flatness, isotropic and monopole problems - which were not addressed by the ΛCDM and the Hot Big Bang models. The inflationary period is expected to have been dominated by a cosmological constant Λ_i. During this time, the scale factor a was an exponential where $a = \exp(H_\mathrm{i} t)$ and H_i is the Hubble constant during the inflationary phase. The size the scale factor increased during inflation is parameterized as e^N, where N is the number of e-foldings and depends on the theoretical model.

It is predicted that quantum fluctuations in an inflationary field ϕ_i generated gravitational waves, or tensor perturbations, during inflation, which produced quadrupole anisotropies. These quadrupole anisotropies cause Thomson scattering that can uniquely produce B-mode polarization. Thus a measurement of the primordial B-mode angular power spectrum C_ℓ^{BB}

would be a probe into the inflationary period. The amplitude of the tensor-to-scalar ratio (i.e. C_ℓ^{BB}-to-C_ℓ^{EE}) is defined as r. The amplitude of r is not well constrained by theory; in Fig. 1.3b, a range of possible r values are plotted. A simple model of the inflationary potential $V(\phi_{\rm i})$ is given as $V^{1/4} \sim 10^{16}(r/.01)^{1/4}$ GeV [Abazajian et al., 2016]. Thus, a measurement of r would yield the energy scale at which inflation occurred and indirectly measure primordial gravitational waves.

B-mode polarization generated by primordial gravitational waves have not yet been measured. As illustrated in Fig. 1.3b, this will be a difficult measurement as there are contaminents at higher amplitudes than any expected primordial B-mode signal. A measurement will first require measuring and removing the lensed B-mode signal and foregrounds. Given the current upper bound is $r < 0.064$ [Planck Collaboration et al., 2018c], the expected primordial B-mode polarization signal is then at least two orders of magnitude less than the E-mode polarization signal. This measurement will require unprecedented sensitivity at millimeter wavelengths [Abazajian et al., 2016].

1.1.2 Sunyaev-Zel'dovich effect

The SZE is secondary scattering of CMB photons by galaxies [Sunyaev and Zeldovich, 1970]. CMB photons that encounter galaxy clusters can be shifted up in frequency and energy. This boost occurs from inverse Compton scattering, in which a CMB photon collides with and gains energy from a high-energy electron. The signature of the thermal SZE (tSZE) is a decrement in intensity at 150 GHz and an increase above 220 GHz, relative to the CMB background. There is also a secondary effect due to the CMB photon interaction with the galaxy cluster: the kinematic SZE (kSZE), in which the photon is Doppler shifted due to the motion of the galaxy cluster.

CMB experiments with relatively small beams ($\sim 1'$) will be able to detect galaxy clusters. Measurements of the SZE have revealed on the order of 1000 galaxy clusters [Planck Collaboration et al., 2016b] and having a larger statistical sample could enable independent

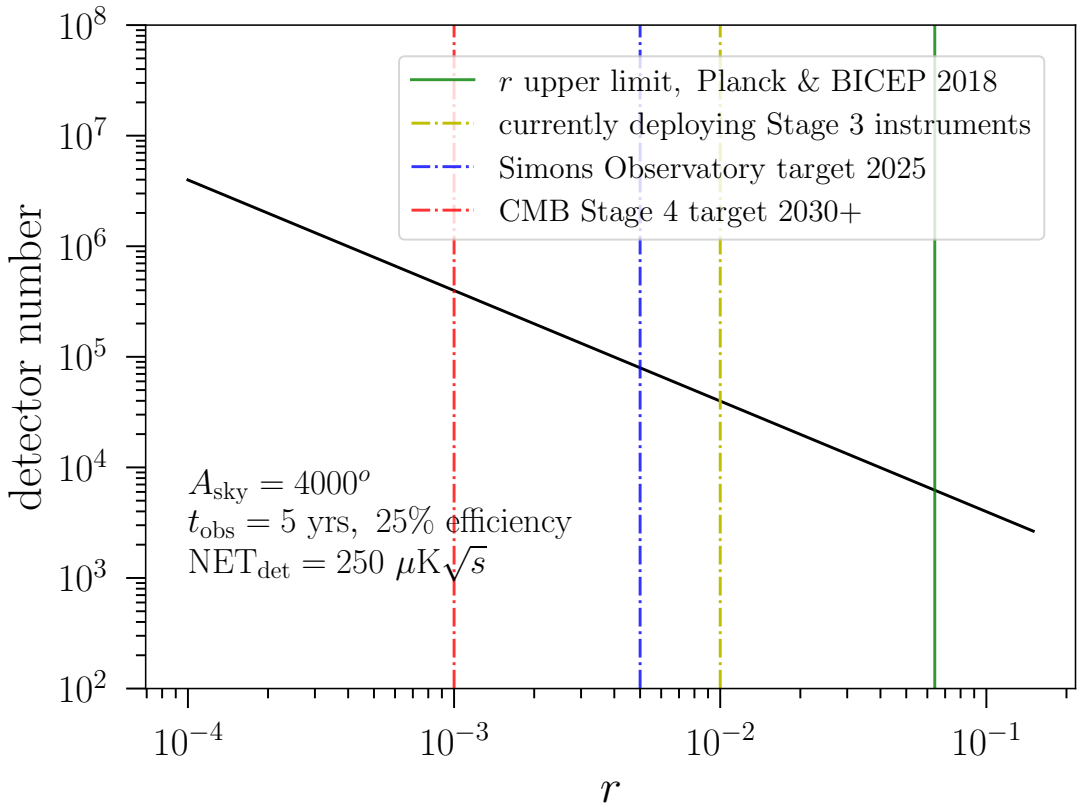

Figure 1.4: Required detector number as a function of targeted tensor-to-scalar ratio r for a ground based experiment. The current upper limit is $r < 0.064$ [Planck Collaboration et al., 2018c], marked in green. Experiments that are currently deploying (yellow), are typically using focal planes of thousands of detectors. These are commonly referred to as 'Stage 3' instruments. The next funded experiment currently under development is Simons Observatory [Galitzki et al., 2018, Simons Observatory Collaboration, 2018], which will target $r = 0.01$ at 3σ and require on the order of 10^4 detectors. Finally, the large-scale experiment being planned by the community is CMB-S4 [Abitbol et al., 2017, Abazajian et al., 2016] and will require at least 4×10^5 to reach the target $r = 0.001$.

constraints on ΛCDM parameters. Large aperture telescopes with narrower beams ($\sim 10''$), which are typically separate from CMB surveys, can resolve clusters and enable studies of galaxy dynamics. In addition, experiments are being planned to measure the kSZE [Stacey et al., 2018], which could also be a probe of dark energy and neutrinos [Bhattacharya and Kosowsky, 2008, Kosowsky and Bhattacharya, 2009].

1.2 CMB experiments

Current CMB experiments are primarily designed to search for the primordial B-mode signal. CMB survey experiments include ACT [Louis et al., 2017], SPT [Simard et al., 2018], BICEP/KECK [BICEP2 Collaboration et al., 2016], CLASS [Harrington et al., 2016], and POLARBEAR [Kermish et al., 2012]. The original experiments are commonly referred to as Stage 2 experiments, and the upgrades taking place (for example, ACT to Advanced ACTPol [Niemack et al., 2010]) are referred to as Stage 3. Simons Observatory [Galitzki et al., 2018] is new, planned experiment, which will be more sensitive than the Stage 3 experiments and bridges to the CMB Stage-4 experiment, which is being planned collectively by the CMB community [Abazajian et al., 2016, Abitbol et al., 2017].

The current upper bound is $r = 0.064$ as set by Planck with the BICEP/KECK experiment [Planck Collaboration et al., 2018c]. Future experiments like Simons Observatory [Simons Observatory Collaboration, 2018] and CMB-S4 [Abitbol et al., 2017, Abazajian et al., 2016] are being designed to target $r = 0.01$ and 0.001, respectively. The B-mode signal peaks around 150 GHz at $\ell = 80$ for recombination and $\ell = 10$ for reionization, which corresponds to ~ 18 and 2^o scales. Gravitationally lensed B-mode polarization, due to the rotation of E into B-mode polarization by galactic masses, has been measured [The Polarbear Collaboration: P. A. R. Ade et al., 2014]. The lensing B-mode signal peaks at $\ell \sim 300$ and will need to be cleaned in order to reach the primordial B-mode signal (see Fig 1.3). In addition, there are two polarized foregrounds – synchrotron radiation (at low frequencies) and galactic thermal dust emission (at high frequencies) – which have higher amplitudes than any expected primordial B-mode polarization signal. The foregrounds generally follow a power-law, with high contamination at low-ℓ, falling off with increasing ℓ. These foregrounds have spectral dependencies, which should allow them to be separated from the CMB polarization signal. However, this requires observations at multiple frequencies in order to accurately measure and subtract the foreground spectra. Current and recent experiments are designed to target and clean at low (~ 5 GHz) [Jones et al., 2018] and high (~ 857 GHz) [Planck Collaboration

et al., 2016a] frequencies but additional measurements are needed. To summarize, detection of the primordial B-mode polarization signal will require observations of multiple frequency bands with multiple angular resolutions.

CMB experiments can be performed from the ground, high-altitude balloons or satellites in space. Ground-based experiments are constrained in both scan strategy and spectral bandwidth. The detector spectral bandwidths are limited by atmospheric lines. The typical mid and high frequency millimeter-wave bands are centered near 150 and 235 GHz with 20% bandwidth. Balloon-borne experiments have lower loading than ground-based experiments as they are above most of the atmosphere. Satellites have the lowest loading and also have access to the full sky and can thus perform low-ℓ measurements.

CMB experiments typically use photon-noise limited detectors. Therefore, to increase instrument sensitivity for future experiments, the number of detectors must be increased, as depicted in in Fig. 1.4. We can approximate the number of detectors needed to measure $r = 0.001$. The noise of a map from an experiment is given in the units nKdeg. Map noise can be forecast as

$$\text{Noise}_{\text{map}} = \frac{\text{NET}_{\text{detector}}\sqrt{A_{\text{sky}}}}{\sqrt{N_{\text{detector}}}\sqrt{t_{\text{obs}}}}, \tag{1.1}$$

where $\text{NET}_{\text{detector}}$ is the noise equivalent temperature (NET) for a single detector, A_{sky} is the sky area observed, N_{detector} is the number of detectors and t_{obs} is the observation time. Typically, a good, ground-based CMB detector will have a $\text{NET}_{\text{detector}} \approx 250\ \mu\text{K}\sqrt{\text{s}}$; an observation time of 5 years with a 25% experiment efficiency for $t_{\text{obs}} = 1.25$ years; and an observed sky area containing a small, clean patch with $A_{\text{sky}} \approx 4000\ \text{deg}^2$ (approximately 10% of the total sky) [Barron et al., 2018]. The tensor-to-scalar ratio $r = 0.001$ at the $\ell = 80$ recombination peak corresponds to a primordial B-mode amplitude of 12 nKdeg. Therefore to achieve a signal-to-noise (SNR) ratio of 3, we would like $\text{Noise}_{\text{map}} = 4$ nKdeg. From this we can calculate that approximately 400,000 photon-noise limited detectors are needed to reach $r = 0.001$.

This is a two order of magnitude increase compared to the number of detectors currently

fielded. To achieve this, it is necessary for there to be advances in detector and readout systems and in this thesis I present a candidate with KIDs. The KIDs discussed in this thesis are optimized for ground-based CMB polarimetry.

1.2.1 Detectors

There are stringent requirements on each part of a CMB experiment and the same holds true for the detectors. The requirements come from three main factors – one, the spectral bands as described above; two, the faintness of the expected signal; and three, preserving the CMB polarization through the experiment. From this, we can elaborate on the requirements for the devices.

CMB telescopes in the millimeter-wave regime use cryogenic focal planes, which are cooled to ~ 0.1 K (see Fig. 1.5), and superconducting detectors. The total noise level of the detector should be below the photon noise due to the random arrivals of photons from the CMB and atmosphere. In addition, the shape of the spectral density of the device noise is important as the device needs to be stable over long periods of long time during observations while also having enough bandwidth to accommodate the astrophysical signals. The device must be responsive enough to detect small changes in sky intensity while at the same time having a large enough linear range that it does not saturate due to large changes in load from the atmosphere or ground pick-up. Finally, the detectors should have high absorption and polarization efficiencies to increase mapping speed.

Current CMB experiments typically use transition-edge sensor (TES) bolometers as the detectors [Irwin and Hilton, 2005]. TES bolometers are proven to have the above qualities and have produced precise CMB measurements. However, there are a number of limitations: they have relatively low multiplexing factors (on the order of 1:64), multi-stage cryogenic electronics, and expensive multi-layer fabrication. As discussed, future experiments plan to increase the number of fielded detectors by two orders of magnitude - from thousands to hundreds of thousands - and current detectors are not easily scalable to accommodate this.

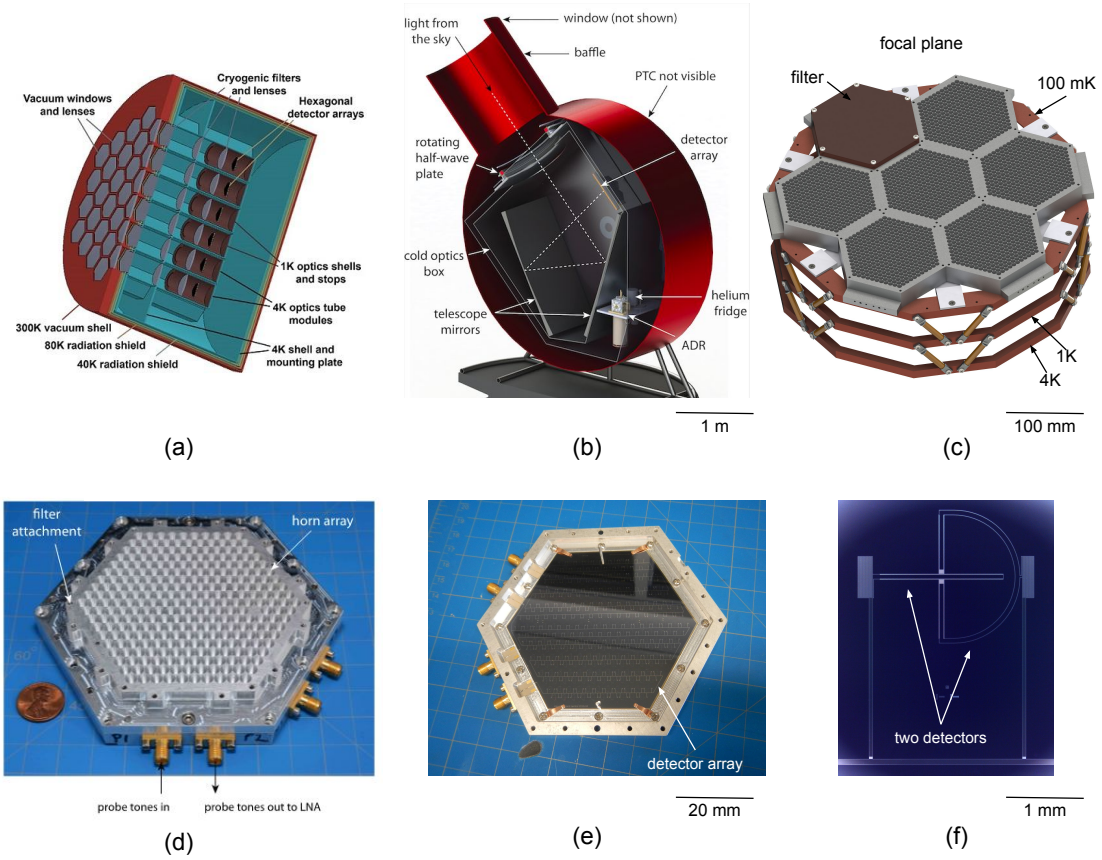

Figure 1.5: **a.** Concept of a receiver for CMB-S4, the next-generation CMB experiment the community is building towards. In order to measure $r = 0.001$, approximately 5×10^5 detectors are needed. This would require a large receiver like this, with 50 optics tubes, which could hold 10^5 detectors. Each optics tube would hold a focal plane, likely to be similar to the hex-packed version shown in panel c. Figure from Abitbol et al. [2017]. **b.** Cross-sectional view of a smaller, concept CMB telescope, which shows the components typical of a CMB experiment. CMB telescopes have cryogenic receivers with the focal planes cooled to ~ 0.1 K. To couple light to the focal plane, experiments use mirrors, lenses or a combination, many of which are cooled to 4 K to reduce loading on the detectors. Figure from Araujo et al. [2014]. **c.** Rendering of a hex-packed focal plane. This focal plane is comprised of 7 modules. The horn apertures are facing up. The modules are typically square or hexagonal for efficient use of the focal plane area. Each focal plane contains thousands of detectors. **d.** Photograph of a single focal plane module with the horn array facing up. This is a LEKID module, similar to those discussed in Ch. 7. Focal plane modules in current experiments look similar from the outside, in that horns or lenses are typically used to couple the light to the detectors. LEKIDs are an attractive detector option for future experiments because each module can be read out using a single pair of coaxial cables; the SMAs to which the cables connect are visible in the photo. With the current detectors used for CMB experiments, focal planes typically require hundreds of wires. **e.** Photograph of a LEKID array with the horn array removed. CMB experiments typically use 100 or 150 mm diameter, monolithic arrays of detectors. In this array, there are $\sim$ 500 LEKIDs. **f.** Photograph a dual-polarization LEKID, which is discussed in Ch. 7. CMB detectors are typically on the size of an incident wavelength (2 mm). Modern CMB experiments use superconducting detectors that are photon-noise limited.

KIDs provide an alternative option for future experiments. First, KIDs have been demonstrated to achieve high-multiplexing factors of up to 1000 [Gordon et al., 2016, van Rantwijk et al., 2016], enabling an entire, monolithic array of detectors to be read out with a single pair of coaxial lines. Fewer wires going to the cold-stage have additional benefits including lower heat loads that result in simpler cryogenics and fewer readout systems. Second, KIDs have simple cold-electronics, with a single, cold amplification stage. Third, the design of many KID arrays are simple to fabricate, potentially leading to increased yield and decreased cost.

In the next chapter, I physically motivate KIDs and show that they should be able to achieve the necessary qualities of a CMB detector. Subsequently, in the rest of this thesis, I present KID designs and measured performance, experimentally demonstrating their readiness for astrophysical observations in the millimeter-wave regime.

Chapter 2

Kinetic inductance detectors

In this chapter, I review the physics of KIDs and follow the signal chain from the absorption of a photon through the measured KID response. First, I present an overview of KIDs. Second, I introduce the relevant physics of superconductors necessary to understand the devices (Sec. 2.2). To do this, I cover some important effects of superconductivity as explained by Bardeen–Cooper-Schrieffer (BCS) theory (Sec. 2.2.1). Then, superconductivity is framed in terms of electrodynamics by Mattis-Bardeen theory, from which we can express the complex conductivity of the film as function of quasiparticle density (Sec. 2.2.3). From there, we can relate the complex conductivity to the surface impedance of the film, which is probed by the readout tone via the resonator (Sec. 2.2.3). Third, I present the resonator model and its parameters which allow us to characterize the resonator and measure its response (Sec. 2.3). Fourth, I describe the detector properties of the KID as related to their application as photon detectors: this includes relating the absorption of photons to the observable resonator parameters and forecasting the expected noise (Sec. 2.4). While aspects of this chapter and the equations within it show up again in this thesis, they are presented here more comprehensively and with greater context in order to give the reader a better understanding of the research in the remainder of the thesis.

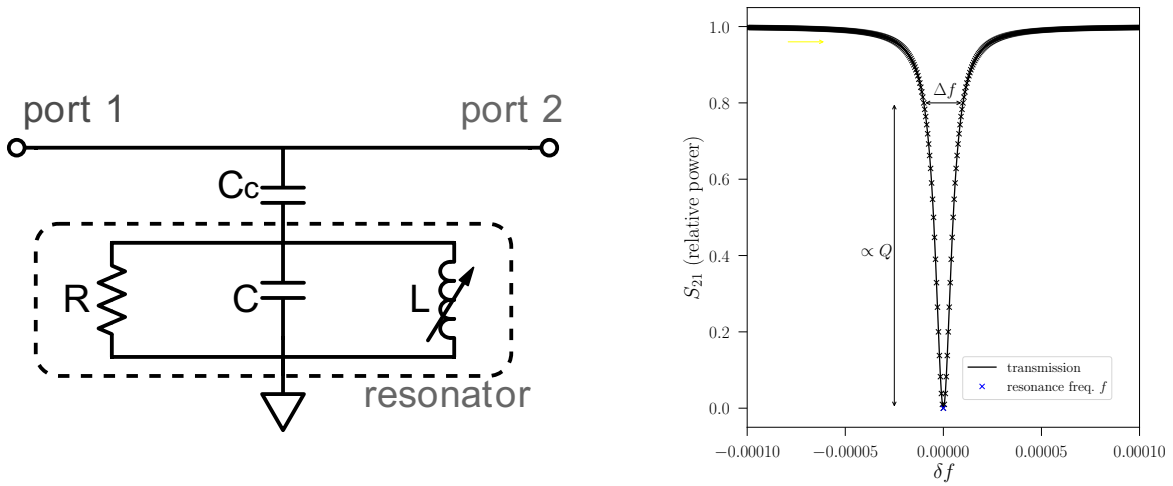

(a) (b)

Figure 2.1: **a.** Circuit diagram of a single KID. The KID is an RLC resonator circuit with a resonance frequency f_0. The inductance L is the sum of both the geometric inductance L_g and kinetic inductance L_k. The resonator is capacitively coupled to a transmission line from which a probe tone excites the resonator. An incoming photon can break Cooper pairs in the superconductor, changing the kinetic inductance L_K and resistance R and thus the resonator f_0 and Q. **b.** Transmission or S_{21} plot showing the resonance of a single KID. The KID has a resonance frequency f_0, and a quality factor $Q \approx f_0/\Delta f$, where Δf is the width of a the resonance. The depth of the resonance gives a sense of the resonator Q.

2.1 Overview

A KID is a highly-sensitive photon detector, which can be optimized for astrophysical observations. The detector is a planar, superconducting resonator with a resonance frequency f_0, as shown in Fig. 2.1. Below its critical temperature T_c, a superconductor has a kinetic inductance L_k, which can be a significant fraction α_k of the total inductance L. The kinetic inductance arises from the Cooper pairs in the superconductor with a density n_{cp}. The unpaired electrons, or quasiparticles, have a density n_{qp}. Photons with an energy greater than the gap energy of the material $\Delta_0 = 1.76 k_B T_c$, where k_B is the Boltzmann constant, can break Cooper pairs, which changes n_{qp}. This changes the complex conductivity σ of the superconductor. This change is reflected in a shift in the detector f_0 and Q, which can be measured by monitoring the probe tone that drives the resonator. A schematic of the signal chain, from the absorption of a photon through the measured response of the detector, is

$$\delta P \rightarrow \delta n_{\rm qp} \rightarrow \delta\sigma_2 \rightarrow \delta L_{\rm K} \rightarrow \delta Z_{\rm s} \rightarrow \delta f_0 \rightarrow \delta\theta \rightarrow \delta{\rm Im}(S_{21}) \rightarrow \delta x$$

Figure 2.2: Schematic illustrating how a change in absorbed power P is detected. The absorbed power P breaks Cooper pairs, increasing the quasiparticle density $n_{\rm qp}$. This causes a change in the imaginary part of the conductivity σ_2, which effects both the kinetic inductance $L_{\rm K}$ and thus the surface impedance $Z_{\rm s}$ of the resonator. This shifts the resonator frequency f_0. The resonator probe tone detects this shift as a change in phase $\delta\theta$, which is captured by the imaginary part of the S_{21} value. This measured value gives the resonator fractional frequency response x. In this chapter, we find the relationships between these parameters.

shown in Fig. 2.2. KIDs are naturally multiplexable as each resonator on an array is designed to have a unique f_0, which is typically achieved by giving each resonator a different capacitor. The probe tones for all the detectors on an array are simultaneously sent down and read out on a single transmission line, which enables the high multiplexing factors.

2.2 Superconducting films

2.2.1 Superconductivity

Below $T_{\rm c}$, electrons in a superconductor are paired into Cooper pairs, which have bosonic properties [Tinkham, 2004]. The Cooper pairs form due to phonon-electron interactions. A free electron will attract a phonon which in turn attracts another electron. The two electrons become weakly coupled and have a minimum size given by the coherence length ξ_0.

In a superconductor, there is an energy gap of Δ_0 on either side of the Fermi energy $E_{\rm f}$. The energy which binds a Cooper pair is given as

$$2\Delta_0 = 3.5 k_{\rm B} T_{\rm c}, \tag{2.1}$$

where Δ_0 is the binding energy at $T = 0$. Relative to $E_{\rm f}$, Cooper pairs will have energy

$E_{\rm cp} < -\Delta_0$, while quasiparticles must have energies $E_{\rm qp} > \Delta_0$. In order to break a Cooper pair, the electrons must absorb energy $E > 2\Delta_0$. This corresponds to a photon with a frequency $\nu > 2\Delta_0/h \approx (T_{\rm c}/1\ {\rm K})74$ GHz.

At non-zero temperatures but below $T_{\rm c}$, Cooper pairs can be thermally broken into two electrons, or quasiparticles. The quasiparticle density is calculated using statistical mechanics. The distribution of quasiparticles is given by the Fermi-Dirac distribution

$$f(E) = [\exp(E/k_{\rm B}T) + 1]^{-1}. \tag{2.2}$$

From BCS theory, the density of states for a superconductor is

$$\rho(E) = \frac{E}{\sqrt{E^2 - \Delta^2}}, \tag{2.3}$$

where Δ is the gap energy at $0 < T < T_{\rm c}$, which we usually approximate as Δ_0. With these two equations, $n_{\rm qp}$ is calculated as

$$n_{\rm qp} = 4N_0 \int_0^\infty f(E)\rho(E){\rm d}E = 4N_0 \int_\Delta^\infty \frac{E}{\sqrt{E^2 - \Delta^2}} \frac{1}{\exp(E/k_{\rm B}T) + 1}{\rm d}E. \tag{2.4}$$

Here, N_0 is the material-dependent single-spin density of states at the Fermi energy. This integral can be approximated as [Noroozian et al., 2012]

$$n_{\rm qp}(T) \approx 2N_0\sqrt{2\pi k_{\rm B}T\Delta_0}\exp(-\Delta_0/(k_{\rm B}T)). \tag{2.5}$$

Superconductors can be described by a two-fluid model, in which the superconducting fluid, with a density $n_{\rm s}$, and normal fluid, with a density $n_{\rm n}$, are treated separately [Tinkham, 2004]. The complex conductivity of a superconductor in electromagnetic field with angular frequency ω can be expressed as $\sigma(\omega) = \sigma_1 - i\sigma_2$, where σ_1 and σ_2 are the real and complex

parts, respectively. This can be written in terms of the fluid densities as:

$$\sigma_1 = \frac{n_\mathrm{n} e^2 \tau_\mathrm{n}}{m_\mathrm{e}} \tag{2.6}$$

$$\sigma_2 = \frac{n_\mathrm{s} e^2}{m_\mathrm{e} \omega} \tag{2.7}$$

We can see that the real part σ_1 is due to the normal component and the imaginary part σ_2 is due to the superconducting component. A superconductor has zero DC resistance ($\omega = 0$) at temperatures $T < T_\mathrm{c}$, and we can see this property is recovered in the above equations. The two fluids can be thought of as being in parallel with n_n producing a resistance R and n_s producing an inductance L_K; this is modeled in the KID circuit in Fig. 2.1.

In a superconductor, the penetration depth λ is the characteristic depth a field can enter the material. The superconducting part of the metal is made up of Cooper pairs, which have a mass $2m_\mathrm{e}$, where m_e is the mass of a single electron. In a penetrating AC field with frequency ω, Cooper pairs lag behind the changing electric field due to their inertia. This lag stores energy in the Cooper pairs and will appear as the inductive impedance discussed above. While the two-fluid model is instructive, a more accurate expression of the conductivity of a superconductor is needed to understand the behavior of KIDs.

2.2.2 Mattis-Bardeen conductivity

Mattis-Bardeen (MB) theory explains the electrodynamic properties of superconductors [Mattis and Bardeen, 1958] and allows us to accurately relate the complex conductivity of the superconductor σ to the quasiparticle density n_qp. Following Gao [2008] and Noroozian [2012], MB theory expresses the ratio σ_1 and σ_2 to the normal state conductivity σ_n as

$$\frac{\sigma_1}{\sigma_\mathrm{n}} = \frac{2}{\hbar\omega} \int_\Delta^\infty \frac{E^2 + \Delta^2 + \hbar\omega E}{\sqrt{E^2 - \Delta^2}\sqrt{(E+\hbar\omega)^2 - \Delta^2}} [f(E) - f(E+\hbar\omega)] \mathrm{d}E \tag{2.8}$$

$$\frac{\sigma_2}{\sigma_\mathrm{n}} = \frac{1}{\hbar\omega}\int_{\Delta-\hbar\omega}^{\Delta} \frac{E^2+\Delta^2+\hbar\omega E}{\sqrt{\Delta^2-E^2}\sqrt{(E+\hbar\omega)^2-\Delta^2}}[1-2f(E)]\mathrm{d}E. \tag{2.9}$$

In the limit $\hbar\omega \ll \Delta$, $k_\mathrm{B}T \ll \Delta$, the integrals can be solved as

$$\frac{\sigma_1}{\sigma_\mathrm{n}} = \frac{4\Delta}{\hbar\omega}\exp(-\Delta/(k_\mathrm{B}T))\sinh(\xi_0)K_0(\xi_0) \tag{2.10}$$

$$\frac{\sigma_2}{\sigma_\mathrm{n}} = \frac{\pi\Delta}{\hbar\omega}\big[1-2\exp(-\Delta/(k_\mathrm{B}T))\exp(-\xi_0)I_0(\xi_0)\big]. \tag{2.11}$$

Here, K_0 and I_0 are the zeroth-order modified Bessel functions of the first and second kind, respectively, and the coherence length is $\xi_0 = h\omega/2k_\mathrm{B}T$. We can now find the relation between σ_1 and σ_2 with n_qp using Eq. 2.5, which yields

$$\frac{\sigma_1}{\sigma_\mathrm{n}} = \frac{n_\mathrm{qp}}{N_0\hbar\omega}\sqrt{\frac{2\Delta_0}{\pi k_\mathrm{B}T}}\sinh(\xi_0)K_0(\xi_0) \tag{2.12}$$

$$\frac{\sigma_2}{\sigma_\mathrm{n}} = \frac{\pi\Delta_0}{\hbar\omega}\Big[1-\frac{n_\mathrm{qp}}{2N_0\Delta_0}(1+\sqrt{\frac{2\Delta_0}{\pi k_\mathrm{B}T}}\exp(-\xi_0)I_0(\xi_0))\Big]. \tag{2.13}$$

Here, we have made use of the approximation that $\Delta \approx \Delta_0[1+n_\mathrm{qp}/(2N_0)\Delta)]$ and ignored the second order n_qp dependence.

To examine the relationship of n_qp with σ_1 and σ_2, we can consider a perturbation from a steady state value. To make this step, we must make the assumption that a perturbation in the quasiparticle distribution function $\delta f(E)$ has the same shape as $f(E)$ [Zmuidzinas, 2012]. We can then write

$$\frac{\delta\sigma_1}{\sigma_1} = \frac{\delta n_\mathrm{qp}}{n_\mathrm{qp}} \tag{2.14}$$

$$\frac{\delta\sigma_2}{\sigma_2-\sigma_2(n_\mathrm{qp}=0)} = \frac{\delta n_\mathrm{qp}}{n_\mathrm{qp}}. \tag{2.15}$$

These equations are essential to understanding the detection of an absorbed photon: a fractional change in the quasiparticle density δn_qp results in a proportional change in the complex conductivity.

2.2.3 Surface impedance

In this section, I present the relationship between the surface impedance Z_s, which we probe via the resonator, and the complex conductivity σ equations derived in the previous section (Sec. 2.2.2) and n_{qp}.

The complex surface impedance is defined as

$$Z_s = R_s + iX_s = R_s + i\omega L_K, \tag{2.16}$$

where R_s is the surface resistance and X_s is the surface reactance. The resistance is due to the quasiparticles, while the inductance is due to the Cooper pairs, as discussed above.

In the thin film limit where the film thickness is $t_f \ll \lambda$, Z_s can be expressed as a function of σ [Gao, 2008, Noroozian, 2012], where

$$Z_s = \frac{1}{\sigma t_f} = \frac{1}{(\sigma_1 - i\sigma_2)t_f} \tag{2.17}$$

From this, we find

$$\frac{\delta Z_s}{Z_s} = -\frac{\delta\sigma}{\sigma}, \tag{2.18}$$

At $T = 0$, $Z_s = iX_s = i\omega L_K$ and $\sigma = -i\sigma_2$. The perturbation δZ_s is defined as $\delta Z_s = Z_s - Z_s(T = 0)$. Near zero temperature, we can write

$$\frac{\delta R_s}{X_s(0)} = \frac{\delta\sigma_1}{\sigma_2(0)} \tag{2.19}$$

$$\frac{\delta X_s}{X_s(0)} = \frac{-\delta\sigma_2}{\sigma_2(0)}. \tag{2.20}$$

Now we would like to show the dependence of the surface impedance on the quasiparticle density. Using the expressions for $\delta\sigma_1$ and $\delta\sigma_2$ (Eqs. 2.14 and 2.15) in combination with the

expressions for σ_1 and σ_2 (Eqs. 2.12 and 2.13), we can rewrite the above in terms of $n_{\rm qp}$ as

$$\frac{\delta R_s}{X_{\rm s}(0)} = \frac{S_1(\omega)}{2\Delta_0 N_0}\delta n_{\rm qp} \tag{2.21}$$

$$\frac{\delta X_s}{X_{\rm s}(0)} = \frac{-S_2(\omega)}{2\Delta_0 N_0}\delta n_{\rm qp}. \tag{2.22}$$

For convenience, we have defined S_1 and S_2 as

$$S_1 = \frac{2}{\pi}\sqrt{\frac{2\Delta_0}{\pi k_{\rm B}T}}\sinh(\xi_0)K_0(\xi_0) \tag{2.23}$$

$$S_2 = 1 + \sqrt{\frac{2\Delta_0}{\pi k_{\rm B}T}}\exp(-\xi_0)I_0(\xi_0). \tag{2.24}$$

The quasiparticle density can be dominated by quasiparticles produced by an optical power P_0. We will show the dependence of $n_{\rm qp}$ on P_0 after the next section, when discussing the resonators as photon detectors. First, we will introduce the resonator parameters, which provide a measurable probe of the surface impedance.

2.3 Resonator circuit and parameters

In this section, I describe the resonator circuit which comprises a KID. I also describe the properties and characterization of a resonator, which will be important when using them as photon detectors.

2.3.1 Resonator circuit

Each KID is a RLC circuit, which is depicted in Fig. 2.1. While KIDs can have various designs, in principle they all have the same components, which can be expressed in different ways. There are two common types of KIDs: microwave KIDs (MKIDs) and lumped-element KIDs (LEKIDs). MKIDs have distributed components along the length of the device.

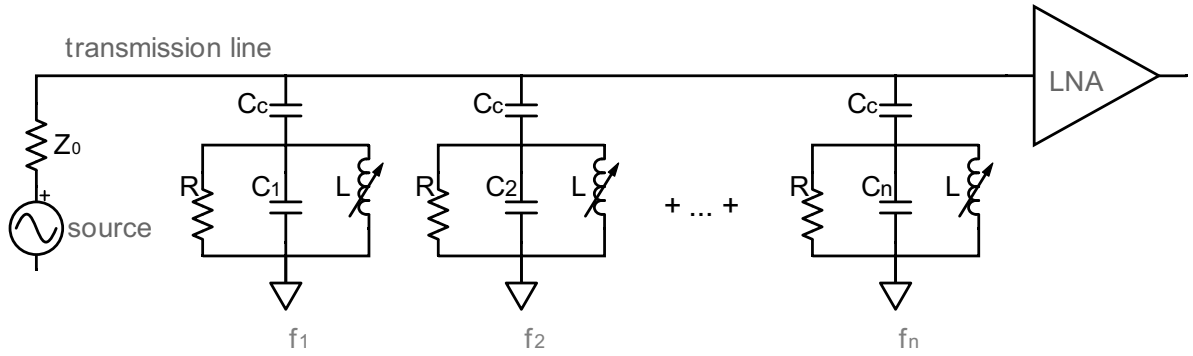

Figure 2.3: Circuit diagram demonstrating how KIDs are multiplexed. Each device has a unique resonance frequency f_0 (f_1, f_2, etc.). In the case of LEKIDs, depicted here, this is due to each device having a unique capacitance (C_1, C_2, etc.). The devices are all coupled to a single transmission line, down which the excitation tones for each resonator are simultaneously sent.

LEKIDs have discrete capacitive and inductive sections and the circuit element dimensions are much smaller than the operating wavelength. LEKIDs can be optimally designed to be direct photon absorbers, using the inductor as an antenna. This thesis focuses on LEKIDs.

The resonance frequency of a RLC circuit is given as

$$f_0 = \frac{1}{2\pi\sqrt{LC}} \tag{2.25}$$

where L is the sum of the kinetic inductance L_{K} and the geometric inductance L_{g}.

The KIDs are multiplexed onto a single transmission line. This is possible because each resonator is designed to have a unique resonance frequency f_0 as is depicted in Fig. 2.3. For a MKID, such as a quarter-wave resonator, this amounts to changing the total length of the resonator. For a LEKID, the device inductor, which is also the absorber, is constant across the resonators, while the capacitor is modified.

2.3.2 Quality factors

The resonator quality factor Q is determined by both the coupling quality factor Q_c and the internal quality factor Q_i. The quality factors add as

$$Q^{-1} = Q_c^{-1} + Q_i^{-1}. \tag{2.26}$$

The internal quality factor Q_i is set by the loss within the resonator. This includes the loss due to quasiparticles produced by the absorption of photons. The coupling quality factor Q_c depends on how strongly coupled the resonator is to the transmission line. The resonator must be sufficiently coupled to the transmission line to be driven by the probe tone but over-coupling will lead to a very diminished Q. We will see that the sensitivity is dependent on Q, as well as the achievable multiplexing factor.

2.3.3 Forwarding scatter parameter S_{21}

The information that we receive about the device is contained in the the forward scattering parameter S_{21}, or the transmission through the circuit. S_{21} is the ratio of the complex voltage at port 2 (see Fig. 2.1), the output of the system, to the complex voltage at port 1, the input:

$$S_{21} = \frac{V_2}{V_1}. \tag{2.27}$$

In Khalil et al. [2012], the forward scattering parameter across a resonator is related to the resonator Q and f_0 parameters. It can be modeled as

$$S_{21} = 1 - \frac{Q}{Q_c}\frac{1}{1 + 2iQx}, \tag{2.28}$$

where $\omega_0 = 2\pi f_0$, $x = (\omega - \omega_0)/\omega_0$, and Q_c is complex. The magnitude of the S_{21} model ($|S_{21}| = [\mathrm{I}^2 + \mathrm{Q}^2]^{1/2}$) is plotted as function of frequency in Fig. 2.4b and we see the expected dip of the resonator. The same data can be mapped to the complex plane IQ as shown

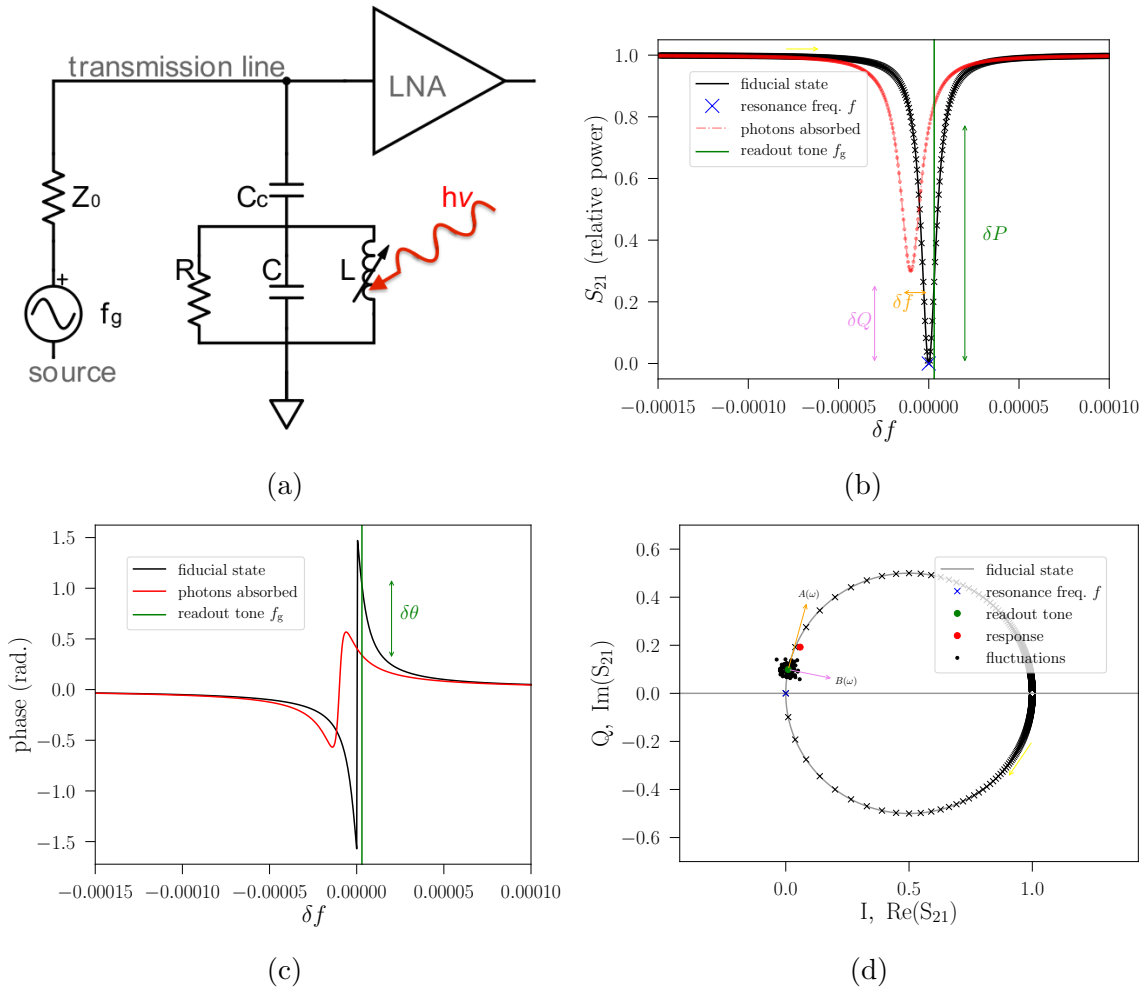

Figure 2.4: **a.** Schematic of the resonator and photon circuit. The resonator directly absorbs photons in the inductor changing the kinetic inductance L_k and resistance R and thus f_0 and Q. **b.** The magnitude of S_{21} plotted as a function of frequency. Each point corresponds to how much power is transmitted through the system at a given frequency. Starting off resonance, S_{21} is 1 as expected. On resonance, we see the characteristic dip of the resonator, as most of the power is coupling into the resonator. As the tone steps off progressively further from the resonance frequency, S_{21} again approaches unity. The readout tone frequency is marked by the vertical green line. As the KID absorbs photons, the total power transmitted changes δP. The same data is shown in the complex plane in panel d. **c.** As the KID absorbs photons, the phase of the probe tone, corresponding to the frequency response, changes by $\delta\theta$. **d.** Frequency sweep for an ideal resonator in the IQ plane. Stepping through the complex plane, we move along the circle clockwise (up in frequency space). The same references are plotted as in panel a. Movement along the circle can be decomposed into normal and tangential components, which correspond to the dissipation $B(\omega)$ and frequency $A(\omega)$ changes. The black dots are represent a 'noise' ball, which is how TOD taken under a relatively stable environment would appear.

in Fig. 2.4d, where the real and imaginary parts of S_{21} correspond to the in-phase (I) and quadrature (Q) components of the signal.

2.4 Detector properties

In this section, I focus on the properties of KIDs as related to their function as photon detectors. First, we calculate the expected response to absorbed photons. Second, we examine how to extract the change in the resonator parameters from the S_{21} data. Third, we forecast the expected performance of the KIDs.

2.4.1 Response to photons

2.4.1.1 Quasiparticle generation

In this part, we calculate the dependence of $n_{\rm qp}$ on absorbed optical power.

The quasiparticles in a superconducting film are generated when Cooper pairs split with a generation rate $\Gamma_{\rm g}$ and are later recombined with a recombination rate $\Gamma_{\rm r}$. In equilibrium, $\Gamma_{\rm g} = \Gamma_{\rm r}$. The paired electrons can be split by either thermal excitations at a rate $\Gamma_{\rm th}$, external photons at a rate $\Gamma_{\rm opt}$, or by the probe tone power at a rate $\Gamma_{\rm p}$ [Zmuidzinas, 2012]. The generation rate is then given by

$$\Gamma_{\rm g} = \Gamma_{\rm th}(T) + \Gamma_{\rm opt}(P_0) + \Gamma_{\rm p}(P_{\rm g}), \tag{2.29}$$

where P_0 is the incident optical power and $P_{\rm g}$ is the readout tone power.

The optical generation rate $\Gamma_{\rm opt}$ is found in the following way. First, we define the absorbed power as $P = \eta P_0$, where η is the optical efficiency of the device. Second, we define the efficiency with which absorbed photons create quasiparticles as $\eta_{\rm pb} = q\Delta/(h\nu)$, where q is the number of quasiparticles. For each Cooper pair broken, two quasiparticles are created. We operate in the limit where a single photon can break one Cooper pair as $h\nu \approx \Delta$, so

$q = 2$. Typically, we use the value $\eta = 0.69$. The optical generation rate is then given by

$$\Gamma_{\mathrm{opt}} = \frac{\eta_{\mathrm{pb}} P}{\Delta}. \tag{2.30}$$

The responsivity of δn_{qp} with respect to δP, can be written as

$$\delta n_{\mathrm{qp}} = \frac{1}{V_{\mathrm{L}}} \frac{\partial N_{\mathrm{qp}}}{\partial \Gamma_{\mathrm{g}}} \frac{\partial \Gamma_{\mathrm{g}}}{\partial P} \delta P \tag{2.31}$$

where $N_{\mathrm{qp}} = n_{\mathrm{qp}} V_{\mathrm{L}}$, the total number of quasiparticles in the active volume V_{L} of the KID. The two terms in the second part of the equation can be solved for using known expressions, which come from solving the quasiparticles dynamics equation [Noroozian, 2012]. We make use of the expressions for n_{qp} and τ_{qp} as a function of τ_{max} and n^*, which are the empirically observed maximum τ_{qp} lifetime and characteristic quasiparticle density of the film [Zmuidzinas, 2012]. The lifetime is expressed as

$$\tau_{\mathrm{qp}} = \frac{\tau_{\mathrm{max}}}{\sqrt{1 + 2\Gamma_{\mathrm{g}} \tau_{\mathrm{max}} / N^*}}. \tag{2.32}$$

For the first term, we use the quasiparticle density equation, into which we substitute the above equation, and take the derivative:

$$n_{\mathrm{qp}} = n^* \sqrt{1 + 2\Gamma_{\mathrm{g}} \tau_{\mathrm{max}} / N^*} - n^* \Rightarrow \frac{\partial N_{\mathrm{qp}}}{\partial \Gamma_{\mathrm{g}}}. = \tau_{\mathrm{qp}} \tag{2.33}$$

For the second, from Eq. 2.29, we have

$$\Gamma_{\mathrm{g}} = \Gamma_{\mathrm{th}}(T) + \frac{\eta_{\mathrm{pb}} P}{\Delta_0} + \Gamma_{\mathrm{p}}(P_{\mathrm{g}}) \Rightarrow \frac{\partial \Gamma_{\mathrm{g}}}{\partial P} = \frac{\eta_{\mathrm{pb}}}{\Delta_0}. \tag{2.34}$$

Putting it together, we find the quasiparticle density dependence on power:

$$\frac{\delta n_{\mathrm{qp}}}{\delta P} = \frac{\eta_{\mathrm{pb}} \tau_{\mathrm{qp}}}{\Delta_0 V_{\mathrm{L}}}. \tag{2.35}$$

2.4.1.2 Resonator response

In this part, we calculate the dependence of f_0 and Q on absorbed optical power.

We probe the change in quasiparticle density via the surface impedance using the resonator properties x and Q_i. First, let us relate x and Q_i to the surface impedance $Z_s = R_\mathrm{s} + iX_\mathrm{s}$ [Noroozian, 2012]. We will use the relations $f_0 \propto L^{-1/2}$ and $X_\mathrm{s} = \omega L_\mathrm{K}$. The geometric component L_g is constant, so any perturbation in L is due to L_K. Thus a perturbation in f_0 can be written as

$$\delta x = \frac{\delta f_0}{f_0} = \frac{-\delta L}{2L} = \frac{-\delta L_\mathrm{K}}{2L} = \frac{-\alpha_\mathrm{k}\delta L_\mathrm{K}}{2L_\mathrm{k}} = \frac{-\alpha_\mathrm{k}\delta X_\mathrm{s}}{2X_\mathrm{s}} \tag{2.36}$$

Similarly, we can use the definition $Q_\mathrm{i}^{-1} = R(wL)^{-1}$. For a perturbation in Q_i, we have

$$\delta Q_\mathrm{i}^{-1} = \frac{\delta R}{\omega L} = \frac{\alpha_\mathrm{k}\delta R}{\omega L_\mathrm{K}} = \frac{\alpha_\mathrm{k}\delta R_\mathrm{s}}{X_\mathrm{s}}. \tag{2.37}$$

We can then find the perturbations δx and δQ_i^{-1} as a function of quasiparticle density n_qp using Eqs. 2.21 and 2.22 and as a function of P using Eq. 2.35. This yields

$$\delta x = \frac{\alpha_\mathrm{k} S_2(\omega)}{4N_0\Delta_0}\delta n_\mathrm{qp} = \frac{\alpha_\mathrm{k} S_2(\omega)\eta_\mathrm{pb}\tau_\mathrm{qp}}{4N_0\Delta_0^2 V_\mathrm{L}}\delta P \tag{2.38}$$

$$\delta Q_\mathrm{i}^{-1} = \frac{\alpha_\mathrm{k} S_1(\omega)}{2N_0\Delta_0}\delta n_\mathrm{qp} = \frac{\alpha_\mathrm{k} S_1(\omega)\eta_\mathrm{pb}\tau_\mathrm{qp}}{2N_0\Delta_0^2 V_\mathrm{L}}\delta P. \tag{2.39}$$

Re-arranging the above equations, we find the responsivity of x and Q_i^{-1} with respect to absorbed optical power P:

$$R_x = \frac{\delta x}{\delta P} = \frac{\alpha_\mathrm{k} S_2(\omega)\eta_\mathrm{pb}}{4N_0\Delta_0^2 V_\mathrm{L}}\tau_\mathrm{qp} \tag{2.40}$$

$$R_{Q\mathrm{i}^{-1}} = \frac{\delta Q_i^{-1}}{\delta P} = \frac{\alpha_\mathrm{k} S_1(\omega)\eta_\mathrm{pb}}{2N_0\Delta_0^2 V_\mathrm{L}}\tau_\mathrm{qp}. \tag{2.41}$$

Comparing R_x and $R_{Q\mathrm{i}^{-1}}$, we can see that the frequency response R_x is a factor of $S_2/2S_1$ larger than the dissipation response and thus is generally used in our experiments. The

quantity S_2/S_1 is referred to as β and is ~ 40 across our bandwidth and temperature range.

Finally, we would like to write R_x as a function of P to understand the expected response of the device under incident power. We assume the generation rate is dominated by the optical signal so $\Gamma_\mathrm{g} = \Gamma_\mathrm{opt} = \eta_\mathrm{pb} P/\Delta_0$ (Eq. 2.30). We can substitute $\tau_\mathrm{qp}(P)$ (Eq. 2.32) into the above equation, which yields

$$R_x = \frac{\alpha_\mathrm{k}\eta_\mathrm{pb}\tau_\mathrm{max}S_2}{4N_0\Delta_0^2 V_\mathrm{L}}\left[1 + \frac{2\eta_\mathrm{pb}\tau_\mathrm{max}}{\Delta_0 N^*}P\right]^{-1/2}. \tag{2.42}$$

We thus see that the response of the device in the frequency direction R_x goes as $P^{-1/2}$.

2.4.2 Measurements

2.4.2.1 Frequency sweep

In practice, we identify the LEKID parameters by taking a frequency sweep. This is done by stepping through the frequencies across the bandwidth of the resonator and measuring the transmitted complex voltage, from which we derive the forward scattering parameter S_{21} at each point. This frequency sweep, or S_{21} sweep, is fit to the resonator model. This yields the resonance frequency f_0, Q, and Q_c of the device.

It is instructive to look at the S_{21} data plotted as a function of frequency and in the IQ plane in Fig. 2.4. Starting off resonance, S_{21} is 1 as expected, and this corresponds to the point (1,0) in the IQ plane. Stepping up in frequency and clockwise in the complex plane, we approach the resonance frequency where $x = 0$ and thus $S_{21} = 1 - Q/Q_\mathrm{c}$. This corresponds to the red x in the plots. As the tone steps off progressively further from the resonance frequency, S_{21} again approaches unity.

2.4.2.2 Time ordered data

In order to measure a change in the KID the following procedure takes place. A resonance tone f_g is placed close to f_0, as determined by the frequency sweep. Time ordered data

(TOD) is then collected at f_g. The readout tone remains at the same frequency f_g and it does not 'track' the resonance frequency. Instead, the complex amplitude of the probe tone changes, as the resonance moves in frequency space, and the tone lands on a different part of the resonance (see Figs. 2.4b and 2.4c).

The TOD of the detector $S_{21}(t)$ in a relatively stable environment will show up as a 'noise ball', as shown on the plot. The vector between two points on the circle can be decomposed into tangent and normal vectors. The vector tangent to the circle corresponds to the response of S_{21} to the change in resonance frequency (dS_{21}/df) and is referred to as the frequency direction. The normal vector corresponds the response of S_{21} to the change in the quality factor (dS_{21}/dQ) and is referred to as the dissipation (or amplitude) direction.

With larger variations in loading, $S_{21}(t)$ will follow a curved path, with a greater response in the frequency direction (see Sec. 2.4.1.2). We use the resonator model (Eq. 2.28) from the frequency sweep to find the time-independent parameter of the resonator, Q_c. Rearranging the resonator model, we have

$$Q_i^{-1}(t) + 2ix(t) = Q_c^{-1}\Big[\frac{1}{1 - S_{21}(t)} - 1\Big] \tag{2.43}$$

The real and imaginary parts of the right hand side then correspond to the dissipation $Q(t)$ and frequency $x(t)$ time ordered data, respectively.

We are usually interested in the fractional frequency fluctuations TOD $x(t)$, which is unitless. This will result in a power spectral density (PSD) in units of Hz^{-1}. This is often referred to as S_{xx}. The PSD in the dissipation direction is referred to as S_{yy}, although we rarely use it for measurements because it is dominated by amplifier noise.

2.4.3 Sensitivity and noise

In this section, we consider the sensitivity of a KID. The sensitivity can be quantified by the noise equivalent power (NEP) which is defined as the amount of power the device can detect

in 0.5 seconds with a signal-to-noise ratio of 1. The individual components contributing to the total NEP add in quadrature. The sources of noise to consider are photon noise, generation-recombination noise, readout noise and nuisance noise sources. For an ideal detector, photon noise would be the largest noise source and the total noise of the other sources would be significantly sub-dominant.

In general, the NEP can be calculated from the spectral density S of the noise and the detector response R as

$$\mathrm{NEP} = \sqrt{S}R^{-1}. \tag{2.44}$$

2.4.3.1 Photon noise

The noise from the arrival of photons is

$$\mathrm{NEP}_{\gamma}^{2} = 2Ph\nu(1 + \eta n_0) \tag{2.45}$$

where B is the bandwidth of the observed spectral band, ν is the central frequency, and n_0 is the photon occupation number. Using $P = \eta n_0 B h\nu$, we can equivalently write

$$\mathrm{NEP}_{\gamma}^{2} = 2h\nu P + 2P^2/B. \tag{2.46}$$

The first term is referred to as shot noise and is due to the uncorrelated arrival of photons. The second term is referred to as wave noise and is due to the correlated arrival of photons.

2.4.3.2 Recombination noise

The fundamental noise limit intrinsic to the device is set by the generation and recombination (g-r) of quasiparticles, which have been excited from an optical or thermal pair-breaking signal. The quasiparticles will combine back into Cooper pairs, maintaining the steady state density $\bar{n}_{\mathrm{qp}}$.

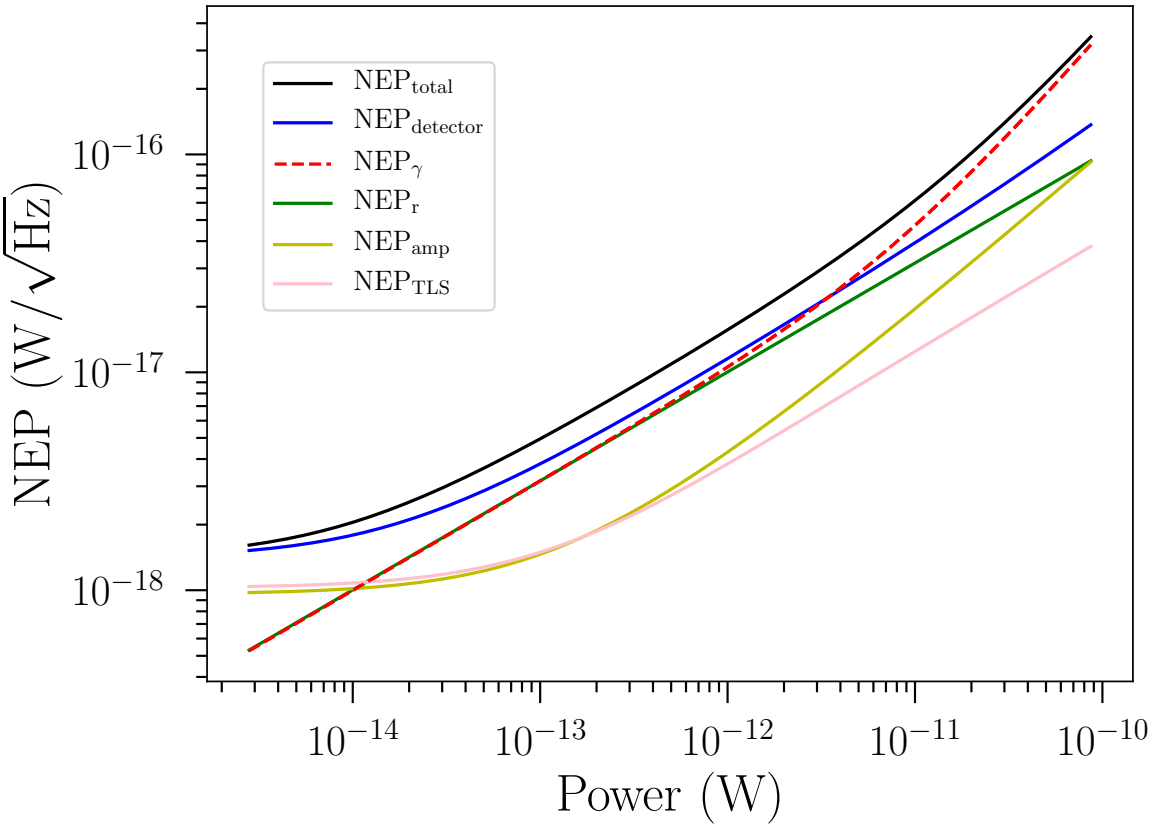

Figure 2.5: Forecasted NEP as a function of absorbed power. The expected NEPs of the individual detector noise sources are shown: recombination (green), amplifier (yellow), and TLS (pink). The total detector NEP (blue) is shown as well as the NEP$_\gamma$ due to photon noise (red). The total of the detector and photon noise (black) is $\sqrt{2}$ higher than the photon noise at 1 pW and approximately equal to the photon noise at higher powers. Ground-based CMB experiments typically have a lower loading limit of approximately 1 pW.

In the limit that there is no optical generation and only thermal generation (i.e. a 'dark' environment), N_{qp} will be set by the random generation and recombination of thermal quasiparticles. The spectral density for the g-r noise is then [Flanigan, 2018, Barry, 2014]

$$S_{\text{gr}}(f_{\text{s}}) = 4N_{\text{qp}}\tau_{\text{qp}}\Big[\frac{1}{1+(2\pi f_{\text{s}}\tau_{\text{qp}})^2}\Big]. \tag{2.47}$$

The term in parentheses is a high-frequency roll-off set by the quasiparticle lifetime τ_{qp}.

In the limit that optical generation dominates the quasiparticle production, the spectral

density follows the photon noise discussed in the above section. It can be shown that the expected recombination NEP is given by [Flanigan et al., 2016]

$$\mathrm{NEP}_{\mathrm{r}}^2 = \frac{4\Delta_0 P}{\eta_{pb}}. \tag{2.48}$$

For our devices, $\eta_{\mathrm{pb}} = 2\Delta/(h\nu)$ and we can see that the recombination noise is equal to the expected photon shot noise at a given power P. Thus, it would be advantageous to either be in the wave noise limit from the optical loading or choose a detector material for which $q > 2$ given that $\eta_{\mathrm{pb}} = q\Delta/(h\nu)$.

2.4.3.3 Readout and amplifier noise

The readout noise is dominated by the first-stage amplifier noise. The low-noise amplifiers (LNAs) we use have noise levels of $T_{\mathrm{amp}} \approx 5$ K over the readout frequency bands (0.1 - 4 GHz). The spectral density of the amplifier [Barry, 2014] is given as

$$S_{\mathrm{amp}} = \frac{Q_{\mathrm{c}}^2}{Q^4}\frac{k_{\mathrm{B}}T_{\mathrm{amp}}}{4P_{\mathrm{g}}} \tag{2.49}$$

where P_{g} is the tone power. For the amplifier, $\mathrm{NEP}_{\mathrm{amp}}$ in the frequency direction is thus

$$\mathrm{NEP}_{\mathrm{amp}}^2 = \frac{Q_{\mathrm{c}}^2}{Q^4}\left[\frac{k_{\mathrm{B}}T_{\mathrm{a}}}{4P_{\mathrm{g}}}\right]R_x^{-2} \tag{2.50}$$

where R_x was previously defined in Eq. 2.40. We see that a high Q and P_{g} are advantageous for suppressing the amplifier noise. P_{g} is limited because at high power the detectors begin to bifurcate [Swenson et al., 2012, Zmuidzinas, 2012], which causes their response to be non-linear. In practice, well-designed KIDs can be driven with sufficiently high power while also having sufficiently high Qs so that the amplifier noise is routinely below the other noise terms, as will be seen in Chs. 4– 7.

2.4.3.4 Other noise sources

Additional noise sources can possibly contribute to the total noise of the detector. The most commonly encountered is noise from two-level systems (TLS). TLS are electric dipoles in the dielectric (typically silicon) on which the KIDs are fabricated. The dipoles couple to the electric field of the readout tone and in doing so are excited to transition between different states. This causes fluctuations in the dielectric constant of the material which causes fluctuations in f_0, appearing as frequency noise. The noise spectral density due to TLS $\mathrm{NEP}_{\mathrm{TLS}}$ has been empirically determined to scale with a number of parameters, including power and frequency [Gao et al., 2008a]. From this we can write the spectral dependency as

$$S_{\mathrm{TLS}}(f_{\mathrm{s}}, P_{\mathrm{g}}) \propto f_{\mathrm{s}}^{-1/2}\Big[1+\frac{P_{\mathrm{g}}}{P_c}\Big]^{-1/2}, \tag{2.51}$$

where P_c is an empirically determined critical power level. From this above equation, we can tell that TLS noise has a $f_{\mathrm{s}}^{-1/2}$ shape and the overall level can be reduced with increasing probe tone power.

Mitigating the effects of TLS on KIDs has been carefully studied [Zmuidzinas, 2012, Gao, 2008, McKenney et al., 2012]. The semi-empirical models that have been developed should allow us to design LEKIDs that should reduce the TLS effects to a negligible level. The additional scaling dependencies that have been found are

$$S_{\mathrm{TLS}} \propto \Big(\frac{T^\star}{T}\Big)^2\Big(\frac{A_{\mathrm{c}}^\star}{A_{\mathrm{c}}}\Big)^{0.5}\Big(\frac{g_{\mathrm{c}}^\star}{g_{\mathrm{c}}}\Big)^{2.1}\Big(\frac{N_0^\star}{N_0}\Big)^{0.5}\Big(\frac{V_{\mathrm{L}}^\star}{V_{\mathrm{L}}}\Big)^{0.5}\Big(\frac{Q_{\mathrm{r}}}{Q_{\mathrm{r}}^\star}\Big)^{0.5}\frac{\Delta_0^\star}{\Delta_0} \tag{2.52}$$

where A_{c} is the area of the capacitor, g_{c} is the gap between the interdigitated capacitor fingers (IDC) that comprise the LEKID capacitor, and the starred values are fiducial scaling values. We can see that ideally the LEKIDs should have large capacitor areas A_{c} and gaps between fingers g_{c}.

The $\mathrm{NEP}_{\mathrm{TLS}}$ is thus

$$\mathrm{NEP}_{\mathrm{TLS}}^2 \propto S_{\mathrm{TLS}} R_x^{-2}. \tag{2.53}$$

The overall level of TLS noise is difficult to predict. In practice, we typically look for signatures of it, such as the noise level scaling with power or the spectrum having a $f_{\rm s}^{-1/2}$ slope.

2.4.3.5 Noise summary

The total detector NEP will be given by

$$\mathrm{NEP}^2 = \mathrm{NEP}_\gamma^2 + \mathrm{NEP}_{\rm r}^2 + \mathrm{NEP}_{\rm amp}^2 + \mathrm{NEP}_{\rm TLS}^2. \tag{2.54}$$

The expected contributions of each NEP term for a nominal design sensitive to millimeter-wave radiation is shown in Fig. 2.5. In this section, I have shown that we expect photon-noise limited performance as $\mathrm{NEP}_\gamma \geq \mathrm{NEP}_{\rm r}$, which sets the fundamental sensitivity. Additionally, since we understand how $\mathrm{NEP}_{\rm amp}$ and $\mathrm{NEP}_{\rm TLS}$ scale with the resonator parameters, we optimize the KIDs so these terms should also be less than NEP_γ.

2.4.3.6 Noise spectral density

In this part, I comment on the expected shape of the noise spectral density for a KID. The shape of the detector noise spectrum, and not only the overall noise level, is important for clean astrophysical measurements. Correlated noise will not average down and $1/f_{\rm s}$ noise, or low frequency noise, can rise above the expected signal. The band the astrophysical signal appears is given by a Gaussian centered on 0 with a width given by scan speed/(2π object size). CMB experiments often use a modulator, like a half-wave plate, to cleanly separate the polarization signal from the intensity signal. A half-wave plate with a frequency $f_{\rm hwp}$ will move the polarization signals to $4f_{\rm hwp}$, which is typically above a few hertz.

With an optical load, the generation and recombination of quasiparticles due to pair-breaking photons is the largest detector noise term. As described above, this has a high-frequency roll off due to the quasiparticle lifetime $\tau_{\rm qp}$. The resonator has a ring-down time

τ_r, which also acts as a low pass filter. The ring-down time goes as $\tau_r = Q(\pi f_0)^{-1}$. Which process is longer - and thus rolls of the noise spectrum in frequency space first - depends on the device design.

The other two detector noise sources are TLS and amplifier noise. As discussed, the TLS spectral density goes as $S_{TLS} \propto f_s^{1/2}$. The overall level of S_{TLS} is scalable. Therefore, even at a realistically low frequency, which is set by the observation strategy, it should still be below the S_γ level. The amplifier contribution S_{amp} does not have frequency dependence. Given typical parameters, $S_{amp} < S_\gamma$. In summary, the level of the detector noise spectral density should be set by the photon noise; furthermore, it should be flat down to low frequencies and rolled off at high frequencies (> 100 Hz). Therefore, there is adequate bandwidth for the astrophysical signal.

Chapter 3

Experimental system

In this chapter, I present the experimental setup used in Chs. 4– 7. First, I discuss the design of the cryogenic testbed and cold stage (Sec. 3.1.1). Second, I give an overview of the two photon sources, which are used in many of the experiments (Sec. 3.1.2). Third, I discuss the KID readout, which can be divided into warm and cold signal processing (Secs. 3.2.1, 3.2.2) as well as the acquisition and analysis software (Secs. 3.2.3, 3.2.4). The aim of this chapter is to give a comprehensive overview of the testbed. The exact state of the testbed depends on the particular experiment being conducted and the details are given where necessary in the later chapters.

3.1 Cryogenic testbed and photon sources

The cryostat in which the majority of experiments and testing took place is a DRC-102 adiabatic demagnetization refrigerator (ADR) cryostat made by STAR Cryoelectronics, as shown in Fig. 3.1. The cryostat has a Cryomech PT407 Pulse Tube Cooler (PTC) and a two-stage ADR. The two-stage PTC has 45 K and 3 K stages. The ADR provides 1 K and 50 mK stages. The ADR has 112 mJ of cooling energy at 50 mK. The 50 mK stage, referred to as the 'cold stage', can be varied in temperature. There are two 'fingers', which are directly connected to the ADR thermal stages. Our experimental testbed is thermally

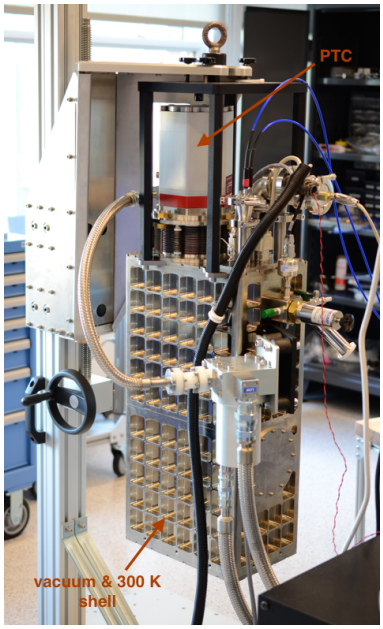

(a)

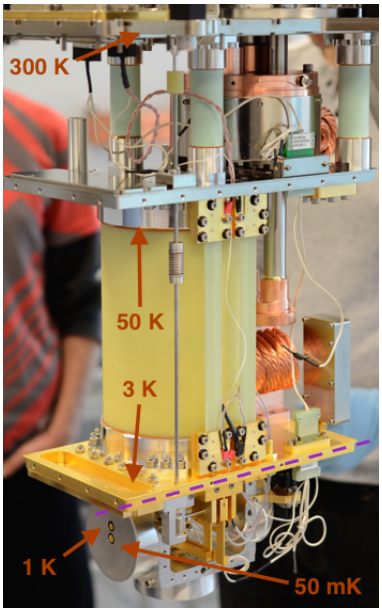

(b)

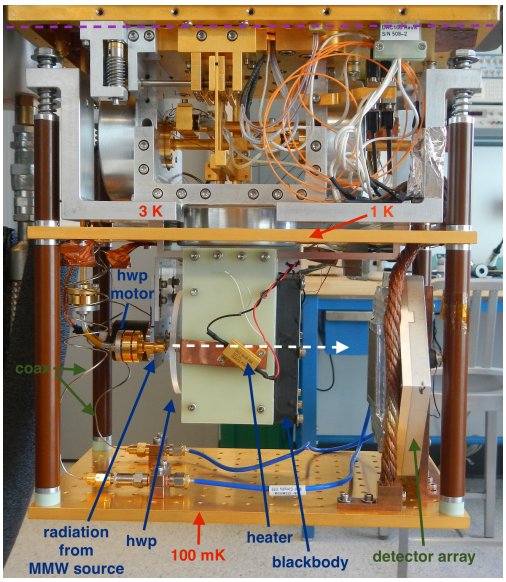

(c)

Figure 3.1: **a.** Picture of the cryostat with the shields on. The vacuum and 300 K shield is visible, as well as the PTC and helium lines. **b.** Picture of the cryostat with the shields removed. The PTC provides 50 K and 3 K thermal stages. The ADR provides 1 K and 50 mK thermal stages to which we thermally couple our experiments. **c.** Picture of the cryogenic testbed built for an experiment. This photo corresponds to below the purple line in panel b. The cryogenic testbed has 3 K, 1 K, and 100 mK stages, which are annotated in red. Components of the blackbody and MMW sources are shown in blue. The MMW source emits radiation between 145–165 GHz, and the center of the beam is shown in the dotted white line. The resonator probe tones are brought in on superconducting coaxial between the 3 K and 100 mK stages. In this set up, the detector array is mounted vertically, so it can be optically illuminated. Different testbed configurations for specific experiments are shown in Figs. 4.4 and F.1.

heat sunk to these fingers.

3.1.1 Cryogenic stage

It is necessary to build a cryogenic stage to provide a mechanical interface on which to cool the KIDs, as shown in Fig. 3.1. We have used a few cryogenic stages over the course of different experiments (for instance, see Fig. 4.4). In each case, the cryogenic stage has three thermal stages at 3 K, 1 K and 50 mK, which are each heat sunk to the respective ADR parts. The 1 K and 50 mK stages are made of gold-plated high-oxygen-free copper (HOFC) due to its excellent thermal conductivity.

To maintain the temperatures of the cold stage, the thermal loading from the mechanical support and readout electronics must be minimized. The thermal loading on each stage is the sum of the loading from the mechanical supports, bias wires, and coaxial cables. We model the thermal loading by using the rate of heat transfer

$$\dot{Q} = \frac{A}{L}\kappa(T_{\mathrm{i}} - T_{\mathrm{f}}) = \frac{A}{L}\int_{T_{\mathrm{i}}}^{T_{\mathrm{f}}} \kappa(T')dT', \tag{3.1}$$

where an object with a cross-sectional area A, length L, and thermal conductivity κ is connecting an initial temperature T_{i} to a final temperature T_{f}. At cryogenic temperatures (< 200 K), it is necessary to take the thermal conductivity dependence on temperature into account, which is shown in the third part of the equation. We can see from these equations that is advantageous to have a small A/L. The mechanical supports are made of 10 mil thick vespel tubes, which thermally isolate the stages from one another. The bias wires for low-temperature thermometers, amplifiers and more are generally thin phosphor bronze, which has a very low thermal conductivity, and are appropriately heat sunk at the different thermal stages. I review the coaxial cable thermal considerations when discussing the cold signal processing in Sec. 3.2.2.

Similarly, we can calculate the energy needed to cool an object

$$Q = mC(T_\mathrm{i} - T_\mathrm{f}) = m \int_{T_\mathrm{i}}^{T_\mathrm{f}} C(T')dT', \tag{3.2}$$

where m is the mass of the object and C the specific heat. Therefore any mass to be cooled, like the detector package or the cold stage itself, needs to be minimized. This leads to the light-weighting many of the copper and aluminum parts, where any non-integral material is removed.

3.1.2 Sources

We use two photon sources to optically characterize the KIDs: (i) a variable blackbody source and (ii) an electronic source that can produce broadband or coherent radiation at millimeter-wave (MMW) wavelengths.

3.1.2.1 Blackbody source

The blackbody source is made from Eccosorb absorber, which is anti-reflection (AR) coated with etched Teflon. It is weakly thermally coupled to a cold stage, typically the 3 K stage. The blackbody temperature T_bb can be adjusted using a resistive heater mounted on the source. We use a programmable function generator to change the applied voltage and can change the temperature from approximately 3–9 K. Above 9 K, the source appreciably heats the cold stage. We have designed a variety of blackbody sources for this testbed (see Figs. 3.1 and 4.4). The blackbody source allows us to calibrate and measure the response of the detectors, and, in particular, measure the NET of the detectors.

3.1.2.2 Millimeter-wave source and cryogenic half-wave plate

The electronic MMW source provides radiation, which illuminates the detectors, between 140–165 GHz. The source is at room temperature outside the cryostat. MMW radiation

is produced by two 12× active multipliers, which are connected to either a 50 Ω termination that produces broadband white noise or a signal generator that produces a coherent tone [Flanigan et al., 2016]. The source power is then controlled by two in-line attenuators. The source output is rectangular WR6 (110–170 GHz) waveguide, and so the radiation is linearly polarized. This brings the radiation to a directional coupler, which splits the signal. A calibrated zero-bias detector (ZBD) measures the power emitted by the source P_{s} at one port. This gives a measurement proportional to the power emitted at the detectors. Radiation from the other port is routed into the cryostat via the waveguide. The waveguide is alternating pieces of stainless steel and copper, in order to both isolate the different thermal stages and heat sink the waveguide. At 2.7 K, the radiation is then launched from the conical horn. The radiation passes through the HWP (discussed below) and then the blackbody. In this case, the blackbody acts as a millimeter-wave attenuator, and is seen as a low-temperature background by the detectors. The MMW source output is broadband radiation (140–165 GHz) or coherent radiation (e.g. at 148 GHZ). The frequency of the single tone can be swept allowing us to characterize the spectrum of the detectors.

A stepped HWP allows the polarization of the radiation emitted from the waveguide to be modulated. The HWP is sapphire with fused silica AR coatings. It is rotated by a cryogenic motor also mounted at 2.7 K, which is controlled by an Arduino-based system at room temperature. The HWP allows us to measure the polarization properties of the KIDs.

3.2 Readout

The readout for a KID is based on the excitation of the resonator via a carrier or probe tone. After the resonance frequency is determined, the probe tone is loaded into the field-programmable gate array (FPGA). The probe tone is a sine wave very close to the resonance frequency of the KID. The FPGA continuously plays the sine wave, which goes through a digital-to-analog converter (DAC) and is converted into a voltage. The sine wave is driven

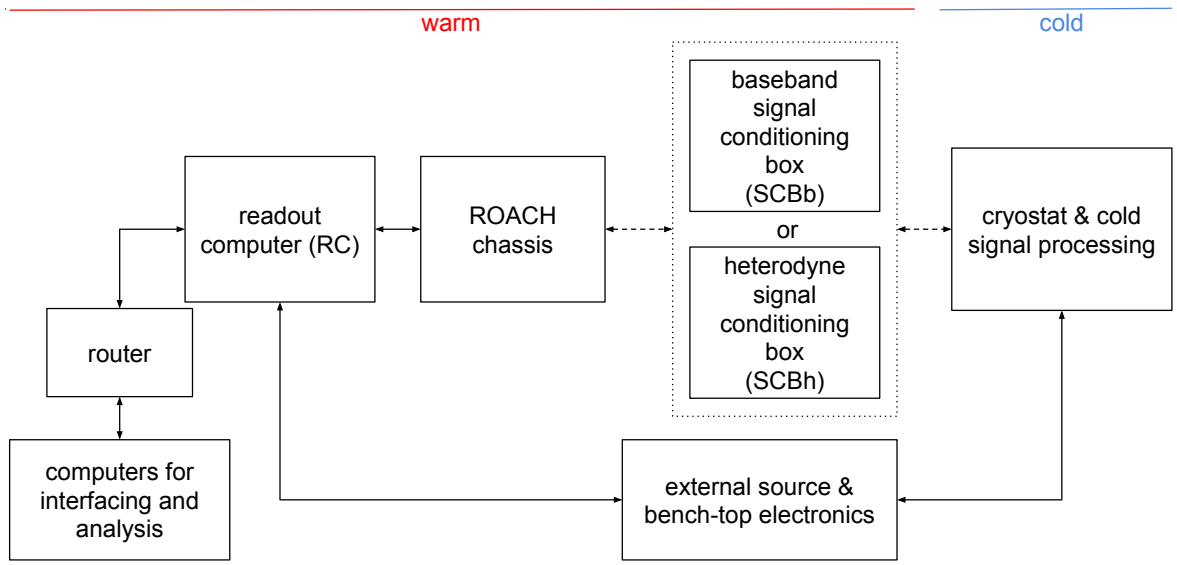

Figure 3.2: Overview of the major components of the experimental testbed and readout. The dashed lines represent the probe tones, while the solid lines mainly represent the digital signals. The readout computer communicates with the ROACH, which hosts the FPGA and ADC/DAC. The dotted box contains the analog signal conditioning boxes. For frequencies between 0–250 MHz, the baseband signal conditioning box is used, and for frequencies between 0.75–4 GHz, the heterodyne signal conditioning box is used. From there the probe tones are sent to the cryostat. The external source and bench-top electronics include the MMW source, power-source for controlling the blackbody source, LNA bias, and HWP motor-controller.

down the transmission line into the cryostat. The probe tone excites the resonator and in turn the KID modulates the sine wave. The signal goes through a low-noise amplifier (LNA), then out of the cryostat to room temperature where it passes through analog-to-digital converter (ADC). The sine wave is then demodulated and the effect of the KID on the tone is determined. Relative changes in the amplitude and phase of the tone are the response of the device.

The readout system can be divided into the following parts:

1. Warm signal processing

2. Cold signal processing

3. Acquisition software

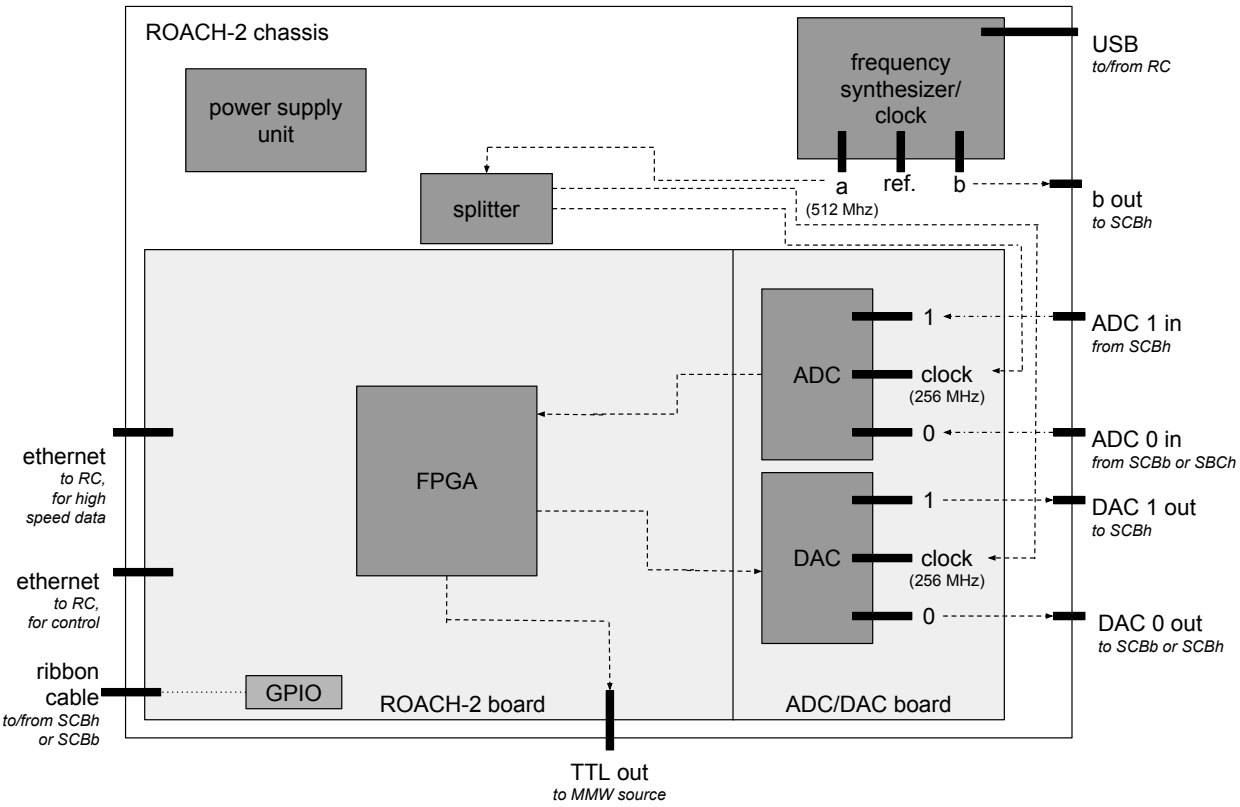

Figure 3.3: Schematic of a top-down view of the ROACH-2 chassis which contains the ROACH-2 and ADC/DAC boards.

4. Analysis software.

A schematic giving an overview of the components is shown in Fig. 3.2.

3.2.1 Warm signal processing

The warm signal processing takes place at room temperature. It can be divided into two parts: digital and analog signal processing. In the digital component, the readout tones are created and demodulated. In the analog component, the readout tones are conditioned to have the appropriate shape and amplitude.

3.2.1.1 Digital signal processing

The center of the digital readout system is a Reconfigurable Open Architecture Computing Hardware (ROACH) board, which hosts the FPGA. We have used two versions of these open-source boards - the ROACH-1 (Chs. 4, 5) and ROACH-2 (Chs. 6, 7) - both of which are designed by the Collaboration for Astronomy Signal Processing and Electronics Research (CASPER)[1]. Since the ROACH-1 board has been deprecated in our system, I will focus on the ROACH-2 board. The advantage to using the ROACH boards is the tools that have been developed to write firmware for it.

The ROACH-2 chassis and board are schematically depicted in Fig. 3.3. The ROACH-2 board hosts a Xilinx Virtex-6 FPGA. The ROACH-2 board communicates with a computer, which, in this case, is called the readout computer (RC). The waveforms are generated on the computer and loaded onto the FPGA. The firmware for the ROACH that enables this is designed in Matlab-SIMULINK. When compiled, this produces a BOF file, which programs the ROACH, and dictates parameters such as the sampling frequency and number of usable tones. Higher level functions, written in Python (discussed more in Sec. 3.2.3), interface with the computer on the ROACH, which then communicates with the FPGA.

The signals then travel to the ADC where they are converted into analog signals. The ROACH-2 board hosts an ADC/DAC daughter board (Techne Instruments, MKID ADC/-DAC) that provides two 12-bit ADCs and two 16-bit DACs. These are each capable of synthesizing and analyzing signals with 250 MHz of bandwidth. For directly synthesized signals (0–250 MHz), only one ADC (and thus DAC on the return) is used, for 250 MHz of bandwidth. For signals which need to be upconverted with mixers (0.7–4.0 GHz), both ADCs are used in order to provide both an I and Q signal to the in-phase/quadrature (IQ) mixers, and thus there is 500 MHz of bandwidth.

A frequency synthesizer (Valon, 5008), provides a common clock for the readout electronics. This programmable synthesizer provides a 512 MHz signal, which is split into two

[1] https://casper.berkeley.edu

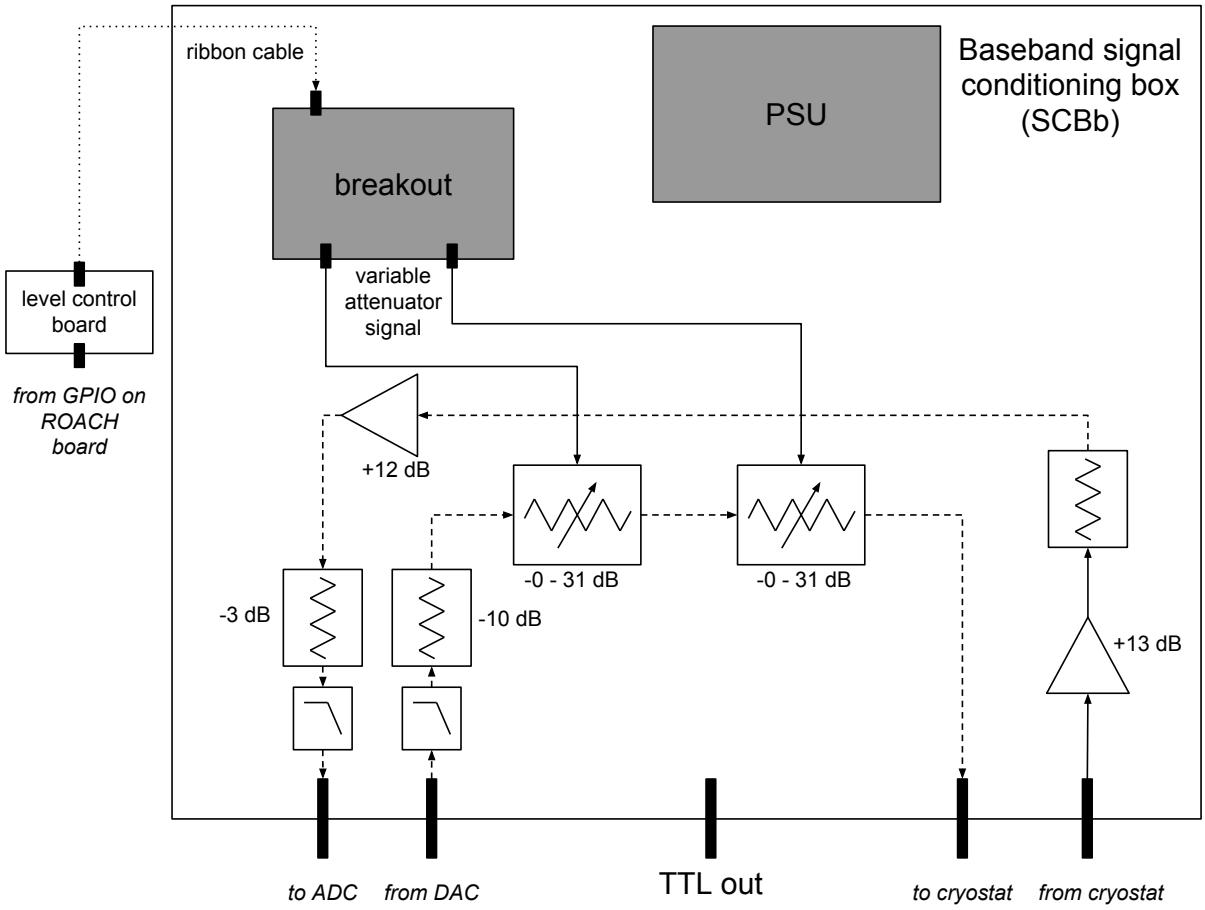

Figure 3.4: Schematic of the baseband signal conditioning box (SCBb). The SCBb operates over frequencies between 0–250 MHz. On the way to the KIDs, the SCBb sets the power level of the probe tones using the variable, digital attenuators. On the return, the SCBb provides warm, second-stage amplification of the tone.

256 MHz signals which are the reference for the the ADCs and DACs. This also provides the reference for the mixers (discussed Sec. 3.2.1.2). From the ADCs, the signal is sent to an analog signal conditioning box where it continues down the signal path.

On the return, the DACs digitize the signal. The signal is then channelized using a polyphase filter bank (PFB). The channels which contain the resonator probe tones are selected and saved to the external readout computer. On the readout computer the tones are demodulated and remainder of the processing takes place.

3.2.1.2 Analog signal conditioning

There are two versions of the signal conditioning boxes which perform the analog signal processing. The two correspond to baseband frequencies (0–250 MHz) and higher frequencies (0.75–4.0 GHz). They are referred to respectively as the baseband and heterodyne signal conditioning boxes. There have been two versions of the heterodyne boxes - heterodyne I and II.

The signals used to read out the lower-frequency 100–200 MHz resonators can be directly synthesized and analyzed using the ADC/DAC board. A schematic of the baseband signal conditioning box is shown in Fig. 3.4. After coming from the ROACH-2 chassis, a low-pass filter smooths the sine wave. A series of digital, variable attenuators allow us to control the power driving the devices. As mentioned in Sec. 2.4.3.3, the devices need to be driven sufficiently hard to overcome amplifier noise, but not so much as to bifurcate. The ideal operating spot is dependent on the specific detector design and is experimentally found by taking and analyzing data over different power levels. From the signal conditioning box, the probe tones are sent to the cryostat. On the return, a series of room temperature amplifiers further boost the signal, which is then low-pass filtered to prevent aliasing, and sent to the ROACH-2 board.

For the higher frequency readout ($>$ 750 MHz), we built a signal conditioning box to up- and down-convert the baseband signal. Details of the high frequency signal conditioning box can be found in Abitbol [2018]. The primary components of the signal conditioning box are the IQ mixers which convert the baseband signals up to the band of interest by moving the local oscillator (LO), which is provided by another frequency synthesizer. For instance, if the detectors has resonance frequencies between 1.0–1.5 GHz, the LO would be placed at 1.25 GHz with the signals up-converted to 250 MHz on either side of the LO. After the signal returns from the devices, the mixer down converts the signals back to 0–250 MHz, which allows it to be digitized by the DACs. The other components in the heterodyne box are functionally similar to that of the baseband box with variable attenuators, filters, etc.

3.2.2 Cold signal processing

The cold electronics are designed to bring the readout tones to the detectors while attenuating the 300 K radiation and then efficiently preserve the signal from the detectors on the return.

After the signal conditioning box, the signal travels on coaxial cables to the cryostat where it passes through the 300 K vacuum shell. To minimize the loading from the coaxial cables on the 4 K stage, a 1 m long 2.16 mm (85 mil) diameter stainless steel inner and outer conductor coaxial (SSI Cable Corps UT085-SS) runs from 300 K to 4 K. The coaxial is heat sunk at the 45 K and 4 K with DC blocks (Inmet 8040), which provide the thermal breaks for the center conductor of the coax. A -20 dB attenuator (Inmet GAH-20) attenuates the 300 K radiation propagating down the coaxial and dissipates the power at the 4 K stage. A 60 cm long section of 0.86 mm (34 mil) diameter cupronickel (CuNi) coaxial cable (Coax Co. SC-033/50-CN-CN) carries the signal from 4 K to another -20 dB attenuator mounted on the 100 mK stage which reduces the noise contribution from the 4 K stage attenuator. There is additional heat sinking from the shield of the CuNI coaxial to the 1 K stage. A short length of standard copper coaxial brings the signal from a second attenuator on the 100 mK stage to the cooled package. This coaxial cable terminates in an SMA connector on the package, which is soldered to a gold-plated microstrip interface board. The interface board is made of Duroid 6010 ($\epsilon_r = 10.8$). Aluminum wire bonds connect the microstrip to the detector array. Depending on the transmission line geometry, wire bonds could be used to explicitly connect the ground return of the detectors to the package. On the return path, a 50 cm long superconducting NbTi coaxial (Coax Co. SC-033/50-NbTi-NbTi) carries the signal from 100 mK to 4 K, which has both extremely low thermal conductivity and low loss [Kushino et al., 2008].

The signal is then amplified by a low-noise amplifier (LNA). The LNA used depends on the readout frequency range of the detectors. For baseband frequencies (0–250 MHz), we use a SiGe bipolar cryogenic low-noise amplifier (LNA), Caltech LF-2 [Weinreb et al., 2007], with a noise temperature, $T_{\rm amp}$ <5 K, over the array bandwidth. For higher frequencies

(0.5–3.0 MHz), we use an LNA from Arizona State University (ASU) with a similar noise temperature. The gain of the LNA is sufficiently high that the noise temperature of the cascaded readout chain is dominated by that of the LNA, which itself is sub-dominant to the noise of the detector in the frequency direction. Stainless steel coaxial cables carry the signal from 4 K to 45 K and finally to 300 K, with a DC block at the 45 K stage.

3.2.3 Acquisition software

The high-level acquisition and analysis software[2] is written in Python. The code consists of a suite of modules. The main modules for taking data are: `roach`, which communicates with the ROACH boards; `measurement`, which organizes the collected data; and `equipment`, which communicates with various hardware.

The first step is to identify the resonance frequencies. This can be done by using the readout like a vector network analyzer (VNA), by stepping through large bands of frequency space in order to identify the resonances. Then, there are two main types of data we acquire: frequency sweeps (see Sec. 2.4.2.1) and TOD (see Sec. 2.4.2.2). We combine these measurements with commands using the `equipment` module to control the millimeter-wave source, blackbody temperature, etc. depending on the desired measurement. An example of a simple data acquisition script is given in Appendix B.

3.2.4 Analysis software

In the readout software we have developed, the `analysis` module contains many useful functions to help manipulate and analyze the data. Each data file can contain a frequency sweep and TOD for all the resonators. The frequency sweep and TOD data acquired are stored into variables called `SweepArray` and `StreamArray`, which are combined into a `SweepStreamArray`. This data has been pre-processed, meaning the resonators have been fit to the model and the TOD calculated in terms of x and Q_i^{-1}. Once an individual detector has been selected,

[2] https://github.com/ColumbiaCMB/kid_readout

parameters associated with the sweep and TOD can be accessed via `SweepStreamArray.sweep` and `SweepStreamArray.stream`. The `SweepStreamArray` also has the `resonator` class, which contains the resonator parameters like f_0 and Q.

We also make use of the python library *pandas* [3]. The heart of *pandas* are the DataFrames, which provide a convenient way to access and organize data. We can use DataFrames to access multiple files and datasets at once. Examples of simple analysis scripts are given in Appendix B. Between the `SweepStreamArray` and DataFrames, it is possible to manipulate the pre-processed data. Code is typically then written individually to further analyze the data depending on the experiment - for example, one might want to fit noise spectra or extract the polarization efficiency of a detector.

I have reviewed the experimental setup including the cryogenic testbed and readout. This should give the reader a solid foundation from which to understand how many of the following measurements and analyses were conducted. The bulk of the remainder of this thesis presents the development – including design, testing, and analysis – of KIDs for CMB polarimetry.

[3] https://pandas.pydata.org/

Chapter 4

Single polarization, horn-coupled LEKIDs

We discuss the design, fabrication, and testing of prototype horn-coupled, lumped-element kinetic inductance detectors (LEKIDs) designed for cosmic microwave background (CMB) studies. The LEKIDs are made from a thin aluminum film deposited on a silicon wafer and patterned using standard photolithographic techniques at STAR Cryoelectronics, a commercial device foundry. We fabricated twenty-element arrays, optimized for a spectral band centered on 150 GHz, to test the sensitivity and yield of the devices as well as the multiplexing scheme. We characterized the detectors in two configurations. First, the detectors were tested in a dark environment with the horn apertures covered, and second, the horn apertures were pointed towards a beam-filling cryogenic blackbody load. These tests show that the multiplexing scheme is robust and scalable, the yield across multiple LEKID arrays is 91%, and the measured noise-equivalent temperatures (NET) for a 4 K optical load are in the range 26 ± 6 $\mu\mathrm{K}\sqrt{\mathrm{s}}$.

4.1 Introduction

In this chapter we present the design and measured performance of horn-coupled, aluminum lumped-element kinetic inductance detectors (LEKIDs). These devices were designed for cosmic microwave background (CMB) studies [Johnson et al., 2014, Araujo et al., 2014], so they operate in a spectral band centered on 150 GHz, which is where the CMB frequency spectrum peaks. Our LEKID design is scalable to higher frequencies, so these devices could be used for a range of millimeter-wave and sub-millimeter-wave activities. The detectors were fabricated in industry, which is a unique aspect of this study. To date, millimeter-wave detectors for CMB studies have exclusively been fabricated in government laboratories or at universities. Here, we report the performance of the first generation of our commercially-fabricated devices.

LEKIDs are superconducting thin-film resonators also designed to be photon absorbers. Absorbed photons with energies greater than the superconducting gap break Cooper pairs, changing the density of quasiparticles. The quasiparticle density affects the kinetic inductance and dissipation of the superconducting film, so a changing optical signal will cause the resonance frequency and internal quality factor of the resonator to shift. These changes in the properties of the resonator can be detected as changes in the amplitude and phase of a probe tone that drives the resonator at its resonance frequency. This detector technology is particularly well-suited for sub-kelvin, kilo-pixel detector arrays because each detector element can be dimensioned to have a unique resonance frequency, and the probe tones for hundreds to thousands of detectors can be carried into and out of the cryostat on a single pair of coaxial cables.

Current experiments focused on studying the CMB polarization anisotropies use arrays of thousands of detectors. Transition edge sensor (TES) bolometers are the current detector standard for these studies. In general, TES devices are composed of a photon absorber suspended by a weak thermal link. The absorber temperature is related to the incident photon power, and this temperature is detected with a superconducting temperature sensor

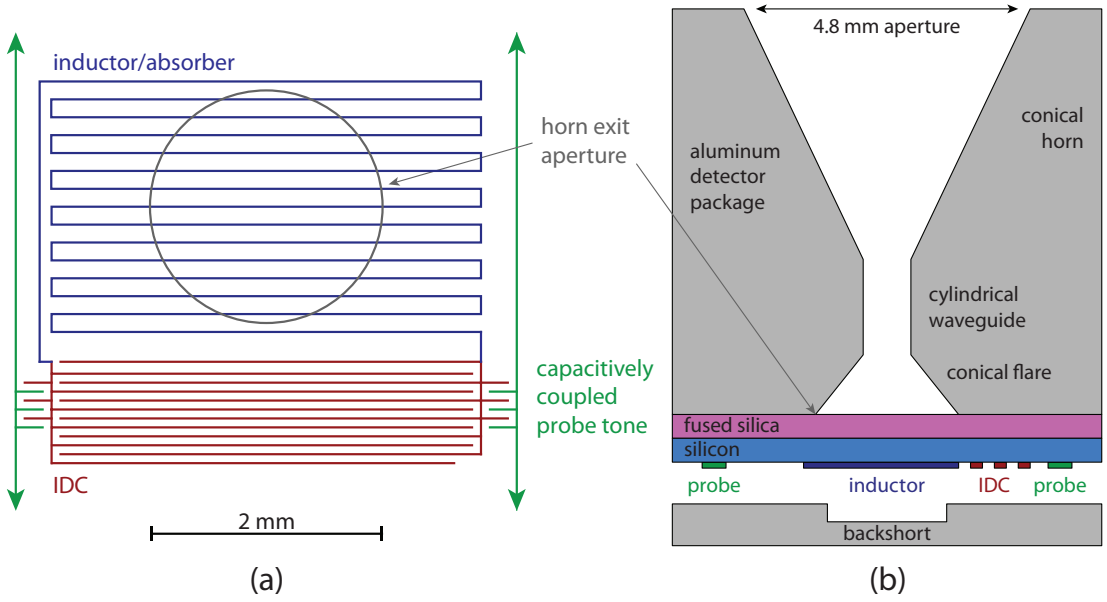

Figure 4.1: **a.** A schematic of a single LEKID. The meandered inductor in the resonator is also the photon absorbing element. The interdigitated capacitor (IDC) completes the resonance circuit. The resonator is capacitively coupled to a transmission line, which carries the probe tone that is used to read out the detector. **b.** Cross-sectional view of a single array element showing the horn plate, the dielectric stack, one LEKID, and the backshort plate. For clarity, this schematic is not drawn to scale.

and read out with a superconducting quantum interference device (SQUID). The operational details of these detectors are thoroughly described in the literature [Irwin and Hilton, 2005]. A variety of TES architectures have already been deployed for CMB studies [Kermish et al., 2012, Ogburn et al., 2010, George et al., 2012, Reichborn-Kjennerud et al., 2010, Schwan et al., 2011, Niemack et al., 2010]. The next generation of CMB experiments will require an even greater number of detectors for improved sensitivity. The inherent scalability of LEKIDs makes them a potential candidate for these future CMB measurements, so we conducted the study we describe here to explore this hypothesis further.

Microwave kinetic inductance detectors (MKIDs) were first published in 2003 [Day et al., 2003], and the lumped-element MKID variety was published in 2008 [Doyle, 2008]. Over the past decade, a number of groups around the world have pursued MKID technologies for a variety of astrophysical studies at different wavelengths, and our work builds from this experience. Experiments that have deployed or plan to use MKID-based cameras include

ARCONS [Mazin et al., 2013], MAKO [McKenney et al., 2012], MicroSpec [Patel et al., 2013], MUSIC [Golwala et al., 2012], NIKA [Monfardini et al., 2011], BLAST-TNG [Dober et al., 2014], and SuperSpec [Kovács et al., 2012]. Laboratory studies show that state-of-the-art LEKID designs can achieve photon noise limited performance [Mauskopf et al., 2014, McKenney et al., 2012], and photon noise limited horn-coupled LEKIDs sensitive to 1.2 THz were recently demonstrated [Hubmayr et al., 2015].

The fundamental detector performance goal for CMB studies is to reduce the intrinsic detector noise so that it is negligible when compared with the noise due to the arrival statistics of the photon background. The detector performance reported in this chapter is consistent with photon noise limited performance. LEKID noise has been extensively studied, and it includes contributions from three sources: generation-recombination (g-r) noise, amplifier noise, and two-level system (TLS) noise. These noise sources are thoroughly described in the literature [Zmuidzinas, 2012]. The generation-recombination noise is due to fluctuations in the quasiparticle number from recombination into Cooper pairs and from thermal generation of quasiparticles. Under typical loading conditions, this noise is caused mostly by randomness in the recombination of optically excited quasiparticles, and the thermal generation of quasiparticles is negligible. The amplifier noise is the electronic noise of the readout system referred to the detector array. It is set by the noise figure of the cryogenic microwave low-noise amplifier (LNA) immediately following the detectors. TLS noise is produced by dielectric fluctuations due to quantum two-level systems in amorphous materials near the resonators. The scaling of TLS noise with the operating temperature, probe tone power, resonance frequency, and geometry of the capacitor has been extensively studied experimentally. This knowledge has been captured in a semi-empirical noise model, which gives us the ability to make empirically-grounded predictions of the TLS noise we should expect for a given capacitor and inductor design [Gao et al., 2008a]. We designed our detectors using this semi-empirical model for the range of optical loads that are typical for ground-based and sub-orbital CMB experiments.

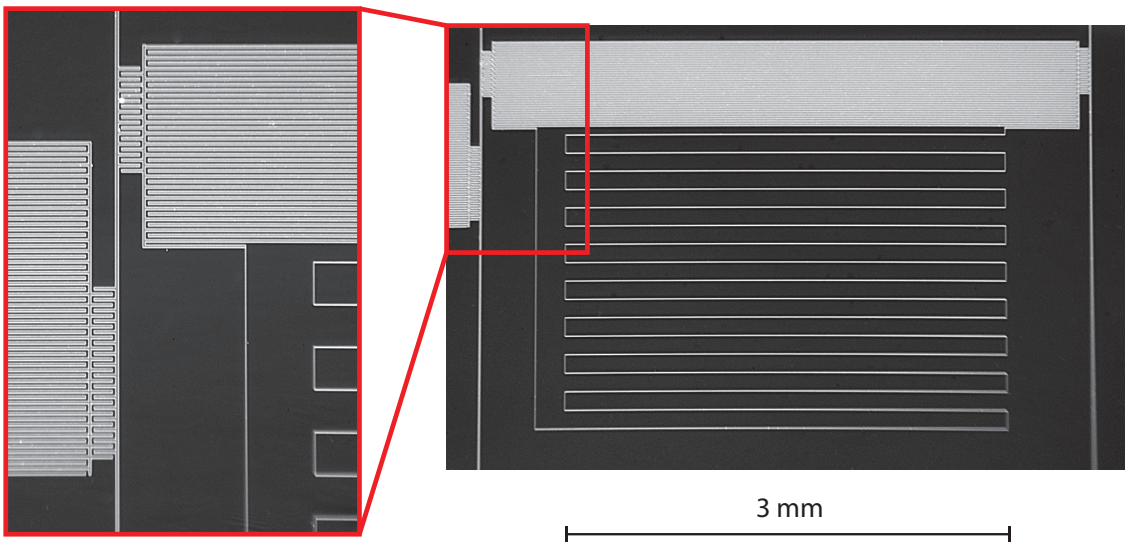

Figure 4.2: Photomicrographs of a single LEKID. All components are fabricated from thin-film aluminum with a single mask.

The remainder of the chapter is organized in the following way. In Section 4.2 we present the design of the horns and the detectors. This section also describes the experimental setup, including the cryogenic system and the detector readout. In Section 4.3, we present measurements of the LEKIDs with and without optical loading. In Section 4.4, we summarize our design and measurement results and describe our future plans. One goal of this chapter is to provide a detailed end-to-end description of our design and testing process, which could be useful for uninitiated readers or groups interested in starting to make LEKIDs. For clarity, in many places we provide the equations and other bits of practical information collected from the literature that were essential to our design and analysis process.

4.2 Methods

We designed and built a prototype twenty-element, horn-coupled LEKID module that is sensitive to a spectral band centered on 150 GHz. The module consists of a LEKID array on a silicon chip and an aluminum horn package. The LEKIDs were fabricated in the foundry at STAR Cryoelectronics in New Mexico. The aluminum horn package was manufactured in the Micromachining Laboratory at Arizona State University. The modules were designed, assem-

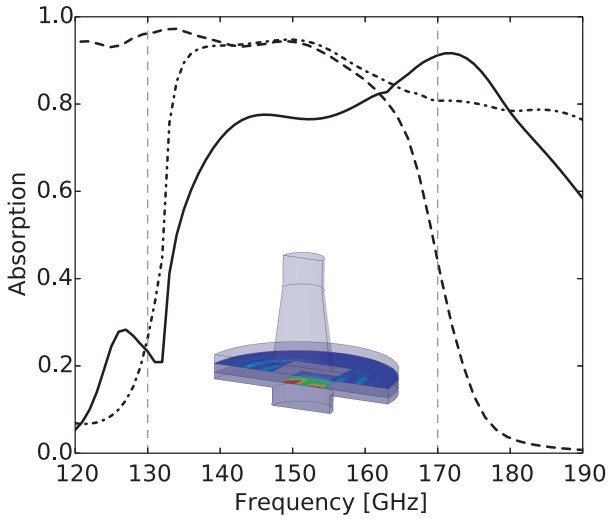

Figure 4.3: Electromagnetic simulation results show the absorptance as a function of frequency for the horn-coupled aluminum LEKID design. The dot-dash line shows the single-polarization absorptance spectrum for the inductor/absorber using the nominal design value of 1.2 $\Omega/\square$ resistivity for aluminum. The solid line shows the simulated absorptance spectrum for the measured resistivity of the devices, 4 $\Omega/\square$, which has an average absorptance of 72% across the single-mode spectral band. The dashed line is the measured transmittance spectrum of the metal-mesh low-pass filter, used to define the upper edge of the spectral band. The inset shows the simulation set up and the simulated current density over the absorbing area.

bled and tested at Columbia University. For LEKIDs, the various construction parameters must simultaneously satisfy both the requirements of the resonator circuit and the optical coupling to millimeter-wavelength radiation. It is instructive to first describe the photon coupling design (Section 4.2.1) and then describe the resonator circuit (Section 4.2.2).

4.2.1 Optical coupling design

Our design uses horn-coupled detectors for a number of reasons. First, the horn beam reduces sensitivity to stray light inside the cryostat and couples well with the telescope optics in instruments we are developing [Johnson et al., 2014, Araujo et al., 2014]. Second, the waveguide in the horn provides an integrated high-pass filter. Third, the horn pitch creates space for the large interdigitated capacitor, which allows for resonance frequencies below 250 MHz and reduces the effects of TLS noise. Finally, electrical cross-talk is reduced

because the final configuration is not tightly packed.

A cross-sectional view of one array element and a schematic of one detector are shown in Fig. 4.1, a photograph of a device is shown in Fig. 4.2, and the detector module is shown in Fig. 4.4. The conical horn flare narrows down to a single-mode cylindrical waveguide section, which defines the low-frequency edge of the spectral band at 127 GHz. The high-frequency edge is defined by a quasi-optical metal-mesh low-pass filter. The waveguide is then re-expanded with a second conical flare to reduce the wave impedance at the low-frequency edge of the spectral band, which improves optical coupling and allows the radiation to be launched efficiently into the subsequent dielectric stack. The dielectric stack is composed of an approximately quarter-wavelength layer of fused silica (300 μm) and the silicon wafer (300 μm). The fused silica helps match the wave impedance to the silicon substrate. The radiation launched from the waveguide remains fairly well collimated as it travels through the dielectric stack and back-illuminates the inductor/absorber, which is patterned on the silicon and dimensioned to match the wave impedance. There is a metal cavity behind each detector that is a quarter wavelength deep that acts as a backshort. The dielectric stack is mounted directly to the horn plate using a spring-loaded aluminum clip. The aluminum clip provides force that increases the thermal conductivity at the interface between the dielectric stack and the horn plate. A metal back plate, with the backshort cavities, is attached to seal the module. Electromagnetic simulations using the Ansoft HFSS software package predict that the maximum coupling efficiency to a single-polarization for this design is 90% and averages $> 70\%$ over the 130 to 170 GHz band, as shown in Fig. 4.3.

The conical flare produces a very small mixing of electromagnetic modes from the small aperture TE11 to the exit aperture into the quartz of less than 1%. There will be some reflection at the exit aperture and at the interface between the quartz and silicon and also at the detector. The electromagnetic simulations of the coupling to the detector, shown in Fig. 4.3, take all of these effects into account by launching a single mode (or one for each polarization) from the single mode circular waveguide section and then computing

the electric field through the rest of the structure including the conical flare, the dielectric layers, the aluminum LEKID and the backshort. No resonances are seen in the band where the detector operates in part due to absorption of power by the aluminum and damping of any resonances. The size of the detector is large enough that it can effectively absorb multiple modes of incident electromagnetic radiation.

4.2.2 Detector design

The detectors are designed to have the following properties: high absorptance and responsivity, low detector noise, and optimal electrical coupling. The overall design of the detector requires balancing competing constraints on various construction parameters. In the following paragraphs we describe the design of the inductor, which largely controls the absorptance and responsivity, the capacitor geometry, which influences the TLS noise, the transmission line, and the electrical coupling.

The detector array consists of back-illuminated LEKIDs fabricated from a 20 nm thick aluminum film deposited on a 300 μm thick high-resistivity ($>$ 10 kΩcm), float-zone silicon substrate. The inductor/absorber is a meandered aluminum trace on silicon with a filling factor of 1.5%, calculated as the inductor trace width divided by the gap width plus trace width. This filling factor is designed to match the wave impedance of the incoming radiation in silicon, which has a dielectric constant, $\epsilon_{\rm r} = 11.9$ and a wave impedance of $\sim$110 Ω. The effective impedance of the inductor is $Z_{\rm eff} \approx (\rho\, g_{\rm L})/(w_{\rm L}\, t_{\rm f})$, where $t_{\rm f}$ is the film thickness, $g_{\rm L}$ is the gap width between meanders, $w_{\rm L}$ the meander width, and ρ the material resistivity, for which we used the typical value for 20 nm thick aluminum, 1.2 $\Omega/\square$.

To efficiently absorb incident photons and approximate a solid sheet, the pitch between the inductor meanders should be less than $\lambda/20$ where λ is the incident wavelength [Doyle, 2008]. The choice of a 2 μm wide trace and 125 μm spacing between meanders, gives an effective sheet impedance of 76 Ω with a 15% efficiency loss, using the standard value for 20 nm thick aluminum resistivity. Although this does not perfectly match the wave

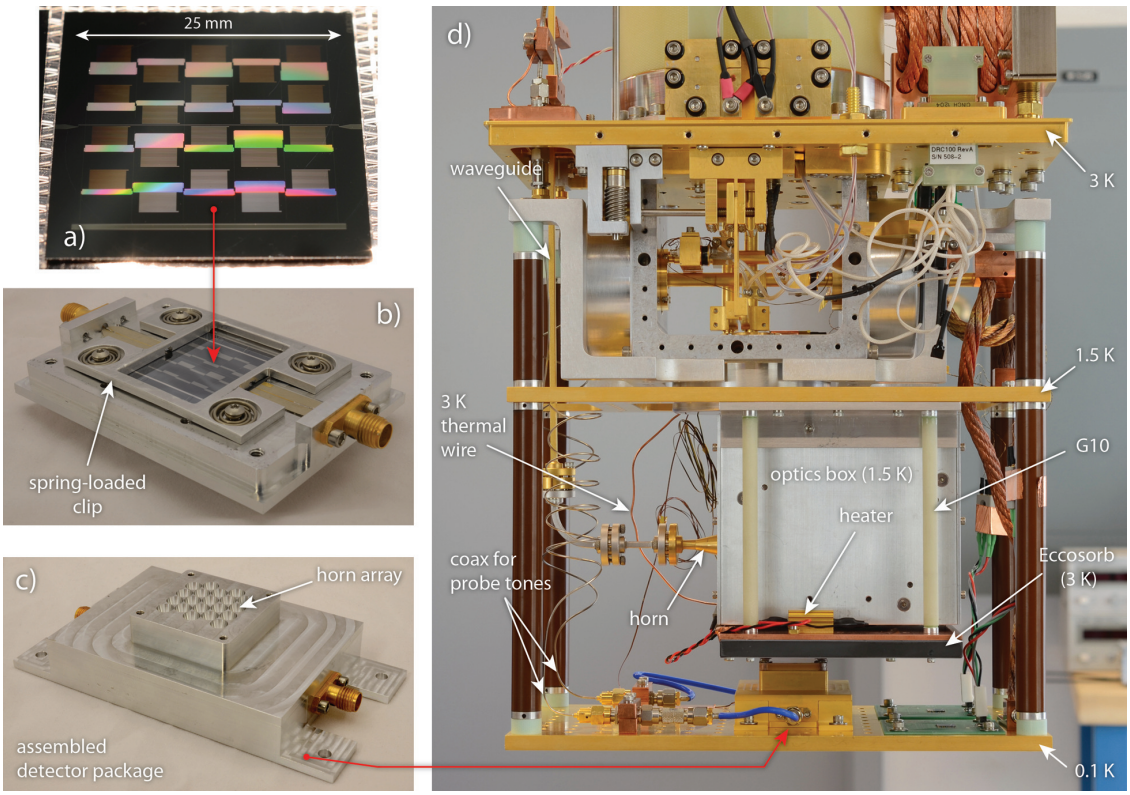

Figure 4.4: **a.** Photograph of a 20-element LEKID array. The LEKID inductors have a 4.8 mm hexagonal pitch, and the varying sizes of the interdigitated capacitors are evident. **b.** The LEKID array mounted to the aluminum horn plate with the spring-loaded clip. The horn apertures are facing down and therefore not visible in this photograph. **c.** The fully-assembled detector package with the conical horns facing up. For clarity, the low-pass filter, which is normally attached directly to the horn array using the four visible tapped holes, was removed for this photograph. **d.** The cryogenic test setup. The detector package is mounted to the 100 mK stage. The Eccosorb is the optical load for this study, and the Eccosorb temperature was adjusted with the heater resistor. The load is mechanically mounted to the 1.5 K stage with thermally isolating G10 legs and thermally connected to the 3 K stage with a copper wire, so the base temperature of the optical load should closely track the temperature of the 3 K stage. The indicated waveguide, horn and optics box are elements of a second kind of load, which is under development and will be used in future studies.

impedance in the silicon, the absorption is not particularly sensitive to this parameter. In Fig. 4.1, electromagnetic simulations using the HFSS software package show the detector absorption using both the nominal design resistivity and the measured resistivity of the devices, 4 $\Omega/\square$. Electromagnetic simulations also show that the incident radiation spreads preferentially in the direction perpendicular to the E-field and thus the inductor/absorber has dimensions of 2×3 mm.

In addition to absorbing the incident photons, the inductor is also part of the resonator circuit. Thus, the meandered inductor must be carefully designed to match the wave impedance of the incident photons yet have a high kinetic inductance fraction, $\alpha_{\rm k} = L_{\rm k}/(L_{\rm k} + L_{\rm g})$. The kinetic inductance can be predicted using

$$L_{\rm k} = \frac{A_{\rm L}}{w_{\rm L}(w_{\rm L} + g_{\rm L})} \frac{hR_{\rm s}}{2\pi^2 \Delta_0}, \tag{4.1}$$

where $w_{\rm L}$ is the width of the inductor trace, $A_{\rm L}$ the total area of the inductor, $R_{\rm s}$ the normal surface resistance, h the Planck constant, and Δ_0 the gap energy, defined as [Tinkham, 2004] $\Delta_0 \approx 1.76 k_{\rm B} T_{\rm c}$. Here, $T_{\rm c}$ is the superconducting transition temperature and $k_{\rm B}$ is the Boltzmann constant. The first term is simply the number of squares of material and the second term in the expression is the kinetic surface inductance $L_{\rm s}$. The value for the geometric inductance was obtained from electromagnetic simulations using the Sonnet software package (see Appendix C). Practical fabrication constraints with a contact mask limit the film thickness to approximately 20 nm and the trace width to approximately 2 μm. For a 20 nm thick by 2 μm wide aluminum trace, the predicted $L_{\rm k} \approx 35$ nH and $\alpha_{\rm k} \approx 0.4$.

Fluctuations in the absorbed optical power are proportional to fluctuations in the total quasiparticle number $N_{\rm qp}$ and as such, fluctuations in the quasiparticle density $n_{\rm qp} = N_{\rm qp}/V_{\rm L}$ are inversely proportional to inductor volume. Thus, for a given optical load, decreasing the volume of the inductor increases the responsivity. Given the above constraints, the inductor volume is $V_{\rm L} = 1870\ \mu{\rm m}^3$. The geometric inductance of the resulting design is approximately

59 nH.

Changes in the quasiparticle density in the resonator cause changes in both the resonance frequency and the quality factor, which is related to the internal dissipation. These changes cause deviations of the complex transmission in orthogonal directions, which are referred to as the frequency and dissipation directions. Two-level systems produce noise only in the frequency direction [Gao et al., 2007, 2008b].

Suppressing the TLS noise has historically been challenging. Gao et al. [2008a] have shown that TLS noise scales with the capacitor digit gap widths as $g_{\mathrm{IDC}}^{-1.6}$, and thus we want to maximize the gap widths. We also chose to target resonance frequencies below 200 MHz to match the baseband bandwidth of the readout system, avoiding the need for mixers. Using a low readout frequency allows us to fit more detectors in a given bandwidth. Lower readout frequencies should in theory couple less strongly to the TLS fluctuators in the resonators, thus reducing their impact [Zmuidzinas, 2012]. To simplify modeling, we imposed the constraint on the interdigitated capacitors that the digit widths and the gaps between them be of equal size [Lim and Moore, 1968]. We maximized the gap widths, while maintaining a resonance frequency less than 200 MHz using the available area as determined by the horn and detector pitch. The resulting capacitor geometry has a gap width of 8 μm. The area of the largest capacitor is 9 mm^2. The capacitors have values in the range 6 to 28 pF.

The resonators are capacitively coupled to the transmission line, which carries the probe tones. We use an aluminum transmission line structure that has a central trace across the array and tines which distribute the signal to the individual detectors, as shown in Fig. 4.5. The transmission line structure acts as a lumped element as its length is much less than the wavelength of the readout frequencies. Ground returns for the resonators are provided by similar tines coming from aluminum strips at the sides of the chip, which are wire bonded to the package. The central transmission line is a trace 20 μm wide. The tines are 15 μm wide. We chose these widths based on simulations, which show that the transmission line is

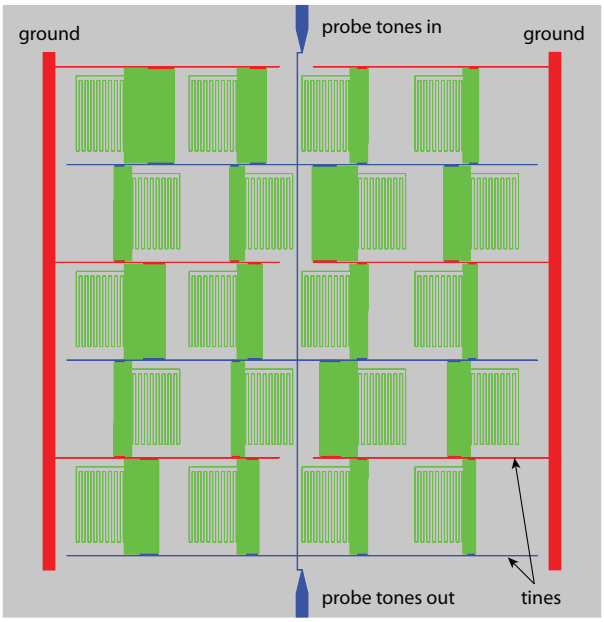

Figure 4.5: The detectors are coupled to a feed line which runs down the center of the array and has tines that distribute the probe tones to the individual LEKIDs.

matched to 50 Ω across the readout bandwidth at the interfaces with the rest of the readout chain.

To achieve sufficient coupling at these low resonance frequencies we used interdigitated capacitors between the resonator and both the signal tine and the ground return tine. This coupling design is schematically shown in Fig. 4.1. Electromagnetic simulations were used to verify this coupling scheme. To maximize responsivity, the coupling quality factor Q_c should equal the internal quality factor Q_i under the expected optical load [Zmuidzinas, 2012]. To calculate the necessary coupling capacitance we begin with the definition of the quality factor

$$Q \equiv \frac{2\pi f_0 E}{P_d}, \tag{4.2}$$

where E is the peak energy stored in the resonator, f_0 is the resonance frequency, and P_d is the average power dissipation. During the phase of the oscillation when the resonator energy

is completely stored in the capacitor, we can write the coupling quality factor Q_c as

$$Q_c = \frac{2\pi f_0}{P_d}\left(\frac{1}{2}C|V|^2\right), \tag{4.3}$$

where P_d is the power dissipated from the resonator into the load impedance Z_0 across the coupling capacitor, C is the capacitance of the main capacitor in the resonator, and V is the peak voltage across the resonator. The power dissipated in the load through the coupling capacitor is then

$$P_d = \frac{1}{2}|I|^2\frac{Z_0}{2}, \tag{4.4}$$

where I is the current that flows through the coupling capacitor, C_c. Since $1/(2\pi f_0 C_c) \gg Z_0$, and taking into account the fact that there are two coupling capacitors in series, we can write

$$P_d = \frac{1}{2}\left|V\frac{2\pi j f_0 C_c}{2}\right|^2\frac{Z_0}{2}. \tag{4.5}$$

Finally, by substituting Equation 4.5 into Equation 4.3, we arrive at

$$C_c = \sqrt{\frac{8C}{2\pi f_0 Q_c Z_0}}, \tag{4.6}$$

and for the optimal coupling of this design we set $Q_c = Q_i = 10^5$. Thus, the coupling capacitors are designed to have C_c values between 0.06 and 0.25 pF.

4.2.3 Detector fabrication

The wafers were processed at STAR Cryoelectronics using standard photolithographic procedures. First, the wafers were cleaned with acetone, isopropyl alcohol, and deionized water. A plasma ashing was used to remove any residual organic material. An argon plasma was then used to remove SiO_2 from the surface of the wafer. The aluminum film was deposited through evaporation. The wafers go through standard lithography: application of hexam-

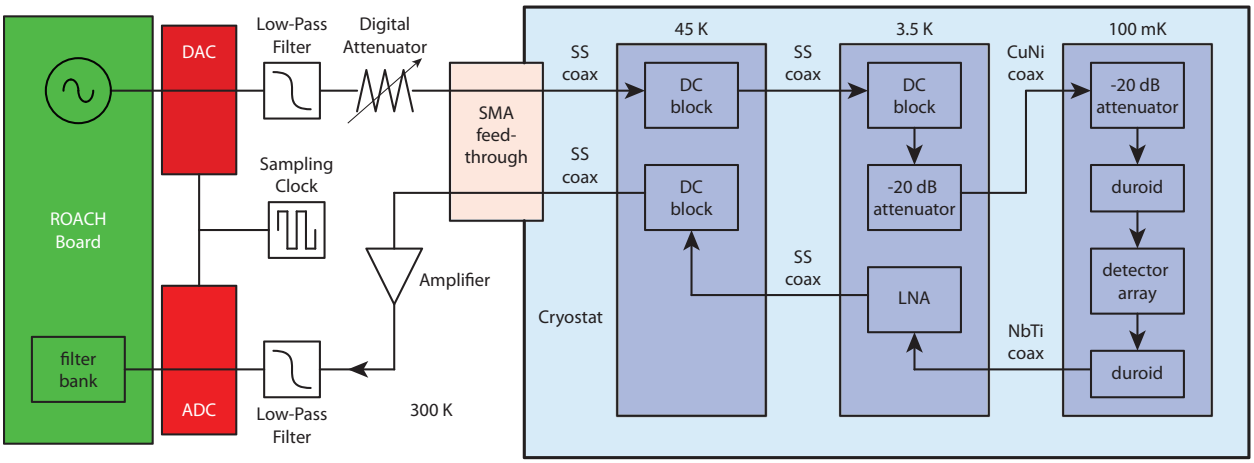

Figure 4.6: A diagram of the probe tone signal chain.

ethyldisilazane (HMDS) to promote resist adhesion, dehydration bake, resist coat, soft bake, resist exposure, resist developing, hard bake, descum and finally ion milling is used to etch away the unwanted aluminum. We used a standard contact mask for patterning the aluminum. The resist was then stripped using acetone, isopropyl alcohol, deionized water, and plasma ashing, put in vacuum to dehydrate, coated with HMDS, and finally a protective resist layer is applied to protect the devices while dicing. Photomicrographs of the fabricated devices are shown in Fig. 4.2.

A common technique used for MKID fabrication on silicon is to dip the wafer in a hydrofluoric acid bath before processing. This etches away any SiO_2 and hydrogen-terminates the silicon, protecting it from further oxidation. This step can help reduce TLS effects. We have fabricated additional devices including this step, the results of which we will describe in future work (see Sec. 4.5).

4.2.4 Experimental setup

The detectors are cooled in a DRC-102 ADR Cryostat System made by STAR Cryoelectronics. This cryostat system uses a Cryomech PT407 Pulse Tube Cooler and a two-stage adiabatic demagnetization refrigerator (ADR), which provides 112 mJ of cooling capacity for the 100 mK stage. The working end of the cryostat is shown without radiation shields

in Fig. 4.4.

All of the detectors in the module are frequency-multiplexed in a readout band between 80 and 160 MHz, and read out with a single SiGe bipolar cryogenic low-noise amplifier (LNA) and one pair of coaxial cables [Weinreb et al., 2007]. The detailed the path of the probe tones is shown schematically in Fig. 4.6 and described in Sec. 3.2.2.

4.2.4.1 Digital readout

Detector data was collected with a digital readout system called CUKIDS that was developed at Columbia University. This system uses the CASPER signal processing tool flow, a ROACH field-programmable gate array (FPGA) board[1], and the 12-bit analog-to-digital converter and 16-bit digital-to-analog converter (DAC) card developed for the MUSIC instrument [Duan et al., 2010]. The room temperature analog signal conditioning consists of amplifiers, low-pass filters, and digital step attenuators from Mini-Circuits, Inc. The readout firmware, control, and analysis software we developed is open-source and available online[2].

Currently, the system is optimized for laboratory testing, essentially providing multiple homodyne test setups in parallel. The probe tone waveforms are generated using a circular playback buffer feeding the DAC. After digitization, the signal is channelized using a polyphase filterbank (PFB). The complex voltage waveforms from the PFB channels that contain the probe tones are sent to the host computer for storage and analysis. All subsequent demodulation and analysis is done offline. For the measurements reported here, the FPGA was configured to provide four simultaneous homodyne readouts, each with a bandwidth of 125 kHz.

4.2.4.2 Blackbody load

For this study, we designed and built the cryogenic test setup shown in Fig. 4.4. This setup includes a blackbody load that has a temperature range from less than 4 K to 6 K. In its

[1] http://casper.berkeley.edu
[2] https://github.com/ColumbiaCMB/kid_readout

coldest state, it should look similar to the CMB. The selected loading range is similar to those that are expected for ground-based and sub-orbital experiments. We use the variable temperature load to directly calibrate our detector noise and responsivity.

The blackbody is constructed from a slab of 6.35 mm (0.25 inch) thick Eccosorb MF-110 absorber coated with a 0.4 mm (0.015 inch) thick sheet of etched Teflon for impedance matching. The etched Teflon is bonded to the Eccosorb with a thin layer of Stycast 2850FT. We designed this load using loss tangent and refractive index information from the literature [Peterson and Richards, 1984]. The emissivity of the load is calculated to be 92%.

The Eccosorb slab is mounted to a copper thermal bus, and this assembly is mechanically supported by G-10 legs that are connected to the 1.5 K ADR stage. The temperature of the Eccosorb is controlled using a weak thermal link to the 4 K pulse-tube cooler stage and a heater resistor, which is mounted on the copper thermal bus. We designed the thermal time constant of the blackbody source to be approximately 20 minutes to minimize the required heat input while still providing a reasonably short settling time when changing temperatures. The blackbody is <1 cm from the detector module, and the entire setup is enclosed in a 4 K shield. There is also a copper shield surrounding the detector module to minimize light leaks. This shield is attached to the 100 mK stage, and it has an aperture exposing the low-pass filter.

4.3 Results

We performed a range of experiments to measure the quality of the fabricated detectors, the results of which are presented in the following sections. We first report the electrical properties of the film, followed by measurements of the detectors themselves in a dark environment. We describe in detail the fitting procedure used to analyze the data. The data are compared to Mattis-Bardeen theory. We then proceed to optical testing with the blackbody load described above, which provides measurements of the optical responsivity and noise.

4.3.1 Film properties

To ascertain the residual resistance ratio (RRR) and the superconducting transition temperature T_c of the aluminum film, we performed a four-wire measurement of the resistance of a $2\,\mu\text{m} \times 35,000\,\mu\text{m}$ meandered trace as a function of temperature. This witness sample was made alongside the LEKIDs on the same silicon wafer and therefore from the same 20 nm thick aluminum film. The resistance of the sample at 3 K is 70 kΩ, yielding a surface resistance of 4.0 $\Omega/\square$. The resistance at 300 K is approximately 210 kΩ, giving a measured RRR of 3.3. We measured $T_c = 1.46\,\text{K}$, which agrees well with the T_c measured independently by the probe tones at the $\sim$100 MHz readout frequencies. Other measurements of thin-film aluminum in the literature [Meservey and Tedrow, 1971] also report values of the critical temperature higher than that of bulk aluminum, which is nominally 1.2 K.

4.3.2 Dark testing

Initial characterization of the resonators is done in a 'dark' package, which is sealed with metal tape to minimize light leaks. Frequency sweeps through the resonances taken at different bath temperatures can be fit to determine the resonance frequencies and quality factors as a function of temperature. Frequency sweeps are done at a variety of probe tone powers to determine the maximum readout power at which the detector can be operated before the device response becomes non-linear due to the non-linear kinetic inductance effect [Swenson et al., 2013]. The bifurcation power is found to be around -100 dBm across the array. This is approximately 10 dB higher than predicted using the theory described by Swenson et al. [2013], assuming that the non-linearity energy scale E_* is equal to the condensation energy of the inductor $E_{\text{cond}} = N_0\Delta_0^2 V_L/2$, which is expected to be the case if $\alpha_k \approx 1$. Here N_0 is the single-spin density of states at the Fermi level. Approximately 4 dB of this discrepancy can be explained by the fact that $\alpha_k \approx 0.66$. In addition, as Swenson et al. point out, it is difficult to directly compare E_{cond} to the value of E_* implied by measurements because the absolute power in the inductor is influenced by unknown temperature dependent loss in the

cryogenic cabling and by mismatches between the transmission line and the resonator. The measurements reported here were taken with a readout power of approximately −111 dBm, well below bifurcation, except where otherwise noted.

4.3.2.1 Yield

Overall, we have tested a total of three 20-element arrays and two 9-element arrays all made on the same wafer. We have found 71 working resonators of the total 78, corresponding to an overall yield fraction of ∼91%. Subsequent test results focus on a single 20-element array. The resonance frequencies were designed to fall between 100 to 200 MHz. We found that all were systematically shifted down in frequency by about 15%. This frequency shift is reasonably well explained when the kinetic inductance is calculated using the measured surface resistance of 4 Ω/□ and T_c = 1.46 K instead of the originally assumed 1.2 Ω/□ and T_c = 1.2 K, giving an L_k of approximately 100 nH and a resonance frequency shift of approximately 20%. Lithographic tolerances (e.g. the under etching of the capacitor resulting in increased capacitance or a different film thickness than desired) could also be responsible for smaller shifts in the resonance frequency.

4.3.2.2 Resonator frequency sweep fitting

We fit the resonators using a model which takes into account the skew of the resonance caused by mismatches in the transmission line [Khalil et al., 2012]. At higher probe powers, we found it necessary to also incorporate the nonlinear model presented by Swenson et al. [2013]. The complete model for the complex forward transmission S_{21} as a function of frequency f is:

$$S_{21}(f) = Ae^{-2\pi jDf}\left(1 - \frac{Q/Q_e}{1 + 2jQx}\right), \tag{4.7}$$

where $A = |A|e^{j\phi}$ is an arbitrary complex scale factor, D is the cable delay, Q is the loaded resonator quality factor, Q_e is the complex coupling quality factor, and x is the detuning parameter, which is simply $(f - f_0)/f_0$ in the case of the basic linear model, where f_0 is the

resonance frequency. For the nonlinear bifurcation model, x is given by the solution to the cubic equation

$$y = y_0 + \frac{a}{1 + 4y^2}, \tag{4.8}$$

where $y_0 = (f - f_0)/f_0$, $x = y/Q$, and a is the bifurcation parameter defined by Swenson et al. [2013].

The real and imaginary parts of the model and data were fit simultaneously using the Levenberg-Marquardt algorithm for non-linear least-squares minimization. We parameterized Q_e in terms of its real and imaginary components, which yielded more robust fits than using its magnitude and phase. By fitting both the real and imaginary parts of the model simultaneously, we found that the resulting fits were very well constrained, even with only a few data points spaced across the resonance. We used the `lmfit` Python package[3] which provides a convenient interface to the underlying algorithm. We also used the `emcee` package [Foreman-Mackey et al., 2013] to perform a Markov-Chain Monte Carlo analysis of the fits to ensure the errors were realistic.

4.3.2.3 Quality factors

We adopt the convention proposed by [Khalil et al., 2012], defining the internal (unloaded) quality factor of the resonator as

$$Q_i^{-1} = Q^{-1} - \mathrm{Re}\, Q_e^{-1}. \tag{4.9}$$

We define an effective real coupling quality factor $Q_c = (\mathrm{Re}(Q_e^{-1}))^{-1}$.

The quality factors for the detectors measured in an aluminum package and a dark environment at 200 mK are greater than 5×10^5 as shown in Fig. 4.7. The package is made of the QC-10 aluminum alloy[4], which is easily machinable and known to superconduct in our operating temperature range. We had originally used a gold-plated copper package, but

[3] http://cars9.uchicago.edu/software/python/lmfit
[4] http://www.alcoaqc10.com

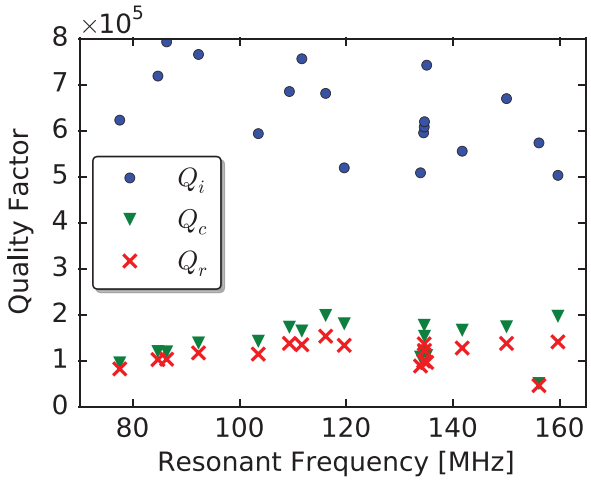

Figure 4.7: Quality factors for the resonators measured at 200 mK in a dark environment. The internal quality factors are all greater than 5×10^5. Here, Q_c refers to $(\mathrm{Re}(Q_e^{-1}))^{-1}$. The errors on Q and Q_c are typically $\sim 1\%$, while the errors on Q_i are around 10%.

found that the internal quality factors were limited to $\sim 4 \times 10^4$, presumably due to coupling between the resonators and the lossy normal metal of the package.

The effective real coupling quality factors are $\sim 2 \times 10^5$ and match reasonably well to the design value. With no loading, the coupling quality factor limits the resonator quality factor. Under optical loading, however, the coupling is better matched. The resonator quality factors are sufficiently high that ~ 300 resonators can be read out in a single octave [Swenson et al., 2012] as required for the proposed experiments. Additionally, the resonance frequencies of five detectors on the tested array were spaced such that greater than 300 resonators could be read out in a single octave. These resonators were all consistently functional and did not collide.

4.3.2.4 Bath temperature sweeps

The bath temperature of the detectors T is stepped in order to measure the device responsivity to thermal quasiparticles, to compare the device response to Mattis-Bardeen theory, and to look for signatures of TLS effects.

At each temperature, a frequency sweep of each resonator was measured and fit to Equa-

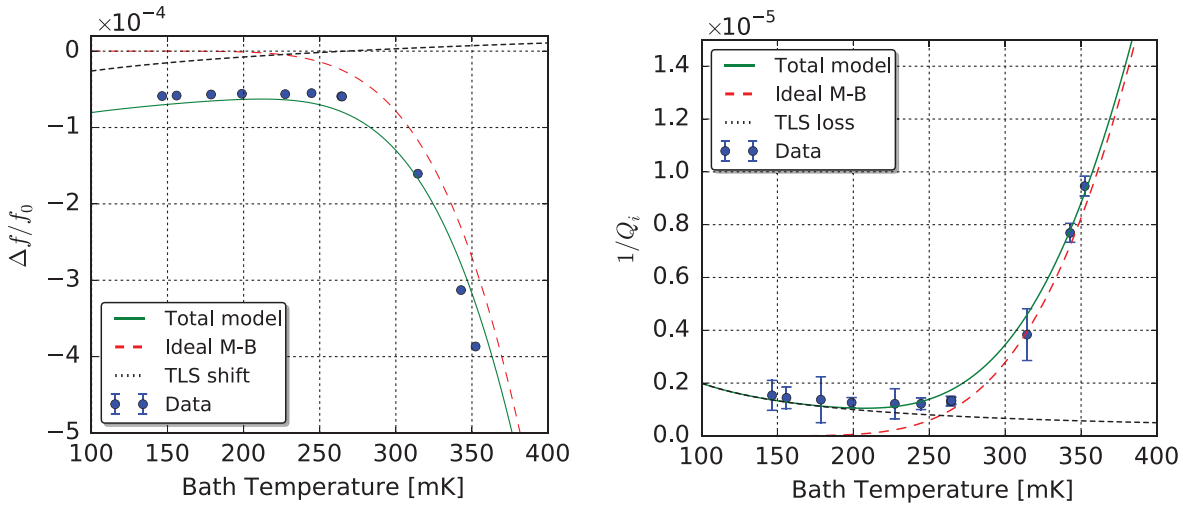

Figure 4.8: Bath temperature sweeps for a single resonator. The resonance frequency at 200 mK is 86 MHz, and the probe power used was ~ -111 dBm. The plot in panel **a** shows the inverse internal quality factor, and the plot in panel **b** shows measurements of the fractional frequency change. Joint fits to the data for three models are plotted: Mattis-Bardeen theory alone (solid green), MB with temperature-dependent TLS loss (dashed red), and MB with a fixed loss term (dotted black). The x_{offset} parameter is also included in the models plotted in panel b. For all models, α_{k} was fixed at 0.65, while T_{c} was allowed to vary. All fits resulted in $T_{\text{c}} \approx 1.60$ K, implying that the relationship between Δ_0 and T_{c} is closer to $\Delta_0 \approx 1.93 k_{\text{B}} T_{\text{c}}$, assuming T_{c} is actually 1.46 K as measured in Section 4.3.1. The MB theory provides a good fit to our data above 250 mK, particularly for the frequency response. The fit to the TLS model yielded $F_{\text{TLS}}\delta_0 \approx 1.4 \times 10^{-4}$, which is driven by the "back-bending" observed in the frequency response. The shape of this curve is inadequate to explain our data, so we do not place much confidence in this model, and hence the resulting value of $F_{\text{TLS}}\delta_0$ for our devices. The model with constant loss term fits the data reasonably well (yielding $Q_{\text{i,loss}}^{-1} \approx 1.0 \times 10^{-6}$) but does not explain the "back-bending" behavior.

tion 4.7 to extract the resonance frequency and quality factors. For each resonator, the fractional change in resonance frequency was computed as $x = (f - f_{\text{max}})/f_{\text{max}}$, where f_{max} is the maximum observed value of the resonance frequency for a resonator for the experiment.

At each temperature step and for each resonator a simultaneous fit was performed to the following two equations:

$$Q_{\text{i,total}}^{-1} = Q_{\text{i,MB}}^{-1} + Q_{\text{TLS}}^{-1} + Q_{\text{loss}}^{-1} \tag{4.10}$$

$$x = x_{\text{MB}} + x_{\text{TLS}} + x_{\text{offset}}. \tag{4.11}$$

The terms in the expression for $Q_{\mathrm{i,total}}^{-1}$ are the prediction from Mattis-Bardeen theory, the loss due to TLS, given below, and a constant loss term to account for effects like radiation to free space or coupling to lossy materials near the device, which do not depend strongly on temperature.

In the following equations, we generally follow the treatment in Noroozian [2012]. The equations assume that the film is thin, that $hf \ll \Delta_0$, and that $k_{\mathrm{B}}T \ll \Delta_0$. All of these assumptions are well satisfied for our devices. Using these assumptions, $Q_{\mathrm{i,MB}}$ is given by

$$Q_{\mathrm{i,MB}} = \frac{2N_0\Delta_0}{\alpha_{\mathrm{k}} S_1 n_{\mathrm{qp}}}, \tag{4.12}$$

where α_{k} is the kinetic inductance fraction, N_0 is the single-spin density of states at the Fermi level (1.72×10^{10} $\mu\mathrm{m}^{-3}\mathrm{eV}^{-1}$ for aluminum [Gao et al., 2008]), and

$$S_1 \approx \frac{2}{\pi}\sqrt{\frac{2\Delta_0}{\pi k_{\mathrm{B}}T}}\sinh\left(\frac{hf}{2k_{\mathrm{B}}T}\right)K_0\left(\frac{hf}{2k_{\mathrm{B}}T}\right), \tag{4.13}$$

expresses the frequency and temperature dependence. Here K_0 is the modified Bessel function of the second kind. When operating our detectors at 200 mK, S_1 ranges from about 0.075 to 0.15 across our readout band. For these dark measurements, we can substitute the thermal quasiparticle density given by [Gao et al., 2008]

$$n_{\mathrm{qp,thermal}} \approx 2N_0\sqrt{2\pi k_{\mathrm{B}}T\Delta_0}\,\exp\left(-\frac{\Delta_0}{k_{\mathrm{B}}T}\right) \tag{4.14}$$

into Equation 4.12 to obtain

$$Q_{\mathrm{i,MB}} \approx \frac{\pi}{4\alpha_{\mathrm{k}}}\frac{e^{\Delta_0/(k_{\mathrm{B}}T)}}{\sinh\left(\frac{hf}{2k_{\mathrm{B}}T}\right)K_0\left(\frac{hf}{2k_{\mathrm{B}}T}\right)}. \tag{4.15}$$

The loss due to TLS is represented by the product of a geometrical filling factor F_{TLS},

and a loss tangent $\delta_{\rm TLS}$ [Gao et al., 2008b]:

$$Q_{\rm TLS}^{-1} = F_{\rm TLS}\delta_{\rm TLS}. \tag{4.16}$$

The TLS loss tangent depends on temperature and electric field as:

$$\delta_{\rm TLS} = \delta_0 \tanh\left(\frac{hf}{2k_{\rm B}T}\right)\left[\frac{1}{\sqrt{1+|E/E_{\rm c}|^2}}\right], \tag{4.17}$$

where δ_0 is the loss tangent at zero temperature and zero field, E is the electric field (which is related to readout power), and $E_{\rm c}$ is the critical field for TLS saturation, defined by Gao et al. [2007]. Since the measurements described in this section were all taken at a fixed readout power and the quality factor does not change appreciably below 300 mK where TLS effects are dominant, the electric field in the resonator E should be roughly constant, so we can treat the electric field dependence term as a constant. Since this constant is guaranteed to be less than one, we simply take it to be equal to one to obtain lower limits on $\delta_{\rm TLS}$. While $F_{\rm TLS}$ can be estimated from electromagnetic simulations, the measurements here cannot disentangle its value from δ_0, so we treat the product as a single parameter in the fit.

The terms in the model for the frequency shift are the prediction from Mattis-Bardeen theory, the effect of TLS, and a constant offset $x_{\rm offset}$, which is added for convenience to take into account the fact that the reference frequency to which the fractional change is measured is arbitrary. The prediction for the fractional frequency shift from Mattis-Bardeen theory is given by

$$x_{\rm MB} = -\frac{\alpha_{\rm k}S_2}{4N_0\Delta_0}n_{\rm qp}, \tag{4.18}$$

where

$$S_2 \approx 1 + \sqrt{\frac{2\Delta_0}{\pi k_{\rm B}T}}\exp\left(-\frac{hf}{2k_{\rm B}T}\right)I_0\left(\frac{hf}{2k_{\rm B}T}\right). \tag{4.19}$$

Here I_0 is the modified Bessel function of the first kind. When operating our detectors at

200 mK, S_2 is approximately 3.8 across our readout band. For these dark measurements we again substitute the equation for the thermal quasiparticle density from Equation 4.14 to obtain

$$x_{\mathrm{MB}} \approx -\frac{\alpha_{\mathrm{k}}}{4N_0\Delta_0}\left[1+\sqrt{\frac{2\Delta_0}{\pi k_{\mathrm{B}}T}}\exp\left(-\frac{hf}{2k_{\mathrm{B}}T}\right)I_0\left(\frac{hf}{2k_{\mathrm{B}}T}\right)\right] \times\left[2N_0\sqrt{2\pi k_{\mathrm{B}}T\Delta_0}e^{-\Delta_0/(k_{\mathrm{B}}T)}\right], \tag{4.20}$$

The frequency shift induced by the temperature dependent TLS loss is:

$$x_{\mathrm{TLS}} = \frac{F_{\mathrm{TLS}}\delta_0}{\pi}\left[\mathrm{Re}\left[\Psi\left(\frac{1}{2}+\frac{hf}{2\pi j k_{\mathrm{B}}T}\right)\right]-\log\left(\frac{hf}{k_{\mathrm{B}}T}\right)\right] \times\left[\frac{1}{\sqrt{1+|E/E_{\mathrm{c}}|^2}}\right], \tag{4.21}$$

where Ψ is the complex digamma function. As before, we assume the electric field dependence term is equal to one and interpret the resulting $F_{\mathrm{TLS}}\delta_0$ as a lower limit. Over the range of temperatures and readout frequencies we use, the term involving Ψ is essentially constant and approximately equal to $\mathrm{Re}(\Psi(1/2)) \approx -1.96$.

In practice, there is a degeneracy between α_{k} and Δ_0. We first attempted to fix $\Delta_0 = 1.76k_{\mathrm{B}}T_{\mathrm{c}}$ using $T_{\mathrm{c}} = 1.46$ K as measured in Section 4.3.1. The resulting fits implied $\alpha_{\mathrm{k}} \approx 0.35$, which is inconsistent with the measured resonance frequencies and film properties. Instead, we fixed $\alpha_{\mathrm{k}} = 0.65$ using those measurements and found that the fits (shown in Fig. 4.8) required that $T_{\mathrm{c}} \approx 1.60$ K, or that $\Delta_0 = 1.93k_{\mathrm{B}}T_{\mathrm{c}}$. Similarly elevated T_{c}-to-Δ_0 conversion factors have been suggested for aluminum resonators in the literature [Janssen et al., 2014].

The free parameters in the fit are then Δ_0, $F_{\mathrm{TLS}}\delta_0$, $Q_{\mathrm{i,loss}}^{-1}$, and the nuisance parameter x_{offset}. We fit the data using three variations of the model, as shown in Fig. 4.8. First, we held $F_{\mathrm{TLS}}\delta_0 = 0$ and $Q_{\mathrm{i,loss}}^{-1} = 0$ and fit only the data above 250 mK, where the response should be well described by the pure Mattis-Bardeen theory. The resulting fit, shown as a solid green line, does indeed describe the data above 250 mK well, but it offers no explanation

of the limited Q_i and non-monotonic "back-bending" behavior seen at lower temperatures. Next, we attempted to fit the full model including $F_\mathrm{TLS}\delta_0$ and $Q^{-1}_\mathrm{i,loss}$. The result is the dashed red line. Here, the "back-bending" in the frequency data dominates the fit, requiring a large value of $F_\mathrm{TLS}\delta_0 \approx 1.4 \times 10^{-4}$, which implies more loss than is actually seen. Thus $Q^{-1}_\mathrm{i,loss} = 0$ in this case. While this model does show "back-bending," the shape is not exactly in agreement with the data. Others have reported similar discrepancies at low temperatures for TiN LEKIDs [Swenson et al., 2013]. Previous studies of the temperature dependance of TLS have been made at much higher readout frequencies, where it is possible to probe the minimum in the x_{TLS} equation that occurs at $T = hf/(2k_\mathrm{B})$. For these devices, the temperature of this minimum is around 2.8 mK, which is not accessible with our cryostat. Finally, we held $F_\mathrm{TLS}\delta_0 = 0$, and found that, aside from the "back-bending," the limit to Q_i could be explained as a constant loss of $Q^{-1}_\mathrm{i,loss} \approx 1.0 \times 10^{-6}$. This value is much more reasonable than the value implied for δ_0 implied by the TLS fit, but of course cannot explain the 'back-bending'. This residual loss could potentially be attributed to a residual, constant population of quasiparticles.

4.3.3 Optical testing

4.3.3.1 Quasiparticle lifetime

The response of the resonances in the readout bandwidth is limited by the resonator ring-down time $\tau_\mathrm{r} = Q/(\pi f_0) \sim 300\ \mu$s. It is thus difficult to measure the quasiparticle lifetime τ_qp using these resonances. We used a vector network analyzer to find higher-order resonances with lower quality factors so that the resonator bandwidth would be large enough to easily measure τ_qp. We targeted resonances with high enough quality factors such that the response to illumination was easily detectable. We read out these resonances with an analog homodyne setup.

We tested a nine-element array from the same wafer as the twenty-element array. The array was mounted in a gold-plated copper package sealed with aluminum tape. The detec-

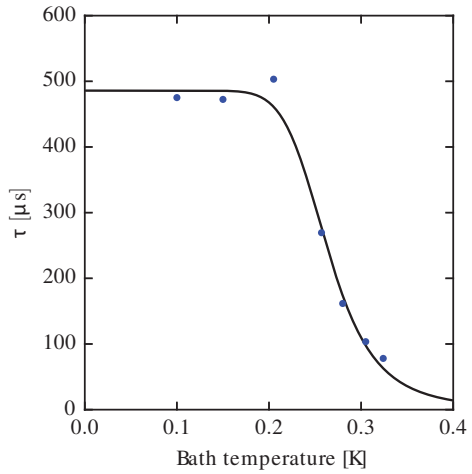

Figure 4.9: Measurements of a detector time constant as a function of bath temperature, extracted from fits to the time-domain response of a higher-order resonance to an LED pulse. Statistical error bars from the fitting process would be smaller than the data points. The solid black curve is a fit of Equation 4.22 to the data, assuming a thermal quasiparticle density, and assuming $\Delta_0 = 1.76 k_B T_c$. The results are $\tau_{max} = 488 \pm 16\,\mu$s and $n^* = 363 \pm 38\,\mu\text{m}^{-3}$. If we instead assume $\Delta_0 = 1.93 k_B T_c$, as implied by the Mattis-Bardeen fits in Section 4.3.2.4, $n^* = 160 \pm 20\,\mu\text{m}^{-3}$.

tors were illuminated through small holes in the tape by a 660 nm red LED coupled to a 2 mm diameter plastic fiber. We studied a resonance with a loaded quality factor of 6300 and a resonance frequency of 810 MHz.

We fit an exponential decay to the time-domain response to an LED pulse and found that the response was fit well by a single time constant. We measured this time constant as a function of bath temperature. As shown in Fig. 4.9, the response time varied approximately as

$$\tau = \frac{\tau_{max}}{1 + n_{qp,thermal}/n^*}, \tag{4.22}$$

where $n_{qp}(T)$ is given by Equation 4.14. This is the expected behavior of the quasiparticle lifetime [Zmuidzinas, 2012].

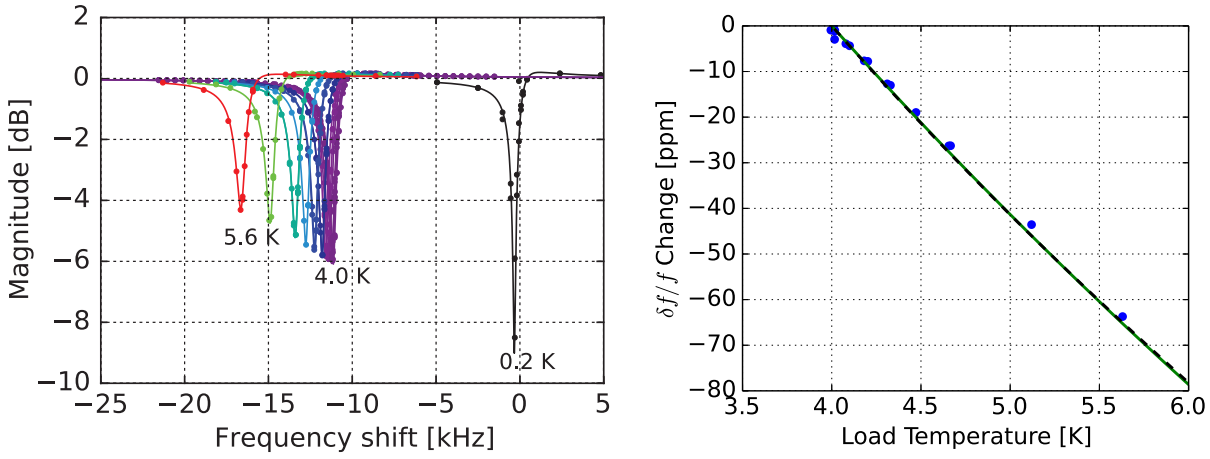

(a) (b)

Figure 4.10: **a.** Resonance sweeps of a single resonator with changing optical load. The dots are measured points and the lines are fits. The resonance frequency at 200 mK is 86.31195 MHz. For these measurements the probe power was ~ -111 dBm, and the bath temperature was 200 mK. The measurement labeled 0.2 K was taken in the dark configuration. **b.** Fitting the resonance curves shown in Fig. 4.10 provides measurements of the resonance frequency as a function of blackbody temperature, plotted here as the fractional frequency change relative to the resonance frequency measured with the blackbody temperature at 4 K. Over the limited range of blackbody temperatures probed, the predicted response deviates by only a small amount from linear. The measured frequency response has a slope of approximately 40 ppm/K. This fractional responsivity is seen consistently across all resonators. The solid green line shows the expected response assuming $\tau_{\rm max} = 500$ μs, and $n^* = 400$ μm^{-3}, as suggested by the time constant measurements, and a total optical efficiency of $\eta = 0.14$. The dashed black line superimposed shows an alternative explanation for the data with the same value of $\tau_{\rm max}$, but with $n^* = 160$ μm^{-3}, which is closer to the typical value reported in the literature [Zmuidzinas, 2012]. In this case, $\eta = 0.32$.

4.3.3.2 Responsivity

The temperature of the blackbody load $T_{\rm bb}$ is changed to measure the responsivity of the device to optically produced quasiparticles. In practice, $T_{\rm bb}$ ranged from 4 to 6 K, or approximately 1.7 to 3 pW for one mode with two polarizations over the 120 to 180 GHz band. The detectors are designed to be predominantly sensitive to a single polarization with an absorption efficiency $\eta_1 = 0.72$. The orthogonal polarization is expected to have $\eta_2 = 0.13$. Since our optical source is unpolarized, the predicted power absorbed by the detectors is calculated using a single mode with two polarizations, and the appropriate optical efficiencies

are applied to each polarization. We refer to the total optical efficiency as η. For use in a polarimeter, there would be a polarization selective element, such as a wire grid, before the devices.

The measured response of a resonator as a function of optical loading is shown in Fig. 4.10. The resonance frequency response is linear across the range of optical powers tested, and is about 40 ppm/K in all the devices.

If thermal quasiparticles are negligible, the quasiparticle density is [McKenney et al., 2012]

$$n_{\rm qp}(P_0) = n^* \sqrt{1 + \frac{2\eta_{\rm pb}\eta P_0 \tau_{\rm max}}{\Delta_0 V_{\rm L} n^*}} - n^*, \tag{4.23}$$

where n^* is the film-dependent characteristic quasiparticle density [Zmuidzinas, 2012], $\eta_{\rm pb}$ is the conversion efficiency (assumed to be ~ 0.7 over our band [Guruswamy et al., 2014]), P_0 is the incident optical power, $\tau_{\rm max}$ is the maximum quasiparticle lifetime, h is the Planck constant, ν is the photon frequency, and $V_{\rm L}$ is the inductor volume. The incident optical power in a waveguide from a blackbody of temperature $T_{\rm bb}$ is

$$P_0 = \int_{\nu_l}^{\nu_h} \frac{2\,h\,\nu^3}{c^2\,(e^{h\,\nu/k\,T_{\rm bb}} - 1)} \frac{n}{\lambda^2} {\rm d}\nu \tag{4.24}$$

where n is the number of dual-polarization modes, λ is the incident wavelength, and ν_l and ν_h are the low and high frequency edges of the spectral band. In this experiment the spectral band is defined by the waveguide cutoff at 130 GHz and the low-pass filter at 170 GHz.

The absorbed power is $P = P_0\eta$. The frequency shift caused by an optical load P_0 can be computed by substituting Equation 4.23 into Equation 4.18 giving

$$x = -\frac{\alpha_{\rm k} S_2}{4 N_0 \Delta_0} \left[n^* \sqrt{1 + \frac{2\eta_{\rm pb}\eta P_0 \tau_{\rm max}}{\Delta_0 V_{\rm L} n^*}} - n^* \right] \tag{4.25}$$

We observe a linear relationship between $T_{\rm bb}$ and the frequency shift as seen in Fig. 4.10. Note that for the experimental setup $T_{\rm bb}$ is very nearly proportional to P_0. The range of optical powers over which we measure the responsivity is small and therefore it is difficult to distinguish a $\sqrt{P_0}$ from a P_0 dependence. A linear (or nearly linear) relationship has been observed by many groups and widely reported in the literature with no clear explanation of the phenomenon for both aluminum [Gao et al., 2008] and TiN devices [Noroozian, 2012, Hubmayr et al., 2015]. These other measurements tested over a wider range of optical power.

By taking the partial derivative of Equation 4.25 with respect to P_0, we can compute the expected responsivity:

$$\frac{\partial x}{\partial P_0} = \frac{\alpha_{\rm k} S_2 \tau_{\rm max} \eta_{\rm pb} \eta}{4 N_0 \Delta_0^2 V_{\rm L}} \left[1 + \frac{2 \eta_{\rm pb} \eta P_0 \tau_{\rm max}}{\Delta_0 V_{\rm L} n^*} \right]^{-1/2}. \tag{4.26}$$

Substituting in $\alpha_{\rm k} = 0.65$, $S_2 = 3.8$, $V_{\rm L} = 1870\ \mu{\rm m}^3$, $\eta_{\rm pb} = 0.7$, $\eta = 0.14$, $\tau_{\rm max} = 500\ \mu{\rm s}$, $n^* = 400\,\mu{\rm m}^{-3}$, and $\nu = 150$ GHz yields $\partial x/\partial P_0 \approx 45$ ppm/pW. For a blackbody load temperature of 4 K, we expect $P_0 \approx 1.75$ pW and $\delta P_0/\delta T_{\rm bb} \approx 0.88$ pW/K, which implies $\partial x/\partial T \approx 40$ ppm/K, in good agreement with our measurements.

Alternatively, if $n^* = 160\,\mu{\rm m}^{-3}$, as would be the case if $\Delta_0 = 1.92 k_{\rm B} T_{\rm c}$ (see Fig. 4.9), $\eta = 0.32$ would also yield a responsivity of 40 ppm/K.

4.3.3.3 Optical versus thermal response

A comparison of the response to optical power and to changing bath temperature is presented in Fig. 4.11. Mattis-Bardeen theory predicts that for a given change in quasiparticle density, the fractional change in resonance frequency should be very nearly linearly related to the change in the quality factor [Gao et al., 2008]. This behavior is evident in these devices. The slope of this linear relationship is the ratio of the frequency responsivity to the dissipation

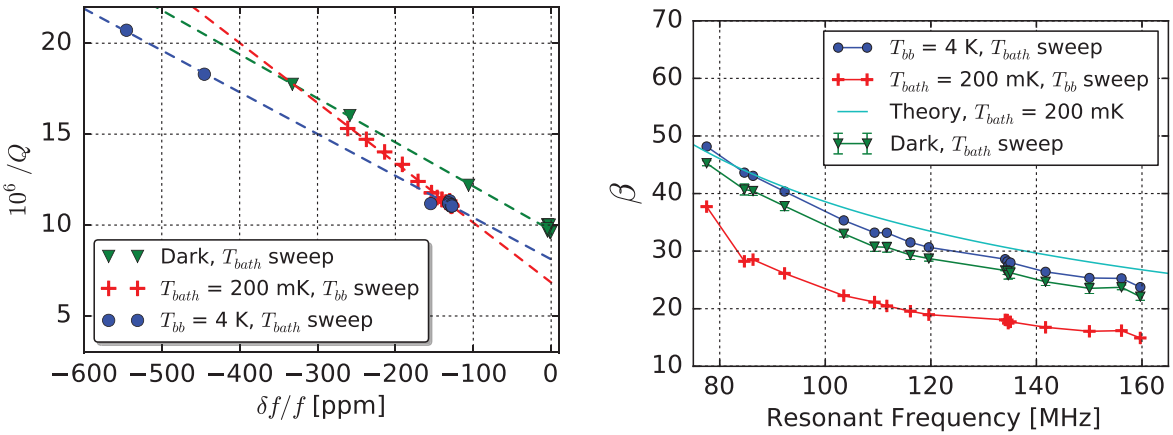

(a) (b)

Figure 4.11: **a.** Resonance frequency shift plotted versus inverse quality factor for a single resonator, showing good agreement to the linear behavior predicted by Mattis-Bardeen theory. The points derived from bath temperature sweeps (blue dots and green triangles) show a consistent slope, which differs from that found when sweeping the blackbody load temperature (red crosses). The dashed lines are linear fits to the data, used to derive the β parameters plotted in Fig. 4.11 **b.** Ratio of frequency responsivity over dissipation responsivity (β) plotted versus resonance frequency for all resonators. The thick line shows the theoretical curve expected for a thermal quasiparticle distribution, given by Equation 4.27. The errors on all measurements are similar to those shown on the dark, T sweep curve. The marker symbols and colors match the corresponding data in Fig. 4.11, from which the values of β are derived.

responsivity, and is defined in the literature as [Zmuidzinas, 2012]:

$$\beta = -\frac{2\delta f_0/f_0}{\delta Q^{-1}} = \frac{S_2}{S_1} = \frac{1+\sqrt{\frac{2\Delta_0}{\pi k_B T}}\exp\left(-\frac{hf}{2k_B T}\right) I_0\left(\frac{hf}{2k_B T}\right)}{\frac{2}{\pi}\sqrt{\frac{2\Delta_0}{\pi k_B T}}\sinh\left(\frac{hf}{2k_B T}\right) K_0\left(\frac{hf}{2k_B T}\right)}. \tag{4.27}$$

This quantity and the theoretical prediction are plotted in Fig. 4.11.

Gao et al. [2008] showed theoretically and experimentally that β should be the same for quasiparticles generated thermally or optically. Our measurements seem to show a different behavior. We find that β matches the theoretical prediction when changing the device temperature, either in a dark environment, or with a constant optical flux from the black body load held at a fixed temperature. However, when the bath temperature is kept fixed and the black body load temperature is varied, β is appreciably smaller. This effect has been

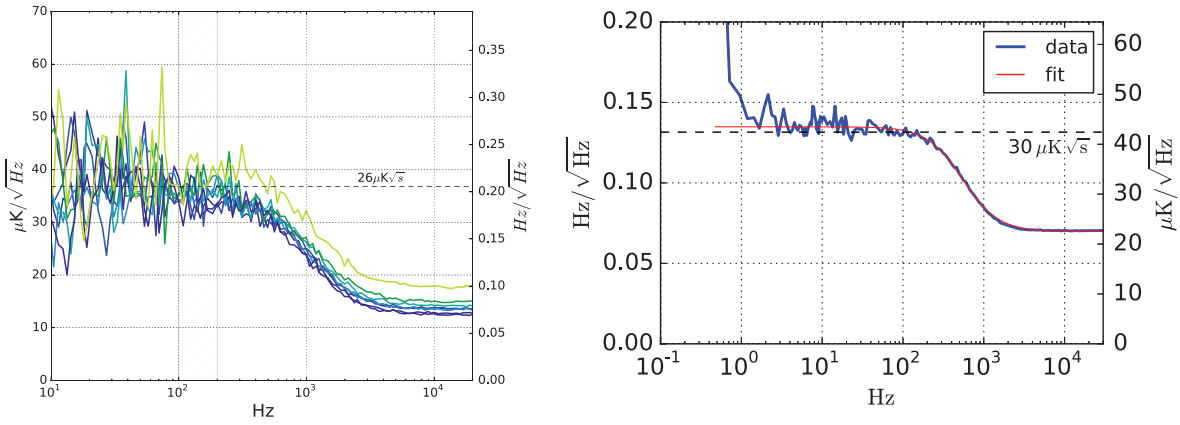

(a) (b)

Figure 4.12: **a.** The noise spectrum of a single, typical detector is shown at different optical loads. The blackbody temperatures range from 4 K (purple) to 5.3 K (yellow), with the noise level increasing slightly with temperature. The average value in the region indicated near 100 Hz corresponds to the measurements shown in Fig. 4.13. The probe tone power was approximately -105 dBm. **b.** The average spectrum (thick blue line) of a resonator obtained from 13 time series, each 30 seconds long. This is a different resonator than that shown in panel a. Multiple time series were taken to see the noise down to very low frequencies, which appears to be very flat. For modulation schemes, such as with a continuously rotating half-wave plate (HWP), that we envision for future CMB projects [Johnson et al., 2014, Araujo et al., 2014], we are particularly interested in the noise performance between 10 and 50 Hz. The thin red line is a fit of the spectrum to a Lorentzian model, showing good agreement. The resonator ring-down causes the roll-off at 460 Hz. The steep rise at the lowest frequencies is due to drift of the blackbody load temperature. The probe tone power for this measurement was approximately -113 dBm.

reported for other devices as well [Janssen et al., 2014]. They suggest that this effect could be explained if the optical pair breaking is non-uniform across the inductor. This could be the case for our devices: we designed them to efficiently couple to the circular waveguide, but electromagnetic simulations do show variations in the electric field of the incident millimeter wavelength radiation across the inductor. We plan to further investigate this phenomenon in the future.

4.3.3.4 Noise

Noise measurements were made by recording time series of the complex transmission at a fixed probe frequency. For each noise measurement, a frequency sweep was performed and

fit to the resonator model given in Equation 4.7 to determine the optimal value of the probe tone frequency. When analyzing the noise data, the complex time series is scaled by the complex dS_{21}/df vector determined from the resonator model. The real and imaginary components of the resulting scaled time series then correspond to the fluctuations in resonance frequency and dissipation, respectively. This also results in the units of the frequency fluctuation time stream being hertz. As a check, we also apply the eigenvector decomposition technique suggested by Gao et al. [2007], which reports a constant rotation angle between the two principal components of the fluctuation spectrum within the device bandwidth, thus confirming that the fluctuations can be decomposed using a simple rotation.

Initially, noise measurements were taken with the pulse-tube cooler on. This did not produce significant low-frequency noise when the devices were in a copper package, as the resonator quality factors were limited by the coupling to the lossy normal metal. However, when testing with the superconducting aluminum package, the larger Q_i increased the responsivity, and noise from the pulse-tube cooler was clearly evident in the noise spectrum. The spectra shown here were taken with the pulse-tube cooler off, while the ADR continued to regulate the temperature of the detector package. Turning off the pulse-tube cooler is not a viable option for a deployed instrument, so we are working to better understand and mitigate the source of this extra noise.

A series of noise spectra are show in Fig. 4.12a for load temperatures between 4 and 5.3 K. Fig. 4.12b shows the result of averaging 13 spectra taken in succession with a fixed 4 K load temperature and 200 mK bath temperature to better show the quality of the noise at low frequencies. The measured $\mathrm{Hz}/\sqrt{\mathrm{Hz}}$ fluctuation spectrum is converted to $\mu\mathrm{K}/\sqrt{\mathrm{Hz}}$ units by multiplying by the slope of the measured frequency shift as a function of blackbody temperature, using the measurements shown in Fig. 4.10. This can in turn be interpreted as noise equivalent temperature (NET) by dividing by $\sqrt{2}\ \sqrt{\mathrm{s}}/\sqrt{\mathrm{Hz}}$. The resonator in Fig. 4.12 response rolls off at ∼460 Hz. This bandwidth corresponds well with the expected half-width at half-maximum (HWHM) resonator bandwidth of $(f_0/Q)/2$, where, for this resonator,

$f_0 = 92.277432$ MHz and $Q = 99595$. The high quality factor and low resonance frequency obscures the roll-off due to the quasiparticle lifetime $\tau_{\rm qp}$.

Using the semi-empirical model, we predicted the noise equivalent power (NEP) contributions for the LEKIDs in our cryogenic set up and then converted them to NET as shown in Fig. 4.13. The photon noise is calculated as $\mathrm{NEP}_\gamma = \sqrt{2\eta P_0 h\nu(1+\eta n_{\rm o})}\,/\eta$, where $n_{\rm o}$ is the photon occupancy number and is negligible for the range of powers tested [de Visser et al., 2014, Zmuidzinas, 2012]. The absorption is expected to be high (>70%) in the polarization for which the detectors were designed to be sensitive, which we refer to as η_1. Additional optical loading may possibly couple into the detectors from the orthogonal polarization (η_2) or leaked power from adjacent resonators ($\eta_{\rm l}$). For the plot in Fig. 4.13, we used $\eta_1 = 0.72$, $\eta_2 = 0.13$, and $\eta_{\rm l} = 0.075$, so $\eta = (\eta_1+\eta_2)/2 + \eta_{\rm l} = 0.5$. The expected generation-recombination noise can be approximated as $\mathrm{NEP}_{\rm gr} \approx \sqrt{2\eta P_0 \Delta_0/\eta_{\rm pb}}/\eta$, and should be the dominant detector noise source in the case of photon noise limited detectors [Yates et al., 2011]. The NET is calculated using $\mathrm{NET} = \mathrm{NEP}/(\sqrt{2}\,dP_0(T)/dT)$. We emphasize this is the NET at the load temperature in our experiment, not $\mathrm{NET}_{\rm CMB}$. The optical efficiency of the detectors influences both the expected photon and g-r noise levels. Due to the uncertainty of the optical efficiency, we predict a range of a expected NET values for the detectors. For a photon noise limited detector, the predicted total detector NET value is approximately 20 to 30 $\mu\mathrm{K}\sqrt{\mathrm{s}}$ at 2 pW of incident power. This predicted NET range is for an optical efficiency range of $\eta = 0.3$ to 0.7 for a single mode with two polarizations.

As seen in Fig. 4.13, the NET of the detectors on the tested array fall in the range 26 ± 6 $\mu\mathrm{K}\sqrt{\mathrm{s}}$ with a 4 K optical load. We estimate the random error on individual NET measurements to be ∼10%. We do not find any systematic relationship between NET and resonance frequency. Over the range of blackbody temperatures tested the noise remains fairly constant. However, as shown in Fig. 4.13 the dependence of the noise on temperature is very shallow. The test setup was designed to directly measure the NET at 4 K using only small changes in load temperature. In future experiments, we will use another optical source

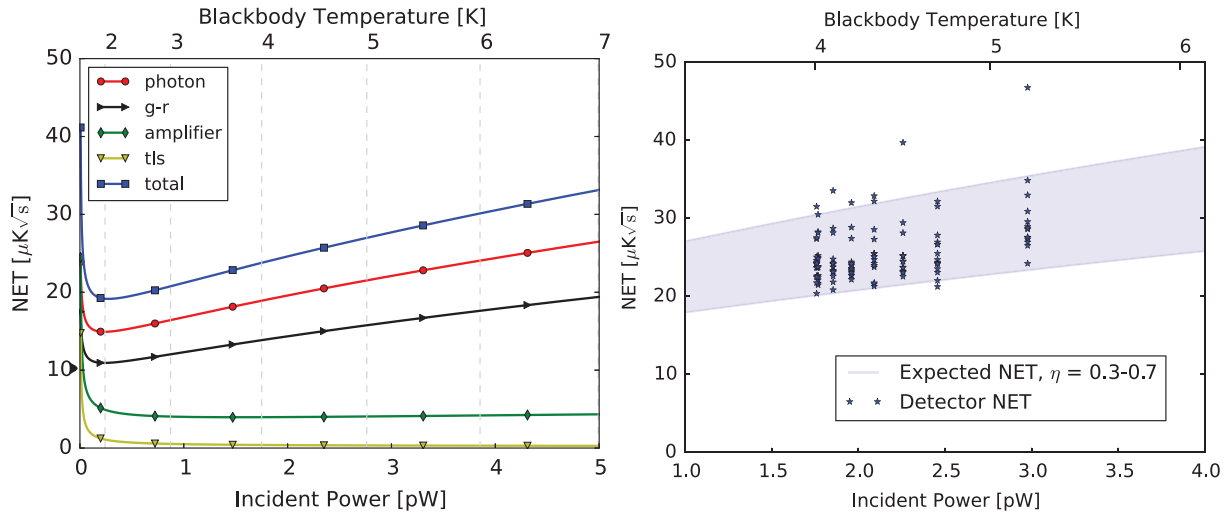

Figure 4.13: **a.** The predicted levels for the different noise sources versus optical power. The total NET is composed of photon noise and detector noise (under load). The detector noise includes three components: g-r noise, readout amplifier noise, and TLS noise. The expected TLS noise level is computed using a semi-empirical formula [Gao et al., 2008a] and fiducial scaling values were provided by MAKO [McKenney et al., 2012]. The expected amplifier and TLS values are calculated assuming operation near bifurcation, which changes with load. The gray vertical lines correspond to blackbody load temperatures from 2 to 6 K in steps of 1 K. **b.** Measured NET values and the predicted NET range. The incident power at the horn aperture is calculated from the blackbody temperature $T_{\rm bb}$ using an emissivity of 0.92 for a single mode in two polarizations. The absorption efficiency of the detectors can be simulated but is unmeasured. The blue band shows the range of NETs expected for absorption efficiencies between $\eta = 0.3$ and $\eta = 0.7$. The stars show measured total NETs including the photon and detector noise. The data were measured with a constant probe tone power of approximately -105 dBm.

to probe the noise over a wider range of optical power.

The predicted amplifier noise contribution in units of Hz/$\sqrt{\rm Hz}$ is [Lee and Hajimiri, 2000]

$$e_{\rm f,amp} = \sqrt{\frac{4k_{\rm B}T_{\rm amp}}{P_{\rm g}}}\frac{Q_{\rm c}}{Q^2}f_0, \tag{4.28}$$

where $T_{\rm amp} \sim 4$ K is the noise temperature of the LNA and $P_{\rm g}$ is the probe tone power. While there is uncertainty in the exact value of $P_{\rm g}$, the estimated value of -105 dBm predicts $e_{\rm f,amp} \sim 0.05$ Hz/$\sqrt{\rm Hz}$ for $f_0 = 100$ MHz, in reasonable agreement with the measurements shown in Fig. 4.12.

Given the uncertainty in our exact optical absorption and pair breaking efficiencies, the measured noise data shown in Fig. 4.13 is consistent with our devices having a contribution from TLS noise at a level ranging from negligible to approximately equal to the photon noise level. We find the noise spectrum is white down to the lowest frequencies measured, as seen in Fig. 4.12. This behavior has been reported by other groups [Shirokoff et al., 2014], however previous measurements of devices with TLS noise typically have a $e_{\mathrm{f,TLS}} \sim f_{\mathrm{s}}^{-0.25}$ shape, where f_{s} is the frequency of the noise spectrum [McKenney et al., 2012].

4.4 Conclusion

In this chapter we presented a LEKID design and a horn-coupling strategy that appears promising for cosmic microwave background (CMB) studies. Our LEKIDs were made from a single thin aluminum film deposited on a silicon wafer and patterned using standard photolithographic techniques at STAR Cryoelectronics. We described the cryogenic testing apparatus and the testing program. Finally, we presented the results from our optical testing, dark testing and aluminum film characterization measurements. Our data were compared with Mattis-Bardeen theory for consistency. These results show the multiplexing scheme works well, the yield across multiple LEKID arrays is 91%, and the NETs are in the range 26 ± 6 $\mu\mathrm{K}\sqrt{\mathrm{s}}$.

Future work will focus on further decreasing the TLS effects, increasing the number of elements in the array, developing a dual-polarization design and better understanding the performance of these devices. In particular, the following items warrant further investigation: (i) the response of the detectors is somewhat more linear than expected, (ii) the measured β is different for thermal and optical quasiparticles, and (iii) the bath temperature T sweeps in Fig. 4.8 show evidence for TLS effects but the relationship between δ_{TLS} and the TLS noise level is unknown, in particular for low-frequency, aluminum LEKIDs. We also plan to measure the noise of these devices over a wider range of optical power using an improved

optical source.

We have already fabricated a second-generation wafer that underwent an hydrofluoric acid dip during fabrication, and we expect the TLS effects of the devices on this wafer will be reduced.

A small fraction of the radiation that is not absorbed or reflected propagates laterally in the dielectric substrates and this signal could produce detector-to-detector cross-talk. To mitigate this effect, we will metalize the fused silica wafer with titanium nitride (TiN) between the horns and patterned to act as an efficient millimeter-wave absorber with an effective sheet resistance of approximately 150 Ω. This TiN layer also helps to absorb ballistic phonons propagating in the silicon from energy deposited by cosmic rays. We are working with STAR Cryoelectronics on TiN films with the desired T_c. This work could also lead naturally to developing commercial TiN LEKID designs sensitive to different frequencies.

The present geometry of the inductor absorbs an average of less than 10% of the cross polarization as predicted by electromagnetic simulations. A rectangular waveguide or wire grid polarizer in front of the focal plane will further define the polarization selectivity of the focal plane, and make it truly single-polarization. We plan to add one of these varieties of polarization selectivity to future detector modules.

4.5 Related work

The paper [McCarrick et al., 2014] that comprises this chapter was the first publication put forth by our collaboration. Much of the research that took place subsequently was directly related. In particular there are two paper for which I will highlight my contributions.

The first paper is Flanigan, McCarrick et al. [2016]. This paper used the same design of detector array, detector package and horn array as for McCarrick et al. [2014]. The detector array underwent an additional processing step prior to fabrication - a hydrofluoric acid bath - to reduce any TLS noise. The same cryogenic testbed was used with the addition of the

MMW source. In this paper, we showed that these LEKIDs definitively achieved photon-noise limited performance above 1 pW of absorbed power. Additionally, the devices were able to measure and differentiate between purely shot noise, from coherent radiation, and wave noise, from broadband radiation. We also measured that the devices had an NEP of $\sim 10^{-17}$ W$\sqrt{\text{Hz}}$ under 1 pW of loading. These measurements strengthened the case that the devices are suitable for CMB experiments.

The second paper is Jones et al. [2017]. I designed the detector array which was used for the experiment. The 8-element array was based on the work on this chapter, and the detectors were of a similar single-polarization LEKID design. This array was fabricated out of aluminum-manganese (Al-Mn), which has a tunable critical temperature T_c. This is attractive because a lower T_c will allow detection of photons with a lower frequency and possibly reduce intrinsic recombination noise for 150 GHz and higher frequency bands (see Sec. 2.4.3.2). In this paper, we showed that Al-Mn resonators with $T_c = 694$ mK (or $h\nu > 70$ GHz) have high quality factors, and that Al-Mn should be a suitable material for KIDs.

Chapter 5

Controlling optical crosstalk in KIDs with a Titanium Nitride mesh

We discuss the design and measured performance of a titanium nitride (TiN) mesh absorber we are developing for controlling optical crosstalk in horn-coupled lumped-element kinetic inductance detector arrays for millimeter-wavelengths. This absorber was added to the fused silica anti-reflection coating attached to previously-characterized, 20-element prototype arrays of LEKIDs fabricated from thin-film aluminum on silicon substrates. To test the TiN crosstalk absorber, we compared the measured response and noise properties of LEKID arrays with and without the TiN mesh. For this test, the LEKIDs were illuminated with an adjustable, incoherent electronic millimeter-wave source. Our measurements show that the optical crosstalk in the LEKID array with the TiN absorber is reduced by 66% on average, so the approach is effective and a viable candidate for future kilo-pixel arrays.

5.1 Introduction

A lumped-element kinetic inductance detector (LEKID) is a superconducting, photon-sensing resonator consisting of a capacitor and an inductor. The inductance has both geometric and kinetic components, the latter arising in alternating currents only and produced by stored energy in the Cooper pairs. When a photon with energy above the gap energy of the detector material is absorbed, the resonance frequency f_0 and quality factor Q of the resonator shift [Day et al., 2003, Zmuidzinas, 2012]. The detector is coupled to a transmission line, allowing these perturbations to be measured with probe tones.

In this chapter, we present the measured performance of a titanium nitride (TiN) mesh designed to control optical crosstalk in arrays of horn-coupled LEKIDs. The 20-element prototype LEKID arrays used in this study [McCarrick et al., 2014] [Ch. 4] are sensitive to a 40 GHz spectral band centered on 150 GHz. These LEKIDs are being developed for cosmic microwave background (CMB) studies at millimeter wavelengths. The LEKIDs and the TiN mesh are shown in Figs. 5.1 and 5.2. The new TiN absorber introduced in this work enhances the performance of these LEKIDs by absorbing photons propagating laterally in the dielectrics inside the detector package. Therefore, the TiN mesh absorbs the photons that produce optical crosstalk.

5.2 Experiment details

Each LEKID is coupled to a conical horn, as shown in Fig. 5.2. A low-pass metal mesh filter [Ade et al., 2006] mounted before the aperture of the conical horn defines the 170 GHz, high-frequency edge of the spectral band. The conical horn flare tapers to a cylindrical, single-moded waveguide, and this waveguide acts as a high-pass filter, which defines the 130 GHz, low-frequency edge of the spectral band. The cylindrical waveguide then expands into a second conical flare that is used to help match the wave impedance between the waveguide and the LEKID. Further, a 300 μm thick fused silica layer was inserted between

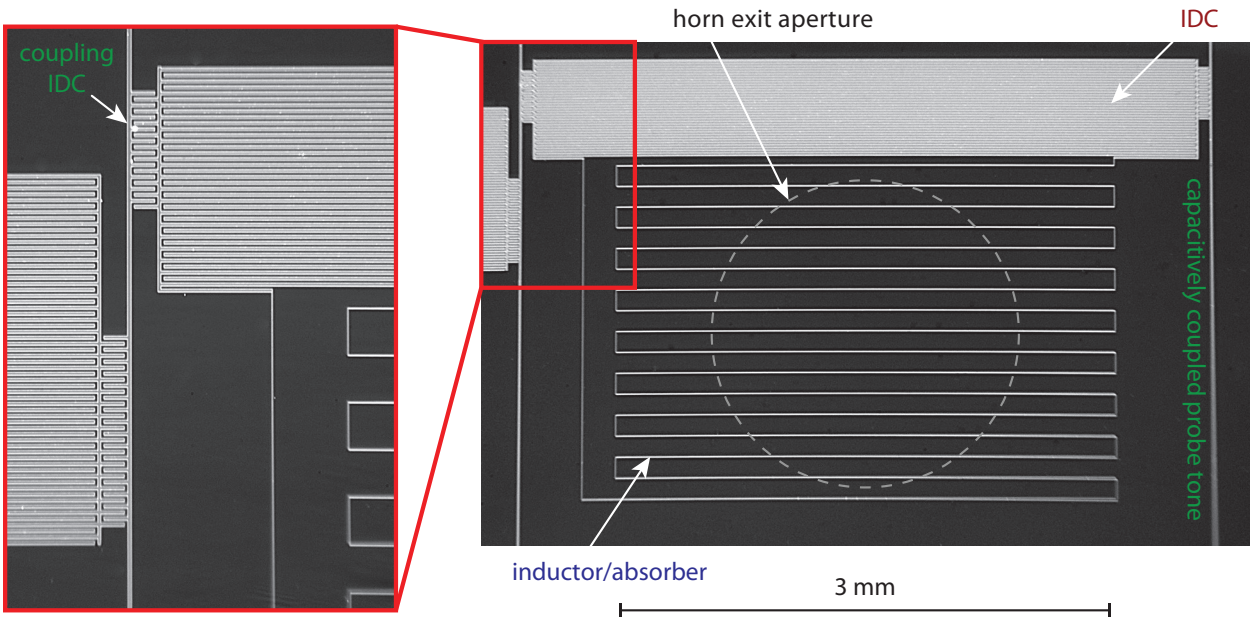

Figure 5.1: Photograph of a LEKID used in this study. The interdigitated capacitor (IDC) and meandered inductor set the resonance frequency for each detector. Incident photons are absorbed in the inductor and break Cooper pairs changing the kinetic inductance. This shifts the resonance frequency of the detector. The inset shows the IDC that couples the resonator to the transmission line, allowing the frequency perturbation to be readout.

the two elements to serve as an anti-reflection (AR) coating. The back-illuminated LEKID arrays were fabricated from a 20 nm thick aluminum film patterned on a 300 μm thick high-resistivity, float-zone silicon wafer. The detectors consist of a meandered inductor and interdigitated capacitor (IDC). Each inductor in the array is identical. Therefore, the unique resonance frequency of each detector is set by the capacitance of the IDC, which varies from device to device. The detectors are operated at approximately 120 mK using a pulse-tube cooler and a two-stage adiabatic demagnetization refrigerator. We use an FPGA-based digital readout system built from a ROACH signal processing board, which provides multiple, parallel homodyne readout chains.

Simulations show that photons can propagate laterally in the two dielectrics, and these photons could produce unwanted optical crosstalk. Therefore, we implemented a 100 nm thick TiN mesh deposited on the detector side of the AR coating. The TiN mesh is designed to have a wave impedance $Z = 194\ \Omega$ matching that of the fused silica substrate. To get

this impedance, we patterned a mesh in the TiN film. The line width of the TiN in the mesh is 5 μm, and the cell size is 100 μm by 100 μm. The mesh is approximately the same size as the LEKID array (22 mm by 26 mm), and rectangular apertures 2 mm by 3 mm are patterned in the mesh in front of each inductor, so the signal photons can pass from the horn to the absorber. Millimeter-wave photons traveling laterally along the dielectrics should be absorbed by this TiN mesh because the measured T_c of the film is 1 K, so the gap frequency is below the passband of the detector module.

The optical response of the detectors was measured using an electronic photon source that produces broadband, incoherent millimeter-wave signals. In this source, thermal noise from a 50 Ω termination resistor is first amplified in the 12 GHz range and then used to drive a 12$\times$ active frequency multiplier to produce 140 to 160 GHz radiation in a WR6 rectangular waveguide. The millimeter-wave signal can be amplitude modulated using a PIN switch at the input of the multiplier. Source signals are coupled into the cryostat through a WR6 waveguide window. Inside the cryostat, a horn and a reflective collimator are used to illuminate the detectors. The source is described in more detail in the literature [Jones et al., 2015, Flanigan et al., 2016]. The power incident on the detectors was swept from approximately 0.1 to 20 pW to measure the responsivity of the devices. The source power was varied using inline WR6 attenuators mounted outside the cryostat.

5.3 Results

For this experiment, two different arrays of the same design, processed on the same wafer, were measured during two separate cryostat cycles. One assembly included the TiN absorber and one did not. All of the horn apertures were covered with aluminum tape except for one allowing just one directly illuminated detector in the study. We will henceforth refer to the taped-over horns as 'dark'.

The measured response of both the illuminated 179 MHz resonator and a representative

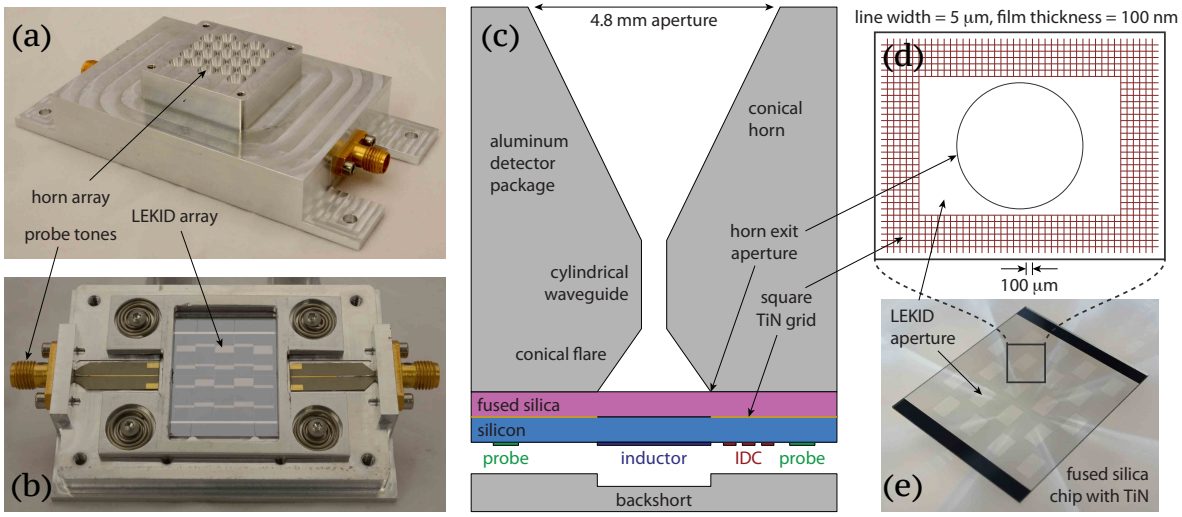

Figure 5.2: **a.** Photograph of the conical horns machined into the aluminum detector package. **b.** Photograph of the LEKID array mounted in the detector package with the backshort plate removed. **c.** Cross-sectional view of one array element. **d.** Schematic of the TiN absorber designed to mitigate optical crosstalk between detectors. The 100 nm thick TiN absorber is fabricated on a fused silica chip, which is nominally used for matching the impedance of the horn to the LEKID array. Rectangular apertures in the mesh the same size as the LEKID inductor/absorber allow photons to propagate from the horn to the detector. **e.** Photograph of the TiN absorber fabricated at NASA/JPL.

dark resonator in the TiN-free assembly is shown in Fig. 5.3. For the assembly with the TiN absorber, the 179 MHz resonator in the array was not working. Therefore, we instead illuminated the 102 MHz resonator. We checked that the responsivity to quasiparticles was consistent across all detectors in both arrays by measuring their response to changes in bath temperature. As shown in Fig. 5.4, the response of the detectors across both arrays is nearly identical, indicating the responsivity of each detector in the test is the same and the two arrays can be meaningfully compared.

Because the optically-produced quasiparticles dominate, the resonator frequency response $x = (f - f_0)/f_0$ should be well described by a function proportional to $(1 + P/P_*)^{1/2} - 1$, where P is the incident power and P_* is a film-dependent constant [McCarrick et al., 2014, McKenney et al., 2012]. We originally fit this model to the illuminated detector response, and used the best-fit model parameters to compute the relative power absorbed by the dark detectors (optical crosstalk). We found this method underestimates the amount of power

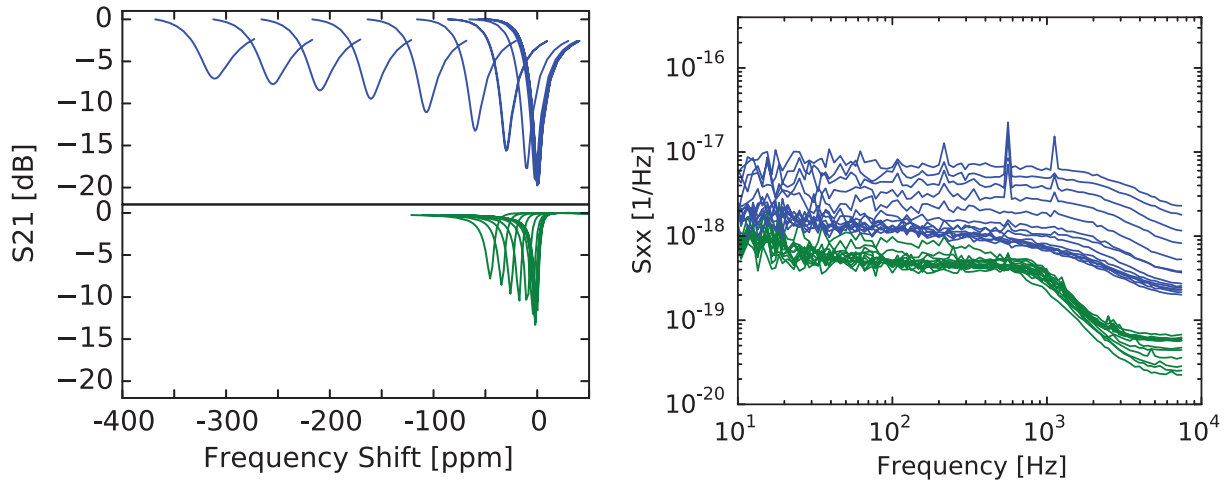

(a) (b)

Figure 5.3: **a.** Measured S_{21} with changing optical load for the illuminated detector (blue) and a representative dark detector (green) before the TiN mesh was added. The optical load was swept from approximately 0.1 to 20 pW. The ambient background loading in the test setup dominates at the low end of this range. **b.** The noise spectrum of the illuminated detector (blue) and a representative dark detector (green) measured with different optical loads and constant probe-tone power. The optical power again varies from from approximately 0.1 to 20 pW. For the illuminated detector the device noise level (below 500 Hz) rises with optical power as the quality factor decreases. For the dark detector the device noise stays relatively constant with an increasing optical load, as expected. The roll off at 1 kHz is due to the resonator ring-down time. The noise level above the roll off is set by the amplifier noise. For clarity, the 60 Hz line and harmonics were removed.

absorbed in the dark detectors because the fit in the lower-power regime ($\ll$ 1 pW of incident power) is poor, likely due to systematic errors produced by the ambient background signal dominating the comparatively small input test signal from our source. Therefore, instead we measured the frequency shifts with 0.3 pW of loading. This loading level should be in the linear regime of the detector response function, meaning the measured frequency shift in parts-per-million [ppm] should be directly proportional to power. We then calculate the optical crosstalk by normalizing the measured frequency shifts to the frequency shift of the illuminated detector. This result serves as an upper bound on the optical crosstalk because any non-linear LEKID response would compress the signal and spuriously decrease the normalization factor. We find that the optical crosstalk with the TiN absorber is lower than the optical crosstalk without the TiN absorber by 66% on average as seen in Fig 5.5.

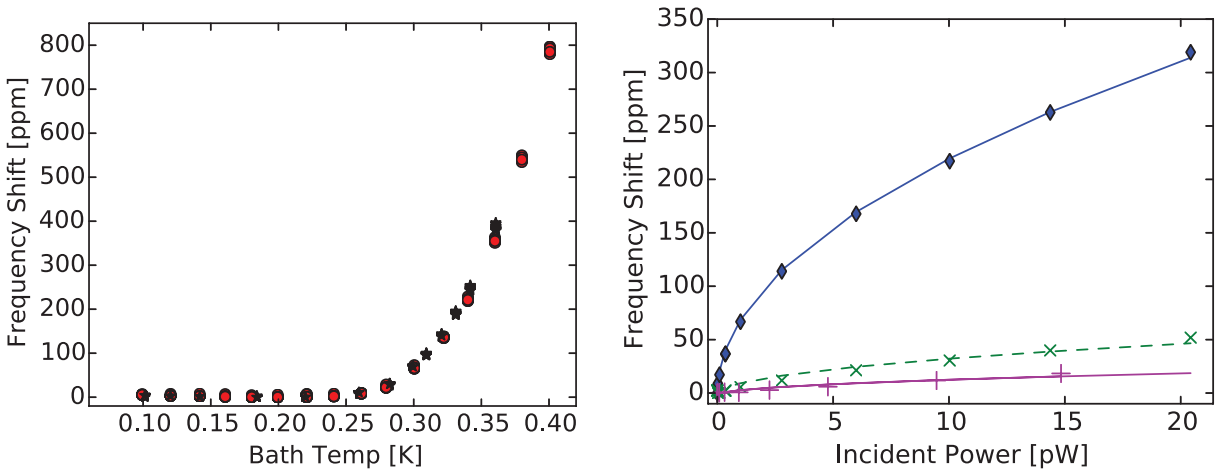

(a) (b)

Figure 5.4: **a.** The fractional frequency change versus bath temperature for the detectors in the two arrays we used for this study. The bath temperature was stepped from 100 mK to 400 mK to check for consistency in device responsivity between the arrays. The detectors without the TiN mesh are plotted as the red circles, and the detectors with the TiN mesh are plotted as the black stars. **b.** The fractional frequency change as a function of optical power for the illuminated detector (blue), a representative dark detector without the TiN mesh (green), and a representative dark detector with the TiN mesh (magenta).

The detectors adjacent to the illuminated detector still show appreciable optical crosstalk that is reduced but not eliminated by the TiN absorber (see discussion in Section 5.4). And the response of the dark detectors not adjacent to the illuminated detector in the module with the TiN absorber is similar to the measured response of a third background/control configuration where all the horns are covered with aluminum tape; the TiN absorber reduces the optical crosstalk to a level that cannot be distinguished from this small systematic error background at the $\sim$1% level.

5.4 Discussion

This study was our first systematic investigation into the level of optical crosstalk in our prototype horn-coupled LEKID modules. Our data reveals that the TiN absorber works well, and it reduces the apparent optical crosstalk to approximately 2% or below for the detectors not adjacent to the illuminated detector in the array. This level is comparable to the

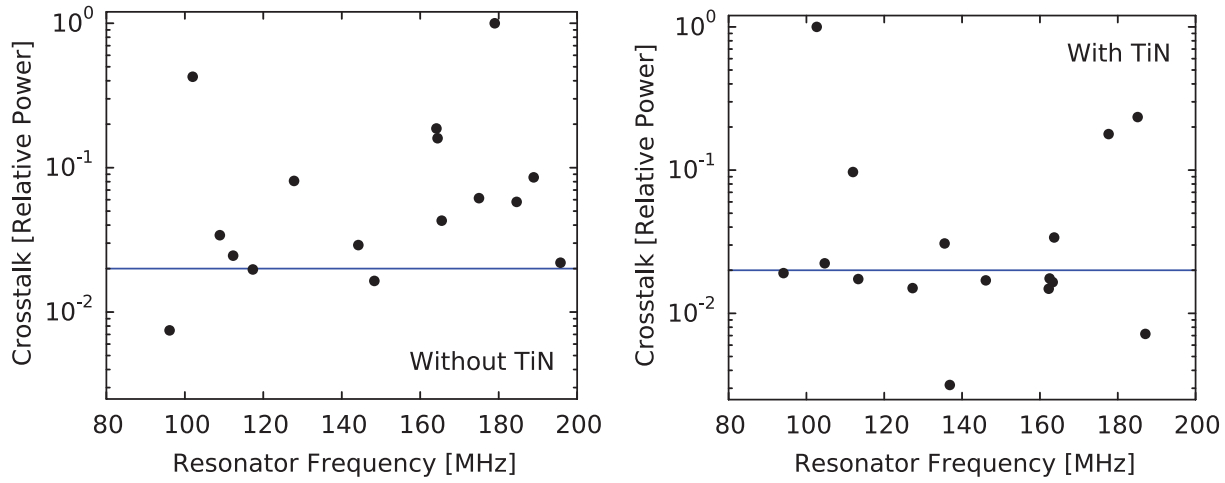

Figure 5.5: **a.** The power absorbed by each LEKID normalized to the power absorbed by the illuminated LEKID. The module configuration used to produce the result in this panel did not include the TiN absorber. Here the illuminated LEKID absorbed approximately 0.3 pW of power. **b.** The same result as that plotted in the left panel, though to produce the result in the right panel, the TiN absorber was used. The TiN absorber reduces the optical crosstalk on average by 66%. The detectors adjacent to the illuminated detector still show appreciable crosstalk response, which indicates our prototype detector module design needs to be optimized (see discussion in Section 5.4). The blue reference line in both panels is plotted at the 2% level.

magnitude of systematic errors produced by the experimental setup, so further investigation is required to understand the optical crosstalk level more precisely; the measured ∼2% crosstalk level is likely an upper limit. Electromagnetic simulations show that approximately 5% of the power from a horn should propagate to the surrounding devices without the TiN mesh, and approximately 1% after adding the TiN mesh. The detectors adjacent to the illuminated detector have a somewhat higher than expected level of optical crosstalk that is reduced but not eliminated by the TiN absorber. This crosstalk signal is likely produced by the detector module design and not a flaw in the LEKIDs themselves. The prototype detector module presented here is our first design, and it requires further optimization. To decrease the crosstalk further we will (i) add an RF choke around the exit aperture of the horn and/or the backshort cavity and (ii) decrease the gap between the LEKID array and the backshort plate to make it more difficult for light to propagate laterally in this space.

Prospects for decreasing ambient pickup further include improving the package seal to make it more light tight and using additional filters on the coaxial line.

Chapter 6

Dual-polarization LEKIDs: development and initial tests

We discuss the design considerations and initial measurements from arrays of dual-polarization, lumped-element kinetic inductance detectors (LEKIDs) nominally designed for cosmic microwave background (CMB) studies. The detectors are horn-coupled, and each array element contains two single-polarization LEKIDs, which are made from thin-film aluminum and optimized for a single spectral band centered on 150 GHz. We are developing two array architectures, one based on 160 micron thick silicon wafers and the other based on silicon-on-insulator (SOI) wafers with a 30 micron thick device layer. The 20-element test arrays (40 LEKIDs) are characterized with both a linearly-polarized electronic millimeter wave source and a thermal source. We present initial measurements including the noise spectra, noise-equivalent temperature, and responsivity. We discuss future testing and further design optimizations to be implemented.

6.1 Introduction

Lumped element kinetic inductance detectors (LEKIDs) are superconducting resonators, which are also photon detectors. The resonance is set by a capacitor and inductor, the

latter of which has both geometric and kinetic components. The LEKID inductor acts as the absorber and is impedance matched to the incoming radiation. The absorbed photons break Cooper pairs which changes the quasiparticle density and subsequently the surface impedance and kinetic inductance. This results in a shift in resonance frequency and quality factor both of which are read out through a transmission line.

LEKIDs, and more broadly microwave kinetic inductance detectors (MKIDs), have been successfully demonstrated and deployed for a range of frequencies [Mazin et al., 2013, Adam et al., 2014]. Photon-noise limited performance has been shown in multiple frequency bands as well [Mauskopf et al., 2014, Hubmayr et al., 2015]. For cosmic microwave background (CMB) polarization studies it is important that the detector noise to be sub-dominant to the photon noise. Current CMB experiments employ thousands of detectors. To further increase the sensitivity, it is necessary to increase the pixel count. LEKIDs are a natural candidate as hundreds of detectors [McHugh et al., 2012, van Rantwijk et al., 2016] can be read out on a single transmission line.

We are developing dual-polarization LEKIDs that have two resonators within a single optical element. The two resonators are sensitive to orthogonal polarizations for observation at a frequency band centered at 150 GHz. Dual-polarization LEKIDs will effectively double the number of detectors for a given focal plane area compared to single polarization detectors. LEKIDs have been demonstrated as sensitive devices for absorbing single-polarization radiation at millimeter wavelengths [McCarrick et al., 2014, Flanigan et al., 2016], and dual-polarization radiation for far infrared [Dober et al., 2016]. In this proceedings we present (i) design considerations for dual-polarization LEKIDs at millimeter-wavelengths, (ii) initial test results, and (iii) steps for further optimization and testing.

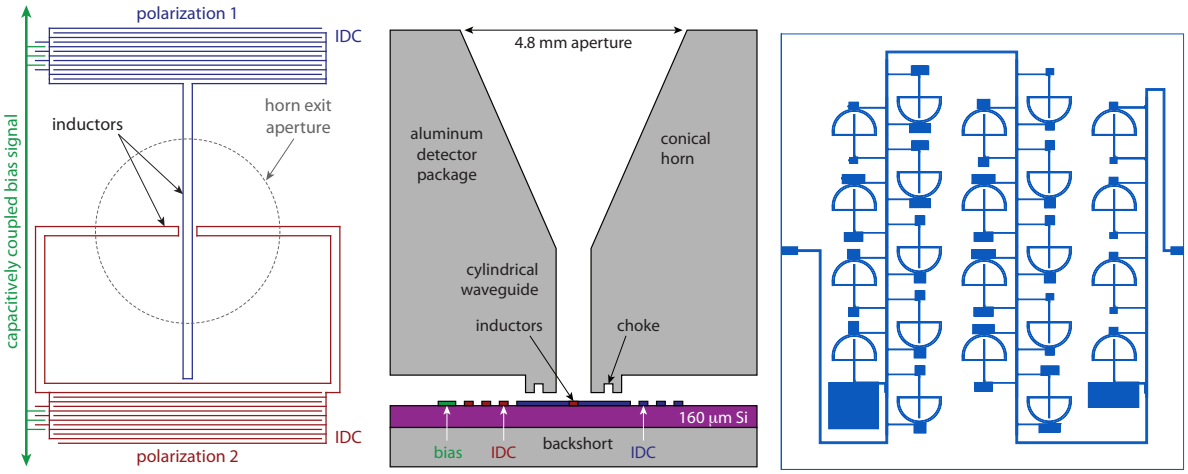

(a) (b) (c)

Figure 6.1: **a.** Schematic of a single detector. The resonators corresponding to the orthogonal polarizations are shown in red and blue. The dotted circle represents the waveguide exit aperture. The resonator inductor acts as the photon absorber. The resonators are capactively coupled to the transmission line. **b.** Cross-sectional view of a single-element. The horn aperture tapers to a cylindrical waveguide which also acts as a high-pass filter. A choke increases the absorption efficiencies while also controlling lateral radiation loss. The detectors are fabricated on silicon and directly illuminated. The package bottom acts as the backshort, the distance of which is set by the silicon wafer thickness. **c.** Layout of the prototype array. There are 20-elements, or 40 resonators, that are horn coupled and 2 dark elements. A single transmission line reads out all the devices. Each resonator has a unique resonance frequency set by the IDC value.

6.2 Design considerations

6.2.1 Design overview

The dual-polarization LEKID design is shown in Fig. 6.1. The resonators consist of two orthogonal inductors connected to interdigitated capacitors (IDC) and are coupled capactively to the transmission line. The focal plane architecture is heavily based on our experience with single-polarization KIDs [McCarrick et al., 2014] [Ch. 4]. A conical horn with a 4.8 mm aperture narrows to a cylindrical waveguide, which acts as a high-pass filter. A choke is used to control crosstalk and by creating a high impedance surrounding the detector. The LEKIDs are horn coupled. The devices are fabricated on high-resistivity silicon. The wafer thickness of $\lambda/4$ sets the distance to the backshort. The detector package acts as the backshort,

increasing optical efficiency.

The layout of a 20-element test array is shown in Fig. 6.1. Each element consists of two resonators as described above, and the elements are arranged in a 4.8 mm hexagonal pitch. There are 44-resonators for each prototype array, with 2 dark elements and 20 coupled to conical horns. The 20-element arrays are prototypes for a 271-element close-packed hex array with 542 detectors.

6.2.2 Design requirements

The detectors have many design parameters which must be optimized to achieve maximal performance. The optimal design parameters for different aspects of detector performance are often in competition. Here we discuss the important requirements considered.

The optical coupling is controlled both by the absorber design and the rest of the optical elements, from horn to backshort, or the focal plane design. The optimization of the absorber is similar to that as described in Bryan et al. [2015]. In the original design, the LEKIDs were deposited on silicon-on-insulator (SOI) and coupled to through the silicon, much of which is removed from behind the device through a DRIE-process. This approach is beneficial because it offers high-optical efficiency over a wide bandwidth. However, this approach involves a complex fabrication process, and we are still developing this architecture.

A simpler approach is to use the wafer thickness itself to set the backshort distance. For this architecture, LEKIDs of a similar absorber design as in the SOI-architecture are deposited on silicon. The array is mounted on the package bottom which acts as the back-short.

The absorbers are long traces. The inductors for the orthogonal polarizations lay perpendicular to one another. The inductors are naturally polarization sensitive, preferentially absorbing radiation with the E-field aligned to the thin inductor trace. A plot showing the simulated absorption efficiencies for the two polarizations and the cross-polarization response is shown in Fig. 6.2.

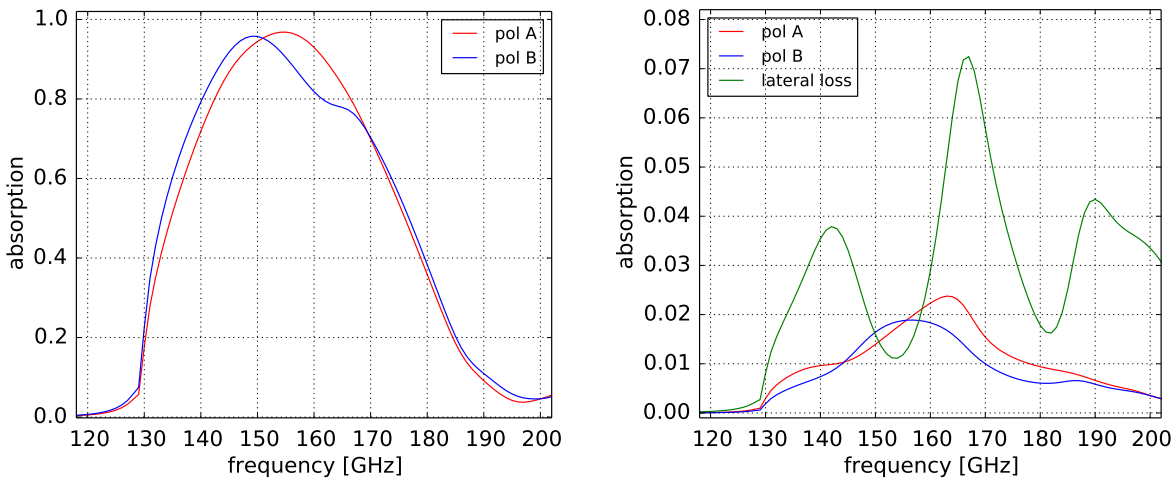

(a) (b)

Figure 6.2: **a.** HFSS simulations of the front-illuminated devices show the absorption spectra for both polarizations. A waveguide defines the high-pass and a metal mesh filter defines the low-pass. **b.** HFSS simulation showing the cross-polarization absorption and the lateral loss, which can be interpreted as the maximum possible detector-to-detector optical crosstalk. This HFSS simulation reflects the design show in Fig. 6.1. As built and tested for the prototype 20-element arrays, the gap between the detectors and waveguide was slightly larger and the chokes not included. This has the effect of decreasing the optical efficiency and increasing the lateral loss by a few percentage points.

The crosstalk between detectors is controlled in the following ways. The area of the absorbing element is small, as compared to many meandered inductors used in other LEKID designs. The radiation can propagate laterally [McCarrick et al., 2016b] [Ch. 5] and we minimize the opportunity to do so by decreasing the gap between the detectors and waveguide exit aperture. Additionally, the waveguide choke suppresses the laterally propagating leakage radiation. The simulated maximum crosstalk is shown in Fig. 6.2.

The readout frequency is centered around 1 GHz. We targeted 1 GHz because of the space available for the capacitor given the 4.8 mm pitch and the availability of microwave mixers in that frequency range. Our FPGA-based readout supports a bandwidth of 500 MHz. In order to achieve a resonance frequency spacing of 10 times the resonance width to avoid collisions between 542 detectors, the quality factors Q of the resonator needs to be $> 10,000$.

The detector noise is made up of contributions from generation-recombination (g-r), two-

level systems (TLS), and amplifier noise. We designed the detectors to minimize TLS noise by using relatively large gaps between the capacitor plates and targeting a low resonance frequency. The amplifier noise can be lowered below the device noise by adjusting the readout power up until the point that non-linear effects come into play. Many of the factors controlling detector noise and responsivity are set above by the optical requirements for the device. The noise mechanisms are quantitatively described more fully in the literature [Zmuidzinas, 2012, McCarrick et al., 2014, Flanigan et al., 2016].

6.3 Results

The LEKIDs were tested in an adiabatic demagnetization refrigerator (ADR) cryostat. The detector package, pictured in Fig. 6.3, is mounted on a 100 mK cold stage. A low-pass quasi-optical metal mesh filter sits on top of the horns. The high-pass filter is provided by the cylindrical waveguides. A variable blackbody load illuminates the detectors. The blackbody can be regulated between 2–7 K. Additionally, an electronic millimeter-wave source can be swept from 140–165 GHz. The tests are similar to those in papers previously published by this collaboration [McCarrick et al., 2014, Flanigan et al., 2016], where they are described in more detail. Dark tests, with the horns covered, were performed at JPL.

The internal quality factors of the devices measured dark were measured to be $\sim 10^6$. The coupling quality factors therefore predominantly set the resonator quality factor, and were in the 10^4 range. When loaded by a beam-filling 3 K blackbody, the quality factors were approximately 10^4. The quality factors are sufficient for the multiplexing requirements at these blackbody temperatures. The yield for this test array was excellent: 100% of the resonators were present. For a ground based experiment, we expect a higher loading, which would appreciably degrade the quality factor of these resonators. As discussed below, this can be compensated for by optimizing the detectors to have a larger active volume.

The optical responsivity was determined by measuring the fractional frequency shift of

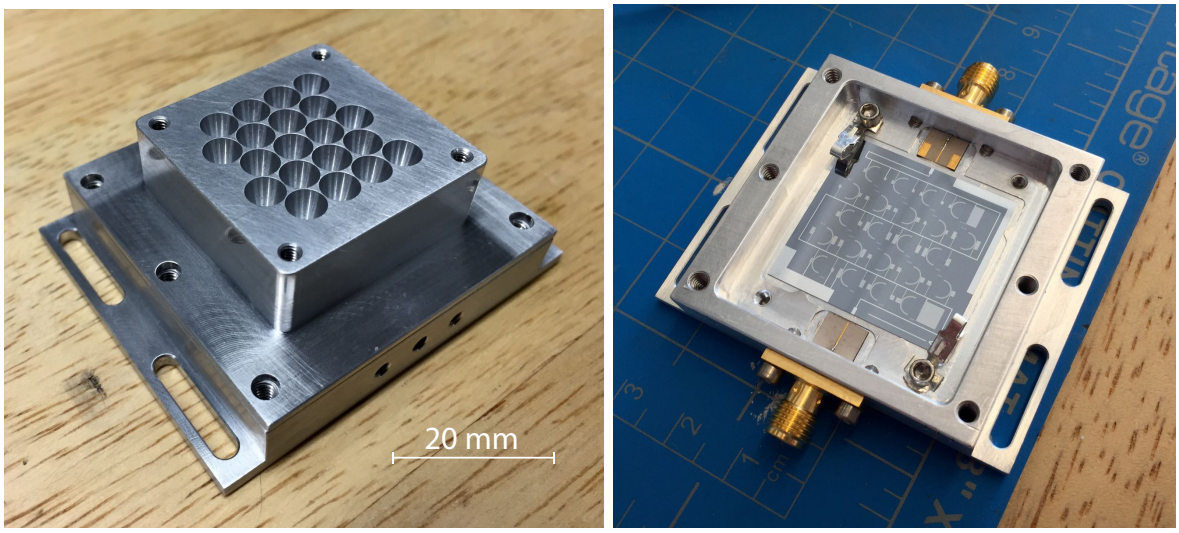

(a) (b)

Figure 6.3: **a.** Photograph of the dual-polarization test module. This module contains 44 dual-polarization LEKIDs. The conical horns (visible in photo) taper to a waveguide that acts as a high-pass filter. At the exit of the waveguide is a choke to control crosstalk. The incoming radiation is then absorbed by the detector, behind which is a $\lambda/4$ backshort. **b.** Photograph of a dual-polarization test LEKID chip in the aluminum test package with the horns removed.

the resonator as a function of blackbody temperature. The fractional frequency shift is defined as $x = (f - f_0)/f_0$, where f and f_0 are the measured resonance frequency at a particular temperature and the maximum resonance frequency respectively. The blackbody temperature is converted to incident power P_0 by integrating from 127 to 170 GHz. We expect the response of the detectors to follow a $\sqrt{P_0}$ dependence. We instead see a linear response in both resonators as shown in Fig. 6.4, which has been observed previously [McCarrick et al., 2014, Hubmayr et al., 2015] and could be due to thermal quasiparticles or high-frequency leaks. Both resonator designs corresponding to the two polarizations have similar responses over the power range measured. We calculate a responsivity of 27 ppm/K and 22 ppm/K for the A and B polarizations, respectively, at 4 K. In terms of incident power, these responsivities correspond to 16 ppm/pW and 12 ppm/pW.

The spectrum of the devices was measured using a millimeter-wave source. The source frequency is swept from 140–165 GHz and piped into the cryostat through a rectangular

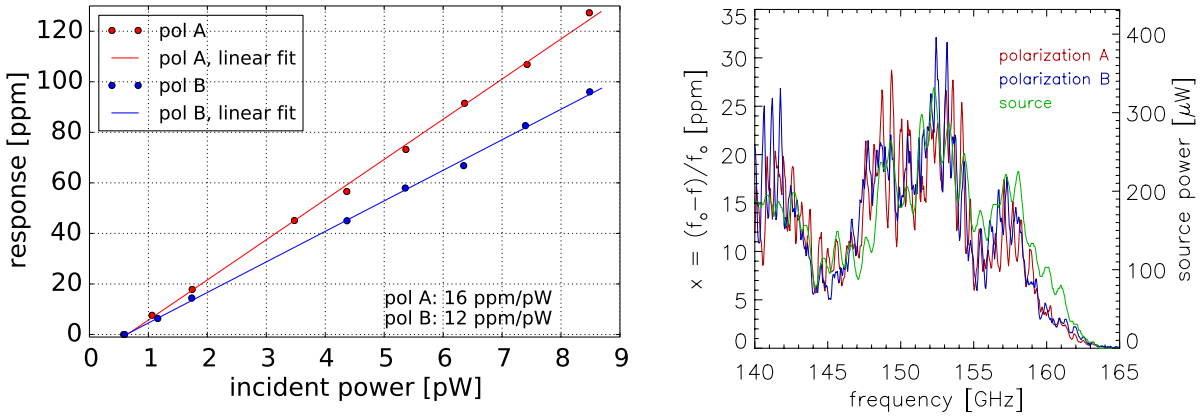

(a) (b)

Figure 6.4: **a.** Plot showing the fractional frequency shift of both polarizations as a function of incident power. The slope of the line, or the responsivity, is 16 ppm/pW and 12 ppm/pW for the polarizations A and B respectively. This corresponds to 27 ppm/K and 22 ppm/K with a 4 K blackbody load, respectively. The conversion from temperature to incident power was calculated using a 127–170 GHz frequency band. **b.** The fractional frequency response of both polarizations as a function of the frequency of the incident power. An electronic millimeter-wave source is swept from 140 to 165 GHz. The source power is plotted for reference in green, and there is good agreement between it and the fractional frequency shifts of the detectors.

waveguide. The radiation is launched out of the waveguide oriented at 45° to the orthogonal resonators, so both devices should receive equal amounts of power. The plot of the fractional frequency response as a function of radiation frequency is shown in Fig. 6.4. The source power is plotted for reference. The response of both detectors track each other well and also match the spectrum of the source itself. The devices are currently undergoing Fourier-transform spectroscopy (FTS) spectra measurements at Cardiff University.

Noise spectra of the detectors measured with the blackbody load temperature held at 3 K are shown in Fig. 6.5. The spectra for the resonators of both devices is flat from approximately 1 Hz to 10^2 Hz. At low frequencies, fluctuations of the blackbody load temperature cause an increase in the noise. More work needs to be done to determine the precise detector low-frequency knee f_k. The amplifier noise is subdominant to the detector noise. The noise equivalent temperature (NET) of the devices is found from the device noise level and the detector response. In the representative detectors shown in Fig. 6.5, the NET is calculated

to be 36 μK$\sqrt{\text{s}}$ and 52 μK$\sqrt{\text{s}}$ for polarizations A and B respectively.

6.4 Continued work

Future work will include measurements of polarization selectivity and beam-mapping of all detectors in the prototype array. We will also fully investigate the noise sources of the devices.

The device design will be further optimized in future iterations. First, for ground-based observations, the expected optical-loading requires a greater absorbing volume. We can increase the volume while maintaining the matched optical impedance by making small wiggles in the inductor and increasing the film thickness. Second, we aim to reduce the cross-polarization response response by adding the chokes as originally designed. Additionally, an adjustment to the absorber geometry directly under the horn aperture should decrease the cross-polarization further.

As a demonstration of a LEKID array suitable for ground-based observations, we have fabricated a hexagonal 271-element array based on the 20-element design discussed in this chapter. The optimizations for ground-based devices discussed above have been incorporated. This array, to be read out with a single coaxial cable pair, will provide a demonstration of the high multiplexing factors achievable with LEKIDs. The corresponding horn array has also been fabricated. As all elements of the optical and readout systems exist, this array is in principle, deployable.

6.5 Conclusion

We have successfully demonstrated dual-polarization devices for millimeter-wavelengths. The devices have flat noise within the device band and measured NETs of 36 and 52 μK$\sqrt{\text{s}}$ referenced to a 4 K load. The devices are responsive, with an optical responsivity of $\sim$20 ppm/K at a 4 K load. Initial tests show the two polarizations have similar responsivities. We

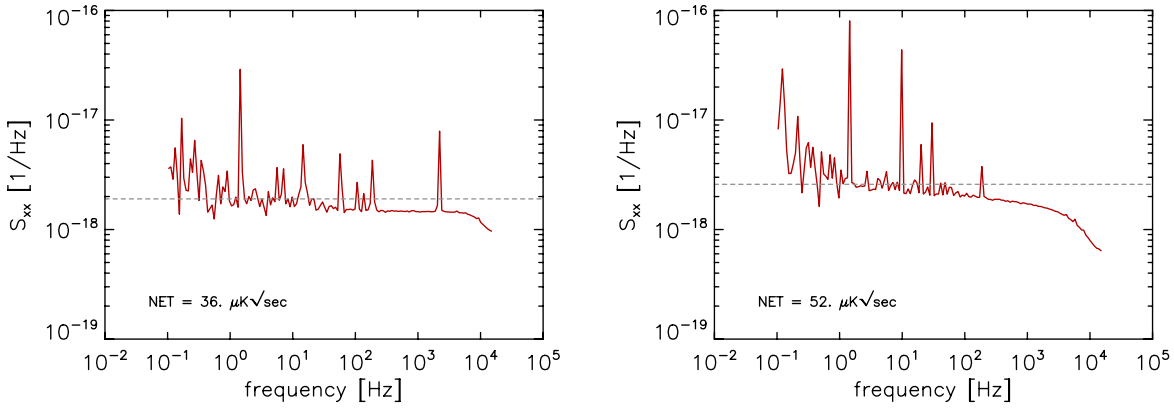

(a) (b)

Figure 6.5: **a.** Representative noise spectra for a resonator of polarization A design. The dotted line corresponds to a noise equivalent temperature (NET) of 36 μK$\sqrt{\text{s}}$ referenced to 4 K. **b.** Representative noise spectra for a resonator of the orthogonal polarization B to that in the left plot. The dotted line corresponds to a NET of 52 μK$\sqrt{\text{s}}$ referenced to 4 K.

are currently performing measurements to determine the polarization selectivity. Further optimizations to the detector design for ground-based observing have been implement in a 542-detector array that will be tested imminently. The large array will also allow the multiplexing capabilities to be further tested. The design presented here and initial test results show that LEKIDs work well and are a promising technology for future CMB polarimetry experiments.

Chapter 7

Dual-polarization LEKIDs: design and performance

Lumped-element kinetic inductance detectors (LEKIDs) are an attractive technology for millimeter-wave observations that require large arrays of extremely low-noise detectors. We designed, fabricated and characterized 64-element (128 LEKID) arrays of horn-coupled, dual-polarization LEKIDs optimized for ground-based CMB polarimetry. Our devices are sensitive to two orthogonal polarizations in a single spectral band centered on 150 GHz with $\Delta\nu/\nu = 0.2$. The 65×65 mm square arrays are designed to be tiled into the focal plane of an optical system. We demonstrate the viability of these dual-polarization LEKIDs with laboratory measurements. The LEKID modules are tested with an FPGA-based readout system in a sub-kelvin cryostat that uses a two-stage adiabatic demagnetization refrigerator. The devices are characterized using a blackbody and a millimeter-wave source. The polarization properties are measured with a cryogenic stepped half-wave plate. We measure the resonator parameters and the detector sensitivity, noise spectrum, dynamic range, and polarization response. The resonators have internal quality factors approaching 1×10^6.

The detectors have uniform response between orthogonal polarizations and a large dynamic range. The detectors are photon-noise limited above 1 pW of absorbed power. The noise-equivalent temperatures under a 3.4 K blackbody load are $< 100\ \mu\mathrm{K}\sqrt{\mathrm{s}}$. The polarization fractions of detectors sensitive to orthogonal polarizations are $> 80\%$. The entire array is multiplexed on a single readout line, demonstrating a multiplexing factor of 128. The array and readout meet the requirements for 4 arrays to be read out simultaneously for a multiplexing factor of 512. This laboratory study demonstrates the first dual-polarization LEKID array optimized specifically for CMB polarimetry and shows the readiness of the detectors for on-sky observations.

7.1 Introduction

Lumped-element kinetic inductance detectors (LEKIDs) are planar, superconducting LC resonators that are also photon absorbers. An absorbed photon with an energy greater than 2Δ, where Δ is the superconducting gap, will break Cooper pair(s) increasing the quasiparticle density n_{qp}, dissipation, and kinetic inductance L_{k} [Day et al., 2003, Doyle et al., 2008]. This results in a shift in the resonator quality factor Q and resonance frequency f_0, which is read out by monitoring a probe tone that is driving the device at its nominal resonance frequency. Each LEKID has a unique resonance frequency set by the geometry of the capacitor. This architecture naturally allows for frequency multiplexing because an array of LEKIDs can be read out on a single transmission line.

Kinetic inductance detectors (KIDs) have been developed for a wide range of wavelengths [Calvo et al., 2016, McCarrick et al., 2014, Mazin et al., 2013, Swenson et al., 2012]. Significant advances have been made in developing dual-polarization and multi-chroic KIDS [Dober et al., 2016, McCarrick et al., 2016a, Johnson et al., 2016], demonstrating photon-noise dominated sensitivity [Bueno et al., 2016, Flanigan et al., 2016, Hubmayr et al., 2015, Mauskopf et al., 2014, Janssen et al., 2013], determining space-readiness in

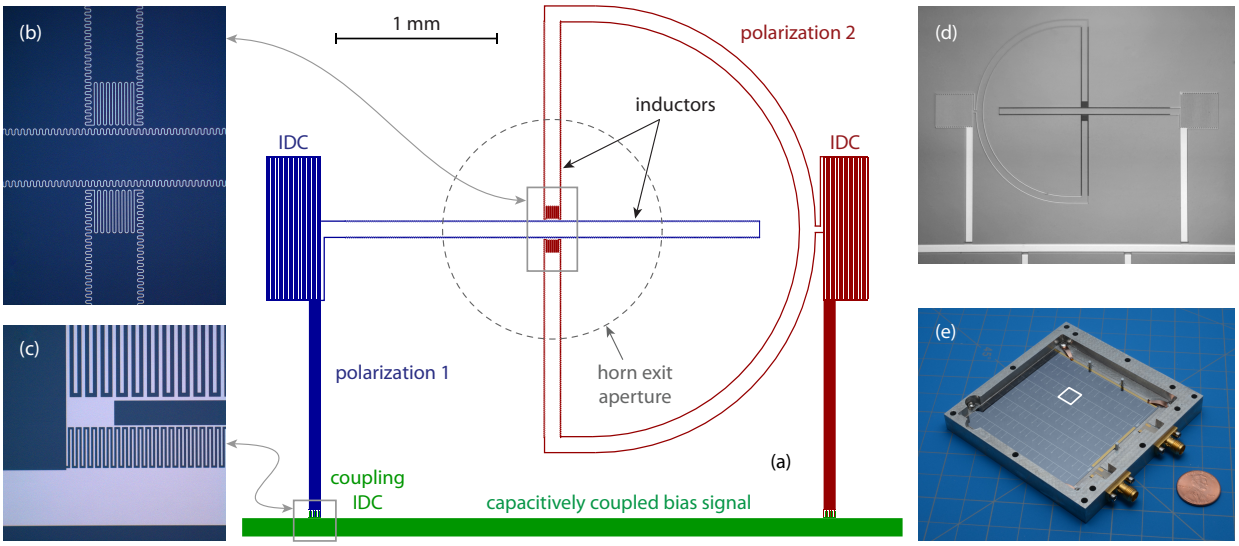

Figure 7.1: **a.** Schematic of a dual-polarization LEKID array element. Each array element consists of two LEKID resonators sensitive to orthogonal polarizations. The resonators sensitive to the two polarizations are shown in red and in blue. Each resonator consists of an inductor and an interdigitated capacitor (IDC). The LEKID absorbs the incident radiation in the inductor. The detectors are horn coupled and the aperture of the waveguide at the end of the horn is shown as the dashed gray line. **b.** Photograph of the millimeter-wave absorbers for a single array element. The inductors are 'wiggled' to increase the active volume of the absorber and thus the dynamic range of the detectors. The meanders at the end of polarization 2 (shown in red in panel a) are used to decrease the absorption of cross-polarization. **c.** Photograph of the coupler and resonator capacitor. This photograph is of a ∼100 MHz resonator that has a large capacitor that is visible in the top of the photo. All detectors are capacitively coupled to, and read out on, a single transmission line. **d.** Photograph of a single dual-polarization LEKID array element with ∼ 1 GHz resonance frequencies. **e.** Photograph of a dual-polarization LEKID array. The white box highlights a single array element, as shown in panel d. A single array consists of 64 elements (128 LEKIDs) fabricated on a 100 mm diameter silicon wafer. The arrays are diced into squares and designed to be tiled to fill the focal plane of a telescope.

the far infrared (FIR) [Baselmans et al., 2017], and deploying arrays for astrophysical observations [Adam et al., 2017a, 2014, Szypryt et al., 2014].

In this chapter we describe the design and measured performance of dual-polarization LEKIDs optimized for cosmic microwave background (CMB) studies. CMB experiments are being designed to search for the divergence-free component of the polarization signal, often referred to as the B-mode signal, which would provide strong evidence for inflation after the Big Bang [Knox and Song, 2002, Seljak and Zaldarriaga, 1997, Kamionkowski

et al., 1997]. The anticipated primordial B-mode signal is faint when compared with the unavoidable photon noise in the CMB itself, and current instruments already use photon-noise limited detectors [Stebor et al., 2016, Henderson et al., 2016, Posada et al., 2016, Harrington et al., 2016, Grayson et al., 2016]. Therefore, to increase instrument sensitivity going forward, the number of detectors must be increased, so scalable detector technologies with high multiplexing factors are needed for next-generation CMB experiments [Abitbol et al., 2017]. LEKIDs could be an attractive option for these next-generation experiments, so we conducted the laboratory study described in this chapter to investigate their suitability. In particular, we focused on measuring the sensitivity and polarization selectivity of our design to see if it is viable, and we tested a multiplexing factor of 128 that advances the state-of-the-art for CMB experiments.

The chapter is organized as follows: In Sec. 7.2.1, we present the detector requirements and subsequent design. In Sec. 7.2.2, we discuss the optical coupling and array design. In Sec. 7.2.3, we describe the experimental system. In Sec. 7.3, we present the tests undertaken to characterize the detectors including measurements of the resonator parameters, optical response, dynamic range, noise, and polarization selectivity. In Sec.7.4, we discuss the measurement results.

7.2 Methods

7.2.1 Detector requirements and design

The dual-polarization LEKIDs are laid out in an 8×8 square array with a 7.8 mm pitch (see Fig. 7.1e). Each array element consists of two resonators for a total of 128 LEKIDs per array. The array element design is shown in Fig. 7.1. The two resonators are sensitive to orthogonal polarizations for observation in a single spectral band centered on 150 GHz. Each resonator consists of an inductor connected in parallel with an interdigitated capacitor (IDC). The inductors for each pixel are identical across the array. Each IDC has a unique

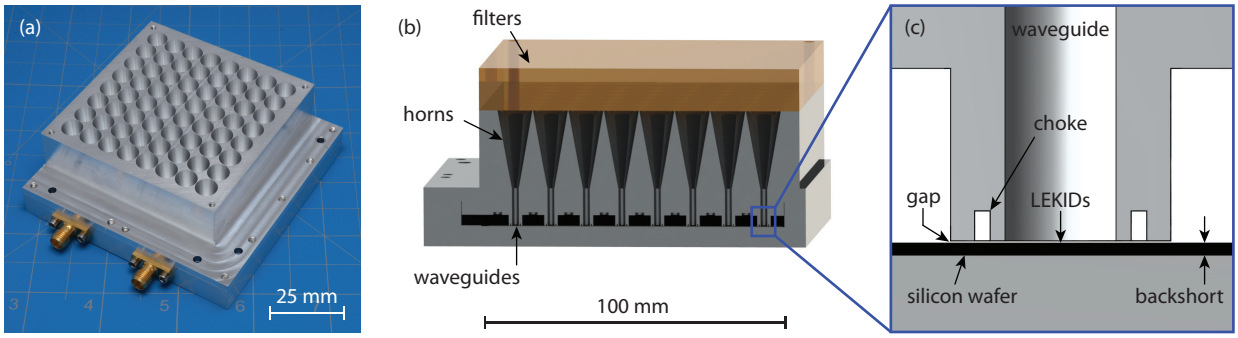

Figure 7.2: **a.** Photograph of the array module with the horn apertures visible. Conical horns are used to couple the incoming radiation to the detectors. **b.** Cross-sectional view of the horn array. Each horn feeds a cylindrical waveguide. At the waveguide exit a choke is used to optimize the coupling between the horn and the detector, as shown in (c). The LEKIDs are front-side illuminated. The detectors are fabricated on a 160 μm thick silicon wafer. The wafer thickness sets the $\lambda/4$ backshort distance and the back side of the wafer is covered with 100 nm thick Al, which acts as a backshort and ground plane. There are pockets between the waveguides into which the spring-loaded pins that press down on the detector array are epoxied. **c.** Cross-sectional view of the coupling between the horn and one LEKID array element.

capacitance and thus each resonator has a unique f_0. Therefore the detectors naturally lend themselves to frequency multiplexing.

The arrays are fabricated on high-resistivity ($>$ 10 kΩcm) silicon wafers. After the detector processing steps are completed, the silicon is thinned to 160 μm by grinding the back side of the wafer. As the final step, the arrays are diced into squares, which are designed to be tiled. The total number of detectors in each array is therefore determined by the choice of pitch and the decision to use 100 mm diameter wafers as the substrate.

The resonators are capacitively coupled to a 50 Ω microstrip transmission line. We chose to metalize the back side of the wafer with a 100 nm thick aluminum (Al) film to provide a ground plane for both the microstrip and the resonators and to optimize the millimeter-wave coupling (see Fig. 7.2 and Sec. 7.2.2). The detectors and transmission line are made out of a single Al film that is 25 nm thick. Wirebonds connect the Al microstrip to the rest of the readout chain (see Sec. 7.2.3.2). We measured the critical temperature of the film to be 1.4 K.

The absorbing element of the detector is the inductor. In our design, the geometry of one inductor is a single, long trace in the shape of a hairpin, while the orthogonal inductor is composed of two hairpins. We chose this architecture so the array can be fabricated with a single film without crossovers.

The detectors are designed for ground-based CMB experiments which have an expected loading of 1 to 10 pW. We started with straight inductors [Bryan et al., 2015, McCarrick et al., 2016a] but found for this absorber geometry the resonator quality factor degraded too rapidly as a function of absorbed power P. To retain sufficiently high Q under ground based loading conditions, we increased the volume V_{L} of the inductor. Solely increasing the film thickness would decrease the surface impedance of the absorber, causing poor coupling to the incoming radiation. Therefore, V_{L} was tuned by 'wiggling' the trace in alternating semi-circles as shown in the photograph in Fig. 7.1b. Wiggling the inductors allows us to add more volume by increasing both the length and film thickness while maintaining a similar effective surface impedance to the millimeter-wave radiation. The wiggles increase the length of the inductors as compared with a straight meander by a factor of $\pi/2$. To maintain the surface impedance needed for high optical coupling, we made the film thickness 25 nm. The detector response $\mathrm{d}x/\mathrm{d}P$ is defined as the ratio of the change in the fractional frequency shift

$$x = (f - f_0)/f_0 \tag{7.1}$$

to the change in absorbed power. As a result of the increased volume, we expect $\mathrm{d}x/\mathrm{d}P$ to decrease as compared with the straight inductor for a given P.

The inductors are naturally polarization sensitive, preferentially absorbing radiation with the E-field aligned to the inductor trace. Electromagnetic simulations[2] were used to optimize the design so that the two polarizations have similar absorption spectra. The simulations included the detector and array design starting from the waveguide (see Sec. 7.2.2) through the

[2]ANSYS Electronics Desktop 2016

array backshort (see Fig. 7.2). We found it necessary to meander the end of the polarization-1 inductor (see Fig. 7.1) to minimize absorption of the cross-polarization. The simulated absorption spectra and cross-polarization spectra are shown in Fig. 7.3.

We have designed arrays with resonance frequencies in the 100–200 MHz or 800–1200 MHz bands. The arrays are fabricated with a stepper. Each stepper field contains a 2×2 sub-array of dual-polarization LEKIDs, so an array is comprised of 16 stepper fields. The stepper fields are exposed in a 4×4 array across the wafer to make the full 8×8 array of dual-polarization LEKIDs. Each stepper field is exposed in two steps. First, the fixed portion of the design, including the inductors, coupling capacitors, transmission line segments, and half of each IDC structure, is exposed identically for each stepper field. A second stepper field including the second half of the IDC structures is then exposed with a relative offset that varies across the wafer. The capacitor lengths set by this relative offset increase linearly across the wafer, resulting in a weakly quadratic frequency spacing across the readout bandwidth. Within each stepper field, the resonance frequencies of the detectors are spaced maximally far apart over the array readout bandwidth to decrease the likelihood of adjacent resonators coupling to one another in frequency space [Noroozian et al., 2012]. The resonance frequencies for the two polarizations are separated into a high and low band within the readout bandwidth of the array.

Our LEKID readout system provides a bandwidth of 250 MHz at baseband frequencies (0–250 MHz) or 500 MHz when using an IQ mixer to target readout frequencies in the range 0.5–4.0 GHz. Although we are demonstrating a multiplexing factor of 128 here, our design goal is to read out 4 modules with a single readout system so we are designing for a future multiplexing factor of 512. To avoid collisions between detectors, we choose a resonance frequency spacing of 10 times the resonance width. This choice means the Q of the resonators needs to be $> 10^4$. The resonator quality factor Q is determined as

$$Q^{-1} = Q_{\mathrm{i}}^{-1} + Q_{\mathrm{c}}^{-1}, \tag{7.2}$$

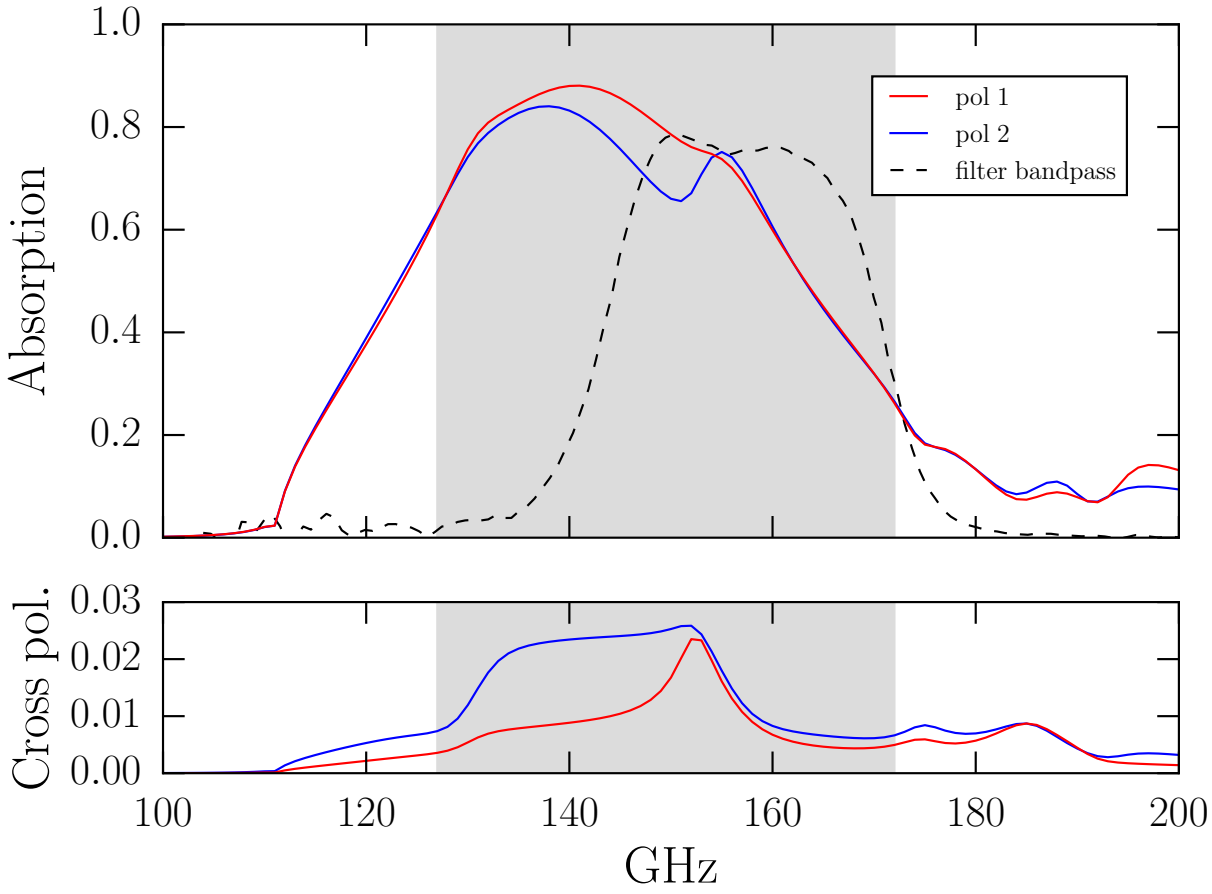

Figure 7.3: Simulated absorption spectra of the detectors sensitive to orthogonal polarizations. The shaded region shows the maximum spectral band the detectors could cover. The dotted black line shows the measured spectrum of the filter that defines the bandpass for the experiments described in this chapter. The bottom plot shows the cross polarization absorption of the detectors.

where Q_i is the internal quality factor and Q_c is the coupling quality factor. We chose Q_c to be approximately 2×10^4 which is set by the value of the coupling capacitor (see Fig. 7.1). These fabricated devices have $Q_\mathrm{i} \sim 10^5$ under an optical load, which is higher than we expected, so the coupling quality factor Q_c predominately sets the total Q as $Q_\mathrm{i} \gg Q_\mathrm{C}$. Ideally, $Q_\mathrm{i} = Q_\mathrm{c}$ under the desired optical load [Zmuidzinas, 2012], so in future iterations of the design the coupling capacitance will be decreased.

7.2.2 Detector array design

The absorption band is defined by metal mesh filters mounted in front of the horn apertures. The bandwidth is defined by a band-pass filter with a measured spectrum from 140–170 GHz as plotted in Fig. 7.3. For future tests or observations, it would be advantageous to use a wider bandpass filter which more closely matches the absorption spectra of the detectors. Additional low-pass and high-pass filters suppress out-of-band spectral leaks.

The detectors are fed with conicals horns that have a 7.8 mm aperture and a 20° flare angle (see Fig. 7.2). One horn feeds one array element (two LEKIDs) so the horns are arranged an 8×8 square array with a 7.8 mm pitch. The horns are designed to couple to an F/2.5 optical system, which means the aperture diameter is 1.6 Fλ at 150 GHz.

The horn flare feeds a cylindrical waveguide with a 1.6 mm diameter. This waveguide diameter has a cut-on frequency below the low-frequency edge of the spectral band defined by the band-pass filter. We chose this diameter because it works well with a profiled-horn design we are developing. Future LEKID modules will use these profiled horns because simulations show the horn beam is more circular. A choke at the waveguide output optimizes detector coupling and minimizes the lateral leakage of fields that can produce crosstalk between detectors. A vacuum gap of 30 μm then precedes the LEKIDs. The 160 μm wafer thickness sets the $\lambda/4$ backshort distance. The metalized ground plane on the backside of the wafer also acts as the backshort, increasing the absorption efficiency of each LEKID.

The LEKID array is mounted to the bottom part of a two-part aluminum package, the top of which is the horn array. The detector array is edge aligned against dowel pins mounted in the bottom of the package. The same pins are used to co-align the horn array in the package lid with the LEKID array in the package bottom. The array is held in place by three beryllium-copper clips positioned in corners of the LEKID array. Small spring-loaded pins[3] epoxied[4] into the package lid press down on the LEKID array in ten positions when the

[3] Mill-Max Manufacturing Corp. ED9000-ND
[4] 3M Scotch-Weld Epoxy Adhesive DP420 Black

module is assembled. These spring-loaded pins help suppress vibrations in the array, which can produce features in the noise spectra (see Sec. 7.3.3). To improve the heat sinking of the silicon substrate, gold bars were patterned on the edge of the detector array and wirebonds connect these bars to the package bottom.

7.2.3 Experimental system

7.2.3.1 Cryogenics

The experimental system is schematically depicted in Fig. 7.4. The detectors are mounted inside a cryostat[5] that uses a two-stage adiabatic demagnetization refrigerator (ADR) backed by a two-stage pulse tube cooler (PTC). The PTC provides 45 K and 2.7 K temperature stages, while the ADR provides a 0.7 K stage and a variable 60–300 mK stage. The detectors are mounted on the variable, sub-kelvin stage.

7.2.3.2 Readout

The readout system used for this study is based on the open-source ROACH-2 board, which hosts a Xilinx Virtex-6 FPGA. The ROACH-2 board[6] is combined with an ADC/DAC daughter board[7] that provides two 12-bit ADCs and two 16-bit DACs, each capable of synthesizing and analyzing signals with 250 MHz of bandwidth.

We have designed two varieties of LEKID arrays. For one variety, the frequencies are designed to be in the range 100–200 MHz and the other in the range 800–1200 MHz. The signals used to read out the lower-frequency 100–200 MHz resonators can be directly synthesized and analyzed using the ADC/DAC board. In this case, the only additional analog signal conditioning hardware needed is a variable attenuator and a warm amplifier. For the higher frequency 800–1200 MHz readout band, quadrature mixers are added to up and down-convert the baseband signals [Johnson et al., 2016].

[5] DRC-102 Cryostat System made by STAR Cryoelectronics
[6] Digicom Electronics
[7] Techne Instruments

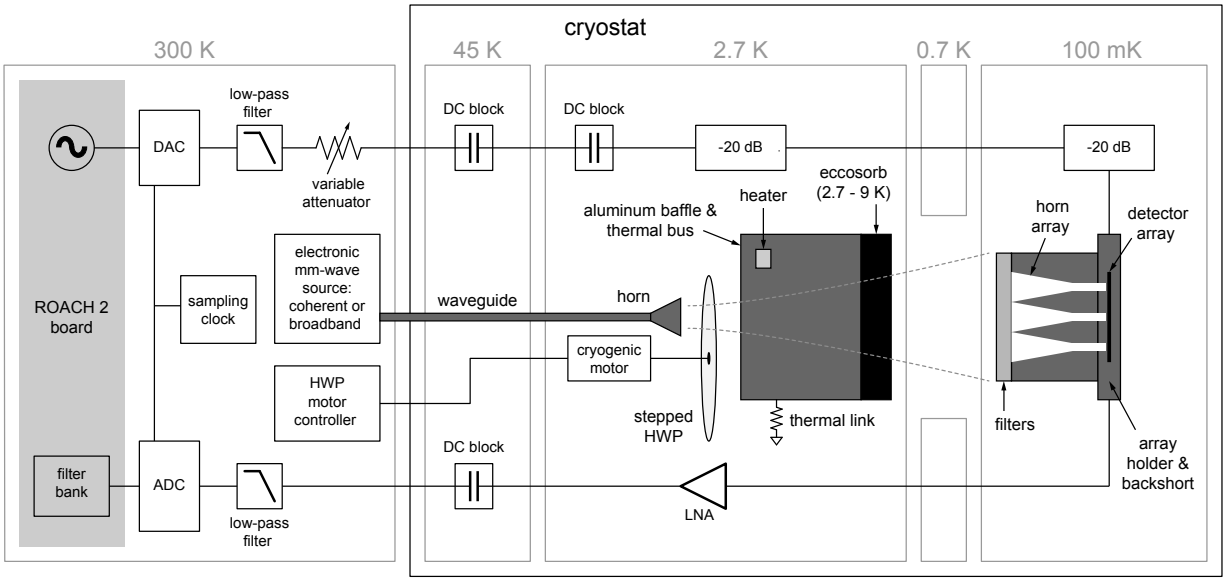

Figure 7.4: Schematic of the LEKID test system. The LEKID readout is based on the ROACH-2 board. The 100–200 MHz resonance frequencies of the LEKIDs allow us to use the ADC/DAC at the baseband frequencies. For arrays with higher resonance frequency KIDs, we use IQ mixers which are not shown here [Johnson et al., 2016]. The entire array is read out on a single pair of coaxial lines. The millimeter-wave (MMW) sources are also shown. A half-wave plate (HWP) mounted at 2.7 K and rotated with a cryogenic stepper motor modulates the MMW radiation that enters the cryostat through a WR6 waveguide. The radiation (140–165 GHz) can either be single frequency (coherent) or broadband (incoherent) [Flanigan et al., 2016]. Additionally, there is a blackbody source made from Eccosorb, the temperature of which can be controlled via a heater resistor.

The LEKID readout system uses a heterogeneous architecture, where the real-time signal processing is split between the ROACH-2 board and the readout computer attached to it. This architecture provides flexibility, allowing us to save time series at full bandwidth (>10 kHz) for diagnostic purposes, as well as low pass filtered signals appropriate for the bandwidth of signals expected while observing with a continuously rotating half-wave plate (HWP) (<200 Hz) in a deployed instrument.

7.2.3.3 Millimeter-wave sources

The system to optically characterize the LEKIDs consists of three main components: (i) a variable blackbody source, (ii) an electronic millimeter-wave (MMW) source that can produce

broadband or coherent radiation, and (iii) a stepped HWP. A diagram of the optical layout is shown in Fig. 7.4.

The blackbody load is a beam-filling piece of Eccosorb absorber (13 mm thick), which is anti-reflection (AR) coated with etched Teflon (380 μm thick). It is weakly thermally coupled to the 2.7 K stage. The blackbody temperature $T_{\rm bb}$ can be adjusted from 3–9 K using a resistive heater.

The MMW source is mounted outside the cryostat. A WR6 directional coupler splits the source signal. Radiation from one port is routed into the cryostat via WR6 waveguide and then launched from a conical horn through the HWP. Radiation from the second port is used to continuously measure the power emitted by the source $P_{\rm s}$ using a calibrated zero-bias detector (ZBD). The MMW source can be operated in broadband mode (140–165 GHz) or continuous wave mode [Flanigan et al., 2016]. In continuous wave mode, the frequency of the single tone can be swept.

The polarization orientation of the source signals can be rotated with the stepped HWP. The HWP is sapphire (3.2 mm thick) with fused silica AR coatings (0.28 mm thick). The HWP is rotated by a cryogenic motor mounted at 2.7 K controlled by an Arduino-based system at room temperature. After the HWP, Eccosorb, which is mounted on an aluminum thermal bus, acts as an 11 dB attenuator for the millimeter-radiation. The Eccosorb therefore acts both as the blackbody source and as an attenuator in the path of the radiation from the MMW source. The capabilities of this system allow us to measure the detector noise spectra, responsivity, absorption spectra, and polarization selectivity.

7.3 Results

The experiments described in the following section refer to a single 128 resonator array with resonance frequencies that fall between 110–170 MHz. We performed a sequence of cryogenic cooldowns in the following configurations: (i) the horn array was removed and an aluminum

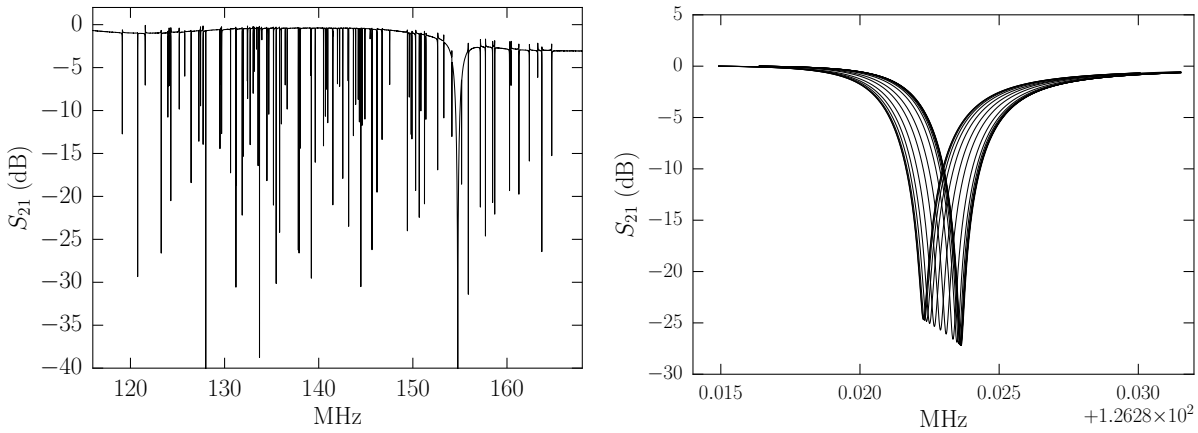

(a) (b)

Figure 7.5: **a.** Frequency sweep across the array. Each dip in transmission corresponds to an individual resonator. The total resonator Q is dominated by Q_c and is in the range of 10^4 across the array as designed. The internal quality factors Q_i approach 1×10^6. **b.** Resonance of a single LEKID responding to increasing optical power. The quasiparticle density n_{qp} increases with optical loading, causing a shift in f_0 and Q.

plate closed the package, (ii) all horn apertures were illuminated by the sources, and (iii) all but one horn aperture was covered.

7.3.1 Resonator characterization

For the first test, the detectors were enclosed in a sealed box and not illuminated by any of the aforementioned sources. The temperature of the array was held at 120 mK. We measured S_{21}, the forward scattering parameter, across the array, as shown in Fig. 7.5 and identified the resonance frequencies. This S_{21} measurement revealed 100 out of 128 resonators for a 78% yield.

Each resonance is fit to the equation

$$S_{21} = 1 - \frac{Q}{Q_c}\left(\frac{1}{1 + 2\mathrm{j}Qx}\right), \tag{7.3}$$

where Q_c is the complex coupling quality factor, Q is the resonator quality factor, x is the fractional frequency shift (Eq. 7.1), and we have omitted an overall phase term for

clarity [Khalil et al., 2012]. The resonators have Q_i approaching 10^6 and Q_c in the range of 10^4 as designed.

We set the probe-tone power slightly below the bifurcation level to strike a balance between suppressing the amplifier noise and ensuring the detectors remain in a linear regime. To determine the bifurcation level of the detectors, we measured S_{21} and collected time-ordered data (TOD) at different probe-tone attenuations. For the dark configuration, the detectors bifurcate at approximately -105 dBm.

In a subsequent cryogenic cooldown, with the horn array installed, we measured the resonator quality factors. The horn apertures faced a beam-filling 3.4 K blackbody load. Under these loading conditions the median internal quality factor Q_i is 3×10^5 and the median resonator quality factor Q is 3×10^4. These quality factors meet the requirements for a 512 multiplexing factor (see Sec. 7.2.1).

7.3.2 Blackbody response

We measured the responsivity of the detectors $\mathrm{d}x/\mathrm{d}T_\mathrm{bb}$ with the blackbody load, where T_bb is the blackbody temperature. The absorbed power P can be related to T_bb by integrating the Planck equation over the spectral band. In the regime above 3 K the relationship between P and T_bb is approximately linear. At low P the relationship between x and P is linear. At high P, $x \propto P^{1/2}$ [Flanigan et al., 2016] and therefore $\mathrm{d}x/\mathrm{d}P \propto P^{-1/2}$.

The fractional frequency shift x is plotted as a function of T_bb for both detectors in a single array element in Fig. 7.6a. The blackbody temperature is stepped from 3.4–7.0 K. We find the data for both polarizations is well fit by a line with a slope of approximately 2 ppm/K, which is the responsivity. Across the array, the median responsivity is 2.7 ppm/K with a standard deviation of 0.7 ppm/K as shown in Fig. 7.6c. Previous iterations of dual-polarization detectors with straight inductors and smaller inductor volumes had responsivities between 12 and 16 ppm/K [McCarrick et al., 2016a]. The increase in inductor volume with the wiggled design has effectively lowered the responsivity and increased the dynamic range

(more in Sec. 7.3.6).

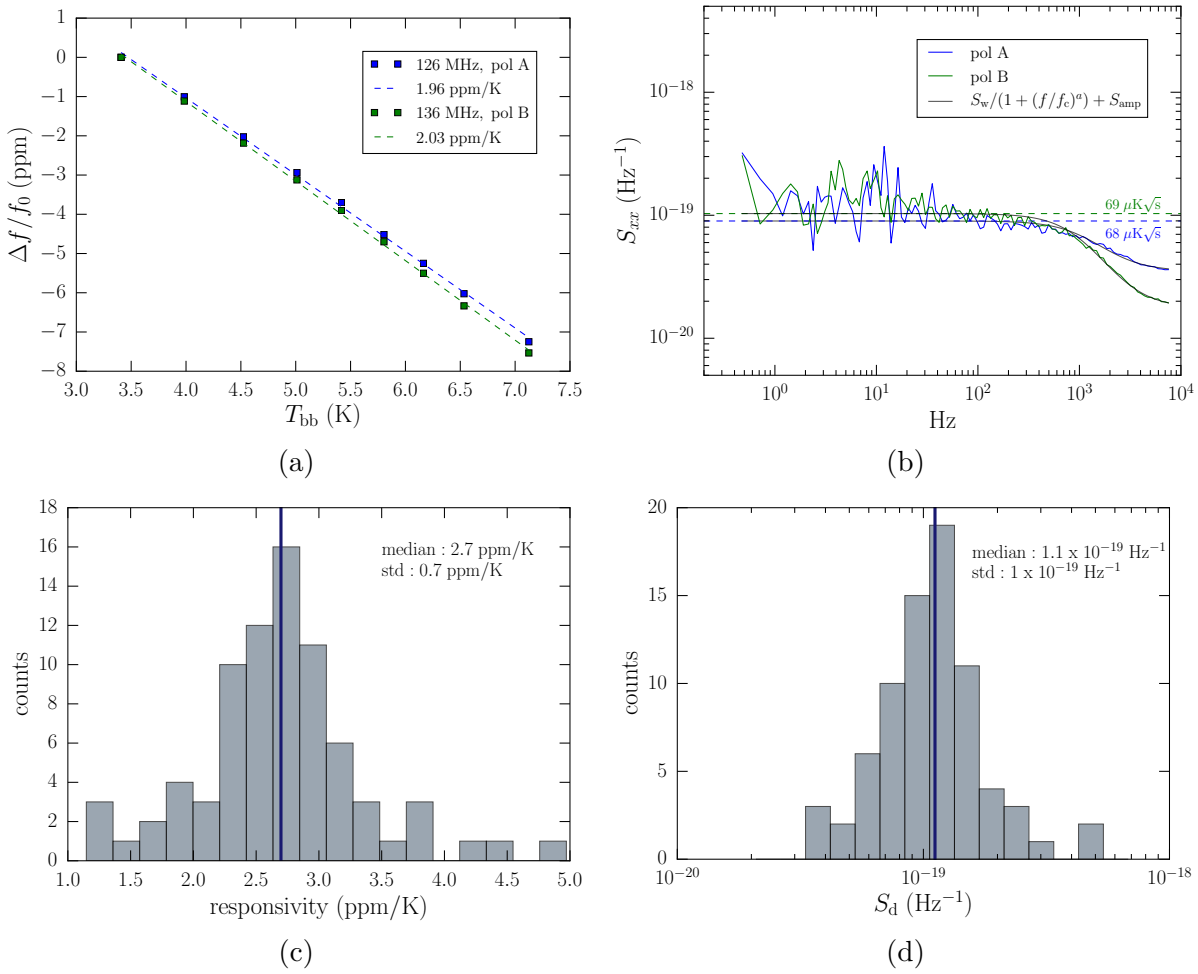

Figure 7.6: **a.** Fractional frequency response ($\Delta f/f_0$) for a pair of LEKIDs plotted as function of the blackbody load temperature. The response of the two resonators sensitive to orthogonal polarizations is approximately 2 ppm/K and linear. **b.** Noise spectra for detectors sensitive to orthogonal polarizations under a 3.4 K blackbody load. The fits of the noise spectra are plotted in solid black. The noise in both detectors is similar in shape with the white noise rolling off at approximately 700 Hz. The device noise is plotted as the dashed line and is used in combination with the response of the detectors to calculate the NET. The NETs referenced to 3.4 K for polarization A and B are 68 and 69 $\mu{\rm k}\sqrt{\rm s}$ respectively. **c.** Histogram of the responsivity of the detectors across the array. The data is for 78 detectors that were read out automatically using our readout software. When read out automatically, the number of detectors with usable data is primarily defined by how many readout tones land sufficiently close to the targeted resonance frequencies without further refinement. **d.** Histogram of the device noise level for 78 detectors across the array.

7.3.3 Noise spectra and NET

We measured the noise properties of the detectors by recording TOD with the probe-tone frequencies fixed at the resonance frequencies determined by S_{21} measurements. The resonator model (Eq. 7.3) is used to transform the TOD into fluctuations in resonance frequency and dissipation δQ^{-1}. We then calculate the power spectral densities (PSD) for both the fractional frequency and dissipation fluctuations, which we refer to as S_{xx} and S_{yy}, respectively. In practice we use the fractional frequency data because it is more responsive than the dissipation data. The noise spectrum S_{xx} is fit to the model

$$S_{xx} = S_{\mathrm{w}} \left(\frac{1 + (f_{\mathrm{k}}/f)^{\alpha}}{1 + (f/f_{\mathrm{r}})^2} \right) + S_{\mathrm{amp}}, \tag{7.4}$$

where S_{w} is the white-noise level, S_{amp} is the amplifier noise level, f_{k} is the low-frequency noise knee, and f_{r} corresponds to the high frequency roll off.

Typical measured detector noise spectra for both polarizations under a 3.4 K blackbody load are shown in Fig. 7.6b. Thirty seconds of TOD were collected with the sub-kelvin stage temperature regulated but the PTC off to eliminate mechanical vibrations. The module temperature was stable during the measurement but the radiation environment in the cryostat detectably changed. The noise spectra are therefore calculated from TOD detrended with a 2nd degree polynomial. The white noise levels S_{w} for this detector pair are 5 and 9×10^{-20} Hz^{-1}. We find that the noise spectra do not show detectable $f^{-\alpha}$ dependence in our measurements. TLS noise is expected to have a $f^{-0.5}$ dependence [Noroozian et al., 2009], so any TLS noise in our devices would have an f_{k} below 0.5 Hz. At high frequencies, the spectrum rolls off at approximately 700 Hz, which is consistent with the resonator bandwidth $b_{\mathrm{r}} = f_0(2Q)^{-1}$.

The noise equivalent temperature (NET) is calculated as

$$\mathrm{NET} = \sqrt{\frac{S_{\mathrm{d}}}{2}} \left(\frac{\mathrm{d}x}{\mathrm{d}T_{\mathrm{bb}}} \right)^{-1}, \tag{7.5}$$

where the device noise level is defined as $S_{\rm d} = S_{\rm w} + S_{\rm amp}$. The latter two terms are found by fitting Eq. 7.4 to the measured noise spectra. The factor of $1/\sqrt{2}$ comes from the Nyquist sampling frequency. Taking the steps described in Sec. 7.3.2, we measure $\mathrm{d}x/\mathrm{d}T_{\rm bb}$. We find that the NETs are 68 and 69 $\mu\mathrm{K}\sqrt{\mathrm{s}}$ referenced to 3.4 K for the two polarizations as shown in Fig. 7.6b.

The median white noise level $S_{\rm w}$ across the array is 6.5×10^{-20} Hz^{-1} and the median device noise level $S_{\rm d}$ is 1.1×10^{-19} Hz^{-1} as shown in Fig. 7.6c. When fitting the noise spectra across the array, we use the frequencies above 100 Hz due to spikes at low frequencies in some resonators, which are caused by mechanical vibrations. To better understand how mechanical vibrations couple to the detector array, we took x TOD from all of the detectors and conducted a spectral coherence analysis. We calculate the coherence estimator as $C_{uv} = |S_{uv}|^2 (S_{uu}\ S_{vv})^{-1}$, where u and v represent different detectors, and S_{uv} represents the cross spectrum of the fractional frequency fluctuations from two detectors. We initially found strong coherence in features across the bandwidth of the detectors. We hypothesized that the thickness of silicon wafer (160 μm) in combination with the large surface area (65×65 mm) caused the array to be sensitive to mechanical vibrations. To test this hypothesis, we installed the aforementioned spring-loaded pins in the module in an effort to suppress any vibrations in the substrate. After the spring loaded pins were installed, we found a large decrease in the coherence. However, there is still some detectable coherence below 100 Hz, which means the vibration suppression technique works but still needs further development.

7.3.4 Quasiparticle lifetime

The quasiparticle lifetime $\tau_{\rm qp}$ was measured by taking TOD at a higher-order resonance (~ 1 GHz) while the detectors were illuminated by a constant 3.4 K blackbody background load and the external MMW source. It is necessary to use a higher-order resonance because the resonator ring-down time is $\tau_{\rm r} = (2\pi b_{\rm r})^{-1} = Q(\pi f_0)^{-1}$, which is longer than $\tau_{\rm qp}$ for the 100 MHz resonances. For this test, the MMW source emits 148 GHz radiation, which

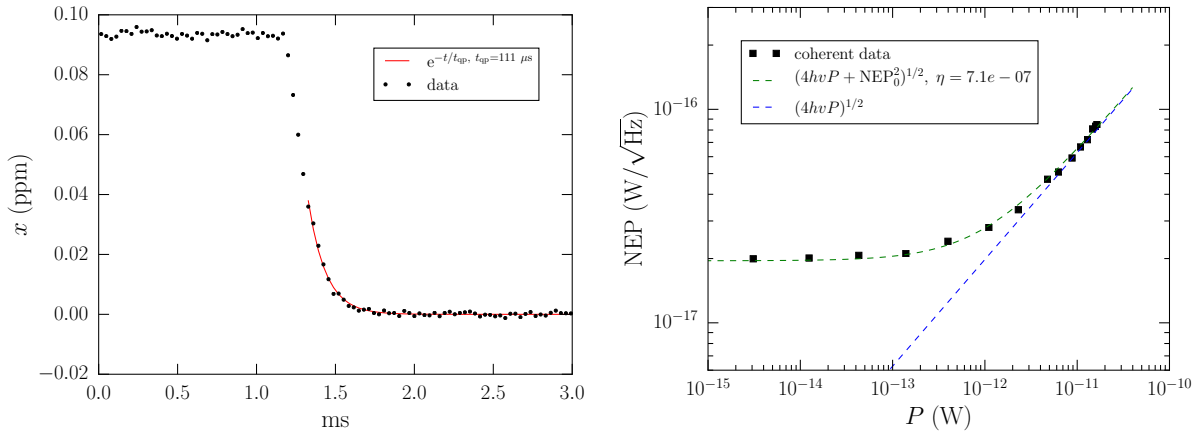

(a) (b)

Figure 7.7: **a.** Resonator response to a 122 Hz chopped signal. The TOD has been folded and averaged. We use a higher mode resonance ($\sim$ 1 GHz) of the LEKID to measure the quasiparticle lifetime. We fit the tail of the falling edge to an exponential model to find the quasiparticle lifetime $\tau_{qp} = 111\ \mu s$. The fit is the red line. **b.** Detector NEP as a function of absorbed power. Plotted in the blue dashed line is the expected photon noise for coherent radiation which is shot noise and GR noise in equal parts. The limiting NEP_0, at the lowest powers, is approximately 2×10^{-17} W/$\sqrt{\text{Hz}}$. The devices are photon noise dominated above approximately 1 pW of absorbed power.

transmits through the Eccosorb, and is switched on and off at 122 Hz with a PIN diode. The switching time of the PIN diode is fast (10 ns) compared to the LEKID response time, so any time constant associated with the MMW source is negligible. The TOD is then folded and averaged, the results of which are plotted in Fig. 7.7. The tail end of the falling edge of the averaged TOD is fit to an exponential model in order to estimate τ_{qp} [Baselmans et al., 2017, 2008]. The fit yields $\tau_{qp} = 111\ \mu$s.

7.3.5 Crosstalk

We define crosstalk as the response of a detector to a mechanism other than the absorption of radiation from its associated horn. The crosstalk is measured with all horns but one covered with aluminum tape, leaving a single array element (one LEKID pair) illuminated. The array is illuminated by the same chopped MMW source and background load as described in Sec. 7.3.4. In practice, we quantify the crosstalk as the relative response of each dark

detector to that of the illuminated pair. All the detectors, both illuminated and dark, are simultaneously read out. At the highest incident power levels the MMW source can emit (where $P \sim 10$ pW) the optical crosstalk is below -20 dB, which suggests the RF choke works well.

7.3.6 Dynamic range

We determined the dynamic range of the detectors. The detectors were illuminated with both the blackbody source, from which we obtain x as a function of T_{bb}, and the MMW source, from which we obtain x as a function of P_{s}, where P_{s} is the power emitted by the MMW source. Thus, P_{s} can be related to T_{bb}, and we can find an equivalent brightness temperature T_{s} for the MMW source. This is advantageous because the MMW source can emit higher brightness temperatures than the blackbody, which starts to appreciably heat the sub-kelvin stage for $T_{\mathrm{bb}} > 9$ K.

The quality factor and noise of the detectors are measured as a function of brightness temperature from the MMW source. Two metrics are used for the dynamic range: (i) the Q remains sufficiently high for the multiplexing requirements and (ii) the detector noise remains clearly elevated above the amplifier noise in the noise spectra. The detector noise remains separated from the amplifier noise, up to the highest brightness temperature of the MMW source, which is equivalent to approximately 90 K. Similarly, we find that $Q > 1 \times 10^4$, the minimum required for the desired multiplexing factor, for all accessible T_{s}. For instance, for one resonator, Q changes from 7.0×10^4 to 4.5×10^4, while Q_{i} decreases from 9×10^5 to 1×10^5 over the entire T_{s} range. This puts a lower limit on the maximum brightness temperature the detectors can observe at 90 K.

7.3.7 NEP

We measured the absorbed noise equivalent power (NEP) as a function of absorbed power using the method from Flanigan et al. [2016]. The detectors were illuminated through the

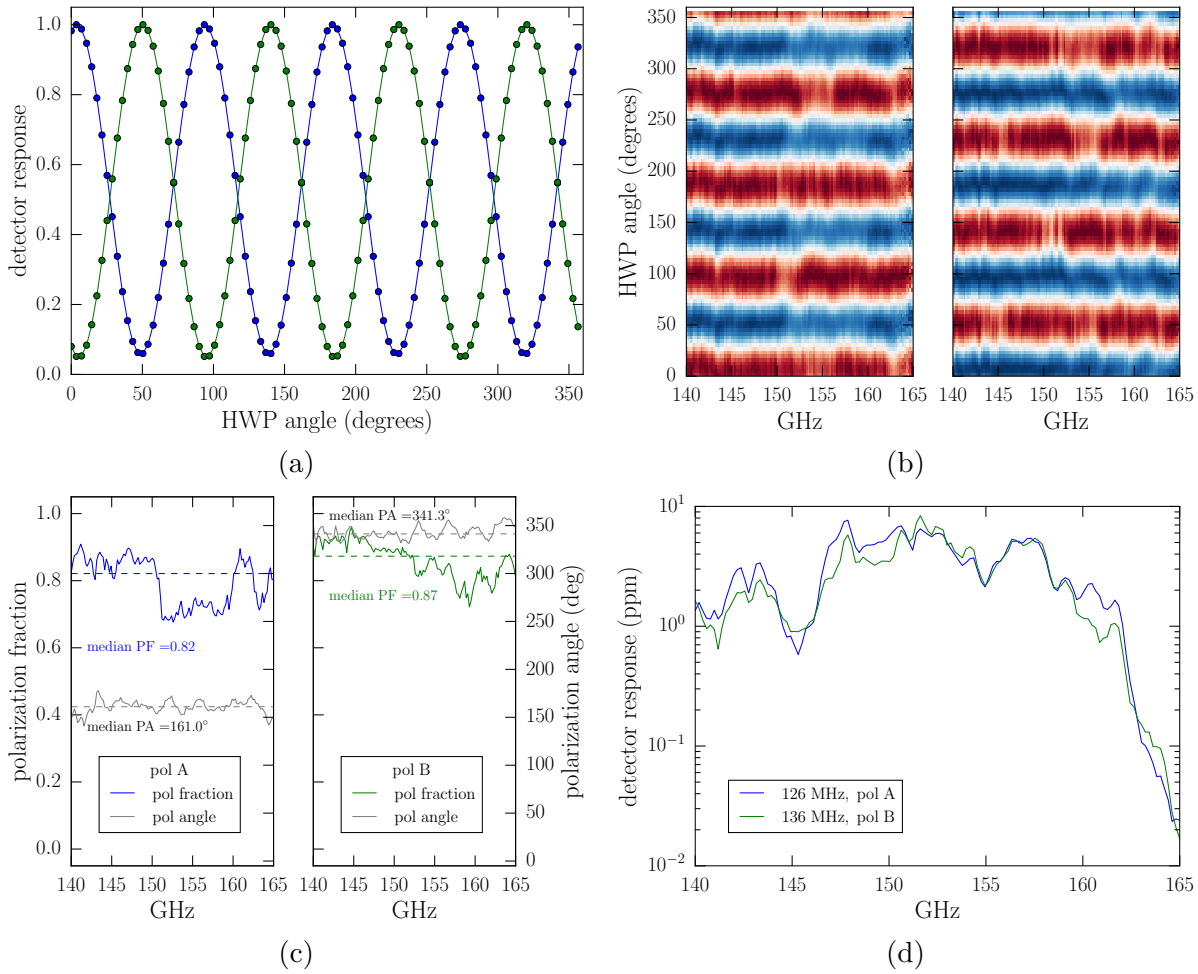

Figure 7.8: **a.** Normalized detector response as a function of HWP angle for a detector pair with detectors that are sensitive to orthogonal polarizations. The blue points and line correspond to polarization A and the green to polarization B. The data is for a single incident frequency at 147 GHz. The plotted data points have been filtered to show only the DC and fourth harmonic components. **b.** Detector response as a function of HWP angle and MMW source frequency for the same two detectors. The responses of the polarization A and B detectors are shown in the left and right panels, respectively. The response is peak normalized for each frequency and the colorbar scale goes from blue to red. Fine-scale frequency structure is assumed to be caused by multipath reflections in the experimental setup. **c.** Polarization fraction and angle as a function of frequency for the two detectors. The left panel shows the polarization fraction (PF) in blue and polarization angle (PA) in gray for the polarization A detector. The right panel shows the PF in green and PA in gray for the polarization B detector. The PF is computed by fitting the fourth harmonic and DC components to the data in (b), as described in the text. The relative phase between the HWP response of the two detectors is 179.8°, corresponding to 89.8° in polarization angle. **d.** Spectral response of the two detectors at the HWP angle giving maximum response for each detector. The rolloff above 160 GHz is due to a filter in the MMW source. Much of the frequency structure is likely due to the MMW source and reflections in the experimental setup. The frequency structure is very similar between the two detectors.

Eccosorb by coherent radiation at 148 GHz from the MMW source. The source power $P_{\rm s}$ was varied and at each power level we measured the detector noise and the fractional frequency shift x. We numerically calculated $\mathrm{d}x/\mathrm{d}P_{\rm s}$ to determine the desired responsivity. Experimentally, the NEP as referenced to the source is calculated as

$$\mathrm{NEP}_{\rm s} = \sqrt{S_{\rm w}} \left(\frac{\mathrm{d}x}{\mathrm{d}P_{\rm s}} \right)^{-1}, \tag{7.6}$$

where $S_{\rm w}$ is the white noise level obtained by fitting Eq. 7.4 to the measured noise spectrum.

The theoretical NEP in the photon-noise limited case is

$$\mathrm{NEP}_{\rm t}^2 = 2h\nu P + 2h\nu P(\eta n_{\rm o}) + 4\Delta P/\eta_{\rm pb}, \tag{7.7}$$

where P is the absorbed power, Δ is the superconducting energy gap, $n_{\rm o}$ is the photon occupancy number and $\eta_{\rm pb}$ is the pair-breaking efficiency of the absorbed radiation. The first two terms are inherently due to photons and are respectively called the shot noise and the wave noise. Coherent radiation will produce only shot noise. The third term is due to the quasiparticle recombination rate and is referred to as recombination noise. We rewrite the theoretical NEP as referenced to the source as

$$\mathrm{NEP}_{\rm s}^2 = 4h\nu P_{\rm s}/\eta_{\rm s} + 2P_{\rm s}^2/B + \mathrm{NEP}_0^2, \tag{7.8}$$

where $\eta_{\rm s}$ is the absorption efficiency of the detector as referenced to the MMW source power. Here, we have made the substitutions $\eta_{\rm pb} = 2\Delta/h\nu$ [de Visser et al., 2015] and $P = h\nu\eta n_{\rm o} B$, where B is the bandwidth of incident radiation. We have also added in a constant term NEP_0 which refers to the limiting NEP.

For one representative detector, we fit the coherent data as referenced to the source power $P_{\rm s}$ to the expected $\mathrm{NEP}_{\rm s}$ model. Using $\nu = 148$ GHz, we find $\eta_{\rm s} = 5.8 \times 10^{-7}$. We use the $\eta_{\rm s}$ parameter to calculate the absorbed NEP as a function of absorbed power P, which is

plotted in Fig. 7.7. We see NEP $\propto P^{1/2}$ when $P > 1$ pW, signifying that the detector is photon-noise limited and detecting shot noise from the coherent radiation. The limiting NEP level is approximately 2×10^{-17} W/$\sqrt{\text{Hz}}$, similar to the NEP expected from a 3 K load.

7.3.8 Polarization response

The polarization selectivity of the devices was characterized using a stepped HWP measurement, as is schematically depicted in Fig. 7.4. Purely linearly polarized MMW radiation is brought into the cryostat on a WR6 waveguide. This signal is then emitted from a conical horn and the emitted beam passes through the HWP, which is mounted directly in front of the horn aperture. The HWP is rotated in 3.6° steps through one full rotation. At each orientation we measured the fractional frequency response x and found that the response showed four cycles of a sinusoid for every rotation of the HWP as expected (see Fig. 7.8a) [Johnson et al., 2007]. The measured polarization fraction (PF) is defined as

$$\text{PF} = \frac{(x_{\max} - x_{\min})}{(x_{\max} + x_{\min})} = \frac{I(4f)}{I(0)} = \frac{2\tilde{I}(4f)}{\tilde{I}(0)}. \tag{7.9}$$

Here, $I(nf)$ corresponds to the intensity of the n^{th} harmonic and $\tilde{I}(nf)$ corresponds to the intensity of the n^{th} harmonic as computed by the discrete Fourier transform (DFT). We are able to calculate the intensity of the harmonics using a DFT as the measurements are taken at evenly spaced intervals over a complete period. For a single frequency at 147 GHz, we find the PF is approximately 89%. We expect this PF to be a lower bound on the polarization selectivity as we do not correct for cross-polarization induced in the setup, such as from the HWP or conical horns.

To measure the PF as a function of frequency, at each HWP orientation the incident MMW radiation frequency is swept from 140–165 GHz in 195 MHz steps. The results are plotted in Fig. 7.8b. We clearly see the two detectors are out of phase by approximately 180° across the spectral band, which is expected if the detectors are sensitive to orthogonal

polarizations.

The response taken at the HWP angle that produced the maximum response is plotted at a function of incident MMW frequency in Fig. 7.8c. The median polarization fraction is 82% and 87% for polarizations A and B, respectively. The detectors are sensitive to orthogonal polarizations and have median responses 179.8° out of phase corresponding to a polarization angle of 89.9°.

The spectral response of a pair of detectors fed by the same horn is plotted in Fig. 7.8d. The maximum response is taken at each incident MMW frequency. The response of both polarizations is similar across the entire MMW band. It is likely that the small scale structure in the spectral response is a systematic effect caused by the MMW source and reflections in the experimental setup.

7.4 Discussion

Future CMB experiments will require additional spectral bands and this dual-polarization LEKID design is directly scalable to other frequencies. While aluminum is sufficient for frequencies of 100–300 GHz, other materials can be used with the same design for both lower and higher spectral bands. For instance, materials such as aluminum manganese with a gap energy suitable for photons with frequencies < 90 GHz are currently being demonstrated [Jones et al., 2017]. For higher frequency bands, like FIR, materials such as TiN are routinely used [Hailey-Dunsheath et al., 2016, Diener et al., 2012, Dober et al., 2016]. Arrays of our design, scaled and fabricated with different materials, could be used to cover the entire bandwidth necessary to fully characterize the CMB and galactic foregrounds. The same design with small modifications could also be used for millimeter-wave observations from space. We expect approximately 0.3 pW of loading in space as compared to approximately 10 pW at ground-based observatories [Johnson et al., 2015]. The lower loading conditions would require only a change to the inductor volume to tune the response and dynamic range.

In these tests we have demonstrated a multiplexing factor of 128, the number of detectors that can fit on the 100 mm diameter substrate. When populating a focal plane, up to 4 arrays can be tiled and connected so only a single pair of cables and one ROACH-based readout is needed for a multiplexing factor of 512. For this multiplexing scheme, each array in the focal plane would have detectors with unique resonance frequencies within the readout bandwidth.

We are working on a number of related projects. First, the number of detectors per array is being increased. For the higher detector density, we have designed and fabricated hex-packed arrays of dual-polarization LEKIDs fabricated on 100 mm silicon wafers with a 4.8 mm pitch. This detector density allows for 542 resonators per module. We are in the early stages of testing these arrays. Second, we are developing dual-polarization LEKIDs, which could be used for terrestrial imaging. The terrestrial imaging detectors are the same design as presented in this chapter but with a larger absorbing volume achieved by increasing the film thickness. Third, we are considering ways to use these detectors for other ground-based, millimeter-wave astrophysical studies such as observations of star forming regions and the Sunyaev-Zel'dovich effect [Svoboda et al., 2016, Abazajian et al., 2016].

Subsequent iterations of the dual-polarization modules will further optimize the optical coupling scheme. The horns should either be profiled, the baseline design for these detectors going forward, or corrugated. For expediency, conical horns were used in the tests outlined in this chapter. The optical coupling will be improved with either of these horn designs. Thermal contractions can cause optical misalignment in the array. HFSS simulations show misalignment can reduce optical efficiency while also increasing cross-polarization. Although we cannot probe the efficacy of the current alignment method (edge alignment) future iterations could use a pin and slot method which may better constrain the motion of the array.

The detector yield and the uniformity of the resonance frequency spacing could be increased. Currently, the detector yield is greater than 75%, however this should be able to reach close to 100%. Non-uniformities in the device metal could cause resonance frequencies

to shift or opens in the resonator circuits. Some of the 160 μm thick wafers have cracked during cryogenic cycling, so we are developing ways to make the arrays more mechanically robust by, for example, bonding them to thick handle wafers.

7.5 Conclusion

The dual-polarization LEKID array we have demonstrated in this study is the first for millimeter wavelengths and the first optimized for ground-based CMB polarization studies. In this chapter, we have presented the design and characterization of the dual-polarization LEKIDs. The array of LEKIDs optimized to observe a 150 GHz spectral band is comprised of detector pairs sensitive to two orthogonal polarizations. The detectors have high internal quality factors which reach 1×10^6. The detectors are shown to have low-noise with an NET < 100 μK$\sqrt{\text{s}}$ under a 3.4 K load for the two polarizations. The detectors have uniform response between polarizations. The detectors have a large dynamic range and were not saturated up to a brightness temperature of 90 K. We demonstrate that the detectors have low crosstalk, below -20 dB. We demonstrate that within a single element, the LEKIDs sensitive to orthogonal polarizations have high polarization selectivity for millimeter-wave radiation at 82% and 87% across the 140–165 GHz band. We show that the detectors are photon-noise limited above 1 pW of absorbed power.

The entire array is read out on a single coaxial line and the 128 multiplexing factor is higher than commonly used by current CMB experiments. The detectors and readout are designed to be straightforwardly increased to a multiplexing factor of 512. Additionally, the detectors are fabricated from a single layer of aluminum. The relatively simple fabrication process is a crucial strength of these devices as the next generation of CMB experiments will need a large increase in detector count. These results show that the dual-polarization LEKIDs are ready for an on-sky demonstration in a ground-based CMB polarimeter.

Acknowledgements

We acknowledge the JPL Microdevices Lab, where the devices were fabricated, ASU, where the horn array was machined, and Cardiff University, where the filters were made. This work is partially funded by the Office of Naval Research. H. M. is supported by a NASA Earth and Space Sciences Fellowship. We thank A. Kerelsky for taking the photomicrographs in Figs. 7.1b and c. We thank the Xilinx University Program for their donation of the FPGA hardware and software tools that were used in the readout system.

Appendices

Four appendices are relevant to this work. One, we present an example of an HFSS simulation used to optimize the detector design in Appendix D. Two, we discuss the technical design considerations that went into the focal plane modules in Appendix E. Three, we have included a photograph of the testbed used in Appendix F for clarity. Four, we have been exploring a new model to measure the quasiparticle lifetime (see Sec 7.3.4). This model is given in Appendix G.

Chapter 8

Data analysis of SZE observations with NIKA2 on the IRAM 30m telescope

In this chapter, I report on the initial analysis of NIKA2 observations of the galaxy cluster Abell 2443. First, I describe the scientific motivation and the instrument used for the observations (Sec. 8.1). Second, I present the initial analysis steps performed on each scan (Sec. 8.2). Third, I present the different data reductions and present preliminary maps of the galaxy cluster (Sec. 8.3). Fourth, I remark on our findings and future work (Sec. 8.4).

8.1 Introduction

Measurements of galaxy clusters can potentially yield both cosmological and galactic information. Typically, CMB survey experiments with relatively narrow beams can detect many galaxy clusters [Hilton et al., 2018, de Haan et al., 2016] but cannot resolve them. These statistical samples of the clusters tell us about the distribution of matter in the universe [Carlstrom et al., 2002] as the SZE is a tracer of galaxies. In particular, the SZE is insensitive to redshift and thus the mass distribution in the universe at high-z can be mea-

sured [Carlstrom et al., 2002]. Separate, resolved measurements of the galaxy clusters can offer complementary and, at times, clarifying information. Resolved tSZE measurements of a cluster can reveal the physical structure and dynamical state. The tSZE signal can be boosted in colliding clusters; this can bias the mass-tSZ scaling ratio, which is used in cluster cosmology. Thus, resolved measurements are important in that they can reveal if a galaxy cluster is not in equilibrium. The resolved kSZE has been measured only recently [Mroczkowski et al., 2012, Sayers et al., 2013]. kSZE measurements can uniquely measure the peculiar velocities of the cluster and intracluster gas. These measurements can be used to test other aspects of physics, such as providing constraints on dark energy and a check on general relativity [Bhattacharya and Kosowsky, 2008, Kosowsky and Bhattacharya, 2009].

The galaxy cluster Abell 2443 was recently identified as a candidate colliding cluster through X-Ray measurements [Clarke et al., 2013]. Abell 2443 is a low-z cluster with $z = 0.108$. Measurements of this cluster in the millimeter-wave regime could confirm the relative velocities measured in the X-ray. If the kSZE is measured in the cluster, we will be able to extract the peculiar cluster velocities. Ultimately, this could lead to a check that the cluster properties are consistent with the ΛCDM model, like was done for the Bullet Cluster [Clowe et al., 2006, Lee and Komatsu, 2010, Thompson et al., 2015].

Observations of Abell 2443 were taken with the NIKA2 instrument on the IRAM 30 m telescope [Catalano et al., 2016], which is depicted in Fig. 8.1a. The NIKA2 focal plane uses LEKIDs as detectors and one is shown in Fig. 8.1b. This is the only fielded millimeter-wave KID instrument. The devices are designed to absorb two polarizations in a single spectral band (i.e. are not inherently polarization sensitive). There are polarizers in the instrument, which direct a single polarization to any one array. NIKA2 has two spectral bands centered on 150 and 260 GHz. There is a single polarization sensitive array at 150 GHz (array 2), and two arrays sensitive to orthogonal polarizations at 260 GHz (arrays 1 and 3). These bands are well suited for SZE observations, as the signal appears as a decrement at 150 GHz and an increase at 260 GHz relative to the CMB, as the photons gain energy through

inverse Compton scattering. Measuring the kSZE signal requires not only observation of the decrement at 150 GHz but also observations at the high frequency band at 260 GHz, in order to disentangle it from the tSZE. The beam size of NIKA2 is 17.7" at 150 GHz and 11.2" at 260 GHz. The field of view (FOV) of NIKA2 is 6.5'. These properties – a wide FOV with high angular resolution – are desirable for making resolved maps of the tSZE and kSZE.

8.2 Analysis

To check the quality of the data, we first analyze a single scan (20171025s261) with code we developed. The scan is performed in a raster pattern. The scan size is approximately $10' \times 5'$, where the dimensions respectively correspond to azimuth and elevation. We define the scan size as the distance a single detector moves in azimuth and elevation. Each scan consists of 35 subscans, which are a single line of the raster along azimuth. Each subscan has a $20''$ increase in elevation as compared to the previous subscan. Between the subscans, there is a turnaround time when the telescope is changing directions outside the $10'$ target.

The timestream of a single detector is seen in Fig. 8.2a. Large scale structure and variations in loading are seen over this representative scan. The majority of this loading comes from atmospheric emission and is mostly common to the detectors. Thus, it is necessary to reduce the data to remove this correlated signal and recover the astronomical information.

8.2.1 Reduction steps

The steps in this section describe the data reduction. The steps are similar to those described in Korngut et al. [2011]. The data reduction takes places after a preprocessing routine from the consortium pipeline, which returns four structures called `data`, `kidpar`, `info`, and `param`. The `data` structure contains the time-ordered information (TOI) or timestreams (see example in Fig. 8.2a) of the detectors, which have been preprocessed. Specifically, the TOI have been calibrated into units of Jy/beam from the original response in units of Hz, and the initial flags

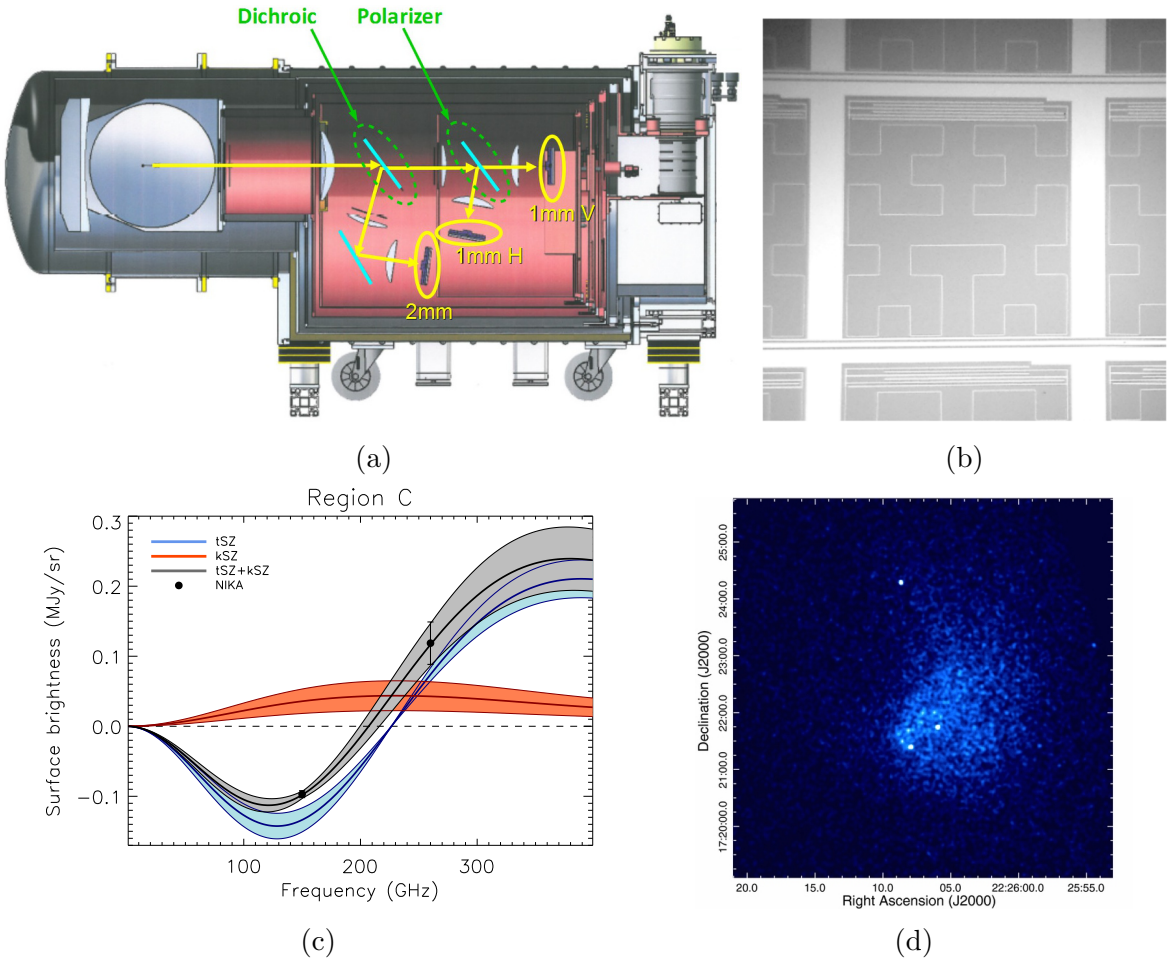

Figure 8.1: **a.** Cross-sectional view of the NIKA2 cryostat. There are three arrays: array 2 is sensitive to 2mm (150 GHz) radiation and arrays 1 and 3 are sensitive to 1 mm (260 GHz) radiation. Figure from Catalano et al. [2016]. **b.** Photograph of a NIKA2 pixel. The NIKA2 detectors are LEKIDs and each pixel is polarization insensitive. The polarization is split before the arrays. NIKA, the predecessor to NIKA2, and NIKA2 are the first millimeter-wave instruments on-sky. The arrays are bare-arrays, as in without horn or lens coupling. Figure adapted from Adam et al. [2017a]. **c.** Plot of SZE constraints from Adam et al. [2017b] from a subcluster in the galaxy cluster MACSJ0717.5+3745. The observations for these constraints were conducted with NIKA. The best fit tSZE is shown in blue and kSZE in orange. The two together are plotted in grey, and the data points from NIKA are shown as black dots. This is one of the few resolved measurements of the kSZE. NIKA2 has better sensitivity than NIKA so similar measurements should be possible with NIKA2. NIKA2 will attempt to measure the tSZE in 50 high red-shift clusters ($z > 0.5$) [Macias-Pérez et al., 2017]. Figure from Adam et al. [2017b]. **d.** X-ray image of the galaxy cluster Abell 2443 from Chandra. Recent analysis of Abell 2443 using Chandra data has revealed a possible merger [Clarke et al., 2013]. In this research, we are trying to verify and directly measure the intracluster velocity via the tSZE in the millimeter-wave regime with NIKA2 observations. We also hope to measure a similar kSZE signature as shown in panel c. Figure adapted from Clarke et al. [2013].

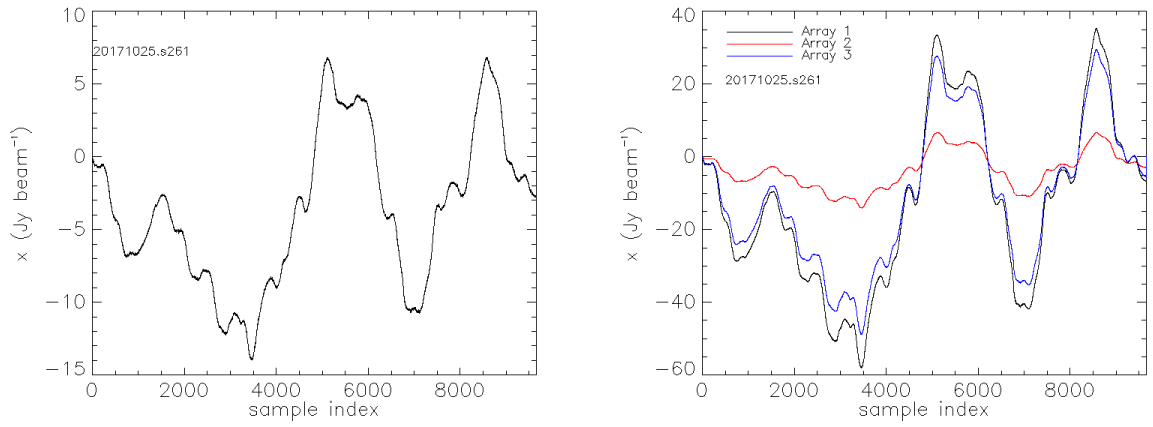

(a) (b)

Figure 8.2: **a.** Preprocessed timestream of a single detector shown over one scan, which is approximately 400 s. **b.** Common mode timestreams from the three arrays. The common mode is calculated here by taking the median of all the detectors in the array. As expected, the 1 mm arrays (arrays 1 and 3) have a much greater range than the 2 mm array (array 2) as atmospheric loading is higher at the shorter wavelength.

have been assigned, which reflect relatively straight-forward issues like glitches. Throughout the reduction steps, we pay attention to flags, excluding detectors when necessary.

The reduction steps are as follow:

1. Common mode calculation

   The common mode (CM) for each array is calculated as the average of the TOI from detectors within each array (see Fig. 8.2b). We calculate the CM using both the mean and median, and use the median for all subsequent calculations.

2. Linear correction to common mode

   The detector TOI are each fit with a line to the CM of their respective array. An example is shown in Fig. 8.3a. The coefficients of the fit show how well the initial flat-field in the preprocessing calibrated the detectors. A histogram of the fit coefficients are shown in Fig. 8.3b. The TOI are then corrected using the results of the fit, yielding corrected $\mathrm{TOI_c}$, as shown in Fig. 8.3c. We check how well the array CM describes each $\mathrm{TOI_c}$ by looking at the correlation between $\mathrm{TOI_c}$ and CM, as shown in Fig. 8.3d.

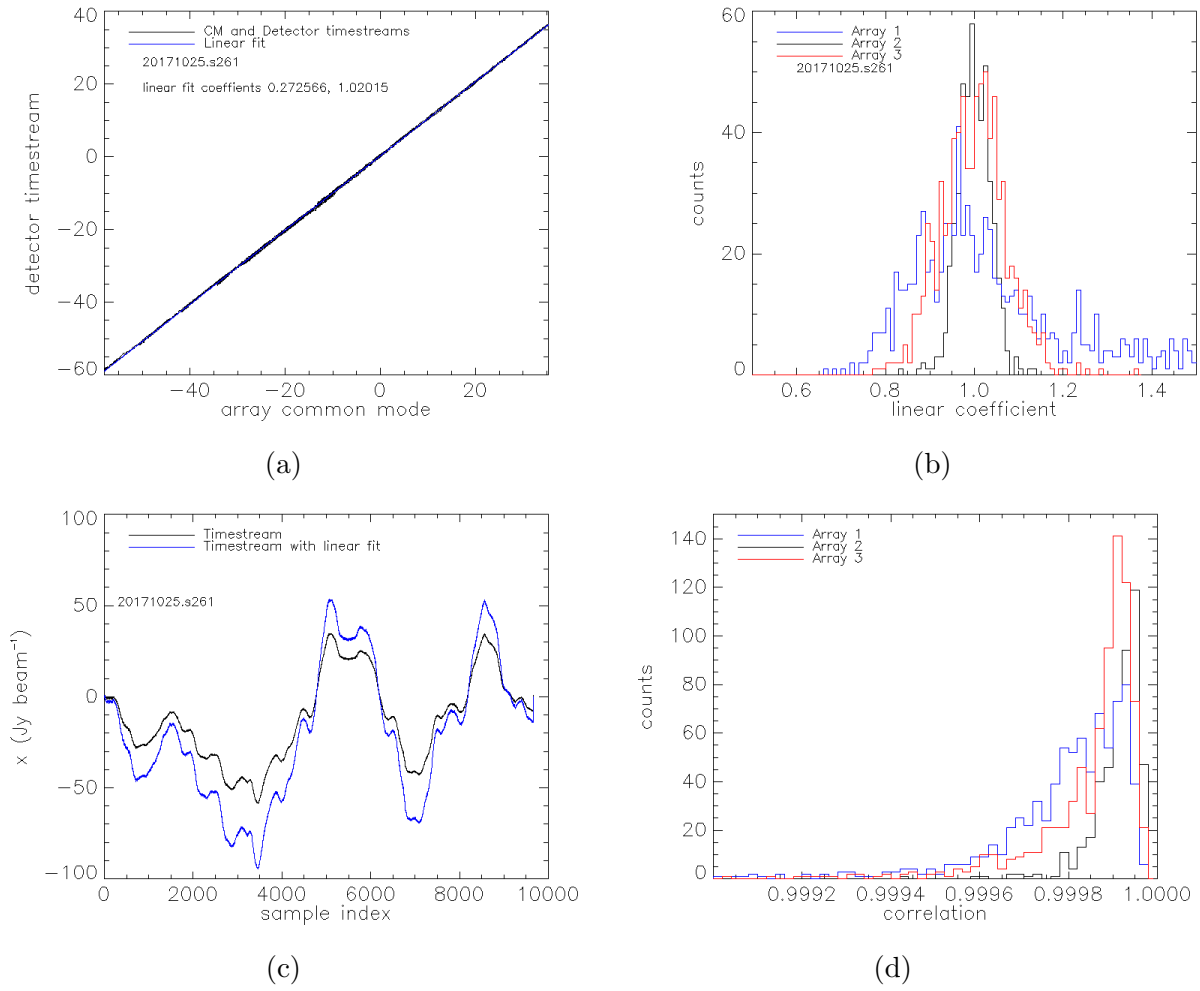

Figure 8.3: Plots illustrating the technical steps and results for reducing the data. **a.** A detector timestream plotted against the array common mode. The timestream is fit to the common mode, which is shown in blue. The coefficients of the fit reflect the accuracy of the initial preprocessing flat-field. **b.** Histogram of the 1st order coefficient of the linear fit for all the detectors in the arrays. **c.** Plot of a detector timestream before and after the linear correction has been applied. **d.** Histogram the correlation between the common modes and the detector timestreams after the linear correction has been applied.

3. Common mode subtraction

   We subtract the CM from each of the corrected $\mathrm{TOI_c}$, which yields $\mathrm{TOI_s}$. Fig. 8.4a shows a plot of CM, $\mathrm{TOI_c}$, and $\mathrm{TOI_s}$ for a single detector. After the CM has been subtracted from the timestream of each detector, the majority of the atmospheric fluctuations have been removed.

4. Polynomial subtraction from subscans (detrending)

We fit a 1st order polynomial to each subscan of each detector, excluding the turnaround time, and subtract the polynomial from the detector timestream, yielding $\mathrm{TOI_d}$. This is plotted in Fig. 8.4b. The detrending accounts for variations between detectors, whereas the CM accounts for atmospheric fluctuations that all the detectors observe. An example for a detector timestream over the entire scan both before and after detrending is plotted in Fig. 8.4c.

8.2.2 Data quality metrics

In order to quantify the quality of the data from each detector and overall, we use the following metrics:

1. Noise spectral density

   We calculate the amplitude spectral density, or the square root of the power spectral density (PSD), of the detectors using a FFT. The detector noise spectra are expected to be well described by two components. One, there is a low frequency $(1/f_\mathrm{k})^\alpha$ component, with a knee at f_k. Two, there is white noise above f_k.

   The noise spectral density at various stages of the reduction are shown in Fig. 8.5a. The PSD of $\mathrm{TOI_c}$, or the timestream without the CM subtracted, shows a 1/f component with a high α that dominates the spectra. The PSD of $\mathrm{TOI_s}$, or the common mode subtracted timestream, makes f_k more apparent and results in a lower α. After a polynomial is subtracted from the timestream of each subscan, the PSD of the entire scan shows low frequency noise below the white noise level. In this case, we have effectively high-pass filtered the data, removing information below the inverse of the time of a subscan.

2. RMS

   We calculate the standard deviation of each detector across the scan, excluding turnaround times. This allows us to quantify the noise in each detector, which will propagate to

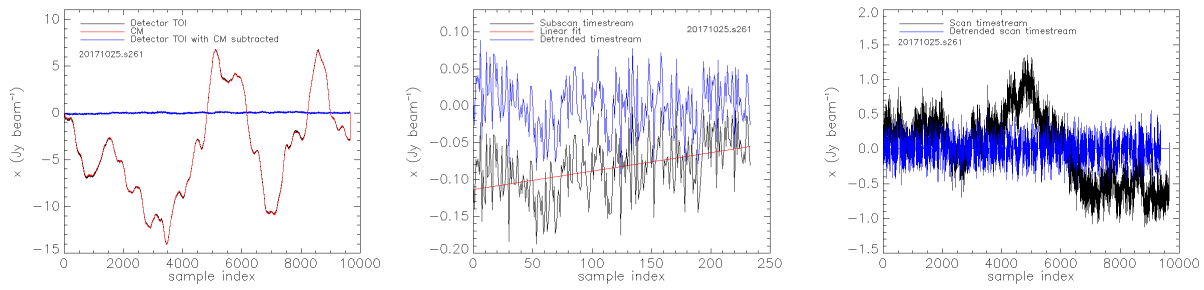

(a) (b) (c)

Figure 8.4: **a.** Plot of the array common mode (red), the linearly corrected TOI (black), and the common mode subtracted TOI (blue) across a scan. **b.** Plot of one subscan (black) that has had the common mode subtracted. A first order polynomial is fit the subscan (red) and then subtracted to produce a detrended subscan timestream (blue). This is done for each subscan for each detector. **c.** Plot of a scan before (black) and after (blue) the subscans have had a first order polynomial fit out.

the noise of the maps. The RMS of each detector is shown at different stages of the reduction in Fig. 8.5b.

We find that array 2 at 2 mm has the lowest variance. The 1 mm arrays are appreciably noisier, with array 1 more so than array 3. From this initial analysis, it appears that the 2 mm data should be fairly robust.

8.2.3 Comparison with consortium pipeline

We compare the noise spectra calculated with the steps above to that of the consortium pipeline in Fig. 8.5c. We compare the RMS of the detectors after our reduction to that of the consortium pipeline in Fig. 8.5d. The consortium pipeline correlates all the detectors with one another and uses highly-correlated detectors to create common modes for specific blocks of detectors. High correlation between detectors could be due to a number of factor, including common readout electronics, crosstalk, or spatial proximity. This additional step could result in some of the differences between our initial results and those of the consortium pipeline.

8.2.4 Astronomical implications

The purpose of the data reduction is to remove the atmospheric signal and to find the signal due to the astronomical objects. The reduction steps each have an effect on the final maps. The CM subtraction removes information on scales larger than the FOV. This includes removal of any common astronomical signal as well. We expect this to be the case for this analysis, as the cluster extends beyond the 6.5′ FOV. The subtraction of a polynomial from each subscan also removes information larger than the subscan length divided by polynomial order. In this case, we fit a first order polynomial to each timestream and thus we remove information on the largest scale accessible in that subscan.

8.3 Multi-scan analysis and maps

The next steps are to reduce multiple scans and make preliminary maps. First, we use the metrics described above to examine each scan. Second, we try a variety of reductions and examine the maps they produce.

8.3.1 Multi-scan reductions

First, we use the reduction code we developed on all of the scans in order to check the quality of the data. These scans are analyzed using the same steps as described in Sec. 8.2.1. There are 70 scans in total from the NIKA2 observations from the October 2017 run. A plot of the RMS of the detectors in the 70 scans is shown in Fig. 8.6. We use this data to identify any scans that need individual treatment or to be excluded. We identify only one scan, 20171024s282, which exhibits scattered RMS values and high noise. We note that the pipeline reduction is able to recover RMS values similar to that of the other scans.

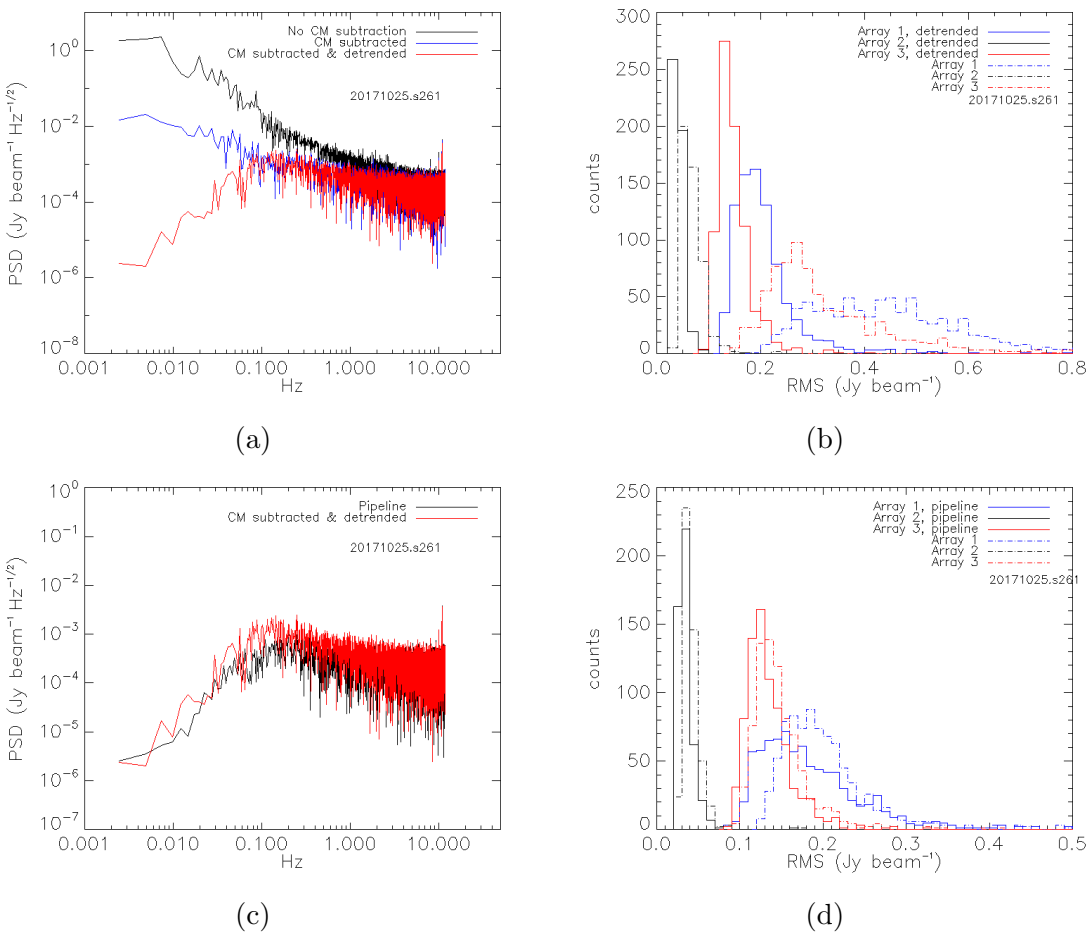

Figure 8.5: **a.** Noise spectra corresponding to detector data without the CM subtracted (black), with the CM subtracted (blue), and with the CM subtracted after detrending (red). **b.** RMS of detectors within the three arrays both with (solid) and without (dotted) detrending after CM subtraction. **c.** Comparison of noise spectra from our data reduction (red) to that of the consortium pipeline (black). **d.** Comparison of detector RMS for each of the three arrays from our data reduction (dotted) to that of consortium pipeline (solid).

8.3.2 Reduction parameters and methods

Second, we primarily use the consortium pipeline to reduce the data from all scans and produce maps. In the reductions, we vary a number of parameters including:

1. The number of detectors $n_{\rm cm}$ used to calculate the common mode.

2. Subtracting a polynomial of order n from the subscan timestreams.

3. Calculating the common mode with or without a mask of a chosen radius $r_{\rm m}$.

Figure 8.6: Histograms of the RMS of the detectors for each scan. We find the performance of the arrays are consistent over all the scans except one (1st column, second row).

4. Iterating n_i times over the reduction steps after subtracting out astronomical signal in the maps defined by signal to noise ratio (SNR) below and above cutoffs given by $\mathrm{SNR_d}$ and $\mathrm{SNR_s}$, respectively. In this analysis, the SNR is defined as the relative map signal divided by the noise map. Therefore a decrement, which we expect at 150 GHz, will have a negative SNR.

The initial reductions we performed are listed in Table 8.1.

8.3.2.1 Number of detectors

The number of detectors used to calculate the common mode n_{cm} is varied. The common mode blocks are determined by creating a correlation matrix between all the detectors. The n_{cm} most highly correlated detectors are chosen and a common mode for this block is cal-

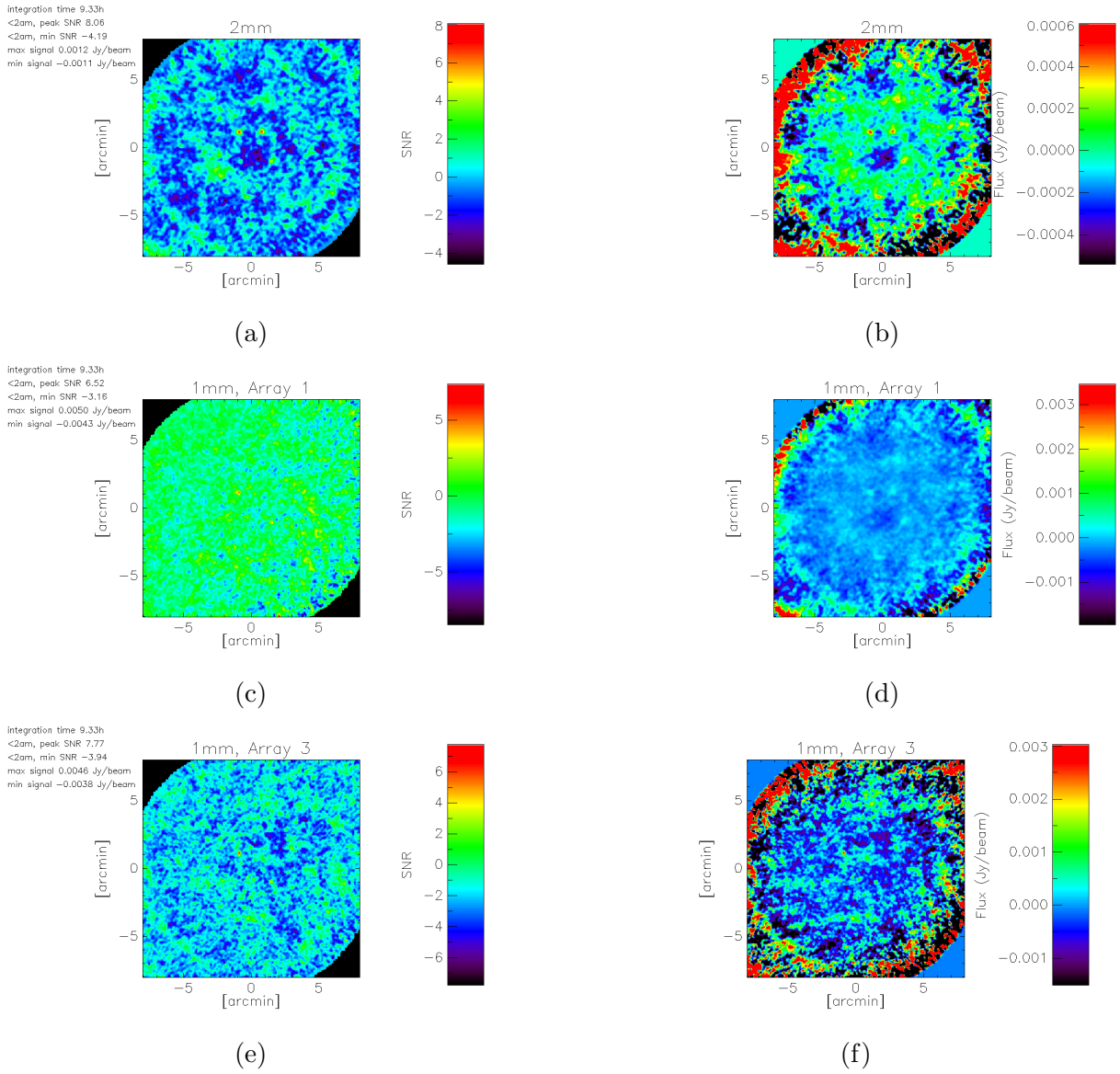

Figure 8.7: SNR and signal maps for the three arrays from reduction 1. **a.** Initial SNR map of array 2 (2 mm). **b.** Signal map of array 2 (2 mm). In this map we can see a decrement in the center of the map as would be expected for the SZE at 150 GHz. **c.** Initial SNR map of array 1 (1 mm). **d.** Signal map of array 1 (1 mm). **e.** Initial SNR map of array 3 (1 mm). **f.** Signal map of array 3 (1 mm). There is no clear astrophysical signal in the 1 mm maps. We explore more advanced reductions to see if it can be recovered.

reduction	$n_{\rm cm}$	$r_{\rm m}$	n	n_i	$\rm SNR_d$	$\rm SNR_s$
1	15	-	-	-	-	-
2	15	2'	-	-	-	-
3	50	2'	-	-	-	-
4	15	2'	2	-	-	-
5	15	-	-	6	-3	4
6	15	2'	2	6	-4	4

Table 8.1: Parameters chosen for the reductions performed. $n_{\rm cm}$ is the number of detectors used to calculate the CM. $r_{\rm m}$ is the radius of the mask used to exclude detectors when calculating the CM. n is the order of the polynomial used to detrend each subscan. n_i is the number of reduction iterations. $\rm SNR_d$ is the decrement SNR exclusion threshold when using the iterative method. $\rm SNR_s$ is the positive SNR exclusion threshold when using the iterative method.

culated. While lower numbers of detectors will produce maps with less non-astronomical structure, it can also create noisier maps, so a balance must be struck. There are approximately 1100 detectors for which timestreams are collected in arrays 2 and 3, and 300 in array 1. The default number of detectors to calculate the common mode with is 15. We present a reduced signal to noise map for each array in Fig. 8.7. In Table 8.1, this is reduction 1 and uses 15 detectors to calculate CM, or $n_{\rm cm} = 15$. The correlation between all detectors is calculated and the 15 most similar are averaged to find the common mode for those. Histograms of the SNR in the maps are shown in Fig. 8.8.

8.3.2.2 Polynomial subtraction

To subtract the baseline from the subscan timestreams, we fit a polynomial of order n to the TOI, which is then subtracted from the TOI. The order of the polynomial must be sufficient to remove the fluctuations in the timestreams due to residual non-astronomical signal. However, this must be balanced against removing astronomical signal and biasing the information on large scales.

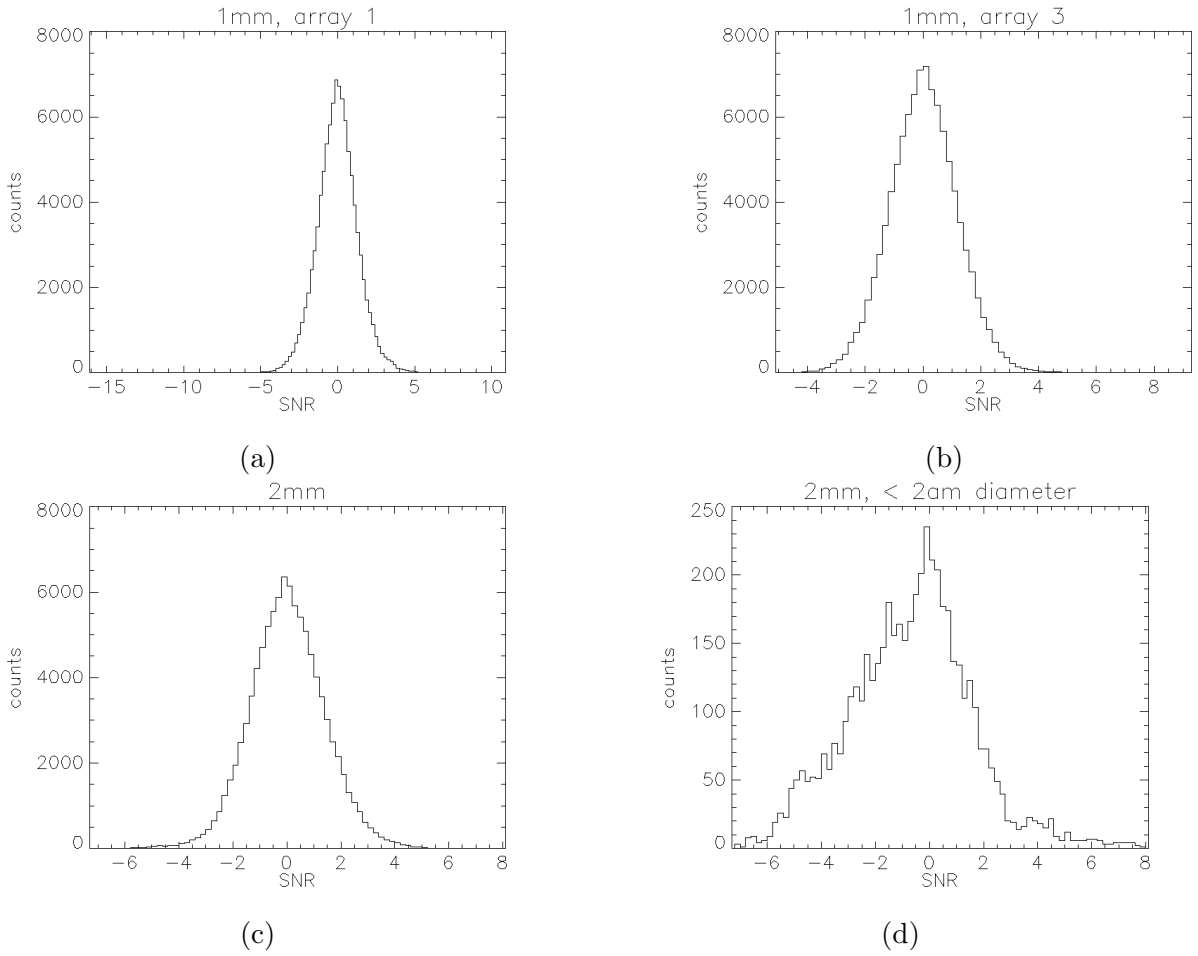

Figure 8.8: **a.** SNR distribution for array 1 (1 mm array). **b.** SNR distribution for array 3 (1 mm array). **c.** SNR distribution for array 2 (2 mm array). **d.** SNR distribution for array 2 within a 2' radius of the center of the scan. The SNR distribution is skewed negative as would be expected for the SZE at 150 GHz.

8.3.2.3 Radial mask

The detectors used to calculate the common mode can be chosen so as to exclude those within a certain radius r_m of the expected source. Including the detectors that observe the expected source when calculating the common mode can lead to subtraction of the astronomical signal. Conversely, excluding too many detectors can cause inaccuracies as well. When r_m approaches the radius of the FOV, there can be insufficient detectors remaining to give a good estimate of the common mode while a scan approaches the source.

The mask we use has $r_{\rm m} = 2'$ and discards the points within this radius from the center

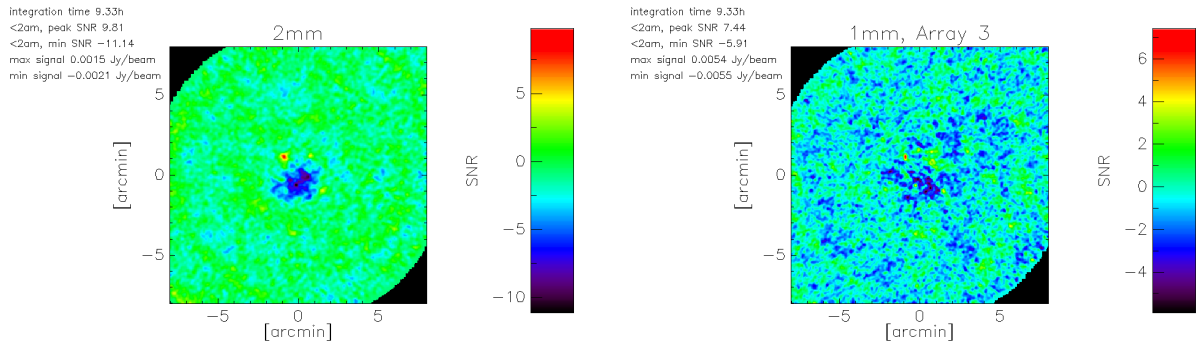

(a) (b)

Figure 8.9: SNR maps made with a 2′ radial mask for calculating the common mode for **a.** array 2 (2 mm array) and **b.** array 3 (1 mm array). This approach appreciably increases the magnitude of the SNR in the 2 mm array.

of the source. We compare the RMS of the detectors with and without the mask. The RMS of the detectors with the mask changes as compared to the RMS without. The shift tends towards higher RMS values although not uniformly. We suspect this is because the mask will exclude points from the the common mode calculation to the point where a good estimate cannot be made, as discussed above. In practice, using a radial mask results in appreciably higher SNR in the point sources and lower SNR, as expected, in the decrement. SNR maps at 1 and 2 mm are shown in Fig. 8.9.

8.3.2.4 Iterative signal subtraction

After an initial SNR map is made, we use an iterative method based on this SNR map. For a 150 GHz map, we select pixels within a radius $r_{\rm d}$ with SNR $<$ SNR$_{\rm d}$, which corresponds to the expected decrement and SZE signal. We also select pixels across the entire map with SNR $>$ SNR$_{\rm p}$, which should correspond to point sources. These are combined as $P_{\rm s}$ = SNR$_{\rm p}$ + SNR$_{\rm d}$. The signal $P_{\rm s}$ is subtracted from the original timestreams, TOI, in the time domain as TOI$_i$ = TOI - TOI$_{\rm s}$, where i is the iteration number and TOI$_{\rm s}$ is the timestream domain equivalent of $P_{\rm s}$. The TOI$_i$ is then reduced and returns TOI$_{\rm i}^{\rm r}$, where i is again the iteration number. Before going to the map domain, the signal timestream TOI$_{\rm s}$ is

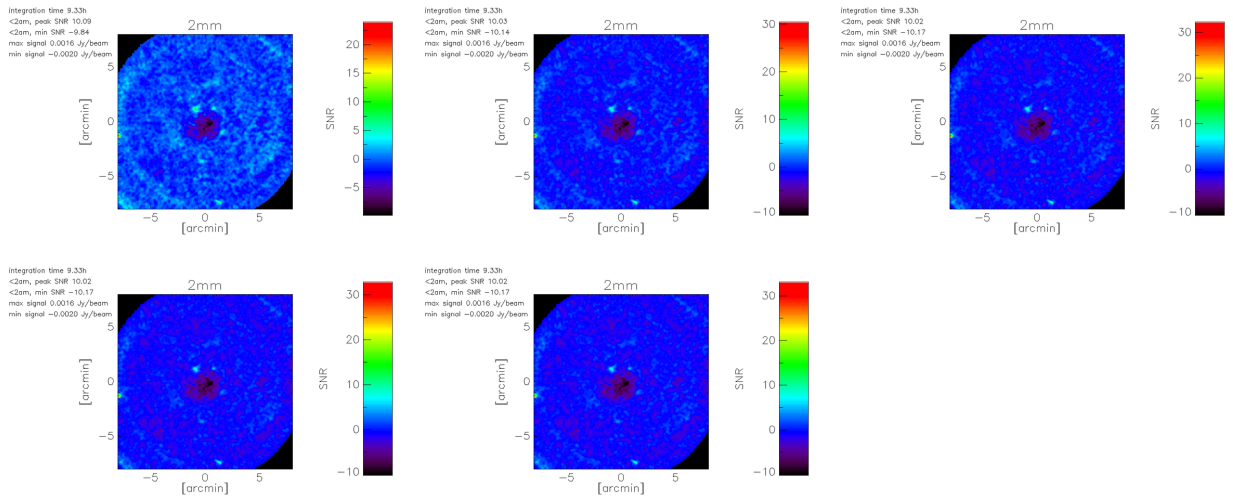

Figure 8.10: SNR maps of the 2 mm array produced with the iterative approach. For convergence criteria, we look at the the minimum and maximum SNR to see if it is changing. We find that the SNR does not improve significantly with the iterative approach.

added back in, giving $\mathrm{TOI}_i^{\mathrm{f}} = \mathrm{TOI}_{\mathrm{s}} + \mathrm{TOI}_i^{\mathrm{r}}$. The reduction can then be iterated over again. For convergence criteria, we look at the the minimum and maximum SNR to see if it is changing. We find that the SNR does not improve significantly with the iterative approach. In Fig. 8.10, we present maps at 150 GHz that are reduced with this iterative method.

8.4 Discussion

In this chapter, I discussed the initial reduction and analysis of the galaxy cluster Abell 2443, which is possibly a merging cluster. We first analyzed the data by scan to check the quality of the data. We found good performance in the 2 mm array. After verifying the data in each scan appeared sensible, we analyzed all the data using the consortium pipeline. We explored varying parameters in the reductions and from these, I presented preliminary maps of the galaxy cluster. The initial data reduction demonstrates that we likely detect a decrement at 150 GHz as would be expected for the SZE. We found that masking the center of the maps, to avoid removing astronomical structure, increases the SNR. We also found that limiting the number of detectors used to calculate the common mode increases the decrement signal.

However, iterating over multiple reductions does not appear to increase the SNR appreciably.

Future analysis work includes stepping over parameters space and possibly using an alternative map-making algorithm. It will be necessary to better understand the analysis to ensure that we are not introducing false structure into the maps. We will also need to calculate the transfer function of the final reduction. Further observations are needed to increase the SNR. In particular, high-quality data from the 1 mm arrays is necessary to measure the kSZE. A measurement of the resolved kSZE would yield the peculiar velocities within the galaxy cluster. These measurements could ultimately help further our understanding of colliding clusters.

Acknowledgements

This work is based on observations carried out under project number 081-17 with the IRAM 30 m telescope. IRAM is supported by INSU/CNRS (France), MPG (Germany) and IGN (Spain). The PI of project 081-17 is T. Mroczkwoski (ESO) and the data reduction was done in collaboration with C. Romero (IRAM).

Chapter 9

Conclusion

In these final pages, I present a brief summary of the research presented in this thesis and comment on future prospects.

The next-generation CMB experiments are being primarily designed to measure primordial B-mode polarization. This detection would provide direct evidence for inflation, which so far has only been postulated. CMB experiments have become increasingly precise and accurate as the blackbody spectrum, temperature and E-mode polarization angular power spectra have been measured. These measurements have revealed the evolution and make-up of the universe. In order to do this, CMB experiments have also grown in every manner of size - from collaboration size to the detector count - as increased sensitivity is needed. Future CMB experiments - such as Simons Observatory [Simons Observatory Collaboration, 2018] and CMB-S4 [Abazajian et al., 2016] - will respectively need at least a 10 and 50 times increase in detector count, and this requires advances in device physics and detector technologies. In the future, it will also be necessary to have a satellite to reach low-ℓ and re-ionization science; large aperture telescopes to measure galactic lensing; and a wide range of frequencies covered - from a few gigahertz to a terahertz - in order to characterize foregrounds. Experimental CMB cosmology has a long and rich path ahead. KIDs appear to be an attractive detector for these next-generation CMB experiments because of their high

multiplexing factors, which are crucial for enabling the large number of detectors needed. However, systematic studies did not exist to show their ability to achieve the performance necessary for CMB survey experiments. In this research, I have broadly tried to advance KIDs for the next-generation of CMB studies that will push our understanding of cosmology further.

First, I presented the design and performance of single-polarization LEKIDs optimized for a spectral band centered on 150 GHz (Ch. 4). With these devices, we demonstrated that KIDs were capable of achieving the low-noise and high-sensitivity necessary for CMB observations. Second, I presented a novel method to reduce crosstalk between KIDs, which is necessary to tightly control instrument systematics (Ch. 5). With this method, we were able to appreciably reduce crosstalk between detectors. Third, I presented the initial design and development of dual-polarization LEKIDs for millimeter-wave lengths (Ch. 6). With dual-polarization LEKIDs, the number of detectors per a focal plane area is doubled, increasing the sensitivity of each array. Fourth, I presented the design and measured performance of an array of dual-polarization LEKIDs, designed to be tiled into the focal plane of a telescope (Ch. 7). These devices performed well and achieved photon-noise limited sensitivity, low NETs, and high polarization efficiency; they should be able to go on-sky competitively. Fifth, I discussed the initial analysis of observations of the galaxy cluster Abell 2443 to measure the SZE and presented preliminary maps (Ch. 8). The overall project will require more observations in the coming years and the initial results are promising.

The path forward for KIDs is multifaceted. The devices are being considered as a candidate technology for CMB-S4 [Abitbol et al., 2017]. Foremost, a pathfinder CMB survey polarimeter with a focal plane of KIDs at millimeter-wave lengths is necessary in order to prepare for CMB-S4 and beyond. Complementary efforts are currently underway and other groups are paving the path as well. First, our collaboration is building an Office of Naval Research (ONR) instrument, which will tile four of the dual-polarization arrays and modules into the focal plane. Second, the TolTEC camera [Austermann et al., 2018] is being devel-

oped for the Large Millimeter Telescope (LMT). TolTEC will use detectors fairly similar to our millimeter-wave dual-polarization LEKIDs for observations of star-forming regions. Third, the CCAT-prime telescope [Stacey et al., 2018] plans to use a focal plane of KIDs at $\sim$ 800 GHz and will measure the SZE and CMB foregrounds. This should be an informative demonstration of KIDs observing the CMB. In addition, the advantages associated with KIDs are partly leading to other new efforts. For instance, a new readout is being developed for TES bolometer arrays in CMB experiments [Dober et al., 2017]; the bolometers are coupled to resonators and then read out in a similar manner to KIDs.

On the device physics side, there are interesting pathways forward. We are developing multi-chroic devices as well; these are sensitive to two spectral bands and two polarizations within each focal plane element, which increases the NET of the array [Johnson et al., 2016, 2018]. Other groups have also more recently begun to develop KIDs for CMB experiments [Barry et al., 2018, Steinbach et al., 2018], and it will be enlightening to see the innovations there. There are many exciting developments underway with KIDs, particularly in the millimeter-wave regime. This research should ultimately lead to more sensitive CMB measurements and a better understanding of the early universe.

References

K. N. Abazajian, P. Adshead, Z. Ahmed, S. W. Allen, D. Alonso, K. S. Arnold, C. Baccigalupi, J. G. Bartlett, N. Battaglia, B. A. Benson, C. A. Bischoff, J. Borrill, V. Buza, E. Calabrese, R. Caldwell, J. E. Carlstrom, C. L. Chang, T. M. Crawford, F.-Y. Cyr-Racine, F. De Bernardis, T. de Haan, S. di Serego Alighieri, J. Dunkley, C. Dvorkin, J. Errard, G. Fabbian, S. Feeney, S. Ferraro, J. P. Filippini, R. Flauger, G. M. Fuller, V. Gluscevic, D. Green, D. Grin, E. Grohs, J. W. Henning, J. C. Hill, R. Hlozek, G. Holder, W. Holzapfel, W. Hu, K. M. Huffenberger, R. Keskitalo, L. Knox, A. Kosowsky, J. Kovac, E. D. Kovetz, C.-L. Kuo, A. Kusaka, M. Le Jeune, A. T. Lee, M. Lilley, M. Loverde, M. S. Madhavacheril, A. Mantz, D. J. E. Marsh, J. McMahon, P. D. Meerburg, J. Meyers, A. D. Miller, J. B. Munoz, H. N. Nguyen, M. D. Niemack, M. Peloso, J. Peloton, L. Pogosian, C. Pryke, M. Raveri, C. L. Reichardt, G. Rocha, A. Rotti, E. Schaan, M. M. Schmittfull, D. Scott, N. Sehgal, S. Shandera, B. D. Sherwin, T. L. Smith, L. Sorbo, G. D. Starkman, K. T. Story, A. van Engelen, J. D. Vieira, S. Watson, N. Whitehorn, and W. L. Kimmy Wu. CMB-S4 Science Book, First Edition. *ArXiv e-prints*, October 2016.

M. H. Abitbol. *Studying the Effects of Galactic and Extragalactic Foregrounds on Cosmic Microwave Background Observations*. PhD thesis, Columbia University, 2018.

M. H. Abitbol, Z. Ahmed, D. Barron, R. Basu Thakur, A. N. Bender, B. A. Benson, C. A. Bischoff, S. A. Bryan, J. E. Carlstrom, C. L. Chang, D. T. Chuss, K. T. Crowley, A. Cukierman, T. de Haan, M. Dobbs, T. Essinger-Hileman, J. P. Filippini, K. Ganga, J. E. Gudmundsson, N. W. Halverson, S. Hanany, S. W. Henderson, C. A. Hill, S.-P. P. Ho, J. Hubmayr, K. Irwin, O. Jeong, B. R. Johnson, S. A. Kernasovskiy, J. M. Kovac, A. Kusaka, A. T. Lee, S. Maria, P. Mauskopf, J. J. McMahon, L. Moncelsi, A. W. Nadolski, J. M. Nagy, M. D. Niemack, R. C. O'Brient, S. Padin, S. C. Parshley, C. Pryke, N. A. Roe, K. Rostem, J. Ruhl, S. M. Simon, S. T. Staggs, A. Suzuki, E. R. Switzer, O. Tajima, K. L. Thompson, P. Timbie, G. S. Tucker, J. D. Vieira, A. G. Vieregg, B. Westbrook, E. J. Wollack, K. W. Yoon, K. S. Young, and E. Y. Young. CMB-S4 Technology Book, First Edition. *ArXiv e-prints*, June 2017.

R. Adam, B. Comis, J. F. Macías-Pérez, A. Adane, P. Ade, P. André, A. Beelen, B. Belier, A. Benoît, A. Bideaud, N. Billot, N. Boudou, O. Bourrion, M. Calvo, A. Catalano, G. Coiffard, A. D'Addabbo, F.-X. Désert, S. Doyle, J. Goupy, C. Kramer, S. Leclercq, J. Martino, P. Mauskopf, F. Mayet, A. Monfardini, F. Pajot, E. Pascale, L. Perotto, E. Pointecouteau, N. Ponthieu, V. Revéret, L. Rodriguez, G. Savini, K. Schuster, A. Sievers, C. Tucker, and R. Zylka. First observation of the thermal Sunyaev-Zel'dovich effect with kinetic inductance detectors. *A&A*, 569:A66, September 2014. doi: 10.1051/0004-6361/201322902.

R. Adam, A. Adane, P. A. R. Ade, P. André, A. Andrianasolo, H. Aussel, A. Beelen, A. Benoit, A. Bideaud, N. Billot, O. Bourrion, A. Bracco, M. Calvo, A. Catalano, G. Coiffard, B. Comis, M. De Petris, F.-X. Désert, S. Doyle, E. F. C. Driessen, R. Evans, J. Goupy, C. Kramer, G. Lagache, S. Leclercq, J.-P. Leggeri, J.-F. Lestrade, J.-F. Macias-Perez, P. Mauskopf, F. Mayet, A. Maury, A. Monfardini, S. Navarro, E. Pascale, L. Perotto, G. Pisano, N. Ponthieu, V. Reveret, A. Rigby, A. Ritacco, C. Romero, H. Roussel, F. Ruppin, K. Schuster, A. Sievers, S. Triqueneaux, C. Tucker, and R. Zylka. The NIKA2 large field-of-view millimeter continuum camera for the 30-m IRAM telescope. *ArXiv e-prints*, July 2017a.

R. Adam, I. Bartalucci, G. W. Pratt, P. Ade, P. André, M. Arnaud, A. Beelen, A. Benoît, A. Bideaud, N. Billot, H. Bourdin, O. Bourrion, M. Calvo, A. Catalano, G. Coiffard, B. Comis, A. D'Addabbo, M. De Petris, J. Démoclès, F.-X. Désert, S. Doyle, E. Egami, C. Ferrari, J. Goupy, C. Kramer, G. Lagache, S. Leclercq, J.-F. Macías-Pérez, S. Maurogordato, P. Mauskopf, F. Mayet, A. Monfardini, T. Mroczkowski, F. Pajot, E. Pascale, L. Perotto, G. Pisano, E. Pointecouteau, N. Ponthieu, V. Revéret, A. Ritacco, L. Rodriguez, C. Romero, F. Ruppin, K. Schuster, A. Sievers, S. Triqueneaux, C. Tucker, M. Zemcov, and R. Zylka. Mapping the kinetic Sunyaev-Zel'dovich effect toward MACS J0717.5+3745 with NIKA. *A&A*, 598:A115, February 2017b. doi: 10.1051/0004-6361/201629182.

P. A. R. Ade, G. Pisano, C. Tucker, and S. Weaver. A review of metal mesh filters. In *Society of Photo-Optical Instrumentation Engineers (SPIE) Conference Series*, volume 6275 of *Society of Photo-Optical Instrumentation Engineers (SPIE) Conference Series*, July 2006. doi: 10.1117/12.673162.

D. C. Araujo, P. A. R. Ade, J. R. Bond, K. J. Bradford, D. Chapman, G. Che, P. K. Day, J. Didier, S. Doyle, H. K. Eriksen, D. Flanigan, C. E. Groppi, S. N. Hillbrand, B. R. Johnson, G. Jones, M. Limon, A. D. Miller, P. Mauskopf, H. McCarrick, T. Mroczkowski, B. Reichborn-Kjennerud, B. Smiley, J. Sobrin, I. K. Wehus, and J. Zmuidzinas. A LEKID-based CMB instrument design for large-scale observations in Greenland. In *Millimeter, Submillimeter, and Far-Infrared Detectors and Instrumentation for Astronomy VII*, volume 9153 of *Proc. SPIE*, page 91530W, August 2014. doi: 10.1117/12.2056828.

J. E. Austermann, J. A. Beall, S. A. Bryan, B. Dober, J. Gao, G. Hilton, J. Hubmayr, P. Mauskopf, C. M. McKenney, S. M. Simon, J. N. Ullom, M. R. Vissers, and G. W. Wilson. Millimeter-Wave Polarimeters Using Kinetic Inductance Detectors for TolTEC and Beyond. *Journal of Low Temperature Physics*, May 2018. doi: 10.1007/s10909-018-1949-5.

R. Barends, J. J. A. Baselmans, S. J. C. Yates, J. R. Gao, J. N. Hovenier, and T. M. Klapwijk. Quasiparticle Relaxation in Optically Excited High-Q Superconducting Resonators. *Physical Review Letters*, 100(25):257002, June 2008. doi: 10.1103/PhysRevLett.100.257002.

D. Barron, Y. Chinone, A. Kusaka, J. Borril, J. Errard, S. Feeney, S. Ferraro, R. Keskitalo, A. T. Lee, N. A. Roe, B. D. Sherwin, and A. Suzuki. Optimization study for the experimental configuration of CMB-S4. *J. Cosmology Astropart. Phys.*, 2:009, February 2018. doi: 10.1088/1475-7516/2018/02/009.

P. Barry. *On the development of SuperSpec: a fully integrated on-chip spectrometer for far-infrared astronomy.* PhD thesis, Cardiff University, 2014.

P. S. Barry, S. Doyle, A. L. Hornsby, A. Kofman, E. Mayer, A. Nadolski, Q. Y. Tang, J. Vieira, and E. Shirokoff. Design and Performance of the Antenna-Coupled Lumped-Element Kinetic Inductance Detector. *Journal of Low Temperature Physics*, May 2018. doi: 10.1007/s10909-018-1943-y.

J. Baselmans, S. J. C. Yates, R. Barends, Y. J. Y. Lankwarden, J. R. Gao, H. Hoevers, and T. M. Klapwijk. Noise and sensitivity of aluminum kinetic inductance detectors for sub-mm astronomy. *J. Low Temp. Phys.*, 151(1):524–529, 2008.

J. J. A. Baselmans, J. Bueno, S. J. C. Yates, O. Yurduseven, N. Llombart, K. Karatsu, A. M. Baryshev, L. Ferrari, A. Endo, D. J. Thoen, P. J. de Visser, R. M. J. Janssen, V. Murugesan, E. F. C. Driessen, G. Coiffard, J. Martin-Pintado, P. Hargrave, and M. Griffin. A kilo-pixel imaging system for future space based far-infrared observatories using microwave kinetic inductance detectors. *Astronomy and Astrophysics*, 601:A89, May 2017. doi: 10.1051/0004-6361/201629653.

C. L. Bennett, D. Larson, J. L. Weiland, N. Jarosik, G. Hinshaw, N. Odegard, K. M. Smith, R. S. Hill, B. Gold, M. Halpern, E. Komatsu, M. R. Nolta, L. Page, D. N. Spergel, E. Wollack, J. Dunkley, A. Kogut, M. Limon, S. S. Meyer, G. S. Tucker, and E. L. Wright. Nine-year Wilkinson Microwave Anisotropy Probe (WMAP) Observations: Final Maps and Results. *ApJS*, 208:20, October 2013. doi: 10.1088/0067-0049/208/2/20.

S. Bhattacharya and A. Kosowsky. Dark energy constraints from galaxy cluster peculiar velocities. *Phys. Rev. D*, 77(8):083004, April 2008. doi: 10.1103/PhysRevD.77.083004.

BICEP2 Collaboration, Keck Array Collaboration, P. A. R. Ade, Z. Ahmed, R. W. Aikin, K. D. Alexander, D. Barkats, S. J. Benton, C. A. Bischoff, J. J. Bock, R. Bowens-Rubin, J. A. Brevik, I. Buder, E. Bullock, V. Buza, J. Connors, B. P. Crill, L. Duband, C. Dvorkin, J. P. Filippini, S. Fliescher, J. Grayson, M. Halpern, S. Harrison, G. C. Hilton, H. Hui, K. D. Irwin, K. S. Karkare, E. Karpel, J. P. Kaufman, B. G. Keating, S. Kefeli, S. A. Kernasovskiy, J. M. Kovac, C. L. Kuo, E. M. Leitch, M. Lueker, K. G. Megerian, C. B. Netterfield, H. T. Nguyen, R. O'Brient, R. W. Ogburn, A. Orlando, C. Pryke, S. Richter, R. Schwarz, C. D. Sheehy, Z. K. Staniszewski, B. Steinbach, R. V. Sudiwala, G. P. Teply, K. L. Thompson, J. E. Tolan, C. Tucker, A. D. Turner, A. G. Vieregg, A. C. Weber, D. V. Wiebe, J. Willmert, C. L. Wong, W. L. K. Wu, and K. W. Yoon. Improved Constraints on Cosmology and Foregrounds from BICEP2 and Keck Array Cosmic Microwave Background Data with Inclusion of 95 GHz Band. *Physical Review Letters*, 116(3):031302, January 2016. doi: 10.1103/PhysRevLett.116.031302.

S. Bryan, K. Bradford, G. Che, P. Day, D. Flanigan, B. R. Johnson, G. Jones, B. Kjellstrand, M. Limon, P. Mauskopf, H. McCarrick, A. Miller, and B. Smiley. Design of Dual-Polarization Horn-Coupled Kinetic Inductance Detectors for Cosmic Microwave Background Polarimetry. *ArXiv e-prints*, March 2015.

J. Bueno, O. Yurduseven, S. J. C. Yates, N. Llombart, V. Murugesan, D. J. Thoen, A. M. Baryshev, A. Neto, and J. J. A. Baselmans. Photon noise limited performance over an octave of bandwidth of kinetic inductance detectors for sub-millimeter astronomy. In *2016 41st International Conference on Infrared, Millimeter, and Terahertz waves*, pages 1–2, Sept 2016. doi: 10.1109/IRMMW-THz.2016.7758429.

M. Calvo, A. Benoît, A. Catalano, J. Goupy, A. Monfardini, N. Ponthieu, E. Barria, G. Bres, M. Grollier, G. Garde, J.-P. Leggeri, G. Pont, S. Triqueneaux, R. Adam, O. Bourrion, J.-F. Macías-Pérez, M. Rebolo, A. Ritacco, J.-P. Scordilis, D. Tourres, A. Adane, G. Coiffard, S. Leclercq, F.-X. Désert, S. Doyle, P. Mauskopf, C. Tucker, P. Ade, P. André, A. Beelen, B. Belier, A. Bideaud, N. Billot, B. Comis, A. D'Addabbo, C. Kramer, J. Martino, F. Mayet, F. Pajot, E. Pascale, L. Perotto, V. Revéret, A. Ritacco, L. Rodriguez, G. Savini, K. Schuster, A. Sievers, and R. Zylka. The NIKA2 Instrument, A Dual-Band Kilopixel KID Array for Millimetric Astronomy. *J. Low Temp. Phys.*, 184:816–823, August 2016. doi: 10.1007/s10909-016-1582-0.

J. E. Carlstrom, G. P. Holder, and E. D. Reese. Cosmology with the Sunyaev-Zel'dovich Effect. *ARA&A*, 40:643–680, 2002. doi: 10.1146/annurev.astro.40.060401.093803.

A. Catalano, R. Adam, P. Ade, P. André, H. Aussel, A. Beelen, A. Benoît, A. Bideaud, N. Billot, O. Bourrion, M. Calvo, G. Coiffard, B. Comis, F.-X. Désert, S. Doyle, J. Goupy, C. F. Kramer, G. Lagache, S. Leclercq, J. F. Lestrade, J. F. Macías-Pérez, A. Maury, P. Mauskopf, F. Mayet, A. Monfardini, F. Pajot, E. Pascale, L. Perotto, G. Pisano, N. Ponthieu, V. Revéret, A. Ritacco, L. Rodriguez, C. Romero, H. Roussel, F. Ruppin, K. Schuster, A. Sievers, J. Soler, S. Triqueneaux, C. Tucker, and R. Zylka. The NIKA2 commissioning campaign: performance and first results. *ArXiv e-prints*, May 2016.

T. E. Clarke, S. W. Randall, C. L. Sarazin, E. L. Blanton, and S. Giacintucci. Chandra View of the Ultra-steep Spectrum Radio Source in A2443: Merger Shock-induced Compression of Fossil Radio Plasma? *ApJ*, 772:84, August 2013. doi: 10.1088/0004-637X/772/2/84.

D. Clowe, M. Bradač, A. H. Gonzalez, M. Markevitch, S. W. Randall, C. Jones, and D. Zaritsky. A Direct Empirical Proof of the Existence of Dark Matter. *ApJ*, 648:L109–L113, September 2006. doi: 10.1086/508162.

Peter K. Day, Henry G. LeDuc, Benjamin A. Mazin, Anastasios Vayonakis, and Jonas Zmuidzinas. A broadband superconducting detector suitable for use in large arrays. *Nature*, 425(6960):817–821, 10 2003.

T. de Haan, B. A. Benson, L. E. Bleem, S. W. Allen, D. E. Applegate, M. L. N. Ashby, M. Bautz, M. Bayliss, S. Bocquet, M. Brodwin, J. E. Carlstrom, C. L. Chang, I. Chiu, H.-M. Cho, A. Clocchiatti, T. M. Crawford, A. T. Crites, S. Desai, J. P. Dietrich, M. A. Dobbs, A. N. Doucouliagos, R. J. Foley, W. R. Forman, G. P. Garmire, E. M. George, M. D. Gladders, A. H. Gonzalez, N. Gupta, N. W. Halverson, J. Hlavacek-Larrondo, H. Hoekstra, G. P. Holder, W. L. Holzapfel, Z. Hou, J. D. Hrubes, N. Huang, C. Jones, R. Keisler, L. Knox, A. T. Lee, E. M. Leitch, A. von der Linden, D. Luong-Van, A. Mantz, D. P. Marrone, M. McDonald, J. J. McMahon, S. S. Meyer, L. M. Mocanu, J. J. Mohr,

S. S. Murray, S. Padin, C. Pryke, D. Rapetti, C. L. Reichardt, A. Rest, J. Ruel, J. E. Ruhl, B. R. Saliwanchik, A. Saro, J. T. Sayre, K. K. Schaffer, T. Schrabback, E. Shirokoff, J. Song, H. G. Spieler, B. Stalder, S. A. Stanford, Z. Staniszewski, A. A. Stark, K. T. Story, C. W. Stubbs, K. Vanderlinde, J. D. Vieira, A. Vikhlinin, R. Williamson, and A. Zenteno. Cosmological Constraints from Galaxy Clusters in the 2500 Square-degree SPT-SZ Survey. *ApJ*, 832:95, November 2016. doi: 10.3847/0004-637X/832/1/95.

P. J. de Visser, J. J. A. Baselmans, J. Bueno, N. Llombart, and T. M. Klapwijk. Fluctuations in the electron system of a superconductor exposed to a photon flux. *Nature Communications*, 5:3130, February 2014. doi: 10.1038/ncomms4130.

P. J. de Visser, S. J. C. Yates, T. Guruswamy, D. J. Goldie, S. Withington, A. Neto, N. Llombart, A. M. Baryshev, T. M. Klapwijk, and J. J. A. Baselmans. The non-equilibrium response of a superconductor to pair-breaking radiation measured over a broad frequency band. *Appl. Phys. Lett.*, 106(25):252602, June 2015. doi: 10.1063/1.4923097.

R. H. Dicke, P. J. E. Peebles, P. G. Roll, and D. T. Wilkinson. Cosmic Black-Body Radiation. *ApJ*, 142:414–419, July 1965. doi: 10.1086/148306.

P. Diener, H. G. Leduc, S. J. C. Yates, Y. J. Y. Lankwarden, and J. J. A. Baselmans. Design and Testing of Kinetic Inductance Detectors Made of Titanium Nitride. *J. Low Temp. Phys.*, 167:305–310, May 2012. doi: 10.1007/s10909-012-0484-z.

B. Dober, J. A. Austermann, J. A. Beall, D. Becker, G. Che, H. M. Cho, M. Devlin, S. M. Duff, N. Galitzki, J. Gao, C. Groppi, G. C. Hilton, J. Hubmayr, K. D. Irwin, C. M. McKenney, D. Li, N. Lourie, P. Mauskopf, M. R. Vissers, and Y. Wang. Optical Demonstration of THz, Dual-Polarization Sensitive Microwave Kinetic Inductance Detectors. *J. Low Temp. Phys.*, 184:173–179, July 2016. doi: 10.1007/s10909-015-1434-3.

B. Dober, D. T. Becker, D. A. Bennett, S. A. Bryan, S. M. Duff, J. D. Gard, J. P. Hays-Wehle, G. C. Hilton, J. Hubmayr, J. A. B. Mates, C. D. Reintsema, L. R. Vale, and J. N. Ullom. Microwave SQUID multiplexer demonstration for cosmic microwave background imagers. *Applied Physics Letters*, 111(24):243510, December 2017. doi: 10.1063/1.5008527.

B. J. Dober, P. A. R. Ade, P. Ashton, F. E. Angilè, J. A. Beall, D. Becker, K. J. Bradford, G. Che, H.-M. Cho, M. J. Devlin, L. M. Fissel, Y. Fukui, N. Galitzki, J. Gao, C. E. Groppi, S. Hillbrand, G. C. Hilton, J. Hubmayr, K. D. Irwin, J. Klein, J. Van Lanen, D. Li, Z.-Y. Li, N. P. Lourie, H. Mani, P. G. Martin, P. Mauskopf, F. Nakamura, G. Novak, D. P. Pappas, E. Pascale, F. P. Santos, G. Savini, D. Scott, S. Stanchfield, J. N. Ullom, M. Underhill, M. R. Vissers, and D. Ward-Thompson. The next-generation BLASTPol experiment. In *Society of Photo-Optical Instrumentation Engineers (SPIE) Conference Series*, volume 9153 of *Society of Photo-Optical Instrumentation Engineers (SPIE) Conference Series*, page 0, July 2014. doi: 10.1117/12.2054419.

S. Dodelson. *Modern cosmology*. 2003.

S. Doyle. *Lumped Element Kinetic Inductance Detectors*. PhD thesis, Cardiff University, 2008.

S. Doyle, P. Mauskopf, J. Naylon, A. Porch, and C. Duncombe. Lumped Element Kinetic Inductance Detectors. *J. Low Temp. Phys.*, 151:530–536, April 2008. doi: 10.1007/s10909-007-9685-2.

R. Duan, S. McHugh, B. Serfass, B. A. Mazin, A. Merrill, S. R. Golwala, T. P. Downes, N. G. Czakon, P. K. Day, J. Gao, J. Glenn, M. I. Hollister, H. G. Leduc, P. R. Maloney, O. Noroozian, H. T. Nguyen, J. Sayers, J. A. Schlaerth, S. Siegel, J. E. Vaillancourt, A. Vayonakis, P. R. Wilson, and J. Zmuidzinas. An open-source readout for MKIDs. In *Society of Photo-Optical Instrumentation Engineers (SPIE) Conference Series*, volume 7741, July 2010. doi: 10.1117/12.856832.

D. J. Fixsen, E. S. Cheng, J. M. Gales, J. C. Mather, R. A. Shafer, and E. L. Wright. The Cosmic Microwave Background Spectrum from the Full COBE FIRAS Data Set. *ApJ*, 473:576, December 1996. doi: 10.1086/178173.

D. Flanigan. *Kinetic inductance detectors for measuring the polarization of the cosmic microwave background*. PhD thesis, Columbia University, 2018.

D. Flanigan, H. McCarrick, G. Jones, B. R. Johnson, M. H. Abitbol, P. Ade, D. Araujo, K. Bradford, R. Cantor, G. Che, P. Day, S. Doyle, C. B. Kjellstrand, H. Leduc, M. Limon, V. Luu, P. Mauskopf, A. Miller, T. Mroczkowski, C. Tucker, and J. Zmuidzinas. Photon noise from chaotic and coherent millimeter-wave sources measured with horn-coupled, aluminum lumped-element kinetic inductance detectors. *Appl. Phys. Lett.*, 108(8):083504, 2016. doi: http://dx.doi.org/10.1063/1.4942804. URL http://scitation.aip.org/content/aip/journal/apl/108/8/10.1063/1.4942804.

D. Foreman-Mackey, D. W. Hogg, D. Lang, and J. Goodman. emcee: The MCMC Hammer. *The Publications of the Astronomical Society of the Pacific*, 125:306–312, March 2013. doi: 10.1086/670067.

N. Galitzki, A. Ali, K. S. Arnold, P. C. Ashton, J. E. Austermann, C. Baccigalupi, T. Baildon, D. Barron, J. A. Beall\, S. Beckman, S. M. M. Bruno, S. Bryan, P. G. Calisse, G. E. Chesmore, Y. Chinone, S. K. Choi, G. Coppi, K. D. Crowley, K. T. Crowley, A. Cukierman, M. J. Devlin, S. Dicker, B. Dober, S. M. Duff, J. Dunkley, G. Fabbian, P. A. Gallardo, M. Gerbino, N. Goeckner-Wald, J. E. Golec, J. E. Gudmundsson, E. E. Healy, S. Henderson, C. A. Hill, G. C. Hilton, S.-P. P. Ho, L. A. Howe, J. Hubmayr, O. Jeong, B. Keating, B. J. Koopman, K. Kuichi, A. Kusaka, J. Lashner, A. T. Lee, Y. Li, M. Limon, M. Lungu, F. Matsuda, P. D. Mauskopf, A. J. May, N. McCallum, J. McMahon, F. Nati, M. D. Niemack, J. L. Orlowski-Scherer, S. C. Parshley, L. Piccirillo, M. Sathyanarayana Rao, C. Raum, M. Salatino, J. S. Seibert, C. Sierra, M. Silva-Feaver, S. M. Simon, S. T. Staggs, J. R. Stevens, A. Suzuki\, G. Teply, R. Thornton, C. Tsai, J. N. Ullom, E. M. Vavagiakis, M. R. Vissers, B. Westbrook, E. J. Wollack, Z. Xu\, and N. Zhu. The Simons Observatory: Instrument Overview. *ArXiv e-prints*, August 2018.

J. Gao. *The physics of superconducting microwave resonators.* PhD thesis, California Institute of Technology, 2008.

J. Gao, J. Zmuidzinas, B. A. Mazin, H. G. Leduc, and P. K. Day. Noise properties of superconducting coplanar waveguide microwave resonators. *Applied Physics Letters*, 90 (10):102507, March 2007. doi: 10.1063/1.2711770.

J. Gao, M. Daal, J. M. Martinis, A. Vayonakis, J. Zmuidzinas, B. Sadoulet, B. A. Mazin, P. K. Day, and H. G. Leduc. A semiempirical model for two-level system noise in superconducting microresonators. *Applied Physics Letters*, 92(21):212504, May 2008a. doi: 10.1063/1.2937855.

J. Gao, M. Daal, A. Vayonakis, S. Kumar, J. Zmuidzinas, B. Sadoulet, B. A. Mazin, P. K. Day, and H. G. Leduc. Experimental evidence for a surface distribution of two-level systems in superconducting lithographed microwave resonators. *Applied Physics Letters*, 92(15):152505, April 2008b. doi: 10.1063/1.2906373.

J. Gao, J. Zmuidzinas, A. Vayonakis, P. Day, B. Mazin, and H. Leduc. Equivalence of the effects on the complex conductivity of superconductor due to temperature change and external pair breaking. *Journal of Low Temperature Physics*, 151(1-2):557–563, 2008. ISSN 0022-2291. doi: 10.1007/s10909-007-9688-z. URL http://dx.doi.org/10.1007/s10909-007-9688-z.

E. M. George, P. Ade, K. A. Aird, J. E. Austermann, J. A. Beall, D. Becker, A. Bender, B. A. Benson, L. E. Bleem, J. Britton, J. E. Carlstrom, C. L. Chang, H. C. Chiang, H.-M. Cho, T. M. Crawford, A. T. Crites, A. Datesman, T. de Haan, M. A. Dobbs, W. Everett, A. Ewall-Wice, N. W. Halverson, N. Harrington, J. W. Henning, G. C. Hilton, W. L. Holzapfel, S. Hoover, N. Huang, J. Hubmayr, K. D. Irwin, M. Karfunkle, R. Keisler, J. Kennedy, A. T. Lee, E. Leitch, D. Li, M. Lueker, D. P. Marrone, J. J. McMahon, J. Mehl, S. S. Meyer, J. Montgomery, T. E. Montroy, J. Nagy, T. Natoli, J. P. Nibarger, M. D. Niemack, V. Novosad, S. Padin, C. Pryke, C. L. Reichardt, J. E. Ruhl, B. R. Saliwanchik, J. T. Sayre, K. K. Schaffer, E. Shirokoff, K. Story, C. Tucker, K. Vanderlinde, J. D. Vieira, G. Wang, R. Williamson, V. Yefremenko, K. W. Yoon, and E. Young. Performance and on-sky optical characterization of the SPTpol instrument. In *Society of Photo-Optical Instrumentation Engineers (SPIE) Conference Series*, volume 8452 of *Society of Photo-Optical Instrumentation Engineers (SPIE) Conference Series*, September 2012. doi: 10.1117/12.925586.

S. R. Golwala, C. Bockstiegel, S. Brugger, N. G. Czakon, P. K. Day, T. P. Downes, R. Duan, J. Gao, A. K. Gill, J. Glenn, M. I. Hollister, H. G. LeDuc, P. R. Maloney, B. A. Mazin, S. G. McHugh, D. Miller, O. Noroozian, H. T. Nguyen, J. Sayers, J. A. Schlaerth, S. Siegel, A. K. Vayonakis, P. R. Wilson, and J. Zmuidzinas. Status of MUSIC, the MUltiwavelength Sub/millimeter Inductance Camera. In *Society of Photo-Optical Instrumentation Engineers (SPIE) Conference Series*, volume 8452, Sept. 2012. doi: 10.1117/12.926055. URL http://arxiv.org/abs/1211.0595.

S. Gordon, B. Dober, A. Sinclair, S. Rowe, S. Bryan, P. Mauskopf, J. Austermann, M. Devlin, S. Dicker, J. Gao, G. C. Hilton, J. Hubmayr, G. Jones, J. Klein, N. P. Lourie,

C. McKenney, F. Nati, J. D. Soler, M. Strader, and M. Vissers. An Open Source, FPGA-Based LeKID Readout for BLAST-TNG: Pre-Flight Results. *Journal of Astronomical Instrumentation*, 5:1641003, March 2016. doi: 10.1142/S2251171716410038.

J. A. Grayson, P. A. R. Ade, Z. Ahmed, K. D. Alexander, M. Amiri, D. Barkats, S. J. Benton, C. A. Bischoff, J. J. Bock, H. Boenish, R. Bowens-Rubin, I. Buder, E. Bullock, V. Buza, J. Connors, J. P. Filippini, S. Fliescher, M. Halpern, S. Harrison, G. C. Hilton, V. V. Hristov, H. Hui, K. D. Irwin, J. Kang, K. S. Karkare, E. Karpel, S. Kefeli, S. A. Kernasovskiy, J. M. Kovac, C. L. Kuo, E. M. Leitch, M. Lueker, K. G. Megerian, V. Monticue, T. Namikawa, C. B. Netterfield, H. T. Nguyen, R. O'Brient, R. W. Ogburn, C. Pryke, C. D. Reintsema, S. Richter, R. Schwarz, C. Sorenson, C. D. Sheehy, Z. K. Staniszewski, B. Steinbach, G. P. Teply, K. L. Thompson, J. E. Tolan, C. Tucker, A. D. Turner, A. G. Vieregg, A. Wandui, A. C. Weber, D. V. Wiebe, J. Willmert, W. L. K. Wu, and K. W. Yoon. BICEP3 performance overview and planned Keck Array upgrade. In *Millimeter, Submillimeter, and Far-Infrared Detectors and Instrumentation for Astronomy VIII*, volume 9914 of *Proc. SPIE*, page 99140S, July 2016. doi: 10.1117/12.2233894.

T. Guruswamy, D. J. Goldie, and S. Withington. Quasiparticle generation efficiency in superconducting thin films. *Superconductor Science Technology*, 27(5):055012, May 2014. doi: 10.1088/0953-2048/27/5/055012.

Alan H. Guth. Inflationary universe: A possible solution to the horizon and flatness problems. *Phys. Rev. D*, 23:347–356, Jan 1981. doi: 10.1103/PhysRevD.23.347. URL https://link.aps.org/doi/10.1103/PhysRevD.23.347.

S. Hailey-Dunsheath, E. Shirokoff, P. S. Barry, C. M. Bradford, S. Chapman, G. Che, J. Glenn, M. Hollister, A. Kovács, H. G. LeDuc, P. Mauskopf, C. McKenney, R. O'Brient, S. Padin, T. Reck, C. Shiu, C. E. Tucker, J. Wheeler, R. Williamson, and J. Zmuidzinas. Low Noise Titanium Nitride KIDs for SuperSpec: A Millimeter-Wave On-Chip Spectrometer. *J. Low Temp. Phys.*, 184:180–187, July 2016. doi: 10.1007/s10909-015-1375-x.

K. Harrington, T. Marriage, A. Ali, J. W. Appel, C. L. Bennett, F. Boone, M. Brewer, M. Chan, D. T. Chuss, F. Colazo, S. Dahal, K. Denis, R. Dünner, J. Eimer, T. Essinger-Hileman, P. Fluxa, M. Halpern, G. Hilton, G. F. Hinshaw, J. Hubmayr, J. Iuliano, J. Karakla, J. McMahon, N. T. Miller, S. H. Moseley, G. Palma, L. Parker, M. Petroff, B. Pradenas, K. Rostem, M. Sagliocca, D. Valle, D. Watts, E. Wollack, Z. Xu, and L. Zeng. The Cosmology Large Angular Scale Surveyor. In *Millimeter, Submillimeter, and Far-Infrared Detectors and Instrumentation for Astronomy VIII*, volume 9914 of *Proc. SPIE*, page 99141K, July 2016. doi: 10.1117/12.2233125.

S. W. Henderson, J. R. Stevens, M. Amiri, J. Austermann, J. A. Beall, S. Chaudhuri, H.-M. Cho, S. K. Choi, N. F. Cothard, K. T. Crowley, S. M. Duff, C. P. Fitzgerald, P. A. Gallardo, M. Halpern, M. Hasselfield, G. Hilton, S.-P. P. Ho, J. Hubmayr, K. D. Irwin, B. J. Koopman, D. Li, Y. Li, J. McMahon, F. Nati, M. Niemack, C. D. Reintsema, M. Salatino, A. Schillaci, B. L. Schmitt, S. M. Simon, S. T. Staggs, E. M. Vavagiakis, and J. T. Ward. Readout of two-kilopixel transition-edge sensor arrays for Advanced ACTPol. In

Millimeter, Submillimeter, and Far-Infrared Detectors and Instrumentation for Astronomy VIII, volume 9914 of *Proc. SPIE*, page 99141G, July 2016. doi: 10.1117/12.2233895.

M. Hilton, M. Hasselfield, C. Sifón, N. Battaglia, S. Aiola, V. Bharadwaj, J. R. Bond, S. K. Choi, D. Crichton, R. Datta, M. J. Devlin, J. Dunkley, R. Dünner, P. A. Gallardo, M. Gralla, A. D. Hincks, S.-P. P. Ho, J. Hubmayr, K. M. Huffenberger, J. P. Hughes, B. J. Koopman, A. Kosowsky, T. Louis, M. S. Madhavacheril, T. A. Marriage, L. Maurin, J. McMahon, H. Miyatake, K. Moodley, S. Næss, F. Nati, L. Newburgh, M. D. Niemack, M. Oguri, L. A. Page, B. Partridge, B. L. Schmitt, J. Sievers, D. N. Spergel, S. T. Staggs, H. Trac, A. van Engelen, E. M. Vavagiakis, and E. J. Wollack. The Atacama Cosmology Telescope: The Two-season ACTPol Sunyaev-Zel'dovich Effect Selected Cluster Catalog. *ApJS*, 235:20, March 2018. doi: 10.3847/1538-4365/aaa6cb.

J. Hubmayr, J. Beall, D. Becker, H.-M. Cho, M. Devlin, B. Dober, C. Groppi, G. C. Hilton, K. D. Irwin, D. Li, P. Mauskopf, D. P. Pappas, J. Van Lanen, M. R. Vissers, Y. Wang, L. F. Wei, and J. Gao. Photon-noise limited sensitivity in titanium nitride kinetic inductance detectors. *Appl. Phys. Lett.*, 106(7):073505, February 2015. doi: 10.1063/1.4913418.

K. D. Irwin and G. C. Hilton. Transition-edge sensors. In Christian Enss, editor, *Cryogenic Particle Detection*, volume 99 of *Topics in Applied Physics*, pages 63–150. Springer Berlin Heidelberg, 2005.

R. M. J. Janssen, J. J. A. Baselmans, A. Endo, L. Ferrari, S. J. C. Yates, A. M. Baryshev, and T. M. Klapwijk. High optical efficiency and photon noise limited sensitivity of microwave kinetic inductance detectors using phase readout. *Appl. Phys. Lett.*, 103(20):203503, 2013. doi: 10.1063/1.4829657. URL http://dx.doi.org/10.1063/1.4829657.

R. M. J. Janssen, A. Endo, P. J. de Visser, T. M. Klapwijk, and J. J. A. Baselmans. Equivalence of optical and electrical noise equivalent power of hybrid nbtin-al microwave kinetic inductance detectors. *Applied Physics Letters*, 105(19):193504, 2014. doi: http://dx.doi.org/10.1063/1.4901733. URL http://scitation.aip.org/content/aip/journal/apl/105/19/10.1063/1.4901733.

B. R. Johnson, J. Collins, M. E. Abroe, P. A. R. Ade, J. Bock, J. Borrill, A. Boscaleri, P. de Bernardis, S. Hanany, A. H. Jaffe, T. Jones, A. T. Lee, L. Levinson, T. Matsumura, B. Rabii, T. Renbarger, P. L. Richards, G. F. Smoot, R. Stompor, H. T. Tran, C. D. Winant, J. H. P. Wu, and J. Zuntz. MAXIPOL: Cosmic Microwave Background Polarimetry Using a Rotating Half-Wave Plate. *ApJ*, 665:42–54, August 2007. doi: 10.1086/518105.

B. R. Johnson, P. A. R. Ade, D. Araujo, K. J. Bradford, D. Chapman, P. K. Day, J. Didier, S. Doyle, H. K. Eriksen, D. Flanigan, C. Groppi, S. Hillbrand, G. Jones, M. Limon, P. Mauskopf, H. McCarrick, A. Miller, T. Mroczkowski, B. Reichborn-Kjennerud, B. Smiley, J. Sobrin, I. K. Wehus, and J. Zmuidzinas. The Detector System for the Stratospheric Kinetic Inductance Polarimeter (SKIP). *Journal of Low Temperature Physics*, 176:741–748, September 2014. doi: 10.1007/s10909-013-1014-3.

B. R. Johnson, C. J. Vourch, T. D. Drysdale, A. Kalman, S. Fujikawa, B. Keating, and J. Kaufman. A CubeSat for Calibrating Ground-Based and Sub-Orbital Millimeter-Wave

Polarimeters (CalSat). *Journal of Astronomical Instrumentation*, 4:1550007-65, October 2015. doi: 10.1142/S2251171715500075.

B. R. Johnson, D. Flanigan, M. H. Abitbol, P. A. R. Ade, S. Bryan, H.-M. Cho, R. Datta, P. Day, S. Doyle, K. Irwin, G. Jones, S. Kernasovskiy, D. Li, P. Mauskopf, H. McCarrick, J. McMahon, A. Miller, G. Pisano, Y. Song, H. Surdi, and C. Tucker. Polarization sensitive Multi-Chroic MKIDs. In *Millimeter, Submillimeter, and Far-Infrared Detectors and Instrumentation for Astronomy VIII*, volume 9914 of *Proc. SPIE*, page 99140X, July 2016. doi: 10.1117/12.2233243.

B. R. Johnson, D. Flanigan, M. H. Abitbol, P. A. R. Ade, S. Bryan, H.-M. Cho, R. Datta, P. Day, S. Doyle, K. Irwin, G. Jones, D. Li, P. Mauskopf, H. McCarrick, J. McMahon, A. Miller, G. Pisano, Y. Song, H. Surdi, and C. Tucker. Development of Multi-chroic MKIDs for Next-Generation CMB Polarization Studies. *Journal of Low Temperature Physics*, July 2018. doi: 10.1007/s10909-018-2032-y.

G. Jones, B. R. Johnson, H. McCarrick, D. Flanigan, K. J. Bradford, A. D. Miller, M. Limon, B. Smiley, B. Kjellstrand, P. Mauskopf, G. Che, S. Bryan, and P. Day. A cryogenic millimeter wavelength test facility. In *26th International Symposium on Space Terahertz Technology*, ISSTT, 2015.

G. Jones, B. R. Johnson, M. H. Abitbol, P. A. R. Ade, S. Bryan, H.-M. Cho, P. Day, D. Flanigan, K. D. Irwin, D. Li, P. Mauskopf, H. McCarrick, A. Miller, Y. R. Song, and C. Tucker. High quality factor manganese-doped aluminum lumped-element kinetic inductance detectors sensitive to frequencies below 100 GHz. *Appl. Phys. Lett.*, 110(22): 222601, May 2017. doi: 10.1063/1.4984105.

M. E. Jones, A. C. Taylor, M. Aich, C. J. Copley, H. C. Chiang, R. J. Davis, C. Dickinson, R. D. P. Grumitt, Y. Hafez, H. M. Heilgendorff, C. M. Holler, M. O. Irfan, L. R. P. Jew, J. J. John, J. Jonas, O. G. King, J. P. Leahy, J. Leech, E. M. Leitch, S. J. C. Muchovej, T. J. Pearson, M. W. Peel, A. C. S. Readhead, J. Sievers, M. A. Stevenson, and J. Zuntz. The C-Band All-Sky Survey (C-BASS): Design and capabilities. *ArXiv e-prints*, May 2018.

M. Kamionkowski, A. Kosowsky, and A. Stebbins. Statistics of cosmic microwave background polarization. *Phys. Rev. D*, 55:7368–7388, June 1997. doi: 10.1103/PhysRevD.55.7368.

Z. D. Kermish, P. Ade, A. Anthony, K. Arnold, D. Barron, D. Boettger, J. Borrill, S. Chapman, Y. Chinone, M. A. Dobbs, J. Errard, G. Fabbian, D. Flanigan, G. Fuller, A. Ghribi, W. Grainger, N. Halverson, M. Hasegawa, K. Hattori, M. Hazumi, W. L. Holzapfel, J. Howard, P. Hyland, A. Jaffe, B. Keating, T. Kisner, A. T. Lee, M. Le Jeune, E. Linder, M. Lungu, F. Matsuda, T. Matsumura, X. Meng, N. J. Miller, H. Morii, S. Moyerman, M. J. Myers, H. Nishino, H. Paar, E. Quealy, C. L. Reichardt, P. L. Richards, C. Ross, A. Shimizu, M. Shimon, C. Shimmin, M. Sholl, P. Siritanasak, H. Spieler, N. Stebor, B. Steinbach, R. Stompor, A. Suzuki, T. Tomaru, C. Tucker, and O. Zahn. The POLARBEAR experiment. In *Society of Photo-Optical Instrumentation Engineers*

(SPIE) Conference Series, volume 8452 of *Society of Photo-Optical Instrumentation Engineers (SPIE) Conference Series*, September 2012. doi: 10.1117/12.926354. URL http://arxiv.org/abs/1210.7768.

M. S. Khalil, M. J. A. Stoutimore, F. C. Wellstood, and K. D. Osborn. An analysis method for asymmetric resonator transmission applied to superconducting devices. *Journal of Applied Physics*, 111(5):054510-054510-6, March 2012. doi: 10.1063/1.3692073.

L. Knox and Y.-S. Song. Limit on the Detectability of the Energy Scale of Inflation. *Phys. Rev. Lett.*, 89(1):011303, July 2002. doi: 10.1103/PhysRevLett.89.011303.

A. Kogut, D. N. Spergel, C. Barnes, C. L. Bennett, M. Halpern, G. Hinshaw, N. Jarosik, M. Limon, S. S. Meyer, L. Page, G. S. Tucker, E. Wollack, and E. L. Wright. First-Year Wilkinson Microwave Anisotropy Probe (WMAP) Observations: Temperature-Polarization Correlation. *ApJS*, 148:161–173, September 2003. doi: 10.1086/377219.

P. M. Korngut, S. R. Dicker, E. D. Reese, B. S. Mason, M. J. Devlin, T. Mroczkowski, C. L. Sarazin, M. Sun, and J. Sievers. MUSTANG High Angular Resolution Sunyaev-Zel'dovich Effect Imaging of Substructure in Four Galaxy Clusters. *ApJ*, 734:10, June 2011. doi: 10.1088/0004-637X/734/1/10.

A. Kosowsky and S. Bhattacharya. A future test of gravitation using galaxy cluster velocities. *Phys. Rev. D*, 80(6):062003, September 2009. doi: 10.1103/PhysRevD.80.062003.

A. Kovács, P. S. Barry, C. M. Bradford, G. Chattopadhyay, P. Day, S. Doyle, S. Hailey-Dunsheath, M. Hollister, C. McKenney, H. G. LeDuc, N. Llombart, D. P. Marrone, P. Mauskopf, R. C. O'Brient, S. Padin, L. J. Swenson, and J. Zmuidzinas. SuperSpec: design concept and circuit simulations. In *Society of Photo-Optical Instrumentation Engineers (SPIE) Conference Series*, volume 8452 of *Society of Photo-Optical Instrumentation Engineers (SPIE) Conference Series*, September 2012. doi: 10.1117/12.927160.

A. Kushino, S. Kasai, S. Kohjiro, S. Shiki, and M. Ohkubo. Development of superconducting coaxial cables for cryogenic detectors. *Journal of Low Temperature Physics*, 151(3-4):650–654, 2008. ISSN 0022-2291. doi: 10.1007/s10909-008-9721-x. URL http://dx.doi.org/10.1007/s10909-008-9721-x.

J. Lee and E. Komatsu. Bullet Cluster: A Challenge to ΛCDM Cosmology. *ApJ*, 718:60–65, July 2010. doi: 10.1088/0004-637X/718/1/60.

T. H. Lee and A Hajimiri. Oscillator phase noise: a tutorial. *Solid-State Circuits, IEEE Journal of*, 35(3):326–336, March 2000. ISSN 0018-9200. doi: 10.1109/4.826814.

Yu Chin Lim and R.A. Moore. Properties of alternately charged coplanar parallel strips by conformal mappings. *Electron Devices, IEEE Transactions on*, 15(3):173–180, Mar 1968. ISSN 0018-9383. doi: 10.1109/T-ED.1968.16156.

A. D. Linde. A new inflationary universe scenario: A possible solution of the horizon, flatness, homogeneity, isotropy and primordial monopole problems. *Physics Letters B*, 108:389–393, February 1982. doi: 10.1016/0370-2693(82)91219-9.

T. Louis, E. Grace, M. Hasselfield, M. Lungu, L. Maurin, G. E. Addison, P. A. R. Ade, S. Aiola, R. Allison, M. Amiri, E. Angile, N. Battaglia, J. A. Beall, F. de Bernardis, J. R. Bond, J. Britton, E. Calabrese, H.-m. Cho, S. K. Choi, K. Coughlin, D. Crichton, K. Crowley, R. Datta, M. J. Devlin, S. R. Dicker, J. Dunkley, R. Dünner, S. Ferraro, A. E. Fox, P. Gallardo, M. Gralla, M. Halpern, S. Henderson, J. C. Hill, G. C. Hilton, M. Hilton, A. D. Hincks, R. Hlozek, S. P. P. Ho, Z. Huang, J. Hubmayr, K. M. Huffenberger, J. P. Hughes, L. Infante, K. Irwin, S. Muya Kasanda, J. Klein, B. Koopman, A. Kosowsky, D. Li, M. Madhavacheril, T. A. Marriage, J. McMahon, F. Menanteau, K. Moodley, C. Munson, S. Naess, F. Nati, L. Newburgh, J. Nibarger, M. D. Niemack, M. R. Nolta, C. Nuñez, L. A. Page, C. Pappas, B. Partridge, F. Rojas, E. Schaan, B. L. Schmitt, N. Sehgal, B. D. Sherwin, J. Sievers, S. Simon, D. N. Spergel, S. T. Staggs, E. R. Switzer, R. Thornton, H. Trac, J. Treu, C. Tucker, A. Van Engelen, J. T. Ward, and E. J. Wollack. The Atacama Cosmology Telescope: two-season ACTPol spectra and parameters. *J. Cosmology Astropart. Phys.*, 6:031, June 2017. doi: 10.1088/1475-7516/2017/06/031.

J. F. Macias-Pérez, R. Adam, P. Ade, P. André, M. Arnaud., H. Aussel, I. Bartalucci, A. Beelen, A. Benoit, A. Bideaud, O. Bourrion, M. Calvo, A. Catalano, B. Comis, F. X. Désert, S. Doyle, E. F. C. Driessen, J. Goupy, C. Kramer, G. Lagache, S. Leclercq, J. F. Lestrade, P. D. Mauskopf, F. Mayet, A. Monfardini, L. Perotto, E. Pointecouteau, G. Pisano, N. Ponthieu, G. W. Pratt, V. Revéret, A. Ritacco, C. Romero, H. Roussel, F. Ruppin, K. Schuster, A. Sievers, C. Tucker, R. Zylka, and M. De Petris. NIKA2: a mm camera for cluster cosmology. In *Proceedings of the European Physical Society Conference on High Energy Physics. 5-12 July, 2017 Venice, Italy (EPS-HEP2017). Online at ¡A href="http://pos.sissa.it/cgi-bin/reader/conf.cgi?confid=314"¿http://pos.sissa.it/cgi-bin/reader/conf.cgi?confid=314¡/A¿, id.42*, page 42, July 2017.

J. C. Mather, D. J. Fixsen, R. A. Shafer, C. Mosier, and D. T. Wilkinson. Calibrator Design for the COBE Far-Infrared Absolute Spectrophotometer (FIRAS). *ApJ*, 512:511–520, February 1999. doi: 10.1086/306805.

D. C. Mattis and J. Bardeen. Theory of the anomalous skin effect in normal and superconducting metals. *Phys. Rev.*, 111:412–417, Jul 1958. doi: 10.1103/PhysRev.111.412. URL https://link.aps.org/doi/10.1103/PhysRev.111.412.

P. D. Mauskopf, S. Doyle, P. Barry, S. Rowe, A. Bidead, P. A. R. Ade, C. Tucker, E. Castillo, A. Monfardini, J. Goupy, and M. Calvo. Photon-Noise Limited Performance in Aluminum LEKIDs. *J. Low Temp. Phys.*, 176:545–552, August 2014. doi: 10.1007/s10909-013-1069-1.

B. A. Mazin, S. R. Meeker, M. J. Strader, P. Szypryt, D. Marsden, J. C. van Eyken, G. E. Duggan, A. B. Walter, G. Ulbricht, M. Johnson, B. Bumble, K. O'Brien, and C. Stoughton. ARCONS: A 2024 Pixel Optical through Near-IR Cryogenic Imaging Spectrophotometer. *PASP*, 125:1348–1361, November 2013. doi: 10.1086/674013.

H. McCarrick, D. Flanigan, G. Jones, B. R. Johnson, P. Ade, D. Araujo, K. Bradford, R. Cantor, G. Che, P. Day, S. Doyle, H. Leduc, M. Limon, V. Luu, P. Mauskopf, A. Miller, T. Mroczkowski, C. Tucker, and J. Zmuidzinas. Horn-coupled, commercially-fabricated

aluminum lumped-element kinetic inductance detectors for millimeter wavelengths. *Rev. Sci. Instrum.*, 85(12):123117, December 2014. doi: 10.1063/1.4903855.

H. McCarrick, M. H. Abitbol, P. A. R. Ade, P. Barry, S. Bryan, G. Che, P. Day, S. Doyle, D. Flanigan, B. R. Johnson, G. Jones, H. G. LeDuc, M. Limon, P. Mauskopf, A. Miller, C. Tucker, and J. Zmuidzinas. Development of dual-polarization LEKIDs for CMB observations. In *Millimeter, Submillimeter, and Far-Infrared Detectors and Instrumentation for Astronomy VIII*, volume 9914 of *Proc. SPIE*, page 99140O, July 2016a. doi: 10.1117/12.2231830.

H. McCarrick, D. Flanigan, G. Jones, B. R. Johnson, P. A. R. Ade, K. Bradford, S. Bryan, R. Cantor, G. Che, P. Day, S. Doyle, H. Leduc, M. Limon, P. Mauskopf, A. Miller, T. Mroczkowski, C. Tucker, and J. Zmuidzinas. A titanium nitride absorber for controlling optical crosstalk in horn-coupled aluminum lekid arrays for millimeter wavelengths. *Journal of Low Temperature Physics*, 184(1):154–160, July 2016b. doi: 10.1007/s10909-015-1424-5. URL http://dx.doi.org/10.1007/s10909-015-1424-5.

H. McCarrick, G. Jones, B. R. Johnson, M. H. Abitbol, P. A. R. Ade, S. Bryan, P. Day, T. Essinger-Hileman, D. Flanigan, H. G. Leduc, M. Limon, P. Mauskopf, A. Miller, and C. Tucker. Design and performance of dual-polarization lumped-element kinetic inductance detectors for millimeter-wave polarimetry. *A&A*, 610:A45, February 2018. doi: 10.1051/0004-6361/201732044.

S. McHugh, B. A. Mazin, B. Serfass, S. Meeker, K. O'Brien, R. Duan, R. Raffanti, and D. Werthimer. A readout for large arrays of microwave kinetic inductance detectors. *Review of Scientific Instruments*, 83(4):044702, April 2012. doi: 10.1063/1.3700812.

C. McKenney, H. G. Leduc, L. J. Swenson, P. K Day, B. H. Eom, and J. Zmuidzinas. Design considerations for a background limited 350 micron pixel array using lumped element superconducting microresonators. In *Society of Photo-Optical Instrumentation Engineers (SPIE) Conference Series*, volume 8452, pages 84520S–84520S–10, July 2012. doi: 10.1117/12.925759. URL http://dx.doi.org/10.1117/12.925759.

R. Meservey and P. M. Tedrow. Properties of very thin aluminum films. *Journal of Applied Physics*, 42(1):51–53, 1971. URL http://scitation.aip.org/content/aip/journal/jap/42/1/10.1063/1.1659648.

A. Monfardini, A. Benoit, A. Bideaud, L. Swenson, A. Cruciani, P. Camus, C. Hoffmann, F. X. Désert, S. Doyle, P. Ade, P. Mauskopf, C. Tucker, M. Roesch, S. Leclercq, K. F. Schuster, A. Endo, A. Baryshev, J. J. A. Baselmans, L. Ferrari, S. J. C. Yates, O. Bourrion, J. Macias-Perez, C. Vescovi, M. Calvo, and C. Giordano. A Dual-band Millimeter-wave Kinetic Inductance Camera for the IRAM 30 m Telescope. *ApJS*, 194:24, June 2011. doi: 10.1088/0067-0049/194/2/24.

T. Mroczkowski, S. Dicker, J. Sayers, E. D. Reese, B. Mason, N. Czakon, C. Romero, A. Young, M. Devlin, S. Golwala, P. Korngut, C. Sarazin, J. Bock, P. M. Koch, K.-Y. Lin, S. M. Molnar, E. Pierpaoli, K. Umetsu, and M. Zemcov. A Multi-wavelength Study of the

Sunyaev-Zel'dovich Effect in the Triple-merger Cluster MACS J0717.5+3745 with MUSTANG and Bolocam. *ApJ*, 761:47, December 2012. doi: 10.1088/0004-637X/761/1/47.

M. D. Niemack, P. A. R. Ade, J. Aguirre, F. Barrientos, J. A. Beall, J. R. Bond, J. Britton, H. M. Cho, S. Das, M. J. Devlin, S. Dicker, J. Dunkley, R. Dünner, J. W. Fowler, A. Hajian, M. Halpern, M. Hasselfield, G. C. Hilton, M. Hilton, J. Hubmayr, J. P. Hughes, L. Infante, K. D. Irwin, N. Jarosik, J. Klein, A. Kosowsky, T. A. Marriage, J. McMahon, F. Menanteau, K. Moodley, J. P. Nibarger, M. R. Nolta, L. A. Page, B. Partridge, E. D. Reese, J. Sievers, D. N. Spergel, S. T. Staggs, R. Thornton, C. Tucker, E. Wollack, and K. W. Yoon. ACTPol: a polarization-sensitive receiver for the Atacama Cosmology Telescope. In *Society of Photo-Optical Instrumentation Engineers (SPIE) Conference Series*, volume 7741 of *Society of Photo-Optical Instrumentation Engineers (SPIE) Conference Series*, July 2010. doi: 10.1117/12.857464.

O. Noroozian. *Superconducting Microwave Resonator Arrays for Submillimeter/Far-Infrared Imaging*. PhD thesis, California Institute of Technology, 2012.

O. Noroozian, J. Gao, J. Zmuidzinas, H. G. LeDuc, and B. A. Mazin. Two-level system noise reduction for Microwave Kinetic Inductance Detectors. In B. Young, B. Cabrera, and A. Miller, editors, *AIP Conf. Proc.*, volume 1185, pages 148–151, December 2009. doi: 10.1063/1.3292302.

O. Noroozian, P. K. Day, B. H. Eom, H. G. Leduc, and J. Zmuidzinas. Crosstalk reduction for superconducting microwave resonator arrays. *IEEE Transactions on Microwave Theory and Techniques*, 60(5):1235–1243, May 2012. ISSN 0018-9480. doi: 10.1109/TMTT.2012.2187538.

R W IV Ogburn, Peter A R Ade, R W Aikin, M Amiri, S J Benton, James J Appleton Philip Bock, J A Bonetti, J A Brevik, B Burger, C D Dowell, L Duband, J P Filippini, Sunil R Golwala, M Halpern, M Hasselfield, Gene C Hilton, V V Hristov, Kent D Irwin, J P Kaufman, B G Keating, John M Kovac, C L Kuo, Andrew E Lange, E M Leitch, C B Netterfield, Hien T Nguyen, A Orlando, C L Pryke, C Reintsema, S Richter, John E Ruhl, M C Runyan, C D Sheehy, Z K Staniszewski, S A Stokes, R V Sudiwala, G P Teply, J E Tolan, Anthony D Turner, P Wilson, and C L Wong. The BICEP2 CMB polarization experiment. *Millimeter*, 7741:40, July 2010.

A. Patel, A. Brown, W. Hsieh, T. Stevenson, S.H. Moseley, K. U-yen, N. Ehsan, E. Barrentine, G. Manos, and E.J. Wollack. Fabrication of mkids for the microspec spectrometer. *Applied Superconductivity, IEEE Transactions on*, 23(3):2400404–2400404, June 2013. ISSN 1051-8223. doi: 10.1109/TASC.2013.2240152.

A. A. Penzias and R. W. Wilson. A Measurement of Excess Antenna Temperature at 4080 Mc/s. *ApJ*, 142:419–421, July 1965. doi: 10.1086/148307.

S. Perlmutter, G. Aldering, G. Goldhaber, R. A. Knop, P. Nugent, P. G. Castro, S. Deustua, S. Fabbro, A. Goobar, D. E. Groom, I. M. Hook, A. G. Kim, M. Y. Kim, J. C. Lee, N. J. Nunes, R. Pain, C. R. Pennypacker, R. Quimby, C. Lidman, R. S. Ellis, M. Irwin,

R. G. McMahon, P. Ruiz-Lapuente, N. Walton, B. Schaefer, B. J. Boyle, A. V. Filippenko, T. Matheson, A. S. Fruchter, N. Panagia, H. J. M. Newberg, W. J. Couch, and T. S. C. Project. Measurements of Ω and Λ from 42 High-Redshift Supernovae. *ApJ*, 517:565–586, June 1999. doi: 10.1086/307221.

J. B. Peterson and P. L. Richards. A Cryogenic Blackbody for Millimeter Wavelengths. *Inernational Journal of Infared and Millimeter Waves*, 5(12):1507–1515, Nov. 1984.

Planck Collaboration, R. Adam, P. A. R. Ade, N. Aghanim, Y. Akrami, M. I. R. Alves, F. Argüeso, M. Arnaud, F. Arroja, M. Ashdown, and et al. Planck 2015 results. I. Overview of products and scientific results. *A&A*, 594:A1, September 2016a. doi: 10.1051/0004-6361/201527101.

Planck Collaboration, P. A. R. Ade, N. Aghanim, M. Arnaud, M. Ashdown, J. Aumont, C. Baccigalupi, A. J. Banday, R. B. Barreiro, R. Barrena, and et al. Planck 2015 results. XXVII. The second Planck catalogue of Sunyaev-Zeldovich sources. *A&A*, 594:A27, September 2016b. doi: 10.1051/0004-6361/201525823.

Planck Collaboration, N. Aghanim, Y. Akrami, M. Ashdown, J. Aumont, C. Baccigalupi, M. Ballardini, A. J. Banday, R. B. Barreiro, N. Bartolo, S. Basak, R. Battye, K. Benabed, J.-P. Bernard, M. Bersanelli, P. Bielewicz, J. J. Bock, J. R. Bond, J. Borrill, F. R. Bouchet, F. Boulanger, M. Bucher, C. Burigana, R. C. Butler, E. Calabrese, J.-F. Cardoso, J. Carron, A. Challinor, H. C. Chiang, J. Chluba, L. P. L. Colombo, C. Combet, D. Contreras, B. P. Crill, F. Cuttaia, P. de Bernardis, G. de Zotti, J. Delabrouille, J.-M. Delouis, E. Di Valentino, J. M. Diego, O. Doré, M. Douspis, A. Ducout, X. Dupac, S. Dusini, G. Efstathiou, F. Elsner, T. A. Enßlin, H. K. Eriksen, Y. Fantaye, M. Farhang, J. Fergusson, R. Fernandez-Cobos, F. Finelli, F. Forastieri, M. Frailis, E. Franceschi, A. Frolov, S. Galeotta, S. Galli, K. Ganga, R. T. Génova-Santos, M. Gerbino, T. Ghosh, J. González-Nuevo, K. M. Górski, S. Gratton, A. Gruppuso, J. E. Gudmundsson, J. Hamann, W. Handley, D. Herranz, E. Hivon, Z. Huang, A. H. Jaffe, W. C. Jones, A. Karakci, E. Keihänen, R. Keskitalo, K. Kiiveri, J. Kim, T. S. Kisner, L. Knox, N. Krachmalnicoff, M. Kunz, H. Kurki-Suonio, G. Lagache, J.-M. Lamarre, A. Lasenby, M. Lattanzi, C. R. Lawrence, M. Le Jeune, P. Lemos, J. Lesgourgues, F. Levrier, A. Lewis, M. Liguori, P. B. Lilje, M. Lilley, V. Lindholm, M. López-Caniego, P. M. Lubin, Y.-Z. Ma, J. F. Macías-Pérez, G. Maggio, D. Maino, N. Mandolesi, A. Mangilli, A. Marcos-Caballero, M. Maris, P. G. Martin, M. Martinelli, E. Martínez-González, S. Matarrese, N. Mauri, J. D. McEwen, P. R. Meinhold, A. Melchiorri, A. Mennella, M. Migliaccio, M. Millea, S. Mitra, M.-A. Miville-Deschênes, D. Molinari, L. Montier, G. Morgante, A. Moss, P. Natoli, H. U. Nørgaard-Nielsen, L. Pagano, D. Paoletti, B. Partridge, G. Patanchon, H. V. Peiris, F. Perrotta, V. Pettorino, F. Piacentini, L. Polastri, G. Polenta, J.-L. Puget, J. P. Rachen, M. Reinecke, M. Remazeilles, A. Renzi, G. Rocha, C. Rosset, G. Roudier, J. A. Rubiño-Martín, B. Ruiz-Granados, L. Salvati, M. Sandri, M. Savelainen, D. Scott, E. P. S. Shellard, C. Sirignano, G. Sirri, L. D. Spencer, R. Sunyaev, A.-S. Suur-Uski, J. A. Tauber, D. Tavagnacco, M. Tenti, L. Toffolatti, M. Tomasi, T. Trombetti, L. Valenziano, J. Valiviita, B. Van Tent, L. Vibert, P. Vielva, F. Villa, N. Vittorio, B. D. Wandelt, I. K. Wehus, M. White, S. D. M.

White, A. Zacchei, and A. Zonca. Planck 2018 results. VI. Cosmological parameters. *ArXiv e-prints*, July 2018a.

Planck Collaboration, Y. Akrami, F. Arroja, M. Ashdown, J. Aumont, C. Baccigalupi, M. Ballardini, A. J. Banday, R. B. Barreiro, N. Bartolo, S. Basak, R. Battye, K. Benabed, J.-P. Bernard, M. Bersanelli, P. Bielewicz, J. J. Bock, J. R. Bond, J. Borrill, F. R. Bouchet, F. Boulanger, M. Bucher, C. Burigana, R. C. Butler, E. Calabrese, J.-F. Cardoso, J. Carron, B. Casaponsa, A. Challinor, H. C. Chiang, L. P. L. Colombo, C. Combet, D. Contreras, B. P. Crill, F. Cuttaia, P. de Bernardis, G. de Zotti, J. Delabrouille, J.-M. Delouis, F.-X. Désert, E. Di Valentino, C. Dickinson, J. M. Diego, S. Donzelli, O. Doré, M. Douspis, A. Ducout, X. Dupac, G. Efstathiou, F. Elsner, T. A. Enßlin, H. K. Eriksen, E. Falgarone, Y. Fantaye, J. Fergusson, R. Fernandez-Cobos, F. Finelli, F. Forastieri, M. Frailis, E. Franceschi, A. Frolov, S. Galeotta, S. Galli, K. Ganga, R. T. Génova-Santos, M. Gerbino, T. Ghosh, J. González-Nuevo, K. M. Górski, S. Gratton, A. Gruppuso, J. E. Gudmundsson, J. Hamann, W. Handley, F. K. Hansen, G. Helou, D. Herranz, E. Hivon, Z. Huang, A. H. Jaffe, W. C. Jones, A. Karakci, E. Keihänen, R. Keskitalo, K. Kiiveri, J. Kim, T. S. Kisner, L. Knox, N. Krachmalnicoff, M. Kunz, H. Kurki-Suonio, G. Lagache, J.-M. Lamarre, M. Langer, A. Lasenby, M. Lattanzi, C. R. Lawrence, M. Le Jeune, J. P. Leahy, J. Lesgourgues, F. Levrier, A. Lewis, M. Liguori, P. B. Lilje, M. Lilley, V. Lindholm, M. López-Caniego, P. M. Lubin, Y.-Z. Ma, J. F. Macías-Pérez, G. Maggio, D. Maino, N. Mandolesi, A. Mangilli, A. Marcos-Caballero, M. Maris, P. G. Martin, E. Martínez-González, S. Matarrese, N. Mauri, J. D. McEwen, P. D. Meerburg, P. R. Meinhold, A. Melchiorri, A. Mennella, M. Migliaccio, M. Millea, S. Mitra, M.-A. Miville-Deschênes, D. Molinari, A. Moneti, L. Montier, G. Morgante, A. Moss, S. Mottet, M. Münchmeyer, P. Natoli, H. U. Nørgaard-Nielsen, C. A. Oxborrow, L. Pagano, D. Paoletti, B. Partridge, G. Patanchon, T. J. Pearson, M. Peel, H. V. Peiris, F. Perrotta, V. Pettorino, F. Piacentini, L. Polastri, G. Polenta, J.-L. Puget, J. P. Rachen, M. Reinecke, M. Remazeilles, A. Renzi, G. Rocha, C. Rosset, G. Roudier, J. A. Rubiño-Martín, B. Ruiz-Granados, L. Salvati, M. Sandri, M. Savelainen, D. Scott, E. P. S. Shellard, M. Shiraishi, C. Sirignano, G. Sirri, L. D. Spencer, R. Sunyaev, A.-S. Suur-Uski, J. A. Tauber, D. Tavagnacco, M. Tenti, L. Terenzi, L. Toffolatti, M. Tomasi, T. Trombetti, J. Valiviita, B. Van Tent, L. Vibert, P. Vielva, F. Villa, N. Vittorio, B. D. Wandelt, I. K. Wehus, M. White, S. D. M. White, A. Zacchei, and A. Zonca. Planck 2018 results. I. Overview and the cosmological legacy of Planck. *ArXiv e-prints*, July 2018b.

Planck Collaboration, Y. Akrami, F. Arroja, M. Ashdown, J. Aumont, C. Baccigalupi, M. Ballardini, A. J. Banday, R. B. Barreiro, N. Bartolo, S. Basak, K. Benabed, J.-P. Bernard, M. Bersanelli, P. Bielewicz, J. J. Bock, J. R. Bond, J. Borrill, F. R. Bouchet, F. Boulanger, M. Bucher, C. Burigana, R. C. Butler, E. Calabrese, J.-F. Cardoso, J. Carron, A. Challinor, H. C. Chiang, L. P. L. Colombo, C. Combet, D. Contreras, B. P. Crill, F. Cuttaia, P. de Bernardis, G. de Zotti, J. Delabrouille, J.-M. Delouis, E. Di Valentino, J. M. Diego, S. Donzelli, O. Doré, M. Douspis, A. Ducout, X. Dupac, S. Dusini, G. Efstathiou, F. Elsner, T. A. Enßlin, H. K. Eriksen, Y. Fantaye, J. Fergusson, R. Fernandez-Cobos, F. Finelli, F. Forastieri, M. Frailis, E. Franceschi, A. Frolov, S. Galeotta, S. Galli, K. Ganga, C. Gauthier, R. T. Génova-Santos, M. Gerbino, T. Ghosh, J. González-Nuevo,

K. M. Górski, S. Gratton, A. Gruppuso, J. E. Gudmundsson, J. Hamann, W. Handley, F. K. Hansen, D. Herranz, E. Hivon, D. C. Hooper, Z. Huang, A. H. Jaffe, W. C. Jones, E. Keihänen, R. Keskitalo, K. Kiiveri, J. Kim, T. S. Kisner, N. Krachmalnicoff, M. Kunz, H. Kurki-Suonio, G. Lagache, J.-M. Lamarre, A. Lasenby, M. Lattanzi, C. R. Lawrence, M. Le Jeune, J. Lesgourgues, F. Levrier, A. Lewis, M. Liguori, P. B. Lilje, V. Lindholm, M. Lpez-Caniego, P. M. Lubin, Y.-Z. Ma, J. F. Macías-Pérez, G. Maggio, D. Maino, N. Mandolesi, A. Mangilli, A. Marcos-Caballero, M. Maris, P. G. Martin, E. Martínez-González, S. Matarrese, N. Mauri, J. D. McEwen, P. D. Meerburg, P. R. Meinhold, A. Melchiorri, A. Mennella, M. Migliaccio, S. Mitra, M.-A. Miville-Deschênes, D. Molinari, A. Moneti, L. Montier, G. Morgante, A. Moss, M. Münchmeyer, P. Natoli, H. U. Nørgaard-Nielsen, L. Pagano, D. Paoletti, B. Partridge, G. Patanchon, H. V. Peiris, F. Perrotta, V. Pettorino, F. Piacentini, L. Polastri, G. Polenta, J.-L. Puget, J. P. Rachen, M. Reinecke, M. Remazeilles, A. Renzi, G. Rocha, C. Rosset, G. Roudier, J. A. Rubiño-Martín, B. Ruiz-Granados, L. Salvati, M. Sandri, M. Savelainen, D. Scott, E. P. S. Shellard, M. Shiraishi, C. Sirignano, G. Sirri, L. D. Spencer, R. Sunyaev, A.-S. Suur-Uski, J. A. Tauber, D. Tavagnacco, M. Tenti, L. Toffolatti, M. Tomasi, T. Trombetti, J. Valiviita, B. Van Tent, P. Vielva, F. Villa, N. Vittorio, B. D. Wandelt, I. K. Wehus, S. D. M. White, A. Zacchei, J. P. Zibin, and A. Zonca. Planck 2018 results. X. Constraints on inflation. *ArXiv e-prints*, July 2018c.

C. M. Posada, P. A. R. Ade, A. J. Anderson, J. Avva, Z. Ahmed, K. S. Arnold, J. Austermann, A. N. Bender, B. A. Benson, L. Bleem, K. Byrum, J. E. Carlstrom, F. W. Carter, C. Chang, H.-M. Cho, A. Cukierman, D. A. Czaplewski, J. Ding, R. N. S. Divan, T. de Haan, M. Dobbs, D. Dutcher, W. Everett, R. N. Gannon, R. J. Guyser, N. W. Halverson, N. L. Harrington, K. Hattori, J. W. Henning, G. C. Hilton, W. L. Holzapfel, N. Huang, K. D. Irwin, O. Jeong, T. Khaire, M. Korman, D. L. Kubik, C.-L. Kuo, A. T. Lee, E. M. Leitch, S. Lendinez Escudero, S. S. Meyer, C. S. Miller, J. Montgomery, A. Nadolski, T. J. Natoli, H. Nguyen, V. Novosad, S. Padin, Z. Pan, J. E. Pearson, A. Rahlin, C. L. Reichardt, J. E. Ruhl, B. Saliwanchik, I. Shirley, J. T. Sayre, J. A. Shariff, E. D. Shirokoff, L. Stan, A. A. Stark, J. Sobrin, K. Story, A. Suzuki, Q. Y. Tang, R. B. Thakur, K. L. Thompson, C. E. Tucker, K. Vanderlinde, J. D. Vieira, G. Wang, N. Whitehorn, V. Yefremenko, and K. W. Yoon. Large arrays of dual-polarized multichroic TES detectors for CMB measurements with the SPT-3G receiver. In *Millimeter, Submillimeter, and Far-Infrared Detectors and Instrumentation for Astronomy VIII*, volume 9914 of *Proc. SPIE*, page 991417, July 2016. doi: 10.1117/12.2232912.

B. Reichborn-Kjennerud, A. M. Aboobaker, P. Ade, F. Aubin, C. Baccigalupi, C. Bao, J. Borrill, C. Cantalupo, D. Chapman, J. Didier, M. Dobbs, J. Grain, W. Grainger, S. Hanany, S. Hillbrand, J. Hubmayr, A. Jaffe, B. Johnson, T. Jones, T. Kisner, J. Klein, A. Korotkov, S. Leach, A. Lee, L. Levinson, M. Limon, K. MacDermid, T. Matsumura, X. Meng, A. Miller, M. Milligan, E. Pascale, D. Polsgrove, N. Ponthieu, K. Raach, I. Sagiv, G. Smecher, F. Stivoli, R. Stompor, H. Tran, M. Tristram, G. S. Tucker, Y. Vinokurov, A. Yadav, M. Zaldarriaga, and K. Zilic. EBEX: a balloon-borne CMB polarization experiment. In *Millimeter, Submillimeter, and Far-Infrared Detectors and Instru-*

mentation for Astronomy V, volume 7741 of *Proc. SPIE*, page 77411C, July 2010. doi: 10.1117/12.857138.

A. G. Riess, A. V. Filippenko, P. Challis, A. Clocchiatti, A. Diercks, P. M. Garnavich, R. L. Gilliland, C. J. Hogan, S. Jha, R. P. Kirshner, B. Leibundgut, M. M. Phillips, D. Reiss, B. P. Schmidt, R. A. Schommer, R. C. Smith, J. Spyromilio, C. Stubbs, N. B. Suntzeff, and J. Tonry. Observational Evidence from Supernovae for an Accelerating Universe and a Cosmological Constant. *AJ*, 116:1009–1038, September 1998. doi: 10.1086/300499.

J. Sayers, T. Mroczkowski, M. Zemcov, P. M. Korngut, J. Bock, E. Bulbul, N. G. Czakon, E. Egami, S. R. Golwala, P. M. Koch, K.-Y. Lin, A. Mantz, S. M. Molnar, L. Moustakas, E. Pierpaoli, T. D. Rawle, E. D. Reese, M. Rex, J. A. Shitanishi, S. Siegel, and K. Umetsu. A Measurement of the Kinetic Sunyaev-Zel'dovich Signal Toward MACS J0717.5+3745. *ApJ*, 778:52, November 2013. doi: 10.1088/0004-637X/778/1/52.

Daniel Schwan, Peter A R Ade, Kaustuv Basu, Amy N Bender, F Bertoldi, Hsiao-Mei Cho, G Chon, John Clarke, Matt A Dobbs, Daniel Ferrusca, R Guesten, Nils W Halverson, William L Holzapfel, Cathy Horellou, D Johansson, Bradley R Johnson, James Kennedy, Zigmund Kermish, R Kneissl, T M Lanting, Adrian T Lee, Martin Lueker, Jared Mehl, K M Menten, Dirk Muders, Florian Pacaud, Tom Plagge, Christian L Reichardt, Paul L Richards, R Schaaf, P Schilke, M W Sommer, Helmuth G Spieler, C Tucker, A Weiss, Benjamin Westbrook, and O Zahn. Invited Article: Millimeter-wave bolometer array receiver for the Atacama pathfinder experiment Sunyaev-Zel'dovich (APEX-SZ) instrument. *Review of Scientific Instruments*, 82(9), September 2011.

U. Seljak and M. Zaldarriaga. Signature of Gravity Waves in the Polarization of the Microwave Background. *Phys. Rev. Lett.*, 78:2054–2057, March 1997. doi: 10.1103/PhysRevLett.78.2054.

E. Shirokoff, P.S. Barry, C.M. Bradford, G. Chattopadhyay, P. Day, S. Doyle, S. Hailey-Dunsheath, M.I. Hollister, A. Kovács, H.G. Leduc, C.M. McKenney, P. Mauskopf, H.T. Nguyen, R. O'Brient, S. Padin, T.J. Reck, L.J. Swenson, C.E. Tucker, and J. Zmuidzinas. Design and performance of superspec: An on-chip, kid-based, mm-wavelength spectrometer. *Journal of Low Temperature Physics*, 176(5-6):657–662, 2014. ISSN 0022-2291. doi: 10.1007/s10909-014-1122-8. URL http://dx.doi.org/10.1007/s10909-014-1122-8.

J. Silk. Cosmic Black-Body Radiation and Galaxy Formation. *ApJ*, 151:459, February 1968. doi: 10.1086/149449.

G. Simard, Y. Omori, K. Aylor, E. J. Baxter, B. A. Benson, L. E. Bleem, J. E. Carlstrom, C. L. Chang, H.-M. Cho, R. Chown, T. M. Crawford, A. T. Crites, T. de Haan, M. A. Dobbs, W. B. Everett, E. M. George, N. W. Halverson, N. L. Harrington, J. W. Henning, G. P. Holder, Z. Hou, W. L. Holzapfel, J. D. Hrubes, L. Knox, A. T. Lee, E. M. Leitch, D. Luong-Van, A. Manzotti, J. J. McMahon, S. S. Meyer, L. M. Mocanu, J. J. Mohr, T. Natoli, S. Padin, C. Pryke, C. L. Reichardt, J. E. Ruhl, J. T. Sayre, K. K. Schaffer, E. Shirokoff, Z. Staniszewski, A. A. Stark, K. T. Story, K. Vanderlinde, J. D. Vieira, R. Williamson, and W. L. K. Wu. Constraints on Cosmological Parameters from the

Angular Power Spectrum of a Combined 2500 deg^2 SPT-SZ and Planck Gravitational Lensing Map. *ApJ*, 860:137, June 2018. doi: 10.3847/1538-4357/aac264.

Simons Observatory Collaboration. The Simons Observatory: Science goals and forecasts. *ArXiv e-prints*, August 2018. URL https://arxiv.org/abs/1808.07445.

G. F. Smoot, C. L. Bennett, A. Kogut, E. L. Wright, J. Aymon, N. W. Boggess, E. S. Cheng, G. de Amici, S. Gulkis, M. G. Hauser, G. Hinshaw, P. D. Jackson, M. Janssen, E. Kaita, T. Kelsall, P. Keegstra, C. Lineweaver, K. Loewenstein, P. Lubin, J. Mather, S. S. Meyer, S. H. Moseley, T. Murdock, L. Rokke, R. F. Silverberg, L. Tenorio, R. Weiss, and D. T. Wilkinson. Structure in the COBE differential microwave radiometer first-year maps. *ApJ*, 396:L1–L5, September 1992. doi: 10.1086/186504.

D. N. Spergel, L. Verde, H. V. Peiris, E. Komatsu, M. R. Nolta, C. L. Bennett, M. Halpern, G. Hinshaw, N. Jarosik, A. Kogut, M. Limon, S. S. Meyer, L. Page, G. S. Tucker, J. L. Weiland, E. Wollack, and E. L. Wright. First-Year Wilkinson Microwave Anisotropy Probe (WMAP) Observations: Determination of Cosmological Parameters. *ApJS*, 148:175–194, September 2003. doi: 10.1086/377226.

G. J. Stacey, M. A. K. Basu, N. Battaglia, B. Beringue, F. Bertoldi, J. R. Bond, P. Breysse, R. Bustos, S. Chapman, D. T. Chung, N. Cothard, J. Erler, M. Fich, S. Foreman, P. Gallardo, R. Giovanelli, U. U. Graf, M. P. Haynes, R. Herrera-Camus, T. L. Herter, R. Hložek, D. Johnstone, L. Keating, B. Magnelli, D. Meerburg, J. Meyers, N. Murray, M. Niemack, T. Nikola, M. Nolta, S. C. Parshley, D. Riechers, P. Schilke, D. Scott, G. Stein, J. Stevens, J. Stutzki, E. M. Vavagiakis, and M. P. Viero. CCAT-prime: Science with an Ultra-widefield Submillimeter Observatory at Cerro Chajnantor. *ArXiv e-prints*, July 2018.

A. A. Starobinskii. Spectrum of relict gravitational radiation and the early state of the universe. *ZhETF Pisma Redaktsiiu*, 30:719–723, December 1979.

N. Stebor, P. Ade, Y. Akiba, C. Aleman, K. Arnold, C. Baccigalupi, B. Barch, D. Barron, S. Beckman, A. Bender, D. Boettger, J. Borrill, S. Chapman, Y. Chinone, A. Cukierman, T. de Haan, M. Dobbs, A. Ducout, R. Dunner, T. Elleflot, J. Errard, G. Fabbian, S. Feeney, C. Feng, T. Fujino, G. Fuller, A. J. Gilbert, N. Goeckner-Wald, J. Groh, G. Hall, N. Halverson, T. Hamada, M. Hasegawa, K. Hattori, M. Hazumi, C. Hill, W. L. Holzapfel, Y. Hori, L. Howe, Y. Inoue, F. Irie, G. Jaehnig, A. Jaffe, O. Jeong, N. Katayama, J. P. Kaufman, K. Kazemzadeh, B. G. Keating, Z. Kermish, R. Keskitalo, T. Kisner, A. Kusaka, M. Le Jeune, A. T. Lee, D. Leon, E. V. Linder, L. Lowry, F. Matsuda, T. Matsumura, N. Miller, J. Montgomery, M. Navaroli, H. Nishino, H. Paar, J. Peloton, D. Poletti, G. Puglisi, C. R. Raum, G. M. Rebeiz, C. L. Reichardt, P. L. Richards, C. Ross, K. M. Rotermund, Y. Segawa, B. D. Sherwin, I. Shirley, P. Siritanasak, L. Steinmetz, R. Stompor, A. Suzuki, O. Tajima, S. Takada, S. Takatori, G. P. Teply, A. Tikhomirov, T. Tomaru, B. Westbrook, N. Whitehorn, A. Zahn, and O. Zahn. The Simons Array CMB polarization experiment. In *Millimeter, Submillimeter, and Far-Infrared Detectors and Instrumentation for Astronomy VIII*, volume 9914 of *Proc. SPIE*, page 99141H, July 2016. doi: 10.1117/12.2233103.

B. A. Steinbach, J. J. Bock, H. T. Nguyen, R. C. O'Brient, and A. D. Turner. Thermal Kinetic Inductance Detectors for Ground-Based Millimeter-Wave Cosmology. *Journal of Low Temperature Physics*, July 2018. doi: 10.1007/s10909-018-2016-y.

R. A. Sunyaev and Y. B. Zeldovich. Small-Scale Fluctuations of Relic Radiation. *Ap&SS*, 7:3–19, April 1970. doi: 10.1007/BF00653471.

B. E. Svoboda, Y. L. Shirley, C. Battersby, E. W. Rosolowsky, A. G. Ginsburg, T. P. Ellsworth-Bowers, M. R. Pestalozzi, M. K. Dunham, N. J. Evans, II, J. Bally, and J. Glenn. The Bolocam Galactic Plane Survey. XIV. Physical Properties of Massive Starless and Star-forming Clumps. *ApJ*, 822:59, May 2016. doi: 10.3847/0004-637X/822/2/59.

L. J. Swenson, P. K. Day, C. D. Dowell, B. H. Eom, M. I. Hollister, R. Jarnot, A. Kovács, H. G. Leduc, C. M. McKenney, R. Monroe, T. Mroczkowski, H. T. Nguyen, and J. Zmuidzinas. MAKO: a pathfinder instrument for on-sky demonstration of low-cost 350 micron imaging arrays. In *Millimeter, Submillimeter, and Far-Infrared Detectors and Instrumentation for Astronomy VI*, volume 8452 of *Proc. SPIE*, page 84520P, September 2012. doi: 10.1117/12.926223.

L. J. Swenson, P. K. Day, B. H. Eom, H. G. Leduc, N. Llombart, C. M. McKenney, O. Noroozian, and J. Zmuidzinas. Operation of a titanium nitride superconducting microresonator detector in the nonlinear regime. *Journal of Applied Physics*, 113(10):104501, 2013.

P. Szypryt, G. E. Duggan, B. A. Mazin, S. R. Meeker, M. J. Strader, J. C. van Eyken, D. Marsden, K. O'Brien, A. B. Walter, G. Ulbricht, T. A. Prince, C. Stoughton, and B. Bumble. Direct detection of sdss j0926+3624 orbital expansion with arcons. *MNRAS*, 439(3):2765, 2014. doi: 10.1093/mnras/stu137. URL +http://dx.doi.org/10.1093/mnras/stu137.

The Polarbear Collaboration: P. A. R. Ade, Y. Akiba, A. E. Anthony, K. Arnold, M. Atlas, D. Barron, D. Boettger, J. Borrill, S. Chapman, Y. Chinone, M. Dobbs, T. Elleflot, J. Errard, G. Fabbian, C. Feng, D. Flanigan, A. Gilbert, W. Grainger, N. W. Halverson, M. Hasegawa, K. Hattori, M. Hazumi, W. L. Holzapfel, Y. Hori, J. Howard, P. Hyland, Y. Inoue, G. C. Jaehnig, A. H. Jaffe, B. Keating, Z. Kermish, R. Keskitalo, T. Kisner, M. Le Jeune, A. T. Lee, E. M. Leitch, E. Linder, M. Lungu, F. Matsuda, T. Matsumura, X. Meng, N. J. Miller, H. Morii, S. Moyerman, M. J. Myers, M. Navaroli, H. Nishino, A. Orlando, H. Paar, J. Peloton, D. Poletti, E. Quealy, G. Rebeiz, C. L. Reichardt, P. L. Richards, C. Ross, I. Schanning, D. E. Schenck, B. D. Sherwin, A. Shimizu, C. Shimmin, M. Shimon, P. Siritanasak, G. Smecher, H. Spieler, N. Stebor, B. Steinbach, R. Stompor, A. Suzuki, S. Takakura, T. Tomaru, B. Wilson, A. Yadav, and O. Zahn. A Measurement of the Cosmic Microwave Background B-mode Polarization Power Spectrum at Sub-degree Scales with POLARBEAR. *ApJ*, 794:171, October 2014. doi: 10.1088/0004-637X/794/2/171.

R. Thompson, R. Davé, and K. Nagamine. The rise and fall of a challenger: the Bullet Cluster in Λ cold dark matter simulations. *MNRAS*, 452:3030–3037, September 2015. doi: 10.1093/mnras/stv1433.

M. Tinkham. *Introduction to Superconductivity*. Dover Publications, 2nd edition, 2004.

J. van Rantwijk, M. Grim, D. van Loon, S. Yates, A. Baryshev, and J. Baselmans. Multiplexed Readout for 1000-Pixel Arrays of Microwave Kinetic Inductance Detectors. *IEEE Transactions on Microwave Theory Techniques*, 64:1876–1883, June 2016. doi: 10.1109/TMTT.2016.2544303.

C. Wang, Y. Y. Gao, I. M. Pop, U. Vool, C. Axline, T. Brecht, R. W. Heeres, L. Frunzio, M. H. Devoret, G. Catelani, L. I. Glazman, and R. J. Schoelkopf. Measurement and control of quasiparticle dynamics in a superconducting qubit. *Nature Communications*, 5: 5836, December 2014. doi: 10.1038/ncomms6836.

S. Weinreb, J. C. Bardin, and H. Mani. Design of Cryogenic SiGe Low-Noise Amplifiers. *Microwave Theory and Techniques, IEEE Transactions on*, 55(11):2306–2312, Nov. 2007. doi: 10.1109/TMTT.2007.907729.

S. J. C. Yates, J. J. A. Baselmans, A. Endo, R. M. J. Janssen, L. Ferrari, P. Diener, and A. Baryshev. Photon noise limited radiation detection with lens-antenna coupled microwave kinetic inductance detectors. *Appl. Phys. Lett.*, 99(7), 2011.

M. Zaldarriaga. The Polarization of the Cosmic Microwave Background. *Measuring and Modeling the Universe*, page 309, 2004.

Jonas Zmuidzinas. Superconducting microresonators: Physics and applications. *Annual Review of Condensed Matter Physics*, 3(1):169–214, 2012. doi: 10.1146/annurev-conmatphys-020911-125022. URL https://doi.org/10.1146/annurev-conmatphys-020911-125022.

Appendix A

Notation

Symbol	Meaning
f	Microwave frequency ($\sim$ 0.1–4 GHz)
ω	Angular microwave frequency
Δ	Superconducting gap energy
Δ_0	Superconducting gap energy at zero temperature
n_{qp}	Quasiparticle density
N_{qp}	Quasiparticle number
f_0	Resonance frequency
f_{g}	Readout tone frequency
T	Bath temperature
T_{c}	Critical temperature
L	Total inductance
L_{k}	Kinetic inductance
L_{g}	Geometric inductance
C	Capacitance
R	Resistance
α_{k}	Kinetic inductance fraction
Q	Resonator quality factor
Q_{i}	Internal quality factor
Q_{c}	Coupling quality factor

Table A.1: Frequently used symbols.

Symbol	Meaning
N_0	Single-spin density of electrons at the Fermi energy
σ	Complex conductivity
σ_1	Real part of the complex conductivity
σ_2	Imaginary part of the complex conductivity
σ_n	Normal state conductivity
λ	Penetration depth
ξ_0	Quasiparticle coherence length
Z_s	Surface impedance
R_s	Surface resistance
X_s	Surface reactance
τ_qp	Quasiparticle lifetime
Γ	Rate of a process
δ	Perturbation of a quantity

Table A.2: Symbols related to superconductors.

Symbol	Meaning
ν	Incident 'optical' frequency ($\sim$ 150 GHz)
P	Absorbed power
P_0	Incident power
η	Absorption efficiency
η_pb	Pair-breaking efficiency
V_L	Volume of the inductor
x	Response in the frequency direction
R_x	Responsivity (dx/dP) in the frequency direction
T_bb	Temperature of the blackbody
P_s	Power from the millimeter-wave source
T_s	Effective temperature of the millimeter-wave source
τ_r	Resonator ring-down time
b_r	Resonator bandwidth

Table A.3: Symbols related to detector performance and testing.

Symbol	Meaning
f_s	Noise spectral density frequency
S_xx	Noise spectral density in the frequency or phase direction
S_yy	Noise spectral density in the dissipation or amplitude direction
S	Noise spectral density
f_k	Low-frequency noise knee in the noise spectral density
$f_\mathrm{s}^{-\alpha}$	Low-frequency $1/f_\mathrm{s}$ noise in the noise spectral density
f_r	High-frequency roll off in the noise spectral density
NEP	Noise equivalent power
NET	Noise equivalent temperature

Table A.4: Symbols and definitions related to noise.

Subscript	Meaning
γ	Photon
w	White
amp	Amplifier
g	Generation
r	Recombination
gr	Generation-recombination
TLS	Two-level system
t	Theoretical
s	Photon source

Table A.5: Subscript definitions. For example, NEP_{γ} would be the NEP due to photon noise and Γ_{g} would be the generation rate.

Appendix B

Readout and analysis code

Below is a simple example of a data acquisition script:

```
#load modules from kid_readout
from kid_readout.interactive import *
#choose the ROACH-2, baseband signal conditioning box, and associated
   firmware
ri = Roach2Baseband()
#load the resonance frequencies from a file
initial_f0s = np.load('/data/readout/resonances/resonances.npy')/1e6
#set the attenuation, and thus power level, of the tones
dac_atten = 15
ri.set_dac_atten(dac_atten)
#create a new file to put the data in
ncf = new_nc_file(suffix='%d_dB_dac' % dac_atten)
#run a frequency sweep and write it to the file
nsamp = 2**18
offsets = np.arange(-16,16)*512./nsamp
swpa = acquire.run_sweep(ri, tone_banks=initial_f0s[None,:] + offsets[:,
   None], num_tone_samples=nsamp, length_seconds=0, verbose=True,)
ncf.write(swpa)
#identify more accurate resonance frequencies from sweeps if possible
current_f0s = []
for sidx in range(initial_f0s.shape[0]):
  swp = swpa.sweep(sidx)
  res = swp.resonator
  if np.abs(res.f_0 - initial_f0s[sidx]*1e6) > 200e3:
    current_f0s.append(initial_f0s[sidx]*1e6)
  else:
    current_f0s.append(res.f_0)
current_f0s = np.array(current_f0s)/1e6
current_f0s.sort()
#take TOD for 30 seconds, write to file and then close
```

```
ri.set_tone_freqs(current_f0s,nsamp)
ri.select_fft_bins(range(initial_f0s.shape[0]))
meas = ri.get_measurement(num_seconds=30., description='compressor␣off')
ncf.write(meas)
ncf.close()
```

We could then modify the script using the `equipment` module to control the millimeter-wave source, blackbody temperature, etc. depending on the desired measurement.

The following is example code that demonstrates how to begin manipulating the data for analysis.

```
from kid_readout.interactive import *
#open a data file
f = '/data/readout/2017-06-05_152412_mmw_broadband_source_off.nc'
ncf = NCFile(f)
#grab the sweep stream arrays
ssa =  ncf.SweepStreamArray0
#and choose a sweep stream array for a particular detector
det_num = 3
ss = ssa.sweep_stream(det_num)
#plot the noise spectra in the frequency direction for a single resonator
figure()
loglog(ss.S_frequency, ss.S_xx)
xlabel('Hz')
ylabel{'S_\mathrm{xx},␣(Hz^-1)'}
title('%3.3f␣MHz' % ((ss.resonator.f_0)/1e6))
#plot the frequency sweep data points, the model, and the readout
   frequency tone for a single resonator
figure()
fine_freqs = np.linspace(min(ss.sweep.frequency), max(ss.sweep.frequency),
    1000)
model_s21 = ss.resonator.model.eval(params=ss.resonator.current_params,f=
   fine_freqs)
plot(fine_freqs/1e6, dB(model_s21))
plot(ss.sweep.frequency_MHz,dB(ss.sweep.s21_point), 'x', color = 'k')
plot(ss.stream.frequency_MHz, dB(ss.stream.s21_point), 'o')
xlabel('MHz')
ylabel{'S_{21},␣(dB)'}
title('%3.3f␣MHz' % ((ss.resonator.f_0)/1e6)).
```

Below is an example of a script using *pandas* DataFrames, which allows for easy manipulation of multiple detectors and/or datasets at once.

```
from kid_readout.interactive import *
import pandas as pd
```

```
import glob
#grab a file and then the sweep array
f = '/data/readout/2017-05-16_130207_10_dB_load_heater_0.000_V.nc'
ncf = NCFile(f)
swa = ncf.SweepArray0
#send to function to turn into dataframe
df = swa.to_dataframe()
#plot resonance frequency vs Q for all the resonators
figure()
plot(df.res_f_0, df.res_Q, 'x')
ylabel('Q')
xlabel('f')
```

Appendix C

Sonnet simulations

Sonnet is an electromagnetic simulation software that we use when designing LEKIDs. We use it simulate the microwave properties of the resonators. This includes simulating the inductor to find the geometric inductance L_g, the transmission line to check the impedance, and the resonator to verify the resonance frequency is approximately as expected. In this Appendix, I give an example of a Sonnet simulation.

While the IDC value can be calculated using the equation from Lim and Moore [1968], there is no analogous equation for the inductor. Instead, we estimate the geometric inductance L_g using Sonnet. A resonator inductor, similar to those discussed in Ch. 2, is given as an example here.

The setup for a Sonnet simulation is shown in Fig. C.1a. Sonnet is a planar electromagnetic simulator, however we can define the three-dimensional space around it. In this case, we define the dielectric below to have the properties of silicon and the thickness of the wafer, 300 μm. Above, we define the space to be vacuum, which corresponds to the backshort gap. We draw or import the geometry of the inductor. The material properties of the inductor

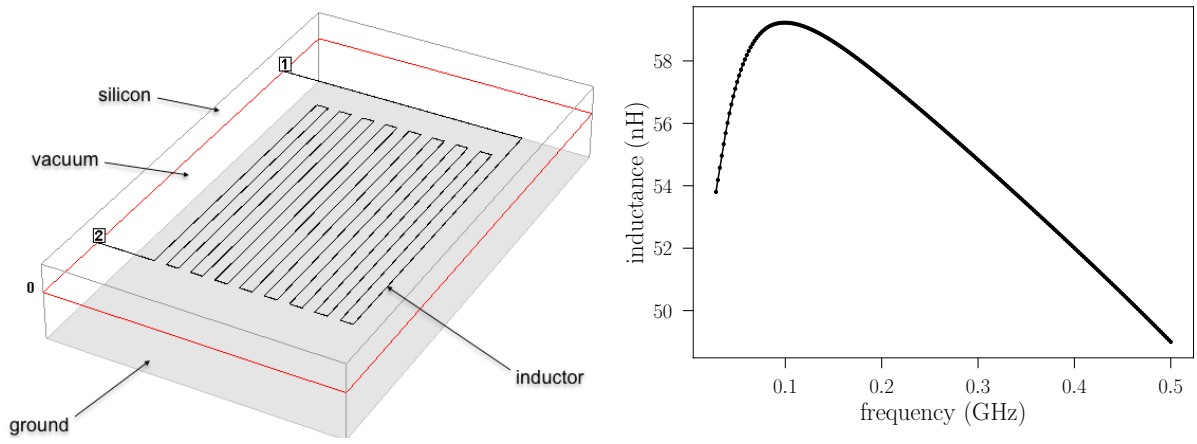

(a) (b)

Figure C.1: **a.** Example of a typical setup for a Sonnet simulation. The planar inductor is surrounded by two dielectrics, which are defined to be silicon and vacuum, reflecting the optical coupling scheme. Sonnet calculates the circuit parameters as a function of frequency. **b.** Plot of the geometric inductance as a function of microwave frequency. After the parameters are calculated by Sonnet, we can plot the circuit parameters. In this instance, we were interested in the inductance of the LEKID absorber, for which there is no analytical expression. The low-frequency readout band we commonly design for is 0.1–0.2 GHz.

can be put in by the user. This is useful as the inductor or resonator can then simulated with kinetic inductance when the surface inductance term is defined. In this example, we are interested in only the geometric inductance so leave the kinetic inductance term as zero and approximate the material as lossless.

Sonnet runs a simulation in which it calculates the circuit parameters, including the S and Y parameters, as a function of frequency. We can then use the parameters to look at the properties of interest. For instance, we use the predefined equation in Sonnet for inductance $L = -\mathrm{Im}(1/Y_{21})(2\pi f)$, where f is the microwave frequency. In Fig. C.1b, the inductance as a function of frequency is shown. This inductance is then used to calculate the approximate LEKID resonance frequencies.

Appendix D

HFSS simulations

HFSS is a 3-dimensional electromagnetic simulation software that we use when designing the detectors. With HFSS, we can simulate the absorption properties of a detector including the absorption spectrum, polarization selectivity, cross-polarization response and radiation leakage. Here, I give an example of simulating a resonator absorber, which is also the LEKID inductor, and the optical couping scheme. This example is similar to the design in Ch. 7.

To setup a simulation in HFSS, we do the following. First, we define the different parts in the optical coupling scheme, as shown in Fig. D.1. This includes the waveguide, waveguide choke, vacuum gap, silicon substrate and finally the metal backshort. We can assign the appropriate material properties to each of these structures. Second, the geometry of the LEKID absorbers are drawn at the interface of the silicon and vacuum. We are able assign the absorber a surface impedance and, for 20 nm Al, we typically use a values between 1.2–4 $\Omega/\square$. Third, we define the excitation at the top of the waveguide, from which the sky signal would enter via the horn. We define the excitation as a single-moded wave with a single polarization that is parallel with one of the absorbers. HFSS simulates the electric

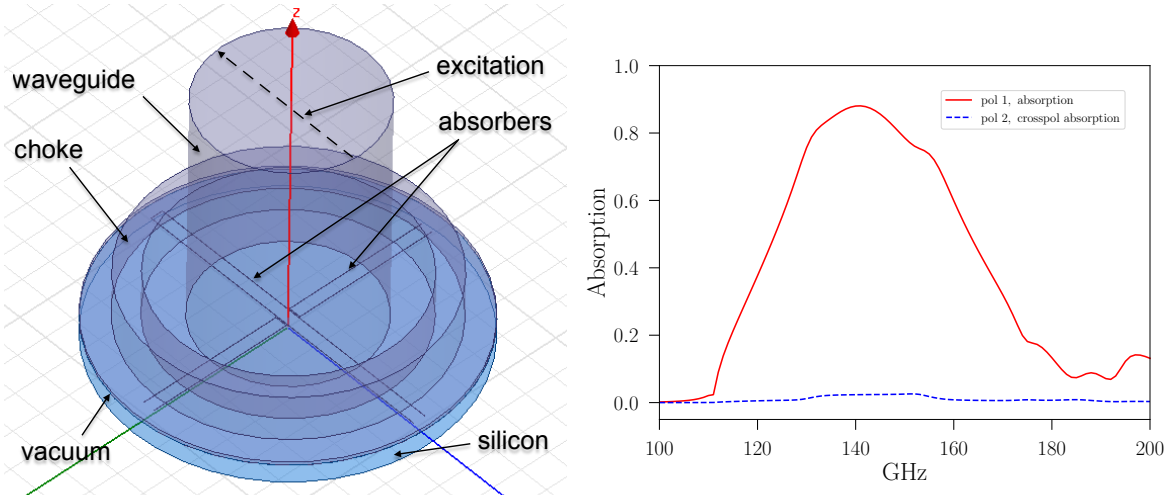

(a) (b)

Figure D.1: **a.** Example of a typical setup for a HFSS simulation. Starting from the top, we define a single-moded, single polarization excitation. The optical coupling scheme is as follows: the waveguide (vacuum) leads to the optical choke (lossless metal), the dielectric (silicon), and finally the backshort (lossless metal). The LEKID inductor is defined as a material with a sheet resistance of 1.2 $\Omega/\square$. HFSS calculates the electric field in the model and at the boundaries as a function of incident millimeter-wave frequency. We can use the simulations to find the absorption in each detector. **b.** Plot of the absorption (pol. 1) and cross-polarization absorption (pol. 2) as a function of incident millimeter-wave frequency.

fields as a function of the frequency of the incident electromagnetic wave. We can then calculate the absorption properties from the simulated electric fields and current densities.

We use these simulations in a number of ways. For instance, to find the absorption properties of pol. 2, we would run the same simulation again with the polarization of incident wave defined perpendicularly. When designing the device, we iterate over parameter space (for example, the spacing of the inductor meander) to find the optimal design. We can also use HFSS to model systematic errors, such as misalignment or deviations from the optimal design due to fabrication or machining tolerances.

Appendix E

Detector module design

We design the detector/focal plane modules using Solidworks, a computer-aided design (CAD) program, as shown in Fig. E.1. A detector module consists of a horn array, which couples the radiation to the detectors, and a bottom, which holds the detector array (see Figs. 4.4, 5.2, and 7.2). We have built both prototype and full-size modules, which are designed to be tiled into the focal plane of a telescope. The overall optical couping design is primarily determined by the HFSS simulations, as discussed in Secs. 4.2.1 and 7.2.1 and shown in Appendix D. The design of the module reflects this optical coupling scheme, however many additional factors need to be considered. This includes alignment between the detectors and horns, thermal contractions, and the interface of the module with the cold-stage, filters, and temperature sensors. These considerations need to be balanced against the achievable machining tolerances. In addition, these tolerances contribute to the systematics of the experiment and need to be modeled.

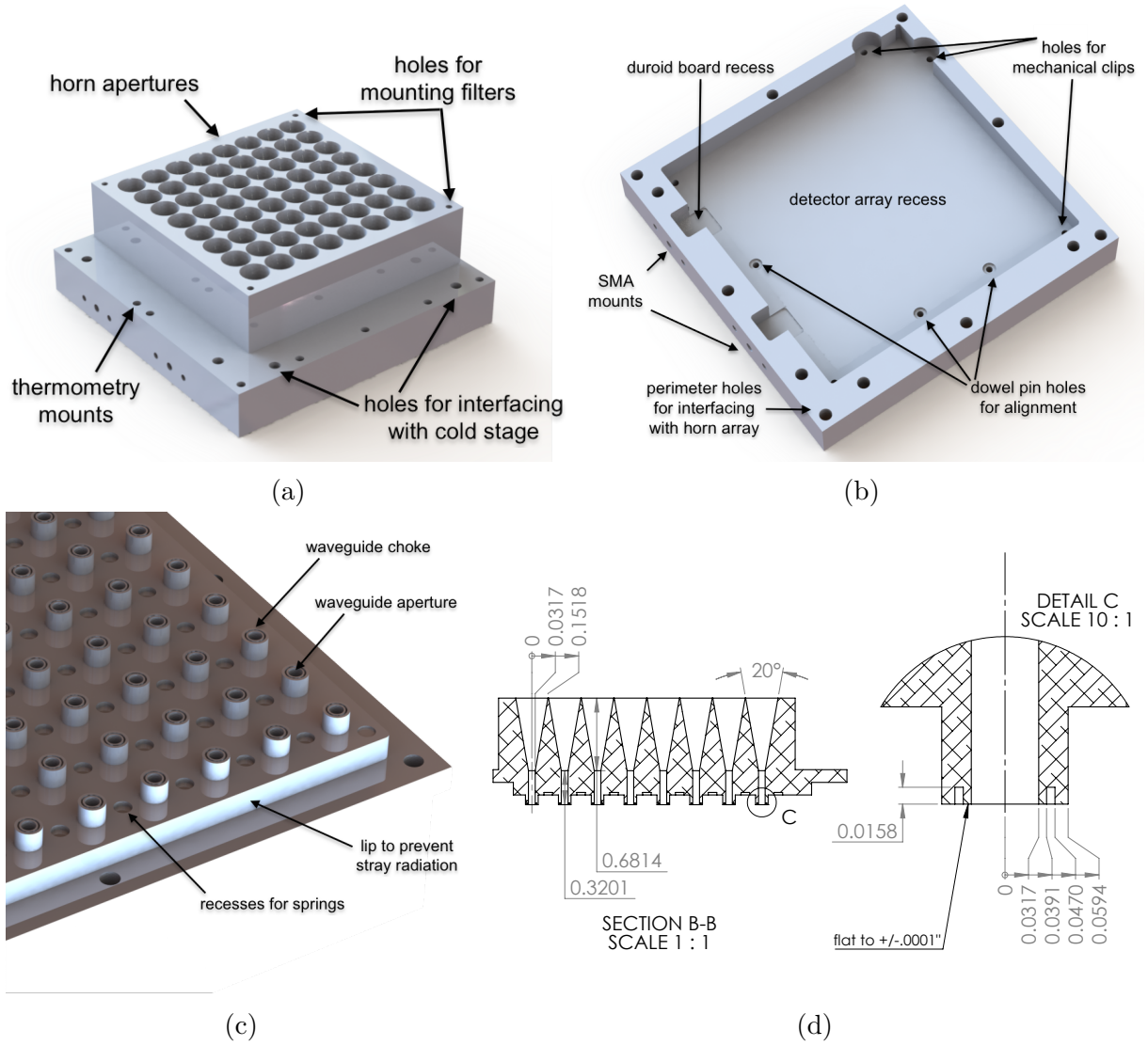

Figure E.1: **a.** CAD model of a detector module. The module has two main parts: the top, which is the horn array, and the bottom, which hosts the detector array. Beyond the optical coupling scheme, there are a number of design considerations that must be taken into account. Visible in this rendering are the holes for mounting the filters, which define the bandpass. Also visible are the holes for mounting the low-temperature thermometers to monitor the module temperature. There are additional holes for interfacing to the cryostat cold stage. **b.** Model of the bottom of the module. The main recess is for the detector array, and must be milled smooth to a tolerance of a few microns. There are mounts for the SMA connectors, as well as for the clips, which hold the detector array against the dowel pins. The dowel pins are the mechanical reference for the detector array and for the horn array to the module bottom. The thermal contraction of them materials must be taken into account; the module is designed so that when cold, the detectors and horns align. **c.** Model of the underside of the horn array. **d.** Example of a drawing specifying tolerances for machining the detector module. The effect of these tolerances can be simulated using HFSS.

Appendix F

Dual-polarization LEKIDs testbed

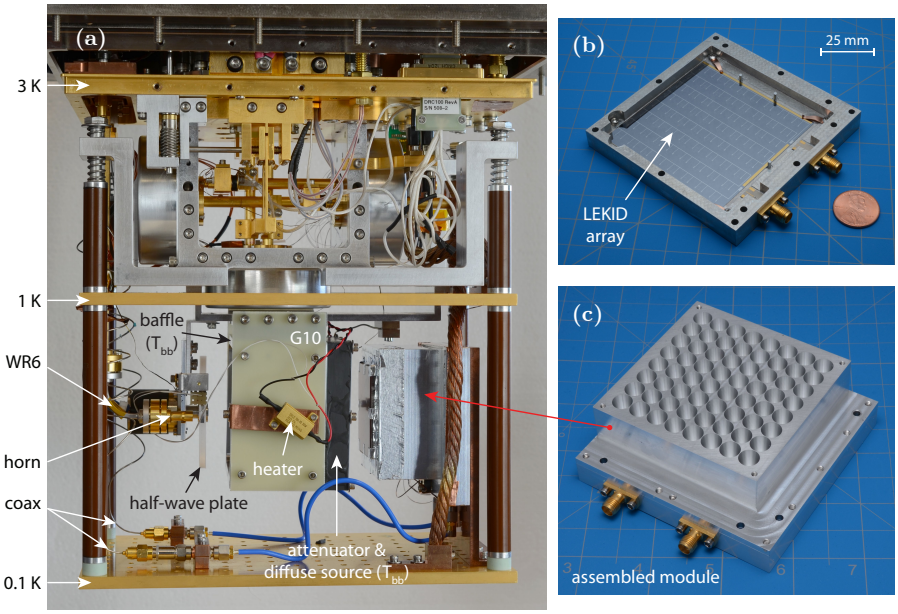

Figure F.1: For clarity, we present an additional figure that shows the testbed used in Ch. 7 [McCarrick et al., 2018]. **a.** Photograph of the cryogenic testbed. The LEKID array is in the module mounted vertically on the 0.1 K stage. The array is illuminated by millimeter-wave radiation, which is routed into the cryostat on the WR6 waveguide. To illuminate the detectors, the radiation is launched from a horn through an attenuator, which also acts as a diffuse background source. A fast pin-switch allows the source to be chopped at 122 Hz creating a square wave. **b.** Photograph of the LEKID array mounted in the aluminum package bottom with the horn array removed. The array consists of 128 LEKIDs with unique resonance frequencies. **c.** Photograph of the LEKID module with the horn apertures facing up. The horn array seals the module.

Appendix G

Measuring quasiparticle lifetimes

Measurements of the change in the complex conductivity of KIDs have been previously used to investigate quasiparticle lifetimes. These experiments typically employ one of two methods to extract τ_{qp}. In the first, τ_{qp} is measured through the roll-off of the device noise spectrum [de Visser et al., 2014]. In the second, the KID is illuminated by an optical pulse. A simple exponential [Barends et al., 2008] is then fit to the response data of the resonator in the time domain. However, the exponential model has been shown to not accurately describe the response decay [Baselmans et al., 2017, McCarrick et al., 2018], so a more complete expression is needed. In Flanigan [2018], the quasiparticle dynamics equation was rewritten in terms of δn_{qp}. The solution to this revised equation can be used to describe the LEKID response to either an instantaneous increase or decrease in illumination. The expression depends on τ_{qp}.

The equation describing quasiparticle dynamics is given as [Wang et al., 2014]

$$\frac{\mathrm{d}n_{\mathrm{qp}}}{\mathrm{d}t} = -Rn_{\mathrm{qp}}^2 - Sn_{\mathrm{qp}} + g. \tag{G.1}$$

Here, R is the recombination constant, S the single-quasiparticle decay constant, and g is the generation rate. If the linear term is dominant, an exponential model describes $n_{\mathrm{qp}}(t)$. If the recombination term dominates, the exponential model is not sufficient. Assuming the generation rate is constant, the differential equation can be rewritten in terms of the change in quasiparticle density $\delta n_{\mathrm{qp}}(t)$ as [Flanigan, 2018]

$$\frac{\mathrm{d}\delta n_{\mathrm{qp}}}{\mathrm{d}t} = -R\delta n_{\mathrm{qp}}^2 - \tau_{\mathrm{qp}}^{-1}\delta n_{\mathrm{qp}}. \tag{G.2}$$

Solving this equation, the perturbations around the steady state quasiparticle density δn_{qp} can be written as

$$\delta n_{\mathrm{qp}}(t) = \frac{\delta n_0 \exp(-t/\tau_{\mathrm{qp}})}{1 + R\tau_{\mathrm{qp}}\delta n_0[1 - \exp(-t/\tau_{\mathrm{qp}})]}. \tag{G.3}$$

This equation describes the response of the detector with the initial condition $\delta n_{\mathrm{qp}}(t)\Big|_0 = \delta n_0$, where δn_0 is the initial perturbation. Solving the differential equation with the initial condition $\delta n_{\mathrm{qp}}(t)\Big|_0 = -\delta n_0$, describes the rising edge and a negative initial perturbation. In this case, $\delta n_{\mathrm{qp}}(t)$ is

$$\delta n_{\mathrm{qp}}(t) = \frac{\delta n_0 \exp(-t/\tau_{\mathrm{qp}})}{R\tau_{\mathrm{qp}}\delta n_0[1 - \exp(-t/\tau_{\mathrm{qp}})] - 1}. \tag{G.4}$$

Given that $\delta n_{\mathrm{qp}}(t) = \xi x(t)$ [Gao et al., 2008a], where ξ is a constant, the explicit equation that we can fit the response of the detector to is

$$\begin{aligned} x(t) = \frac{\alpha \exp(-(t-t_0)/\tau_{\mathrm{qp}})}{\pm 1 + \beta\tau_{\mathrm{qp}}[1 - \exp(-(t-t_0)/\tau_{\mathrm{qp}})]}\Theta(t-t_0) \\ \pm\alpha\Theta(t_0 - t) + x_0. \end{aligned} \tag{G.5}$$

Here t_0 corresponds to the beginning of the decay, x_0 is an offset parameter, and Θ is the step

function. We have made the substitution $\beta = R\delta n_0$ and $\alpha = \xi\delta n_0$. The fit yields $\tau_{\rm qp}$, β, α, t_0 and x_0 where $\tau_{\rm qp}$, β, and α are the physically meaningful parameters. The functional form appears to accurately describe the data. We find the fit can yield a negative β parameter and we are exploring how to physically interpret this.